ORGANIC ELECTRONICS FROM SYNTHESIS TO APPLICATIONS

EDITED BY: John George Hardy, Jae Young Lee, Carlo Augusto Bortolotti,
Wolfgang Knoll and Fabio Biscarini

PUBLISHED IN: Frontiers in Chemistry

frontiers Research Topics

Frontiers eBook Copyright Statement

ISSN 1664-8714
ISBN 978-2-88963-453-8
DOI 10.3389/978-2-88963-453-8

About Frontiers

Frontiers is more than just an open-access publisher of scholarly articles: it is a pioneering approach to the world of academia, radically improving the way scholarly research is managed. The grand vision of Frontiers is a world where all people have an equal opportunity to seek, share and generate knowledge. Frontiers provides immediate and permanent online open access to all its publications, but this alone is not enough to realize our grand goals.

Frontiers Journal Series

The Frontiers Journal Series is a multi-tier and interdisciplinary set of open-access, online journals, promising a paradigm shift from the current review, selection and dissemination processes in academic publishing. All Frontiers journals are driven by researchers for researchers; therefore, they constitute a service to the scholarly community. At the same time, the Frontiers Journal Series operates on a revolutionary invention, the tiered publishing system, initially addressing specific communities of scholars, and gradually climbing up to broader public understanding, thus serving the interests of the lay society, too.

Dedication to Quality

Each Frontiers article is a landmark of the highest quality, thanks to genuinely collaborative interactions between authors and review editors, who include some of the world's best academicians. Research must be certified by peers before entering a stream of knowledge that may eventually reach the public - and shape society; therefore, Frontiers only applies the most rigorous and unbiased reviews.
Frontiers revolutionizes research publishing by freely delivering the most outstanding research, evaluated with no bias from both the academic and social point of view. By applying the most advanced information technologies, Frontiers is catapulting scholarly publishing into a new generation.

What are Frontiers Research Topics?

Frontiers Research Topics are very popular trademarks of the Frontiers Journals Series: they are collections of at least ten articles, all centered on a particular subject. With their unique mix of varied contributions from Original Research to Review Articles, Frontiers Research Topics unify the most influential researchers, the latest key findings and historical advances in a hot research area! Find out more on how to host your own Frontiers Research Topic or contribute to one as an author by contacting the Frontiers Editorial Office: researchtopics@frontiersin.org

ORGANIC ELECTRONICS FROM SYNTHESIS TO APPLICATIONS

Topic Editors:
John George Hardy, Lancaster University, United Kingdom
Jae Young Lee, Gwangju Institute of Science and Technology, South Korea
Carlo Augusto Bortolotti, University of Modena and Reggio Emilia, Italy
Wolfgang Knoll, Austrian Institute of Technology (AIT), Austria
Fabio Biscarini, University of Modena and Reggio Emilia, Italy

Organic electronics is one of the most exciting emerging areas of materials science. It is a highly interdisciplinary research area involving scientists and engineers who develop organic molecules with interesting properties for a variety of applications in technical industries (e.g. circuitry, energy harvesting/storage, etc.) and medical applications (e.g. bioelectronics for sensors, tissue scaffolds for tissue engineering, etc.).

This Research Topic collects articles that report advances in chemistry (e.g. design and synthesis of molecules with various molecular weights and structures); physical chemistry and chemical physics, and computational/theoretical research (e.g. to push the boundaries of our understanding); chemical engineering (e.g. design, prototyping and manufacturing devices); materials scientists and technologists to explore different markets for the technologies employing such materials, the organic bioelectronics field and green/sustainable electronics.

Citation: Hardy, J. G., Lee, J. Y., Bortolotti, C. A., Knoll, W., Biscarini, F., eds. (2020). Organic Electronics From Synthesis To Applications. Lausanne: Frontiers Media SA. doi: 10.3389/978-2-88963-453-8

Table of Contents

frontiers in Chemistry

ORIGINAL RESEARCH
published: 11 March 2019
doi: 10.3389/fchem.2019.00123

Fast and Selective Post-polymerization Modification of Conjugated Polymers Using Dimethyldioxirane

Emmanuel Reichsöllner[1], Adam Creamer[2], Shengyu Cong[2], Abby Casey[2], Simon Eder[1], Martin Heeney[2] and Florian Glöcklhofer[1,2]*

[1] Institute of Applied Synthetic Chemistry, TU Wien, Vienna, Austria, [2] Department of Chemistry and Centre for Plastic Electronics, Imperial College London, London, United Kingdom

Modification of functional groups attached to conjugated polymer backbones can drastically alter the material properties. Oxidation of electron-donating thioalkyl substituents to electron-withdrawing sulfoxides or sulfones is a particularly effective modification. However, so far, this reaction has not been studied for the modification of conjugated polymers used in organic electronics. Crucial questions regarding selectivity and reaction time waited to be addressed. Here, we show that the reaction is highly selective and complete within just a few minutes when using dimethyldioxirane (DMDO) for the oxidation of thioalkyl substituents attached to the well-investigated conjugated polymers poly(9-(1-octylnonyl)carbazole-*alt*-4,7-dithienylbenzothiadiazole) (PCDTBT) and poly(9,9-dioctylfluorene-*alt*-benzothiadiazole) (F8BT). The selectivity was confirmed by comparison with polymers obtained from pre-oxidized monomers and by control experiments using related polymers without thioalkyl substituents. Using DMDO, the oxidation yields acetone as the only side-product, which reduces the work-up to mere evaporation of solvents and excessive reagent. Our results show that this oxidation is an exciting method for the preparation of electron-deficient conjugated polymers. It may even allow the preparation of electron acceptors for solar cells directly from the electron donors.

Keywords: organic electronics, conjugated polymers, post-polymerization modification, oxidation, sulfoxide, sulfone, PCDTBT, F8BT

Edited by:
Carlo Augusto Bortolotti, University of Modena and Reggio Emilia, Italy

Reviewed by:
Florenci Vicent González, University of Jaume I, Spain
Mindy Levine, University of Rhode Island, United States

****Correspondence:***
Florian Glöcklhofer
f.glocklhofer@imperial.ac.uk

Specialty section:
This article was submitted to Organic Chemistry, a section of the journal Frontiers in Chemistry

Received: *15 November 2018*
Accepted: *15 February 2019*
Published: *11 March 2019*

Citation:
Reichsöllner E, Creamer A, Cong S, Casey A, Eder S, Heeney M and Glöcklhofer F (2019) Fast and Selective Post-polymerization Modification of Conjugated Polymers Using Dimethyldioxirane. Front. Chem. 7:123. doi: 10.3389/fchem.2019.00123

INTRODUCTION

Conjugated polymers are most frequently used in organic electronics, but the specific applications strongly depend on the properties of the polymer (Swager, 2017; Ibanez et al., 2018). Functional groups can be used to tune these properties (Guo et al., 2013); the desired functional groups can be introduced either by using appropriate monomers for polymerization or by post-polymerization modification. The latter can be achieved either by introducing new functional groups onto the polymer backbone (Crossley et al., 2017) or by modifying or substituting functional groups already present (Schelkle et al., 2014; Creamer et al., 2018). As the main advantage of post-polymerization modification, polymers with varying properties can be obtained from the same starting polymer by using different reagents for modification or by varying the degree or distribution of modification (statistical or, for example, surface modification). Furthermore, functional groups that would either impair polymerization or degrade during polymerization may be introduced. The modifications can be designed to slightly tune or optimize the optoelectronic properties (e.g., for tuning LUMO/LUMO offsets in solar cells) or to change them drastically (e.g., for turning electron donors into electron acceptors).

One such modification to drastically change the properties is the oxidation of electron donating thioalkyl substituents to electron withdrawing sulfones (or sulfoxides). Sulfone substituents have been reported to greatly lower the HOMO/LUMO energy levels of conjugated polymers, turning them into electron acceptors and improving their air stability (Zhang et al., 2009; Hubijar et al., 2013). To perform this modification on polymers, we considered dimethyldioxirane (DMDO) to be the most suitable reagent, as it yields acetone as the only side-product (González-Núñez et al., 2002), which can be easily removed by evaporation (in contrast to side-products of metal oxidants or larger organic oxidants). The easy removal of the side-products is highly beneficial for applications sensitive to impurities, including applications in organic electronics, and may even allow for post-processing modification, for example surface modification of polymer thin-films or nanoparticles. Using other reagents, such as *meta*-chloroperoxybenzoic acid (mCPBA) or Rozen's reagent, is reported to require washing with aqueous base and water for purification following the oxidation (Wei et al., 2014), which not only adds additional steps to the preparation but also potentially complicates solid state reactions.

We have previously shown that DMDO can be used for post-polymerization modification, but the polymers investigated (obtained by Cu(I)-catalyzed azide-alkyne cycloaddition polymerization) were of low molecular weight (M_n = 3.5–3.6 kDa, M_w = 7.2–7.5 kDa) and did not exhibit properties of conjugated polymers (Glöcklhofer et al., 2014, 2015); neither absorption at longer wavelengths nor electrical conductivity were observed. Therefore, it remained unclear whether DMDO can also be used for the modification of truly conjugated polymers. Furthermore, the selectivity of the reaction as well as the required reaction time have not been addressed so far, although—if fast and selective–such a modification of truly conjugated polymers would be particularly interesting for organic electronics, as it may turn polymers from preferentially hole-transporting to electron-transporting or from electron-donating to electron-accepting.

For the present work, two very well-investigated conjugated polymers were selected for modification to address these questions, PCDTBT and F8BT. Both polymers are frequently used in organic electronics, in particular for organic solar cell and transistor applications (Kim et al., 2004; Zaumseil et al., 2006; Beaupré and Leclerc, 2013). Thioalkyl substituents that enable the modification were attached to the benzothiadiazole units of the polymers (**Figure 1**). Polymers with one (**1a-S** and **2-S**) and two (**1b-S**) thioalkyl substituents at the benzothiadiazole units were selected.

It was our plan to (i) find suitable conditions for modification of the polymers (solvent, temperature, amount of DMDO), (ii) investigate the selectivity of the reaction (considering that thiophene, carbazole, and benzothiadiazole units are present, which are potentially prone to oxidation), and (iii) determine the required reaction time.

RESULTS

PCDTBT-Based Polymers

PCDTBT-based polymer **1a-S** (**Figure 2**, top left) was used for initial investigations focusing on reaction conditions and selectivity, as the carbazole, thiophene, and benzothiadiazole units of the polymer are all potentially prone to oxidation by DMDO (**Table 2** gives an overview of the tested reaction conditions).

The experiments showed that CH_2Cl_2 (which we used previously for modifications with DMDO) is not a suitable solvent for the modification of **1a-S**. The polymer precipitated during reaction, which resulted in side reactions indicated by the same ^{1}H NMR peaks that we found later when treating the polymer with a large excess of DMDO for 24 h (**Figure 3**). Chlorobenzene was found to be a better solvent; testing different amounts of DMDO for the oxidation in this solvent revealed that 2.5 equivalents (equiv) per repeat unit of the polymer resulted in complete oxidation to **1a-SO$_2$**. The oxidation resulted in significant shifts of the ^{1}H NMR peaks of the protons next to the thioalkyl sulfur atom (**Figure 3**): the peak of the benzothiadiazole proton shifted from 8.05 to 8.78 ppm, the peak of the two aliphatic protons shifted from 3.12 to 3.03 ppm. The upfield shift of the aliphatic signal is counterintuitive but may be caused by steric effects. A similar upfield shift from 3.07–3.01 to 2.97–2.86 ppm was observed when oxidizing monomer **3-S** to **3-SO$_2$** (**Figure 2**). Comparison of the ^{13}C

PCDTBT-based polymers: **F8BT-based polymer:**

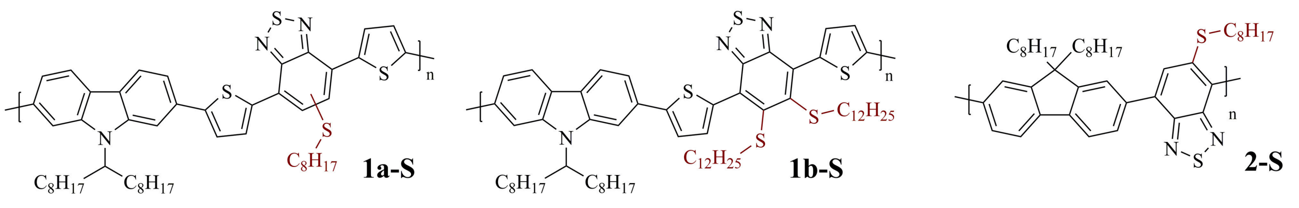

1a-S **1b-S** **2-S**

FIGURE 1 | Conjugated polymers used to investigate the post-polymerization modification with DMDO. Left: PCDTBT-based polymers with one **(1a-S)** and two **(1b-S)** thioalkyl substituents attached to the benzothiadiazole units. Right: F8BT-based polymer with one thioalkyl substituent attached to the benzothiadiazole units **(2-S)**.

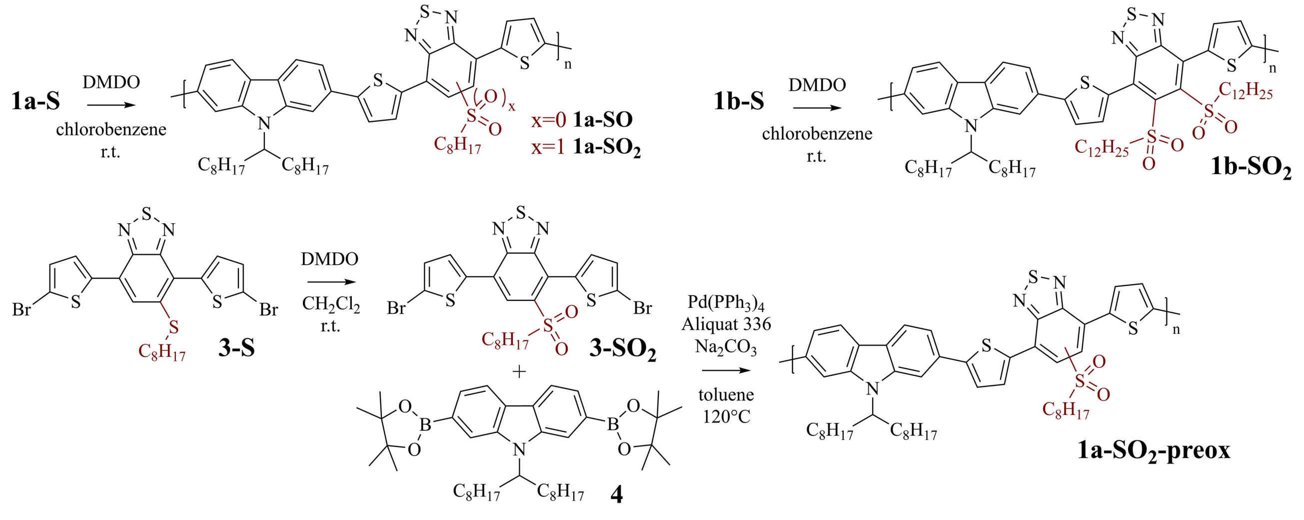

FIGURE 2 | Top: Post-polymerization modification of PCDTBT-based polymers **1a-S** and **1b-S** to sulfoxide-substituted polymer **1a-SO** and sulfone-substituted polymers **1a-SO$_2$** and **1b-SO$_2$**. Bottom: Synthesis of sulfone-substituted monomer **3-SO$_2$** and subsequent polymerization with **4**, affording sulfone-substituted polymer **1a-SO$_2$-preox** for comparison with **1a-SO$_2$**.

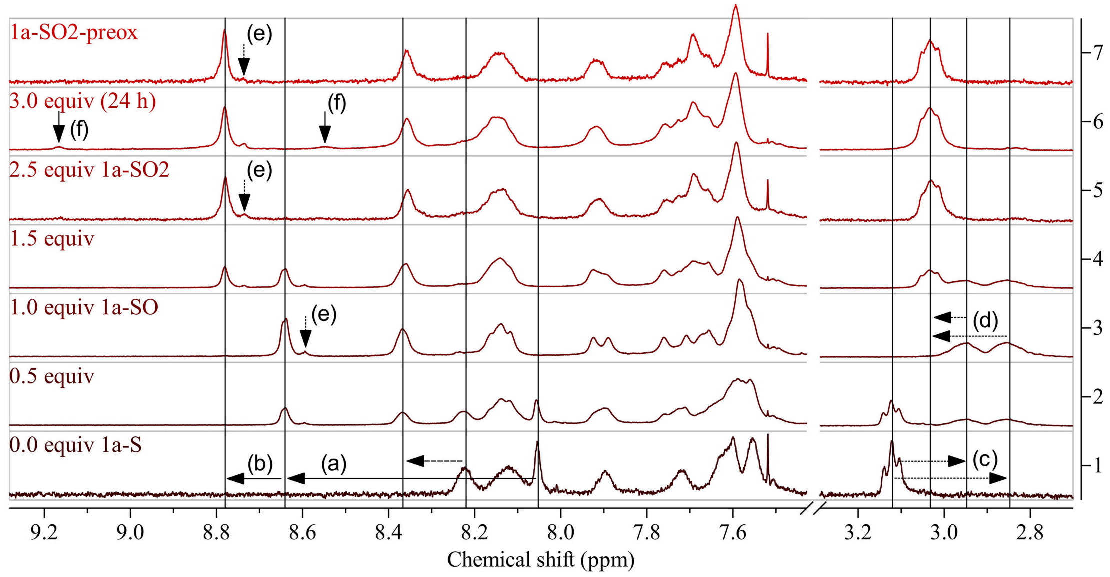

FIGURE 3 | ^{1}H NMR spectra of **1a-S** (bottom) and corresponding polymers obtained by modification using increasing amounts of DMDO (bottom to top: 0.5 equiv, 1.0 equiv: **1a-SO**, 1.5 equiv, 2.5 equiv: **1a-SO$_2$**). The selectivity of the modification was evaluated by treating the starting polymer with a large excess of DMDO for prolonged time [3.0 equiv (24 h)] and by comparison of **1a-SO$_2$** with **1a-SO$_2$-preox** (top). Horizontal arrows show indicative shifts upon modification: (a) downfield shift of the peak of the benzothiadiazole proton upon oxidation to the sulfoxide and (b) further shift upon oxidation to the sulfone, (c) upfield shift and splitting of the peak of the aliphatic protons next to the thioalkyl sulfur upon oxidation to the sulfoxide and (d) downfield shift and reunification upon further oxidation to the sulfone. Vertical arrows indicate (e) peaks attributed to end groups and (f) side reactions. See **Supplementary Material** for full spectra.

NMR signal of the aliphatic carbon next to the thioalkyl sulfur, which should be less affected by steric effects, revealed that–upon oxidation–this peak is shifted downfield as expected, from 34.28 to 54.35 ppm. This corresponds well with the shift from 33.1 to 54.0 ppm observed by us in a similar oxidation (Glöcklhofer et al., 2014).

Interestingly, selective oxidation to the sulfoxide-substituted polymer **1a-SO** occurred when using 1.0 equiv of DMDO. A slightly smaller shift of the benzothiadiazole peak to 8.64 ppm was observed (**Figure 3**(a)); neither the benzothiadiazole peaks of **1a-S** nor **1a-SO$_2$** were present. Oxidation to the sulfoxide was confirmed by the splitting of the aliphatic peak into two peaks at 2.95 and 2.85 ppm (**Figure 3**(c)), a result of the two aliphatic protons becoming diastereotopic. Oxidation with 0.5/1.5 equiv resulted in the presence of the benzothiadiazole peaks of both **1a-SO** and **1a-S** / **1a-SO$_2$** and **1a-SO** in the expected ratio of 1:1. Treating the polymer with 3.0 equiv for 24 h resulted in the appearance of two small additional peaks at 9.17 and 8.55 ppm (**Figure 3**(f), solid vertical arrows), as mentioned above. This is attributed to slow side reactions occurring at other sites of the polymer that are prone to oxidation.

To confirm the selectivity of the modification of **1a-S** to **1a-SO$_2$** under the optimized conditions, we prepared polymer **1a-SO$_2$-preox** for comparison using monomers **3-SO$_2$** and **4** (**Figure 2**, bottom). The ^{1}H NMR spectra of **1a-SO$_2$** and **1a-SO$_2$-preox** turned out to be identical, except for a small peak next to the benzothiadiazole peak, which was slightly larger for **1a-SO$_2$** (**Figure 3**(e), dotted vertical arrows). We attributed this peak to end groups of the polymers, as the corresponding peak was also present in the spectrum of **1a-SO** and as the size of the peak did not increase when treating the polymer with 3.0 equiv DMDO for 24 h. As this meant **1a-SO$_2$-preox** must have a significantly higher average molecular weight than the other polymers, we performed GPC measurements, confirming our assumption (**Table 1**).

TABLE 1 | GPC results of PCDTBT-based polymers **1a-S**, **1a-SO**, **1a-SO$_2$**, and **1a-SO$_2$-preox**.

Polymer	M_n [kDa]	M_w [kDa]	Đ
1a-S	23	52	2.3
1a-SO	23	50	2.2
1a-SO$_2$	22	49	2.2
1a-SO$_2$-preox	53	97	1.8

TABLE 2 | Screening of reaction conditions using PCDTBT-based polymers 1a-S and 1b-S as starting polymers.

Starting polymer	Reaction solvent	DMDO [equiv]	Reaction time	Result (analysis by ^{1}H NMR spectroscopy, also see Figures 3, 4)
1a-S	CH_2Cl_2	2.5	1.5 h	Precipitation of the polymer upon oxidation, byproduct peaks at 9.17 and 8.55 ppm
1a-S	Chlorobenzene	0.5	1.0 h	Partial oxidation to SO, no formation of SO$_2$
1a-S	Chlorobenzene	1.0	1.0 h	Complete and selective oxidation to **1a-SO**, no formation of SO$_2$
1a-S	Chlorobenzene	1.5	1.0 h	SO$_2$:SO ratio: approx.1:1, no byproduct signal
1a-S	Chlorobenzene	2.0	1.0 h	Incomplete oxidation to SO$_2$ (SO$_2$:SO ratio: 9:1)
1a-S	Chlorobenzene	2.5	1.0 h	Complete oxidation to **1a-SO$_2$**, very small byproduct peak at 9.17 ppm, high selectivity
1a-S	Chlorobenzene	3.0	24 h	Complete oxidation to SO$_2$, but byproduct peaks at 9.17 and 8.55 ppm
1b-S	Chlorobenzene	1.0	1.0 h	Formation of SO, also some SO$_2$
1b-S	Chlorobenzene	2.0	1.0 h	Considerable formation of SO$_2$, S still present
1b-S	Chlorobenzene	3.0	1.0 h	Formation of some neighboring SO$_2$, no more S
1b-S	Chlorobenzene	4.5	1.0 h	Complete oxidation to **1b-SO$_2$**

Final conditions for the synthesis of 1a-SO, 1a-SO$_2$, and 1b-SO$_2$ highlighted in gray. Reaction procedure: DMDO in acetone (0.074 M) added to stirred polymer solutions (concentration of repeat unit: 0.01 M) at room temperature. Work-up: evaporation of solvents (and excessive DMDO) under reduced pressure at 50°C.

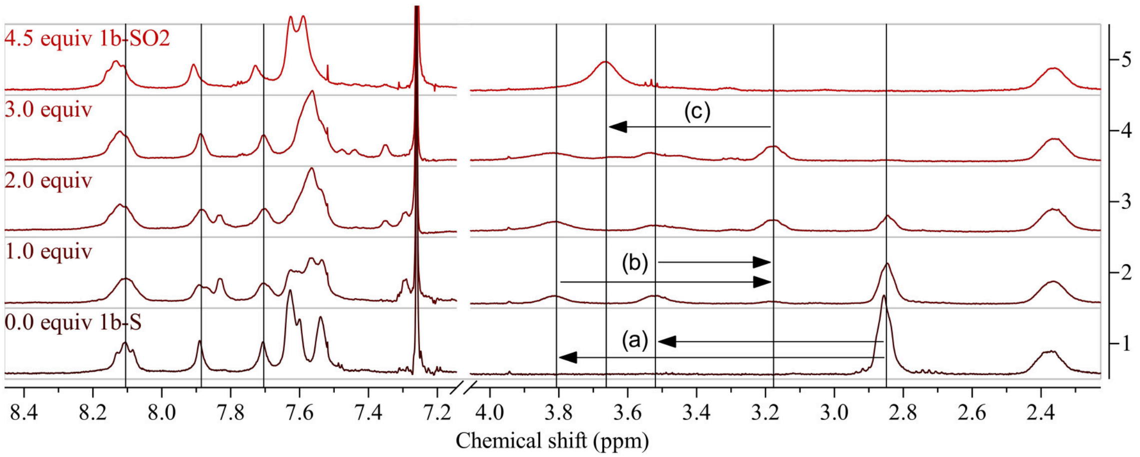

FIGURE 4 | ^{1}H NMR spectra of **1b-S** (bottom) and corresponding polymers obtained by modification using increasing amounts of DMDO (bottom to top; 4.5 equiv: **1b-SO$_2$**). Arrows show the shifts of the peak of the aliphatic protons next to the thioalkyl sulfur upon modification: (a) downfield shift and splitting of the peak of the aliphatic protons next to the thioalkyl sulfur upon oxidation to the sulfoxide, (b) upfield shift and reunification by further oxidation to the sulfone, (c) downfield shift upon occurrence of two neighboring sulfones. See **Supplementary Material** for full spectra.

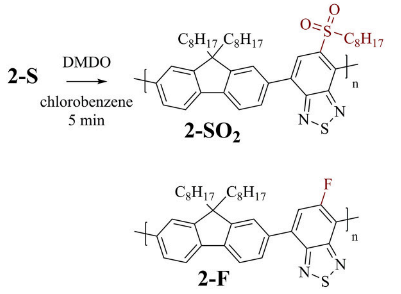

FIGURE 5 | Top: Post-polymerization modification of F8BT-based polymer **2-S** to sulfone-substituted polymer **2-SO$_2$**. Bottom: Related F8BT-based polymer **2-F** (without thioalkyl substituents) used for control experiments.

Post-polymerization modification of **1b-S** was carried out under the same conditions (**Table 2** gives an overview of the experiments). However, as there are twice as many thioalkyl groups per repeat unit present, 4.5 equiv DMDO were used for the oxidation to **1b-SO$_2$** (**Figure 2**, top right). As for the modifications of **1a-S**, the peak of the aliphatic protons next to the sulfur atom shifted significantly, from 2.85 to 3.66 ppm (**Figure 4**). As there are no protons present at the benzothiadiazole units, shifts in the aromatic region were less pronounced.

Using 1.0 equiv DMDO for the modification, the aliphatic peak split into two peaks at 3.81 and 3.52 ppm (**Figure 4**(a)), again confirming the formation of sulfoxides. The weak peak at 3.18 ppm is assigned to some oxidation to sulfones, indicating that the modification to sulfoxides is less selective for **1b-S** than for **1a-S**. Using 2.0 equiv, this peak increased to the same size as the residual peak of the non-oxidized thioalkyl substituents, which is in accordance with the assignment of the peaks. The peak of the thioalkyl substituents disappeared when using 3.0 equiv; the peak of the final polymer **1b-SO$_2$** at 3.66 ppm (attributed to two neighboring sulfone groups) started to appear.

F8BT-Based Polymers

F8BT-based polymer **2-S** (**Figure 5**, top) was used for investigating the time required for complete oxidation to **2-SO$_2$** under the same conditions as used for the modifications of the PCDTBT-based polymers. An overview of the experiments is provided in **Table 3**.

A reaction time of 1 h (before evaporation of solvents and excessive reagent) resulted in complete oxidation to **2-SO$_2$**, indicated by shifts of the protons next to the sulfur atom from 7.95 to 8.71 ppm (benzothiadiazole proton, **Figure 6**(a)) and 2.96 to 2.83 ppm (aliphatic protons, **Figure 6**(b)). Interestingly, when reducing the reaction time to 5 min, the same results were obtained. Addition of DMDO to the reaction and immediate evaporation of solvents and reagent (0 min reaction time) resulted in incomplete oxidation.

In contrast to PCDTBT-based polymer **1a-S**, no side reactions were observed when treating **2-S** with 3.0 equiv DMDO for 24 h. The absence of side reactions was further confirmed for this type of polymer by treating **2-F** (**Figure 5**, bottom) with DMDO, which did not result in any changes of the ^{1}H NMR spectrum.

TABLE 3 | Screening of reaction times using F8BT-based polymer **2-S** as starting polymer.

Starting polymer	DMDO [equiv]	Reaction time	Result (analysis by ^{1}H NMR spectroscopy, also see Figure 6)
2-S	2.5	0 min	Incomplete oxidation
2-S	2.5	5 min	Complete and selective oxidation to **2-SO$_2$**
2-S	2.5	1 h	Complete and selective oxidation to **2-SO$_2$**
2-S	3.0	24 h	Complete and selective oxidation to **2-SO$_2$** (no byproduct signals)
2-F	2.5	5 min	No reaction, no change of ^{1}H NMR spectrum

*Final conditions for the synthesis of **2-SO$_2$** highlighted in gray. The selectivity was investigated by treating **2-S** with a large excess of DMDO for prolonged time (3.0 equiv, 24 h) and by control experiments using **2-F.** Reaction procedure: DMDO in acetone (0.104 M) added to stirred polymer solutions in chlorobenzene (concentration of repeat unit: 0.01 M) at room temperature. Work-up: evaporation of solvents (and excessive DMDO) under reduced pressure at 50°C.*

MATERIALS AND METHODS

Solvents and chemicals were purchased from commercial suppliers and used without further purification. DMDO was prepared scaling down a published protocol (Mikula et al., 2013).

Synthesis of Monomer 3-S and PCDTBT-Based Polymers 1a-S, 1b-S, and 1a-SO$_2$-Preox

Monomer **3-S** and polymer **1a-S** were synthesized according to our previously reported work (Creamer et al., 2017), as was **1b-S** (Casey et al., 2014).

Synthesis of **1a-SO$_2$-preox** was based on these two previously reported works. Monomer **3-SO$_2$** (63.5 mg, 0.100 mmol, 1.0 equiv), 9-(9-heptadecanyl)-9*H*-carbazole-2,7-diboronic acid bis(pinacol) ester (65.8 mg, 0.100 mmol, 1.0 equiv), Pd(PPh$_3$)$_4$ (2.3 mg, 0.002 mmol, 0.02 equiv), and a stirrer bar were added to a 5 mL high-pressure vial. The vial was sealed with a septum and flushed with argon, before degassed toluene (1.4 mL), degassed aqueous 1 M Na_2CO_3 (0.32 mL, 0.32 mmol, 3.2 equiv), and 1 drop of Aliquat 336 were added. The whole solution was then degassed again for 40 min before the reaction was heated to 120°C for 1 day. The reaction was cooled to room temperature, precipitated in methanol, stirred for 30 min and filtered through a Soxhlet thimble. The polymer was then extracted (Soxhlet) using methanol, acetone, hexane, and chloroform in that order. The chloroform fraction was collected and evaporated to yield polymer **1a-SO$_2$-preox** (86 mg, 97%). ^{1}H NMR in accordance with **1a-SO$_2$**; M_n: 53 kDa, M_w: 97 kDa, Đ: 1.8.

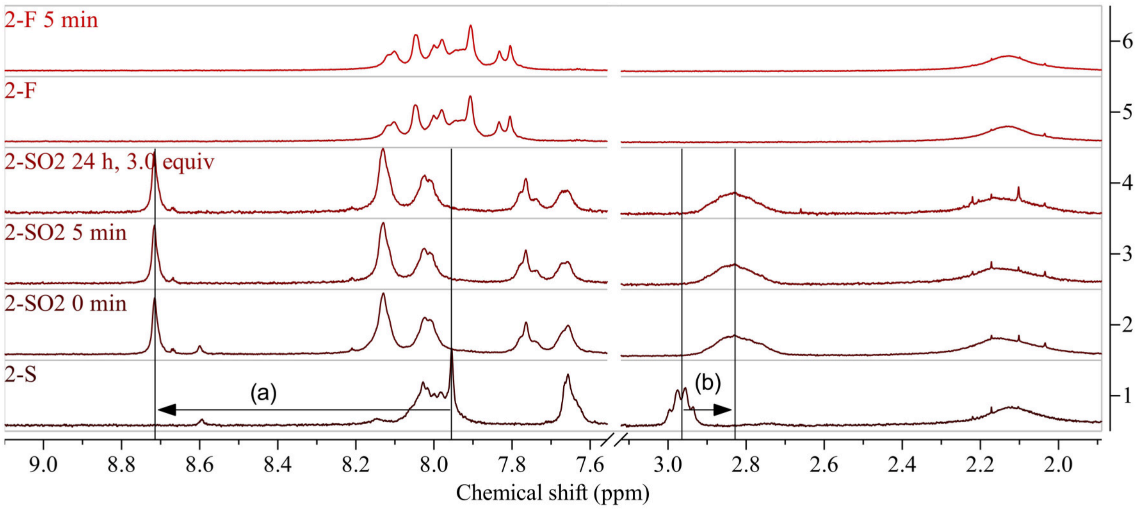

FIGURE 6 | ^{1}H NMR spectra of **2-S** (bottom) and **2-SO$_2$** obtained by modification with DMDO for 0 min and 5 min before work-up (above). Arrows show indicative shifts upon modification. The selectivity of the modification was evaluated by treating the starting polymer with a large excess of DMDO for prolonged time (24 h, 3.0 equiv). Further control experiments were carried out by treating **2-F** with DMDO for 5 min, resulting in no change of the ^{1}H NMR spectrum (top). Arrows show indicative shifts upon modification: (a) downfield shift of the peak of the benzothiadiazole proton by oxidation to the sulfone and (b) upfield shift of the aliphatic protons next to the thioalkyl sulfur upon oxidation to the sulfone. See **Supplementary Material** for full spectra.

Synthesis of F8BT-Based Polymers 2-F and 2-S

2-F was synthesized according to our previously reported work (Creamer et al., 2018).

Synthesis of **2-S** was based on our previously reported method (Creamer et al., 2018). **2-F** (94 mg, 0.174 mmol, 1.0 equiv), octanethiol (0.1 mL, 0.58 mmol, 3.3 equiv) and K_2CO_3 (240 mg, 1.74 mmol, 10.0 equiv) were added to a 5 mL high-pressure vial. The vial was sealed with a septum and degassed with argon, before anhydrous chlorobenzene (3 mL) and DMF (1 mL) were added. The solution was heated at 130°C for 4 h. After cooling, the solution was precipitated into methanol. The suspension was stirred for 30 min, filtered and the precipitate was washed several times with methanol and acetone to remove unreacted thiol and residual DMF. The yellow solid was isolated and dried under vacuum (85 mg, 0.127 mmol, 73%). ^{1}H NMR (400 MHz, $CDCl_3$): 8.23–7.81 (m, 5 H), 7.66 (br, 2H), 3.05–2.87 (m, 2H), 2.43–1.84 (m, 4 H), 1.72–0.92 (m, 36H), 0.91–0.74 (m, 9 H) ppm.

Synthesis of Monomer 3-SO$_2$

To a stirred solution of starting material **3-S** (90 mg, 0.15 mmol, 1.0 equiv) in CH_2Cl_2 (1.5 mL, 0.1 M) was added DMDO (5.1 mL, 0.074 M in acetone, 0.38 mmol, 2.5 equiv) at r.t. The reaction stirred for 90 min and was then evaporated *in vacuo*. The residue was purified by flash chromatography (petroleum ether:CH_2Cl_2 1:1) to afford pure monomer **3-SO$_2$** (75 mg, 0.12 mmol, 79%). ^{1}H NMR (600 MHz, $CDCl_3$): δ = 8.61 (s, 1H), 7.90 (d, J = 4.0 Hz, 1H), 7.38 (d, J = 3.9 Hz, 1H), 7.22 (d, J = 3.9 Hz, 1H), 7.21 (d, J = 4.0 Hz, 1H), 2.97–2.86 (m, 2H), 1.63–1.55 (m, 2H), 1.29–1.11 (m, 10H), 0.84 (t, J = 7.1 Hz, 3H) ppm. ^{13}C(APT) NMR (150 MHz, $CDCl_3$): δ = 155.85 (C), 152.52 (C), 139.91 (C), 139.16 (C), 133.67 (C), 133.48 (CH), 131.13 (CH), 130.44 (CH), 129.02 (CH), 127.25 (C), 125.32 (C), 123.07 (CH), 117.52 (C), 117.04 (C), 54.35 (CH_2), 31.77 (CH_2), 28.99 (CH_2), 28.90 (CH_2), 28.30 (CH_2), 22.83 (CH_2), 22.69 (CH_2), 14.20 (CH_3) ppm. HRMS (APCI/Orbitrap) m/z: $[M]^+$ Calcd for $C_{22}H_{22}Br_2N_2O_2S_4$ 631.89254; Found 631.89270. See **Supplementary Material** for NMR spectra and HRMS results.

General Procedure for Post-polymerization Modification

To a stirred solution in chlorobenzene (concentration of polymer repeat unit: 0.01 M) at r.t. was added DMDO (0.074 M or 0.104 M in acetone, amount per repeat unit given in **Tables 2**, **3**). The reaction stirred at r.t. for the reaction time given in **Tables 2**, **3** and was then evaporated *in vacuo* to afford the modified polymer.

DISCUSSION

Both, PCDTBT- and F8BT-based thioalkyl-substituted polymers, could be modified very selectively using DMDO. Even when treating the polymers for 24 h with a large excess of DMDO, no side reactions were observed for F8BT-based polymer **2-S** and only very weak side reactions were found for PCDTBT-based polymer **1a-S**, which features carbazole and thiophene units potentially prone to oxidation. Oxidation to sulfoxides (instead of sulfones) was surprisingly selective for the investigated polymer **1a-S**, but not selective for **1b-S**, where two adjacent thioalkyl substituents are present.

Chlorobenzene was found to be a better solvent for the modifications than CH_2Cl_2, as the polymers stayed in solution when adding the reagent. Experiments in chlorobenzene revealed that the modification is a very fast reaction. Even when adding the reagent and immediately evaporating the solvent and reagent the reaction was almost complete. Complete modification was observed when stirring the reaction for 5 min before evaporation.

As our findings demonstrate, oxidation of thioalkyl substituents to sulfoxides and sulfones using DMDO is indeed a very useful reaction for the post-polymerization modification of conjugated polymers such as PCDTBT and F8BT. However, for applications requiring very high selectivity of the modification it should be considered that side reactions may take place at other sites prone to oxidation (e.g., carbazoles)—although these side reactions were found to be very slow in our experiments. Fluorene and benzothiadiazole units as in F8BT were found to be a safe choice to avoid all side reactions. For the preparation of sulfoxide-substituted polymers, it should further be considered that adjacent functional groups may impact the selectivity; oxidation to sulfones may occur before complete oxidation to sulfoxides.

We believe this post-polymerization modification method is a very useful tool for changing the properties of polymers drastically and for preparing electron-poor conjugated polymers. The modification may even allow for obtaining electron acceptors for solar cells directly from the electron donors. Furthermore, we envision exciting future applications of this modification ranging from surface modification of conjugated polymer nanoparticles to modification of polymer thin-films.

AUTHOR CONTRIBUTIONS

ER synthesized monomer **3-SO$_2$** and polymer **1a-SO$_2$-preox** and carried out the modifications of PCDTBT-based polymers. AdC prepared **1a-S**, **2-S**, and **3-S** and contributed to writing the manuscript. SC and AbC prepared **2-F** and **1b-S**. SE carried out the modifications of F8BT-based polymers. MH designed and supervised experiments and contributed to writing the manuscript. FG designed and supervised experiments, measured NMR spectra, and prepared the manuscript.

FUNDING

We thank TU Wien for funding this work.

ACKNOWLEDGMENTS

The authors acknowledge the Imperial College Central Library for financial support through the Imperial Open Access Fund.

SUPPLEMENTARY MATERIAL

The Supplementary Material for this article can be found online at: https://www.frontiersin.org/articles/10.3389/fchem.2019.00123/full#supplementary-material

REFERENCES

Beaupré, S., and Leclerc, M. (2013). PCDTBT: en route for low cost plastic solar cells. *J. Mater. Chem. A* 1, 11097–11105. doi: 10.1039/C3TA12420G

Casey, A., Ashraf, R. S., Fei, Z., and Heeney, M. (2014). Thioalkyl-substituted benzothiadiazole acceptors: copolymerization with carbazole affords polymers with large stokes shifts and high solar cell voltages. *Macromolecules* 47, 2279–2288. doi: 10.1021/ma5000943

Creamer, A., Casey, A., Marsh, A. V., Shahid, M., Gao, M., and Heeney, M. (2017). Systematic Tuning of 2,1,3-benzothiadiazole acceptor strength by monofunctionalization with alkylamine, thioalkyl, or alkoxy groups in carbazole donor–acceptor polymers. *Macromolecules* 50, 2736–2746. doi: 10.1021/acs.macromol.7b00235

Creamer, A., Wood, C. S., Howes, P. D., Casey, A., Cong, S., Marsh, A. V., et al. (2018). Post-polymerisation functionalisation of conjugated polymer backbones and its application in multi-functional emissive nanoparticles. *Nat. Commun.* 9:3237. doi: 10.1038/s41467-018-05381-4

Crossley, D. L., Urbano, L., Neumann, R., Bourke, S., Jones, J., Dailey, L. A., et al. (2017). Post-polymerization C–H borylation of donor–acceptor materials gives highly efficient solid state near-infrared emitters for near-IR-OLEDs and effective biological imaging. *ACS Appl. Mater. Interfaces* 9, 28243–28249. doi: 10.1021/acsami.7b08473

Glöcklhofer, F., Lumpi, D., Kohlstädt, M., Yurchenko, O., Würfel, U., and Fröhlich, J. (2015). Towards continuous junction (CJ) organic electronic devices: Fast and clean post-polymerization modification by oxidation using dimethyldioxirane (DMDO). *React. Funct. Polym.* 86, 16–26. doi: 10.1016/j.reactfunctpolym.2014.10.006

Glöcklhofer, F., Lumpi, D., Stöger, B., and Fröhlich, J. (2014). Multigram synthesis of bis[(trimethylsilyl)ethynyl]benzenes suitable for post-polymerization modification. *New J. Chem.* 38, 2229–2232. doi: 10.1039/C4NJ00011K

González-Núñez, M. E., Mello, R., Royo, J., Ríos, J. V., and Asensio, G. (2002). Mechanism of the Oxidation of Sulfides by Dioxiranes. 1. Intermediacy of a 10-S-4 Hypervalent Sulfur Adduct. *J. Am. Chem. Soc.* 124, 9154–9163. doi: 10.1021/ja025868z

Guo, X., Baumgarten, M., and Müllen, K. (2013). Designing π-conjugated polymers for organic electronics. *Progress Polymer Sci.* 38, 1832–1908. doi: 10.1016/j.progpolymsci.2013.09.005

Hubijar, E., Papadimitratos, A., Lee, D., Zakhidov, A., and Ferraris, J. P. (2013). Synthesis and characterization of a novel symmetrical sulfone-substituted polyphenylene vinylene (SO2EH-PPV) for applications in light emitting devices. *J. Phys. Chem. B.* 117, 4442–4448. doi: 10.1021/jp3080964

Ibanez, J. G., Rincón, M. E., Gutierrez-Granados, S., Chahma, M., h., Jaramillo-Quintero, O. A., et al. (2018). Conducting polymers in the fields of energy, environmental remediation, and chemical–chiral sensors. *Chem. Rev.* 118, 4731–4816. doi: 10.1021/acs.chemrev.7b00482

Kim, Y., Cook, S., Choulis, S. A., Nelson, J., Durrant, J. R., and Bradley, D. D. C. (2004). Organic Photovoltaic devices based on blends of regioregular Poly(3-hexylthiophene) and Poly(9,9-dioctylfluorene-co-benzothiadiazole). *Chem. Mater.* 16, 4812–4818. doi: 10.1021/cm049585c

Mikula, H., Svatunek, D., Lumpi, D., Glöcklhofer, F., Hametner, C., and Fröhlich, J. (2013). Practical and efficient large-scale preparation of Dimethyldioxirane. *Org. Process Res. Dev.* 17, 313–316. doi: 10.1021/op300338q

Schelkle, K. M., Becht, S., Faraji, S., Petzoldt, M., Müllen, K., Buckup, T., et al. (2014). Emission Turn-On and solubility turn-off in conjugated polymers: one- and two-photon-induced removal of fluorescence-quenching solubilizing groups. *Macromol. Rapid Commun.* 36, 31–37. doi: 10.1002/marc.201400562

Swager, T. M. (2017). 50th anniversary perspective: conducting/semiconducting conjugated polymers. a personal perspective on the past and the future. *Macromolecules* 50, 4867–4886. doi: 10.1021/acs.macromol.7b00582

Wei, S., Xia, J., Dell, E. J., Jiang, Y., Song, R., Lee, H., et al. (2014). Bandgap engineering through controlled oxidation of polythiophenes. *Angew. Chem.* 126, 1863–1867. doi: 10.1002/ange.201309398

Zaumseil, J., Donley, C. L., Kim, J.-S., Friend, R. H., and Sirringhaus, H. (2006). Efficient top-gate, ambipolar, light-emitting field-effect transistors based on a green-light-emitting polyfluorene. *Adv. Mater.* 18, 2708–2712. doi: 10.1002/adma.200601080

Zhang, C., Nguyen, T. H., Sun, J., Li, R., Black, S., Bonner, C. E., et al. (2009). Design, synthesis, characterization, and modeling of a series of s,s-dioxothienylenevinylene-based conjugated polymers with evolving frontier orbitals. *Macromolecules* 42, 663–670. doi: 10.1021/ma802621b

Conflict of Interest Statement: The authors declare that the research was conducted in the absence of any commercial or financial relationships that could be construed as a potential conflict of interest.

frontiers in Chemistry

ORIGINAL RESEARCH
published: 18 March 2019
doi: 10.3389/fchem.2019.00121

Eumelanin Graphene-Like Integration: The Impact on Physical Properties and Electrical Conductivity

Roberto Di Capua[1], Valentina Gargiulo[2], Michela Alfè[2], Gabriella Maria De Luca[1], Tomáš Skála[3], Gregor Mali[4] and Alessandro Pezzella[5]*

[1] Department of Physics "E. Pancini", University of Naples "Federico II" and Superconducting and Other Innovative Materials and Devices Institute (SPIN), CNR, Naples, Italy, [2] Institute for Research on Combustion (IRC), CNR, Naples, Italy, [3] Faculty of Mathematics and Physics, Charles University, Prague, Czechia, [4] Department of Inorganic Chemistry and Technology, National Institute of Chemistry, Ljubljana, Slovenia, [5] Institute for Polymers, Composites and Biomaterials (IPCB), CNR, Pozzuoli, Italy

The recent development of eumelanin pigment-based blends integrating "classical" organic conducting materials is expanding the scope of eumelanin in bioelectronics. Beyond the achievement of high conductivity level, another major goal lays in the knowledge and feasible control of structure/properties relationship. We systematically investigated different hybrid materials prepared by *in situ* polymerization of the eumelanin precursor 5,6-dihydroxyindole (DHI) in presence of various amounts of graphene-like layers. Spectroscopic studies performed by solid state nuclear magnetic resonance (ss-NMR), x-ray photoemission, and absorption spectroscopies gave a strong indication of the direct impact that the integration of graphene-like layers into the nascent polymerized DHI-based eumelanin has on the structural organization of the pigment itself, while infrared, and photoemission spectroscopies indicated the occurrence of negligible changes as concerns the chemical units. A tighter packing of the constituent units could represent a strong factor responsible for the observed improved electrical conductivity of the hybrid materials, and could be possible exploited as a tool for electrical conductivity tuning.

Keywords: melanin, eumelanin, graphene-like layers, hybrid materials, solid state nuclear magnetic resonance, synchrotron radiation, spectroscopical characterization

Edited by:
Carlo Augusto Bortolotti, University of Modena and Reggio Emilia, Italy

Reviewed by:
Basem Moosa, KAUST Catalysis Center (KCC), Saudi Arabia
Marianna Ambrico, Istituto di Nanotecnologia (NANOTEC), Italy
Jinbo Pang, University of Jinan, China

***Correspondence:**
Alessandro Pezzella
alessandro.pezzella@unina.it

Specialty section:
This article was submitted to Organic Chemistry, a section of the journal Frontiers in Chemistry

Received: *17 November 2018*
Accepted: *15 February 2019*
Published: *18 March 2019*

Citation:
Di Capua R, Gargiulo V, Alfè M, De Luca GM, Skála T, Mali G and Pezzella A (2019) Eumelanin Graphene-Like Integration: The Impact on Physical Properties and Electrical Conductivity. Front. Chem. 7:121. doi: 10.3389/fchem.2019.00121

INTRODUCTION

Eumelanin belongs to the melanin pigments family and it is the pigment type mostly found in bacteria, fungi, plants, animals, and extinct organisms. It is involved in ultraviolet (UV) protection, detoxification, metal binding, and structural coloration (D'Ischia et al., 2013). Eumelanin is biosynthesized in the melanocytes from tyrosine through a series of enzyme-catalyzed reactions: the eumelanin precursors–5,6-dihydroxyindole (DHI), 5,6-dihydroxyindole-2-carboxylic acid (DHICA) and their oxidized forms—are cross-linked into the polymer chain through chemical bonds or physical interactions (D'Ischia et al., 2013).

The possibility to synthesize the eumelanin under biomimetic conditions is attracting deep interest and in the meantime is also expanding eumelanin potential relevance for applications in bioelectronics. In particular, DHI derived eumelanins have been proven to be highly biocompatible (Bettinger et al., 2009; Gargiulo et al., 2015), a feature that, together with their water dependent hybrid ionic-electronic conductor nature (Rettenwander et al., 2014; Gargiulo et al., 2015; Wunsche et al., 2015) linked to the specific functionalization of the pigment (Jastrzebska et al., 1995; Eom et al., 2016), makes such pigments of enormous potential interest for biosensing applications. In particular, the electrical (ionic as well as electronic) conductivity of these pigments suggested their application as biointerface capable to allow wealthy cell culture and at the same time to transfer electrical signaling between the cell culture and underlying electronic devices (D'Ischia et al., 2013; Barra et al., 2015).

A major limiting factor for the actual implementation of eumelanin-based electronic devices comes from the low absolute value of conductivity of this pigment, and from the fact that the actual conduction mechanisms are still matter of debate (Meredith et al., 2013; Mostert et al., 2013; Sheliakina et al., 2018). Different strategies are appearing in order to circumvent the poor conductivity limitation, in order to exploit the biocompatibility and the favorable chemical properties of eumelanin (Meredith et al., 2013; Gargiulo et al., 2015). In this context, by the integration of conductive graphene-like (GL) layers within the eumelanin pigment (EU), we recently explored the possibility to synthesize a novel organic/organic hybrid material (EUGL). EUGL was confirmed to be widely biocompatible, and to strongly enhance the intrinsic poor electrical transport of eumelanin (Gargiulo et al., 2015; Papari et al., 2017). It was speculated that this conductivity increase has a contribution from the improved large-scale homogeneity of the samples associated with a better connection between uniformly distributed grains of the two starting materials and the formation of percolating paths of GL layers inside the material. However, it is hard to clearly correlate the observed macroscopic transport behaviors to microscopic mechanisms, since the eumelanin chemical structure is still not completely known (Huang et al., 2018). Some studies suggested that eumelanin could be regarded as a very high-molecular-weight polymer, with fundamental units randomly linked (chemical disorder) (McGinness et al., 1974; Tran et al., 2006). Morphological and x-ray diffraction experiments (Cheng et al., 1994; Clancy and Simon, 2001; Liu and Simon, 2003), instead, indicated the presence of a supra-molecular order, based on the concept of hierarchical assembly from basic monomers to larger aggregates (Clancy and Simon, 2001). Chemical studies on water-soluble eumelanin and on precipitation phenomena were interpreted ascribing a relevant role to the aggregation-dependent intermolecular perturbation of the π-electron systems (Pezzella et al., 2009; Arzillo et al., 2012; Ascione et al., 2013). In addition to the difficulties in clarifying the transport mechanisms in pure eumelanin, in the case of hybrid compounds it is hard to assign suitable conduction models without direct information on local organization and on the role of functional groups.

The achieved result with the novel organic/organic hybrid material EUGL and the need to get a better understanding of this system spurred the interest toward the investigation of structural factors associated to the electronic conductivity improvement in order to gain valuable tools for a feasible control over the macroscopic properties. Here we present a detailed integrated characterization of three EUGL hybrid compounds containing different amounts of GL layers combining basic laboratory characterizations with experiments of solid state nuclear magnetic resonance (ss-NMR) and advanced photoemission techniques by synchrotron radiation, with the aim of focusing on the modification of molecular packing induced by the integration of the eumelanin pigment with GL layers.

MATERIALS AND METHODS

Materials

Reagents and solvents (analytical grade) were purchased from Sigma Aldrich and used without further purification. Carbon black (CB, furnace black, N110 type, 15–20 nm primary particles diameter, specific BET area 139 m^2 g^{-1}) was purchased from Sid Richardson Carbon Co.

Sample Preparation

GL layers were produced following a two-step oxidation/chemical reduction approach previously reported (Alfè et al., 2012, 2014a,b, 2015). The applied method is briefly described in the following: CB powder (0.5 g) was treated with nitric acid (10 mL of HNO_3 67 % v/v) at 100°C and after 90 h under stirring and reflux the oxidized carbonaceous material, named GL-ox, was recovered by centrifugation, washed with distilled water until the neutrality was reached, dried at 100°C and stored. An amount of GL-ox (0.06 g) was then dispersed in distilled water (60 mL to reach 1 mg mL^{-1} as mass concentration) and treated for 24 h with hydrazine hydrate ($N_2H_{4.} \times H_2O$, 1.35 mL) at 100°C under reflux. After that time, the black suspension was cooled at room temperature and diluted nitric acid (HNO_3 4 M) was dropwise added to neutralize the excess of hydrazine. The decrease of the pH solution allowed the precipitation of the GL layers as a black solid. GL layers were then recovered by centrifugation, washed with distilled water, and recovered again by centrifugation twice. At the end of the purification process, the material was stored as aqueous suspension (mass concentration 1 mg mL^{-1}, pH 3.5) and as powder for bulk characterization after drying at 100°C.

DHI was prepared according to a procedure previously described (Edge et al., 2006; D'Ischia et al., 2013). Eumelanin was synthetized under biomimetic conditions through DHI oxidative polymerization (Edge et al., 2006; Gargiulo et al., 2015; Papari et al., 2017). A proper amount of DHI (20 mg) was dissolved in methanol (1 mL to reach a mass concentration of 20 mg mL^{-1}) by ultrasonic agitation and the resulting solution was stirred for 10 min. Then an ammonia solution (28% v/v in water) was dropwise added to adjust the solution pH to 8 and to allow the auto-oxidization and polymerization of indole molecules; the pH of the mixture is a critical parameter in this process and a fine and accurate control is required. After 30 min, diluted acetic acid (1 M) was dropwise added to quench the reaction by reaching a solution pH around 4. A part of the reaction mixture was stored as it is while another part was dried at 100°C and the resulting powder stored as EU.

The hybrid materials were prepared adapting the procedure previously described (Gargiulo et al., 2015; Papari et al., 2017). The integration of GL was achieved via *in-situ* exposure of GL layers to the nascent polymer under mildly alkaline conditions. Briefly, for the preparation of each hybrid a proper volume of aqueous suspension of GL layers (1 mg mL^{-1}) was added to a DHI methanol solution (20 mg mL^{-1}) before the addition of ammonia solution to induce the DHI oxidation and polymerization. The amount of GL layers was varied to prepare hybrids with different EU/GL mass ratios (**Table 1**). The work-up of the reaction was the same as described for the preparation of pure eumelanin. A sketch of the synthetic procedure is reported in **Figure 1**. Each suspension was in part stored and in part it was dried in an oven at 100°C and the resulting powdered material stored for bulk analysis. After drying, all EUGL hybrids resulted insoluble in water.

A sample simulating the composition of EUGL3 was prepared by mixing polymerized EU and GL both as powders in the following amounts: 6.6 mg of GL and 3.4 mg of EU. The result of such physical mixture was named EU+GL3.

Methods

The elemental composition of the samples in terms of carbon, hydrogen, and nitrogen contents was measured by ultimate analysis performed with a CHN 628 LECO elemental analyzer following the ASTM E870 procedure and using EDTA as standard. For each sample two measurements were performed and the values are reported as average with a maximum relative error around 0.7%. Oxygen content was evaluated by difference.

Fourier Transform Infrared (FTIR) spectra were acquired on pellets prepared by pressing at 10 ton for 10 min solid dispersions containing the powdered materials mixed with KBr (mass concentration 0.5–0.8 wt.%). FTIR spectra in the 3,400–600 cm^{-1} range were acquired in the transmittance mode using a 5,700 Nicolet spectrophotometer.

Thermogravimetric analyses (TGA) were performed on a Perkin–Elmer Pyris 1 thermogravimetric analyzer. The thermal stability of the samples was evaluated under an oxidative environment (air, 30 mL min^{-1}) by heating each material from 50°C up to 800°C at a rate of 10°C min^{-1}.

Each reaction mixture was used without any further treatment for the preparation of the samples for AFM, Scanning electron microscopy (SEM), and IV-measurements. The aqueous mixture was drop-casted onto mica (AFM imaging) or glass plates (SEM imaging and IV measurements) and allowed to dry at room temperature in air for 48 h.

TABLE 1 | Elemental composition of the investigated samples.

Sample label	% GL content	% EU content	Elemental composition			
			C wt.%	H wt.%	N wt.%	O wt.%
GL	100	0	52.9	1.4	6.1	39.6
EU	0	100	52.5	3.3	7.7	36.6
EUGL1	33	67	52.7	3.2	9.5	34.5
EUGL2	50	50	54.4	3.9	9.4	32.3
EUGL3	67	33	56.3	2.8	8.2	32.7

The AFM images were acquired on an XE100 Park instrument operating in the non-contact mode (amplitude modulation, silicon nitride cantilever from Nanosensor) at room temperature and in ambient conditions.

Scanning electron microscopy (SEM) measurements were performed on a FEI Inspect TMS50 Scanning Electron Microscope. Scanning was performed on samples previously sputter coated with a thin layer of gold to avoid charging.

A four-contacts (van der Pauw, 1958) configuration was employed to estimate the dc electrical conductivity of the samples, drop-casted on glass substrates. Voltage supply and current measurements were provided by a Keithley Electrometer 6517A and a Keithley pico-amperemeter 6,485, respectively. The drop-casted samples after drying were contacted by small droplets of silver-based conducting glue, realizing a square-shaped four-contacts geometry (according to the van der Pauw requirements). The electrical measurements were performed in air at a relative humidity (RU) of about 25%.

The solid state Nuclear Magnetic Resonance (ss-NMR) measurements were performed at the Slovenian NMR Center in Ljubljana. ^{1}H and ^{13}C magic-angle spinning (MAS), and ^{1}H-^{13}C cross polarization magic-angle spinning (CPMAS) spectra were recorded on a Varian 600 MHz VNMRS spectrometer equipped with a 3.2 mm HX MAS probe. Larmor frequencies for ^{1}H and ^{13}C nuclei were 599.58 and 150.77 MHz, respectively. In the ^{1}H MAS NMR experiment samples were spun with rotation frequency of 20 kHz, protons were excited with a 90-degree pulse of 2.3 μs, repetition delay was 10 s, and 16 scans were co-added. In the ^{1}H-^{13}C CPMAS experiment the polarization was transferred from protons to carbon nuclei in a 0.8 ms CP block, repetition delay between scans was 0.1 s, and the number of scans was 150,000. Sample rotation frequency was 16 kHz. During acquisition of the carbon signals high-power proton decoupling was employed. The ^{1}H and ^{13}C chemical shift axes were referenced to tetramethylsilane.

X-ray photoemission spectroscopy (XPS) and resonant photoemission spectroscopy (ResPES) experiments were performed at the Materials Science Beamline (MSB), Elettra synchrotron light facility in Trieste, Italy. The MSB, with a bending magnet source, provides synchrotron light in the energy range 21–1,000 eV. The basic set-up at MSB consists in a chamber including a dual Mg/Al X-ray source with a base pressure of 2×10^{-10} mbar and a SPECS Phoibos 150 hemispherical energy analyzer.

Al Kα radiation (1486.6 eV) was used to measure the core levels of C 1s, N 1s, O 1s. The incident photon energies were 410, 475, and 630 eV, respectively, with total resolutions of 350, 500, and 700 meV, respectively. The core level spectra were acquired at constant pass energy and at an emission angle of 0° with respect to the surface normal. The binding energy positions of the features in the XPS spectra were aligned with those measured by the laboratory source, for which the binding energy was referenced to the Fermi edge of Au(100) (EB = 0).

The reproducibility of the spectroscopical and electrical characterization data was assessed by measuring at least two fresh aliquots of selected samples.

RESULTS AND DISCUSSION

In **Table 1**, all samples analyzed in this work are listed with their label. For each sample, the measured elemental composition is reported together with the percentages of GL and EU established on a ponderal basis starting from the milligrams of the GL and the EU precursor used for the preparation of each sample.

The compositions of the parent materials (EU and GL) are quite similar (the elemental composition of DHI-based eumelanin estimated in this work is in accordance with that reported by a similar material in Glass et al. (2012); Saini and Melo (2015)), apart a considerably lower hydrogen amount in GL. As a consequence, the compositions of the hybrid materials do not exhibit large difference among them and with respect to EU and GL.

The measured values of C, H, and N in the hybrids indicated a complete incorporation of the GL layers into the hybrids. As a matter of fact, a good accordance between the measured and the "theoretical" percentages of each element content was found. Related data and trends are provided as (**Figure S1**).

The FTIR spectra of the materials are reported in **Figure 2**. The spectra are characterized by broad peaks, confirming the chemical heterogeneity of the investigated samples: GL, EU, and EUGL samples exhibit complex vibrational spectra with many overlapping modes, making an accurate vibrational mode assignment very challenging.

As previously reported (Alfè et al., 2012; Gargiulo et al., 2015), the main spectral features of the GL layers FTIR spectrum are: a broad band in the 3,000–3,600 cm^{-1} range ascribable to stretching vibrations of O–H in carboxylic and phenolic

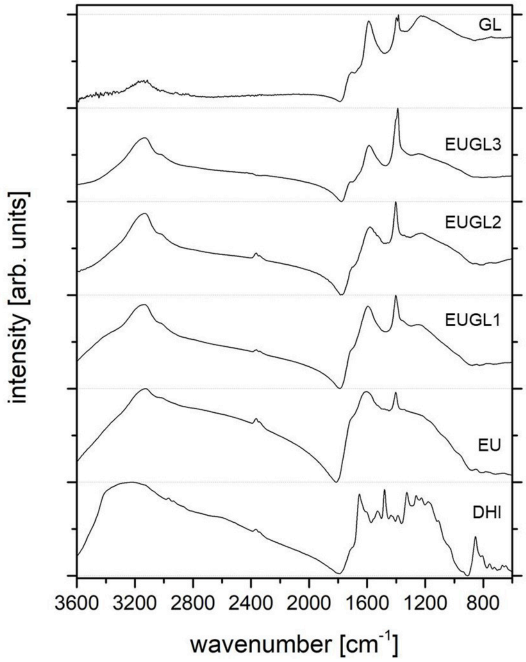

FIGURE 2 | FTIR spectra of all the investigated samples. Height normalized spectra have been vertically shifted for clarity.

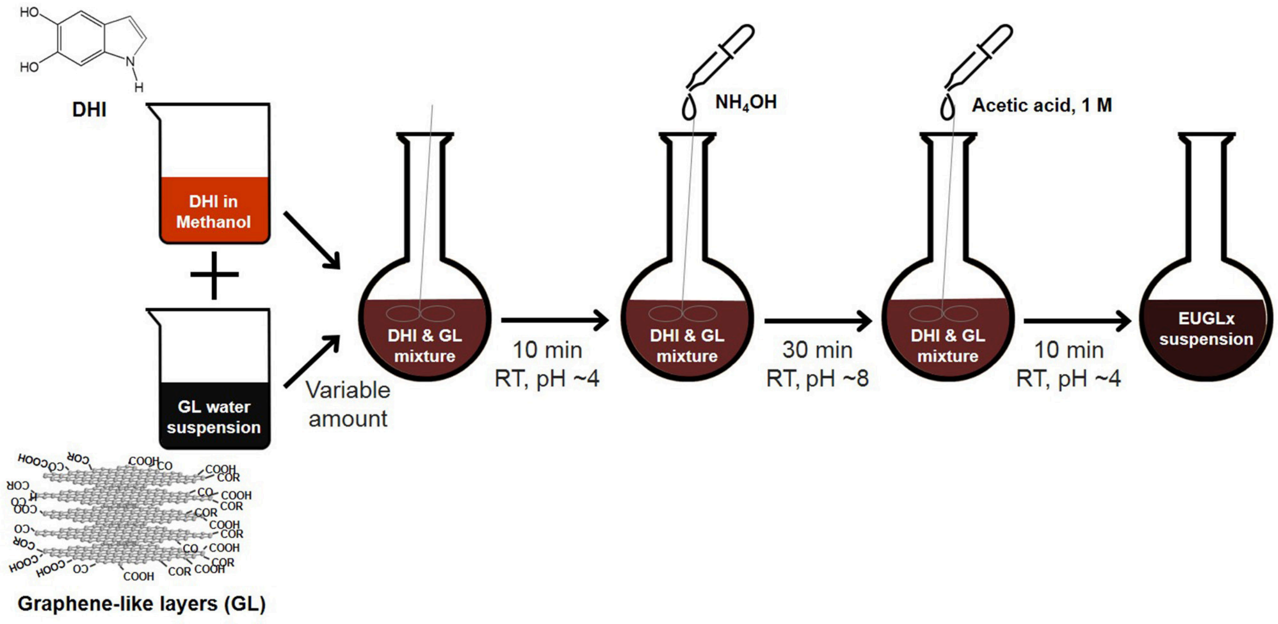

FIGURE 1 | Schematic diagram of the synthetic procedure adopted for the preparation of the EUGLs hybrids.

groups and possibly adsorbed H_2O, and to stretching bands (at lower wavenumbers) of N–H in hydrazones; a band at 1,710 cm^{-1} ascribable to C=O stretching vibrations from carbonyl and carboxyl groups, anhydrides, lactones, single ketones, and quinones; a band around 1,590 cm^{-1} due to skeletal vibrations of the π-conjugated graphitic domains; overlapping bands between 1,500 and 1,100 cm^{-1} due to bending modes of aromatic moieties; an intense band at 1,384 cm^{-1} ascribable to nitric groups.

The EU FTIR spectrum is characterized by a broad band at 3,150 cm^{-1} ascribable mainly to C-H stretching bands of five-membered N-heterocycles (pyrrole) (Cataliotti and Paliani, 1976; Snavely et al., 1992) with a shoulder at 3,000 cm^{-1} ascribable to aromatic C–H stretching modes (Silverstein et al., 2008). In the region between 1,700 and 1,000 cm^{-1}, the broad band at 1,600 cm^{-1} can be assigned to C=C aromatic/pyrrole ring stretching vibrations, while its shoulder at 1,700 cm^{-1} corresponds to C=O stretching in quinone and/or ketone moieties. The presence of C=O stretching signal as a shoulder of the intense band at 1,600 cm^{-1} and not as distinct peak suggests that the content of indole/quinone units is not relevant (Glass et al., 2012). Apart from the intense peak at 1,400 cm^{-1} ascribable to pyrrole ring stretching [C–O, C–C, and C–N in plane modes (Centeno and Shamir, 2008)], the overlapping bands between 1,500 and 1,000 cm^{-1} going to 1,000 cm^{-1} generate a broad profile and no accurate assignment is possible.

The FTIR spectra of all the EUGLs are quite similar to that of EU, yet for the hybrid richest in GL (EUGL3). It is worth noting that, even if GL is very rich in C=O containing groups (Alfè et al., 2015), the peak due to C=O stretching modes at 1,700 cm^{-1} is present only as a shoulder (of increasing sharpness as GL content increases) of the intense peak at 1,600 cm^{-1} related to C=C aromatic/pyrrole ring stretching vibrations. The peak at 3,150 cm^{-1} due to aromatic pyrrolic C–H stretching, and the pyrrole ring stretching peak at 1,400 cm^{-1} are also present in the spectra of all the hybrid compounds. Interestingly, the larger spectral weight of the latter two peaks in EUGLs than in EU, despite the lack of such features in GL, suggests the presence of specific chemical functionalities near to the surface that are partially covered in the pure EU.

The presence of the typical signatures of eumelanin in all the EUGLs FTIR spectra indicates the efficacy of the developed procedure to achieve the merging of the two starting materials. Moreover, by comparing the FTIR spectrum of the starting indole (DHI) with those of the hybrids, the actual formation of eumelanin in the presence of GL layers is proved.

The thermal stability of the samples was investigated by measuring the mass loss of the samples upon heating up to 800°C in an oxidative environment (**Figure S2**) in a thermogravimetric apparatus. The thermal profiles of EUGLs exhibit features similar to those of parent materials: two main weight losses at 200°C and 550°C, the latter corresponding to the EUGL burn-off. The absence of a sharp weight loss at around 550°C, observed for neat GL layers, in the TG profiles of all hybrids suggests an intimate contact between the hybrid components (EU and GL layers).

The morphology of the samples was investigated by SEM and AFM (**Figure 3**). Overall the SEM imaging revealed that the EUGLs samples present a wide homogeneity over a large scale with respect to the granular feature exhibited by EU. Each EU large (macroscopic) agglomerate exhibited a surface characterized by a fine granularity with height of the order of few nm (**Figure 3B**). On the other hand, EUGLs AFM imaging (**Figures 3D,F,H**) showed microscopic grains larger and higher than in EU and slightly increasing with the GL amount, a possible consequence of the different packing discussed in the following.

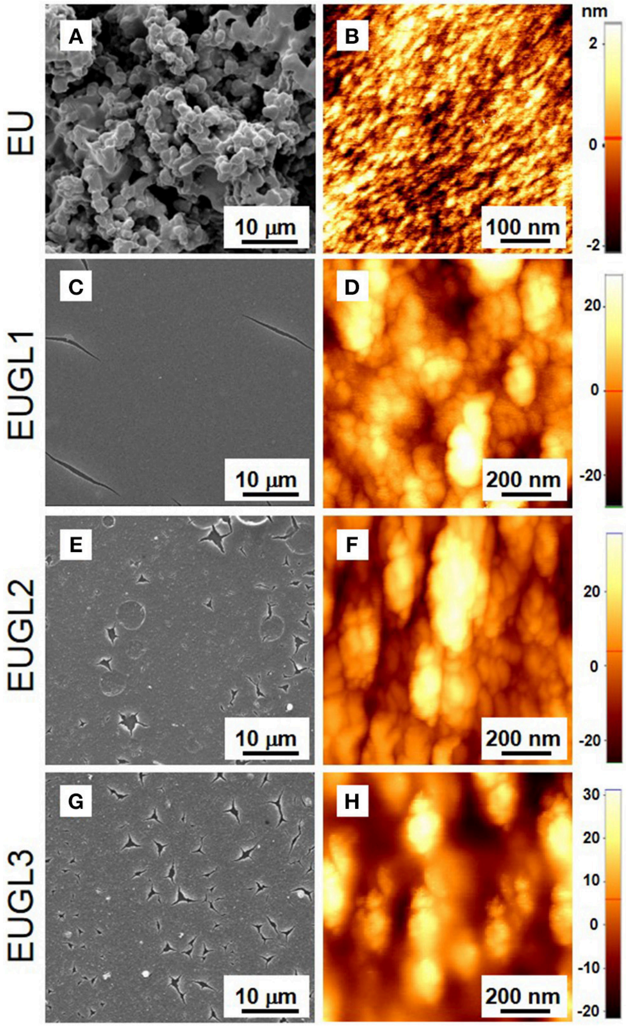

FIGURE 3 | SEM **(A,C,E,G)** and AFM **(B,D,F,H)** images of EU, EUGL1, EUGL2, and EUGL3.

Four-probe measurements performed in the classical van der Pauw configuration (van der Pauw, 1958) provided dc electrical conductivity σ_{dc} of the investigated materials. No deviation from the ohmic behavior was observed in the explored voltage range. The estimated dc electrical conductivities are plotted in **Figure 4**.

As expected, σ_{dc} monotonically increases with the GL content, from the value of 5 µS/m in eumelanin to the GL value of 2.5 S/m. This result confirms what already reported in (Gargiulo et al., 2015), as well as the observed time-decay of σ_{dc} on EU and on the hybrids, shown in the inset of **Figure 4**. On EU, EUGL1, and EUGL2, the σ_{dc} decay appears as the overlapping of two exponential decays on different time scale. The presence of two different time scales can be interpreted as related to both ionic and electronic contributions (Cicco et al., 2015; Gargiulo et al., 2015; Wunsche et al., 2015), the ionic one related to the fastest and larger decay. Indeed, proton transport, which is relevant in eumelanin-based materials, is quickly blocked at the metallic contact in a dc measurement, leaving, after a transient (few seconds for EU, slightly more for EUGLs), only the "conventional" electronic one to contribute to conductivity. The following slower and less evident decay can be then ascribed to a decrease in the electronic transport, probably due to a trapping mechanism (Gargiulo et al., 2015; Wunsche et al., 2015). A simple estimation of the decaying conductivities (double exponential fit of the curves) reveals that ions contribute for more than 50% of the initial conductivity on EU, while in EUGL1, EUGL2, and EUGL3 this contribution is of the order of 20, 10, 5, respectively. It is worth noting that no time decay is observed on GL (indicating both essential electronic and "clean" transport), while on EUGL3 the "slow" decay is not observed (indicating, together with the occurrence of a residual, although strongly reduced, ion contribution, a stronger GL character in the electronic transport). For the main plot, we reported the σ_{dc} values after 900 s; furthermore. Several factors can concur to the strong improvement of σ_{dc} in the hybrids: apart from chemical modifications with related changes in the intrinsic electrical transport properties of basic units, different electrical connections in the samples (of grain or at a molecular/supramolecular level) as well as structural modifications could be responsible of the observed behavior. Spectroscopic measurements have been very helpful to shed light on this issue.

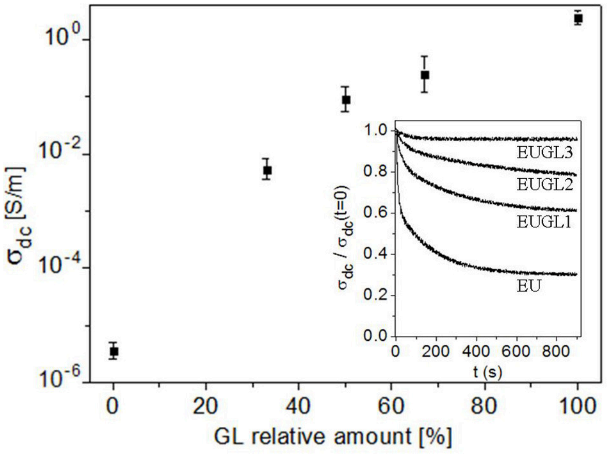

FIGURE 4 | σ_{dc} electrical conductivity of the investigated samples (identified by the GL amount); in the inset, the time-decay of σ_{dc} for EU and EUGLs samples is reported. Measurements have been performed at controlled condition of relative humidity (RU) of about 25%.

First spectroscopic information came from the comparison of photoemission results among the different materials. XPS spectra of GL, EU and hybrid samples at photon energy 410 eV are reported in **Figure 5**. Spectra have been normalized to the same total area and Shirley background has been subtracted. Then the spectra were fitted using 5 Gaussian peaks.

The C 1s XPS spectrum of GL exhibits a very pronounced peak at binding energy of 284.6 eV, corresponding to C=C systems, with the typical asymmetric shape due to the presence of both sp^2 and sp^3 bonds. The second peak around 291 eV is related to the π-π^* satellite band of the graphitic carbon band. The fitting of the spectrum puts also in evidence peaks at 286.5 eV (C–OH from hydroxyl groups), 288.0 eV (C=O from carbonyl groups), 288.7 eV (COOH, carboxylic groups), in a relative amount already recorded on GL samples produced with our method (Alfè et al., 2015; Gargiulo et al., 2018). Compared to such spectrum, on EU sample the main C=C peak is strongly broadened and more symmetric, as expected for non-graphitic materials (Abbas et al., 2011); dominating all the other contributions (**Figure 5**). The photoemission spectrum collected on EUGL3, the hybrid sample with the largest GL amount, strongly resembles the GL one. On the contrary, spectra from EUGL1 and EUGL2 are more influenced by the presence of EU: they exhibit a C=C peak qualitatively similar to GL, but the other spectral contributions clearly resemble those of EU. Therefore, we can say that EUGL3 exhibits spectroscopic features close to those of the GL parent compound, while EUGL1 and EUGL2 are more affected by EU

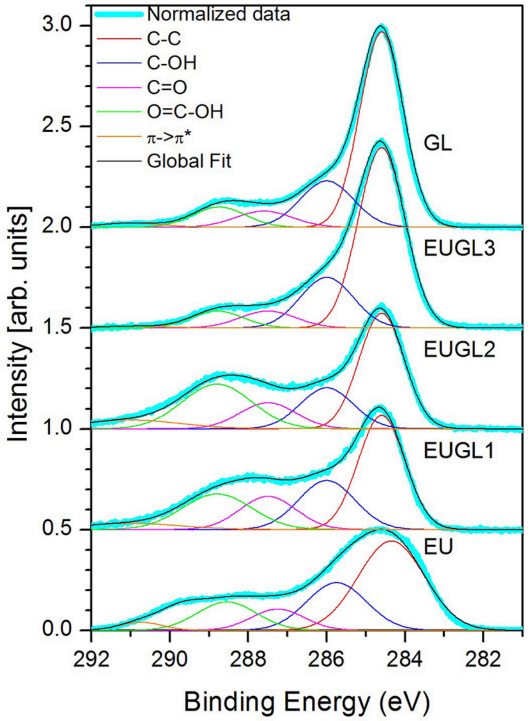

FIGURE 5 | C 1s XPS measurements and related fits. Data and fits for each sample have been area normalized and vertically shifted for clarity.

features. XPS, indeed, reveals a similar relative abundance of the different functional groups between EU, EUGL1, and EUGL2. Analogous similarities have been observed in the FTIR spectra and in the elemental compositions: such remarks resulted to be very helpful for the interpretation of the NMR results, as shown below.

The relative weights of the different spectral components (measured as the relative area of the corresponding Gaussian contribution) in the different XPS spectra are reported in **Table 2**.

Notably the increase of the relative weights of the C=O and COOH groups pairs with the reduction of C-OH group number in the lower graphene-loaded hybrids (EUGL1 and EUGL2).

To get further insights into the spatial arrangement of materials constituents, ss-NMR spectra have been collected on the fabricated parent and hybrid compounds, as well as on the eumelanin precursor (DHI) for comparison.

All the ^{1}H MAS NMR spectra (**Figure S3**) are characterized by a broad signal peaked at 7 ppm, due to aromatic hydrogens of indole or pyrrole rings. The broad shape of this main signal is not only indicative of the strong dipolar coupling among hydrogen nuclei, but also of the various chemical environments around aromatic hydrogens, and of the variety of connections among various groups in the eumelanin and the related hybrids. The sharper peaks detected between 0 and 2 ppm in DHI and EU spectra are due to aliphatic impurities belonging to the synthetic procedure.

The directly excited ^{13}C MAS experiments demonstrated that the spectra of all these materials are the results of a large number of overlapping resonances causing the broadening of the signals and hampering the individual carbon signals assignment (**Figure 6**).

To overcome this limitation and to increase the signal of carbon nuclei, ^{1}H-^{13}C CPMAS NMR experiments were performed. Briefly, the CP experiment relies on the proton-to-carbon polarization transfer (Pines et al., 1973). Since the efficiency of polarization transfer depends on the distances between the protons and the carbons, the CP experiment is particularly suitable to differentiate among the different classes of carbons inside a complex carbon-based network, i.e., among the protonated and the non-protonated carbons.

The ^{1}H-^{13}C CPMAS NMR spectrum of DHI (**Figure 6A**) presents a fine structure with signals directly associable to C–H carbons (C3 at 99 ppm, C7 at 106 ppm), quaternary carbons (C8, C9, and C4 at 121 ppm) and carbons bonded to heteroatoms (C5 and C6 at 141 ppm and C2 at 132 ppm) according to the assignments given for natural eumelanins (Xin et al., 2015). Signals at high magnetic field (20–40 ppm) account for residual C–H signals of those aliphatic impurities also detected in ^{1}H MAS NMR spectrum. Compared to DHI, the spectral features of EU are broader and much less defined, as a consequence of the larger disorder associated to melanin polymer backbone after the oxidative polymerization has occurred. As expected, the EU spectrum contains arenes resonances consistent with the proposed indole-based aromatic structure and signals due to oxygen bearing groups in accordance with the data reported for DHI-based melanin (Hervé et al., 1994; Xiao et al., 2018) and a related material such as polydopamine (Chatterjee et al., 2014). In particular, the signals typical of H-bearing aromatic or quaternary carbons are located in the region between 90 and 140 ppm, and those typical of C–O and C=O groups in the range 170–200 ppm. An aspect deserving attention moving from the spectrum of DHI to the spectra of EU and the hybrids is the presence of signals in the carbonyl region (150–200 ppm), revealing that an increase of the oxidation level of the indoles in the backbone of the pigment takes place during the polymerization process. This finding agrees with the relative weights of the oxygen-containing functional groups estimated by XPS (**Table 2**).

As for EU, ^{1}H-^{13}C CPMAS NMR spectra of hybrid materials contain overlapping signals typical of aromatic C-H or quaternary carbons in the region between 90 and 140 ppm and signals typical of C–O and C=O groups in the range 170–200 ppm. With the increase of GL content, the fine structure of the DHI and EU spectra is lost and some significant spectra modifications reveal the actual occurrence of an intimate contact between EU and GL layers embedded in the hybrid material during the co-polymerization process. More precisely, during the EUGL hybrid synthesis the embedding of GL layers into the nascent EU polymer induces a marked modification of relative intensity ratios of carbon signals with respect to eumelanin (**Figure 6B**): the most striking feature of EUGLs spectra compared to EU one is the enhancement of the signals at 140 and 100 ppm with respect to those in the region around 120 ppm in EUGL1 and EUGL2 (this occurrence is less pronounced in EUGL3, whose spectral response is probably more strongly affected by GL features, consistently with the indication provided in the following by XPS). The observed signal evolution should be ascribed to an enhancement of ^{1}H-^{13}C cross-polarization effect for hydrogen-bonded carbons and/or hydrogen-near substituent carbons and could not be related to an actual increased relative abundance of the carbon species responsible of such signals as a consequence of the inclusion in GL, also considering the relative weakness of these feature in both parent compounds.

To confirm such idea, directly excited ^{13}C MAS NMR spectra recorded on EUGL hybrids are contrasted with the corresponding ^{1}H-^{13}C CPMAS spectra in **Figure 6B**: the spectra collected in direct excitation mode are broadened and characterized by a main signal peaked at 125 ppm ascribable to aromatic carbons inside both the graphitic network of GL and the π-conjugate structure of eumelanin (protonated indole and pyrrole moieties) (Hervé et al., 1994). The lack

TABLE 2 | Summary of C 1s XPS spectra fits.

Peak energy (eV)	Attribution	Relative spectral weight (%) in				
		EU	EUGL1	EUGL2	EUGL3	GL
284.6	C-C and C-H	45	41	41	64	64
286.0	C-OH	23	21	17	20	19
287.6	C=O	10.9	14.3	12.5	7.3	6.9
288.8	O=C-OH	18.2	19	22.7	7.2	8.2
291.0	π-π*	2.9	4.7	6.8	1.5	1.9

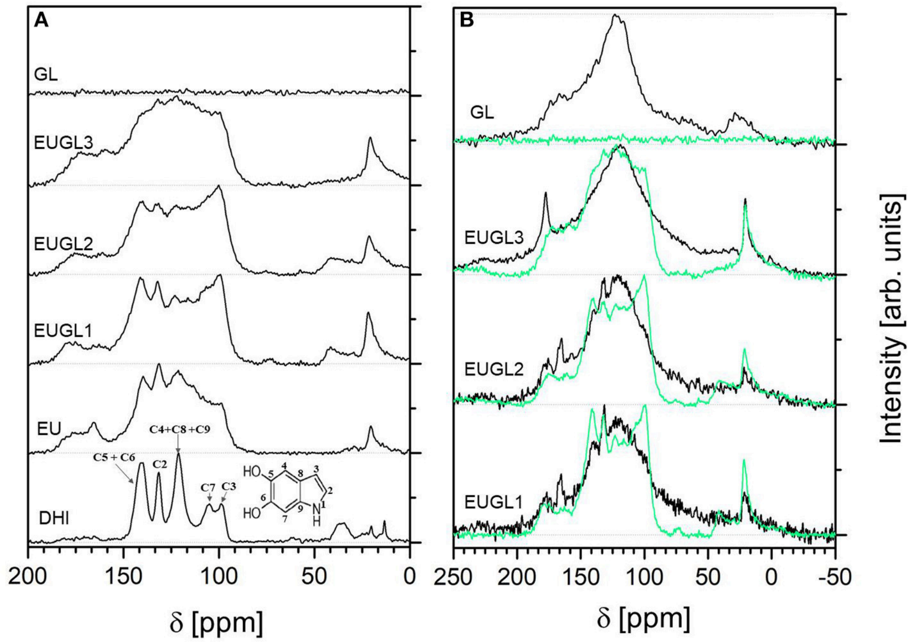

FIGURE 6 | (A) ^1H-^{13}C CPMAS NMR spectra; **(B)** comparison between ^{13}C MAS (black line) and ^1H-^{13}C CPMAS (green line) NMR spectra of GL and the three hybrids. Spectra have been height normalized and vertically shifted for clarity.

of distinguished signals at 100 and 140 ppm in these spectra is a strong indication that the mentioned observations in CPMAS spectra on EUGLs are actually due to ^1H-^{13}C CP mechanism for selected carbon sites, and the profile evolution detected for EUGLs spectra may thus be justified on the basis of relevant intermolecular factors which governs the mutual arrangement of eumelanin components in presence of GL layers.

An added proof of this hypothesis was obtained by performing ^{13}C MAS and ^1H-^{13}C CPMAS NMR experiments on a physical mixture of eumelanin and graphene like layers (EU+GL3) resembling the composition of EUGL3. This supplementary inspection aimed to check the occurrence of cross polarization effects also when EU and GL components are simply mixed. The results of the NMR experiments on this mixture are shown and compared with those of EUGL3 in **Figure S4**. The ^{13}C MAS NMR spectrum of EU+GL3 showed a shape very similar to that of the spectrum of EUGL3; on the contrary the ^1H-^{13}C CPMAS NMR spectrum exhibited a very noisy shape overall dissimilar to that of the EUGL3. As expected, in the ^{13}C MAS NMR experiment the contributes of both components of the mixture generate a spectrum with a broad signal peaked around 120 ppm in the region typical of aromatic carbons. In the case of the ^1H-^{13}C CPMAS NMR experiment the absence of a real spatial proximity between carbons and protons in EU+GL3 mixture (the EU and GL components do not truly interact) as that established in EUGL3 does not allow the instauration of a significant cross polarization effect.

Both findings concur to sustain the hypothesis of an improved eumelanin packing induced by the GL layers presence in the synthetic medium and thus during the polyindole system build-up.

By comparison with the remarks and discussion on FTIR and XPS results, we can infer, in a self-consistent scheme, that the remarked peculiar features in EUGL1 and EUGL2 CPMAS NMR spectra, compared to the EU one, should be ascribed to different arrangement of building blocks and supra-molecular units, rather than differences in the fundamental units themselves coherently with the common origin of these materials from DHI.

The difference in the microscopic mechanisms occurring in the different samples has been deeper investigated by resonant photoemission spectroscopy (ResPES). In such measurements, photon energy is set close to the absorption edge of a core level, so that the excited electron is not (directly) emitted, but it is excited in an empty valence state (resonance): the (possible) consequent decay of the excited electron produces an autoionization, and the emitted electron is detected. A ResPES map is obtained collecting the energy spectrum of the emitted photoelectrons at several photon energies around the resonant edge. In **Figure 7** we report valence band (VB) ResPES plots for EU and for the three EUGL hybrids, as maps of photoemission intensity as a function of photon excitation energy (hν) and of binding energy (BE) of the photoelectron initial state. The photon energy is scanned from 280 to 304 eV across the C 1s absorption threshold, producing resonant excitations of such core electrons toward the first unoccupied orbitals. Total electron yield (TEY) mode X-ray absorption spectrum obtained by integrating ResPES intensity along the binding energy, is shown on the right of each ResPES map, all having a common photon energy scale. The horizontal photoemission

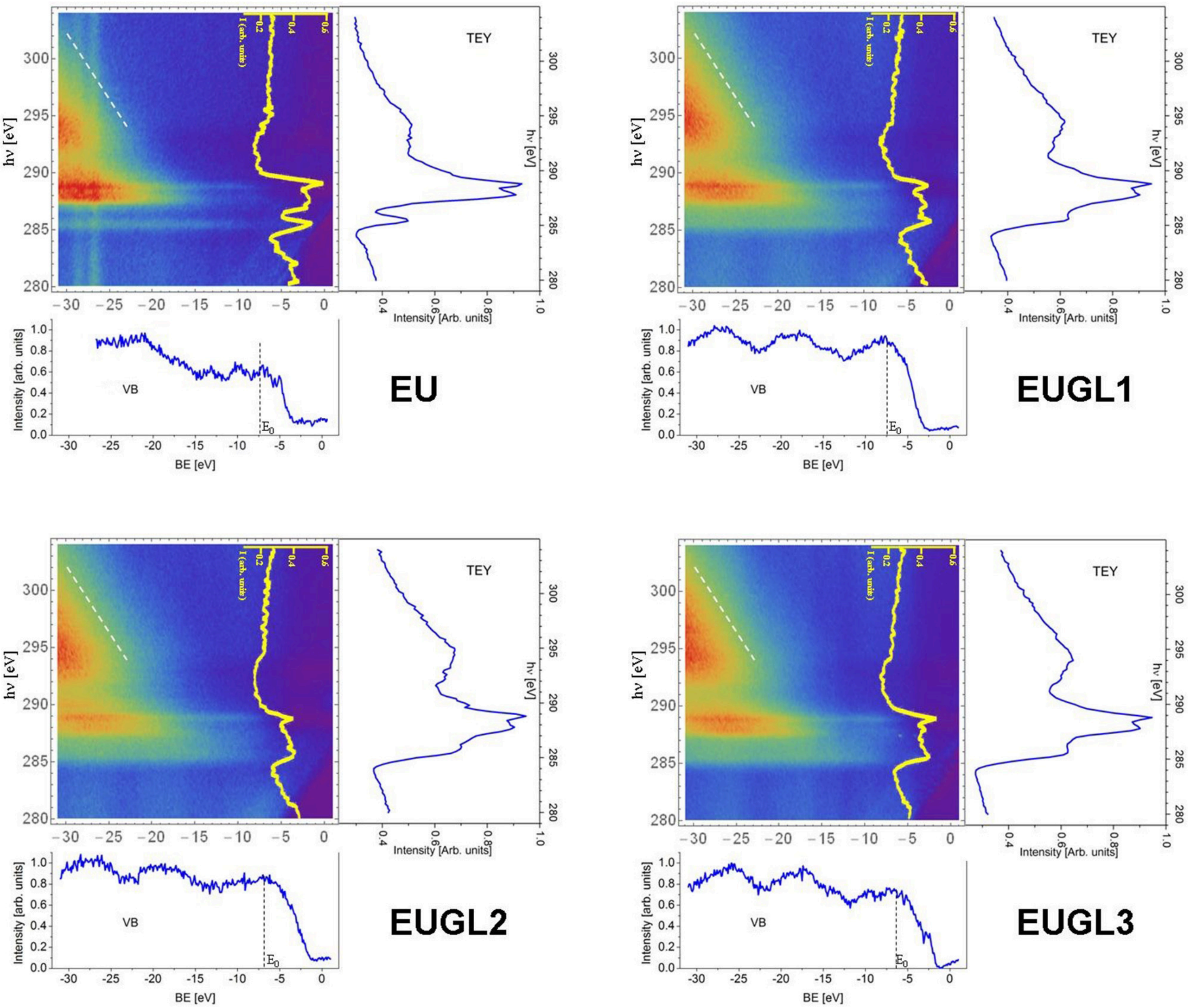

FIGURE 7 | ResPES maps recorded on EU, EUGL1, EUGL2, EUGL3 reported together with the extracted valence band (below each map), XAS spectrum (on the right), and a CIS profile vs. photon energy at a given energy E_0 corresponding to a marked feature in the valence band profile (yellow curve). The dashed white lines indicated the Auger spectroscopic features.

profile at hν = 281 eV (below the resonances) is extracted and reported below each ResPES map (on a common binding energy scale), to highlight the main spectral features of the VB of the samples.

For sake of clarity the ResPES map and the extracted curves of GL are reported in **Figure S5**.

The observed main features, as concerns both EU and EUGL samples, are similar to what was already reported on commercial melanin powders (Sangaletti et al., 2009; Borghetti et al., 2012). The spectral features in the valence band at BE from 0 to about −10 eV are mainly due to N 2p, O 2p, and C 2p orbitals; then, up to BE of about −20 eV there are contributions from σ orbitals, while the features at deeper binding energies come from core levels of oxygen, nitrogen, carbon atoms. In the ResPES map, the most evident features are the Auger emission (dashed white line) with its characteristic dispersive behavior vs. BE, and the resonance detected around the photon energy of the first x-ray absorption peak (excitations toward π* empty orbitals typical of aromatic rings). This resonance occurs when the electron excitation is toward a bound empty level, followed by a core-hole autoionization decay: the final state is a two (core) hole-one (excited) electron state, shifted at higher BE compared to the normal Auger final state (a two-hole state).

On a ResPES intensity map, a constant initial state (CIS) profile, i.e., intensity profiles vs. hν at a fixed BE, can provide information on the charge transfer dynamics. In **Figure 7** we extracted the CIS profile corresponding to BE = E_0 for each presented ResPES map (E_0 being the BE value of a resonance highlighted in each VB profile). The intensity profiles enhance (resonate) at hν around 286 and 289 eV. These are the photon energies of the first two XAS resonances, corresponding to excitations into π^* and σ^* orbitals, respectively. The resonant Auger emission can take place as long as the excited electron remains localized for a time long enough (typically at least comparable to the core-hole lifetime) in order to allow the autoionization decay process. If the excited electron, instead, "quickly" delocalizes, a final state identical to normal Auger emissions happens, therefore not contributing to the resonance in CIS profile. The intensity of the resonance is therefore proportional to the probability that de-excitation occurs before the delocalization of the electron excited into a bound state, which in turn is directly proportional to the delocalization characteristic time. Then, a CIS resonance lacking or weakened indicates a "faster" delocalization, i.e., a stronger interaction with the surrounding material. From the CIS profiles at BE = EB in **Figure 5**, it is evident how the resonance at hν corresponding to XAS peaks is clearly less pronounced for EUGL1 and EUGL2 compared to EU (this is true also of EUGL3, even if less evident: a further similarity between EUGL3 and GL, which also exhibits quite pronounced resonances). For the discussion above, this occurrence indicates a faster delocalization mechanism in the hybrids, which represents another indication of a tighter packing and/or a stronger interaction between single units as a consequence of the inclusion of GL layers.

Several experimental findings from different techniques are therefore agreeing as concerns the occurrence of a stronger packing in the hybrid samples compared to pure eumelanin. From a structural point of view, the most obvious consequence is a reduction of spacing between elementary units and of π-π stacking distance; likely, it also could correspond to a more ordered structure (a point, however, beyond the scope of the present work and deserving deeper investigation), despite the realization of more complex compounds whose pictorial description is proposed in **Figure 8**.

These circumstances can actively contribute to the observed enhancement of electrical dc-conductivity (**Figure 4**). In organic semiconductors, indeed, the distance between π-conjugated oligomers and polymers strongly affects the overlapping between adjacent orbitals, and therefore the amplitude of the electronic transfer integrals between the various interacting units (Brédas et al., 2002). The mobility of charge carriers is increased by an enhancement of the transfer integral, as a consequence of a more efficient hopping between neighbors (Brédas et al., 2002); experimental evidences of such effects have been provided, for examples, for TIPS-pentacene (Giri et al., 2011) (a reduction of 8% in π-π stacking distance leaded to a six times increase of hole mobility), conjugated polymers (Ma et al., 2016) (significant enhancement of electrical conductivity obtained as a consequence of better ordered structure and molecular packing), conductive polymer/carbon nanotube hybrids (Kim et al., 2016) (a dense close packing of nanotubes cores and polymer shells increased the electrical conductivity almost 20 times). Tighter packing and possibly more ordered structure can positively affect the electrical conductivity even in the case of electrical transport driven by percolation mechanism (Sahimi, 1994).

CONCLUSIONS

We investigated different samples prepared by *in situ* polymerization of eumelanin precursor DHI in presence of various amounts of GL layers. Basic characterizations, together with NMR and photoemission studies, provided information about the correlation between structural/spectroscopical rearrangement and the electrical properties as a function of the relative composition. Solid state NMR data indicated that structural and packing modification occur in the hybrid compounds with respect to eumelanin: in particular, the observed enhanced cross-polarization between ^{1}H and ^{13}C demonstrates a stronger synergic interaction of the two materials to gain increased fill factor, which is likely associated to the higher electrical conductivity. ResPES measurements support this interpretation, giving evidence of a stronger interaction, in the hybrids, of the single atom with the surrounding environment through the observation of a faster delocalization mechanism. It is worth to note, however, that in the richest GL hybrid among those investigated, the GL-character starts to become prevalent, as also confirmed by other chemical and physical characterizations. With this work, we performed a first study on the fundamental mechanisms occurring when eumelanin is integrated with graphene-related conducting materials, and responsible of the main observed macroscopic properties (electrical conductivity, biocompatibility, adhesion...), which represent an important knowledge in order to make prediction of results when synthesizing hybrid structures.

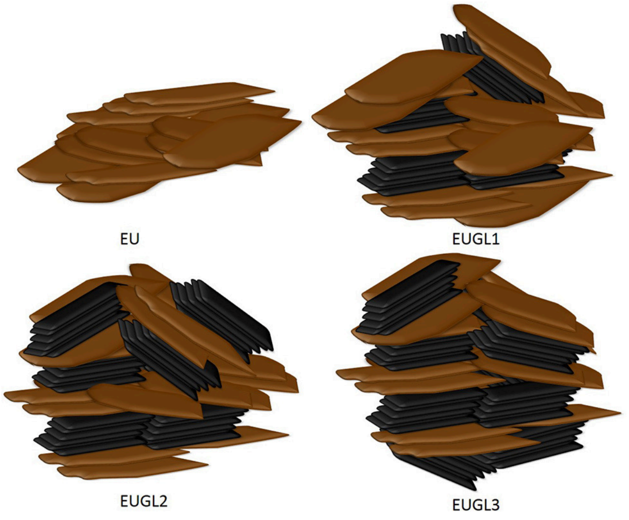

FIGURE 8 | Pictorial description of EU and EUGLx hybrids.

DATA AVAILABILITY

All datasets generated for this study are included in the manuscript and/or the supplementary files.

AUTHOR CONTRIBUTIONS

AP, RDC, MA, and VG contributed to the conception and design of the study. AP, MA, and VG synthetized the materials and their precursors. VG and MA performed elemental analysis, FTIR spectroscopy and thermogravimetric analysis. RDC and GMDL performed electrical material characterization. AP, MA, VG, and GM contributed to ss-NMR data acquisition. RDC, MA, VG, and TS contributed to spectroscopical data acquisition with the use of synchrotron radiation and their elaboration. All authors contributed to the interpretation and the analysis of the data. All the authors wrote sections of the manuscript, contributed to manuscript revision, read, and approved the submitted version.

FUNDING

The authors acknowledge the financial support of CERIC-ERIC Consortium under proposal 20142029 for the access to experimental facilities at Materials Science Beamline (MSB), Elettra Synchrotron in Trieste and at the Slovenian NMR Center of Lubjiana. This work has received support also from the project Electrical and Spectroscopic Properties of Eumelanin for Related Innovative Applications (ESPERIA) funded by the University of Naples Federico II inside the 2016 call for Finanziamento della Ricerca di Ateneo and from Piano Annuale della Ricerca Mise-CNR 2015–2017 "Sistemi elettrochimici per l'accumulo di energia".

ACKNOWLEDGMENTS

The authors acknowledge L. Cortese (IRC-CNR) for SEM imaging, N. Tsud and M. Vorokhta (Charles University) for their helpful suggestions during the photoemission measurements at MSB-Elettra.

SUPPLEMENTARY MATERIAL

The Supplementary Material for this article can be found online at: https://www.frontiersin.org/articles/10.3389/fchem.2019.00121/full#supplementary-material

REFERENCES

Abbas, M., Ali, M., Shah, S. K., D'Amico, F., Postorino, P., Mangialardo, S., et al. (2011). Control of structural, electronic, and optical properties of eumelanin films by electrospray deposition. *J. Phys. Chem. B* 115, 11199–11207. doi: 10.1021/jp2033577

Alfè, M., Gargiulo, V., and Di Capua, R. (2015). Tuning the surface morphology of self-assembled graphene-like thin films through pH variation. *Appl. Surf. Sci.* 353, 628–635. doi: 10.1016/j.apsusc.2015.06.117

Alfè, M., Gargiulo, V., Di Capua, R., Chiarella, F., Rouzaud, J. N., Vergara, A., et al. (2012). Wet chemical method for making graphene-like films from carbon black. *ACS Appl. Mater. Interfaces* 4, 4491–4498. doi: 10.1021/am301197q

Alfè, M., Gargiulo, V., Lisi, L., and Di Capua, R. (2014b). Synthesis and characterization of conductive copper-based metal-organic framework/graphene-like composites. *Mat. Chem. Phys.* 147, 744–750. doi: 10.1016/j.matchemphys.2014.06.015

Alfè, M., Spasiano, D., Gargiulo, V., Vitiello, G., Di Capua, R., and Marotta, R. (2014a). TiO2/graphene-like photocatalysts for selective oxidation of 3-pyridine-methanol to vitamin B3 under UV/solar simulatedradiation in aqueous solution at room conditions: the effect of morphology on catalyst performances. *Appl. Catal. A* 487, 91–99. doi: 10.1016/j.apcata.2014.09.002

Arzillo, M., Mangiapia, G., Pezzella, A., Heenan, R. K., Radulescu, A., Paduano, L., et al. (2012). Eumelanin buildup on the nanoscale: aggregate growth/assembly and visible absorption development in biomimetic 5,6-dihydroxyindole polymerization. *Biomacromolecules* 13, 2379–2390. doi: 10.1021/bm3006159

Ascione, L., Pezzella, A., Ambrogi, V., Carfagna, C., and d'Ischia, M. (2013). Intermolecular π-electron perturbations generate extrinsic visible contributions to eumelanin black chromophore in model polymers with interrupted interring conjugation. *Photochem. Photobiol.* 89, 314–318, doi: 10.1111/php.12003

Barra, M., Bonadies, I., Carfagna, C., Cassinese, A., Cimino, F., and Crescenzi, O., et al. (2015). Eumelanin-based organic bioelectronics: myth or reality? *MRS Adv.* 1, 3801–3810. doi: 10.1557/adv.2015.49

Bettinger, C. J., Bruggeman, J. P., Misra, A., Borenstein, J. T., and Langer, R. (2009). Biocompatibility of biodegradable semiconducting melanin films for nerve tissue engineering. *Biomaterials* 30, 3050–3057. doi: 10.1016/j.biomaterials.2009.02.018

Borghetti, P., Ghosh, P., Castellarin-Cudia, C., Goldoni, A., Floreano, L., Cossaro, A., et al. (2012). Functional K-doping of eumelanin thin films: density functional theory and soft x-ray spectroscopy experiments in the frame of the macrocyclic protomolecule model. *J. Chem. Phys.* 136:204703. doi: 10.1063/1.4719211

Brédas, J. L., Calbert, J. P., da Silva Filho, D. A., and Cornil, J. (2002). Organic semiconductors: a theoretical characterization of the basic parameters governing charge transport. *Proc. Natl Acad. Sci. U.S.A.* 99, 5804–5809, doi: 10.1073/pnas.092143399

Cataliotti, R., and Paliani, G. (1976). Infrared study of the C-H stretching region of five-membered heterocyclic compounds. *Can. J. Chem.* 54, 2451–2457. doi: 10.1139/v76-348

Centeno, S. A., and Shamir, J. (2008). Surface enhanced raman scattering (SERS) and FTIR characterization of the sepia melanin pigment used in works of art. *J. Molecul. Struct.* 873, 149–159, doi: 10.1016/j.molstruc.2007.03.026

Chatterjee, S., Prados-Rosales, R., Tan, S., Itin, B., Casadevall, A., and Stark, R. E. (2014). Demonstration of a common indole-based aromatic core in natural and synthetic eumelanins by solid-state NMR. *Org. Biomol. Chem.* 12, 6730–6736. doi: 10.1039/C4OB01066C

Cheng, J., Moss, S. C., Eisner, M., and Zcshack, P. (1994). X-ray characterization of melanins—II Pigment. *Cell Res.* 7, 263–273. doi: 10.1111/j.1600-0749.1994.tb00061.x

Cicco, S. R., Ambrico, M., Ambrico, P. F., Talamo, M. M., Cardone, A., Ligonzo, T., et al. (2015). A water-soluble eumelanin polymer with typical polyelectrolyte behaviour by triethyleneglycol N-functionalization. *J. Mater. Chem. C* 3, 2810–2816. doi: 10.1039/C4TC01997K

Clancy, C. M., and Simon, J. D. (2001). Ultrastructural organization of eumelanin from sepia officinalis measured by atomic force microscopy. *Biochemistry* 40, 13353–13360. doi: 10.1021/bi010786t

D'Ischia, M., Wakamatsu, K., Napolitano, A., Briganti, S., Garcia-Borron, J. C., Kovacs, D., et al. (2013). Melanins and melanogenesis: methods, standards, protocols. *Pigment Cell Melanoma Res.* 26, 616–633. doi: 10.1111/pcmr.12121

Edge, R., D'Ischia, M., Land, E. J., Napolitano, A., Navaratnam, S., Panzella, L., et al. (2006). Dopaquinone redox exchange with dihydroxyindole and dihydroxyindole carboxylic acid. *Pigment Cell Res*. 19, 443–450. doi: 10.1111/j.1600-0749.2006.00327.x

Eom, T., Woo, K., and Shim, B. S. (2016). Melanin: a naturally existing multifunctional material. *Appl. Chem. Eng*. 27, 115–122. doi: 10.14478/ace.2016.1029

Gargiulo, V., Alfano, B., Di Capua, R., Alfè, M., Vorokhta, M., Polichetti, T., et al. (2018). Graphene-like layers as promising chemiresistive sensing material for detection of alcohols at low concentration. *J. Appl. Phys*. 123:024503. doi: 10.1063/1.5000914

Gargiulo, V. M., Alfè, M., Di Capua, R., Togna, A. R., and Cammisotto, V., Fiorito, S., et al. (2015). Supplementing π-systems: eumelanin and graphene-like integration towards high conductive material for mammalian cell culture bio-interface. *J. Mater. Chem. B* 3, 5070–5079. doi: 10.1039/C5TB00343A

Giri, G., Verploegen, E., Mannsfeld, S. C. B., Atahan-Evrenk, S., Kim, D. H., Lee, S. Y., et al. (2011). Tuning charge transport in solution-sheared organic semiconductors using lattice strain. *Nature* 480, 504–509. doi: 10.1038/nature10683

Glass, K., Ito, S., Wilby, P. R., Sota, T., Nakamura, A., Bowers, C. R., et al. (2012). Direct chemical evidence for eumelanin pigment from the Jurassic period Keely Glassa. *PNAS* 109 10218–10223. doi: 10.1073/pnas.1118448109

Hervé, M., Hirschinger, J., Granger, P., Gilard, P., Deflandre, A., and Goetz, N. (1994). A 13C solid-state NMR study of the structure and auto-oxidation process of natural and synthetic melanins. *Biochim. Biophys. Acta* 1204, 19–27. doi: 10.1016/0167-4838(94)90027-2

Huang, L., Liu, M., Huang, H., Wen, Y., Zhang, X., and Wei, Y. (2018). Recent advances and progress on melanin-like materials and their biomedical applications. *Biomacromolecules* 19, 1858–1868. doi: 10.1021/acs.biomac.8b00437

Jastrzebska, M. M., Isotalo, H., Paloheimo, J., and Stubb, H. (1995). Electrical conductivity of synthetic DOPA-melanin polymer for different hydration states and temperatures. *J. Biomater. Sci*. 7, 577–586. doi: 10.1163/156856295X00490

Kim, S. H., Kim, S. Y., and Shin, U. S. (2016). Core-shell structure and closest packing of electrically conductive polymer/carbon nanotube hybrid: high electrical conductivity of bucky paper. *Compos. Sci. Technol*. 126, 78–85. doi: 10.1016/j.compscitech.2016.02.017

Liu, Y., and Simon, J. D. (2003). Isolation and biophysical studies of natural eumelanins: applications of imaging technologies and ultrafast spectroscopy. *Pigment Cell Res*. 16, 606–618. doi: 10.1046/j.1600-0749.2003.00098.x

Ma, W., Shi, K., Wu, Y., Lu, Z. Y., Liu, H. Y., Wang, J. Y., et al. (2016). Enhanced molecular packing of a conjugated polymer with high organic thermoelectric power factor. *ACS Appl. Mater. Interfaces* 8, 24737–24743. doi: 10.1021/acsami.6b06899

McGinness, J., Corry, P., and Proctor, P. (1974). Amorphous semiconductor switching in melanins. *Science* 183, 853–855. doi: 10.1126/science.183.4127.853

Meredith, P., Bettinger, C. J., Irimia-Vladu, M., Mostert, A. B., and Schwenn, P. E. (2013). Electronic and optoelectronic materials and devices inspired by nature. *Rep. Prog. Phys*. 76:034501. doi: 10.1088/0034-4885/76/3/034501

Mostert, A. B., Powell, B. J., Gentle, I. R., and Meredith, P. (2013). On the origin of electrical conductivity in the bio-electronic material melanin. *Appl. Phys. Lett*. 100:093701. doi: 10.1063/1.3688491

Papari, G. P., Gargiulo, V., Alfè, M., Di Capua, R., Pezzella, A., and Andreone, A. (2017). THz spectroscopy on graphene-like materials for bio-compatible devices. *J. Appl. Phys*. 121:145107. doi: 10.1063/1.4980106

Pezzella, A., Iadonisi, A., Valerio, S., Panzella, L., Napolitano, A., Adinolfi, M., et al. (2009). Disentangling eumelanin "black chromophore": visible absorption changes as signatures of oxidation state- and aggregation-dependent dynamic interactions in a model water-soluble 5,6-dihydroxyindole polymer. *J. Am. Chem. Soc*. 131, 15270–15275. doi: 10.1021/ja905162s

Pines, A., Gibby, M. G., and Waugh, J. S. (1973). Proton-enhanced NMR of dilute spins in solids. *J. Chem. Phys.* 59:569. doi: 10.1063/1.1680061

Rettenwander, D., Blaha, P., Laskowski, R., Schwarz, K., Bottke, P., Wilkening, M., et al. (2014). DFT study of the role of Al3+ in the fast ion-conductor Li7−3xAl3+xLa3Zr2O12. *Chem. Mater*. 26, 2617–2623. doi: 10.1021/cm5000999

Sahimi, M. (1994). *Applications of Percolation Theory.* London: Taylor & Francis Ltd.

Saini, A. S., and Melo, J. S. (2015). One-pot green synthesis of eumelanin: process optimization and its characterization. *RSC Adv*. 5, 47671–47680. doi: 10.1039/C5RA01962A

Sangaletti, L., Borghetti, P., Ghosh, P., Pagliara, S., Vilmercati, P., Castellarin-Cudia, C., et al. (2009). Polymerization effects and localized electronic states in condensed-phase eumelanin. *Phys. Rev. B* 80, 174203–174209. doi: 10.1103/PhysRevB.80.174203

Sheliakina, M., Mostert, A. B., and Meredith, P. (2018). Decoupling ionic and electronic currents in melanin. *Adv. Funct. Mater*. 28:1805514. doi: 10.1002/adfm.201805514

Silverstein, R. M., Webster, F. X., and Kiemle, D. J. (2008). *Spectrometric Identification of Organic Compounds,* 4th edn. Hoboken, NJ: Wiley.

Snavely, D. L., Blackburn, F. R., Ranasinghe, Y., Walters, V. A., and Gonzalez del Riego, M. (1992). Vibrational overtone spectroscopy of pyrrole and pyrrolidine. *J. Phys. Chem*. 96, 3599–3605. doi: 10.1021/j100188a010

Tran, M. L., Powell, B. J., and Meredith, P. (2006). Chemical and structural disorder in eumelanins: a possible explanation for broadband absorbance. *Biohys. J*. 90, 743–752. doi: 10.1529/biophysj.105.069096

van der Pauw, L. J. (1958). A method of measuring specific resistivity and Hall effect on discs of arbitrary shape. *Philips Res. Repts*. 13, 1–9.

Wunsche, J., Deng, Y., Kumar, P., Di Mauro, E., Josberger, E., Sayago, J., et al. (2015). Protonic and electronic transport in hydrated thin films of the pigment eumelanin chem. *Mater* 27, 436–442. doi: 10.1021/cm502939r

Xiao, M., Chen, W., Li, W., Zhao, J., Hong, Y. L., Nishiyama, Y., et al. (2018). Elucidation of the hierarchical structure of natural eumelanins. *J. R. Soc. Interface* 15:20180045. doi: 10.1098/rsif.2018.0045

Xin, C., Ma, J., Tan, C., Yang, Z., Ye, F., Long, C., et al. (2015). Preparation of melanin from *Catharsius molossus* L. and preliminary study on its chemical structure. *J. Biosci. Bioeng*. 119, 446–454. doi: 10.1016/j.jbiosc.2014.09.009

Conflict of Interest Statement: The authors declare that the research was conducted in the absence of any commercial or financial relationships that could be construed as a potential conflict of interest.

frontiers in Chemistry

ORIGINAL RESEARCH
published: 26 March 2019
doi: 10.3389/fchem.2019.00162

Evidence of Unprecedented High Electronic Conductivity in Mammalian Pigment Based Eumelanin Thin Films After Thermal Annealing in Vacuum

Ludovico Migliaccio[1], Paola Manini[1], Davide Altamura[2], Cinzia Giannini[2], Paolo Tassini[3], Maria Grazia Maglione[3], Carla Minarini[3] and Alessandro Pezzella[4]**

[1] Department of Chemical Sciences, University of Naples "Federico II," Naples, Italy, [2] Istituto di Cristallografia (IC), CNR, Bari, Italy, [3] Laboratory for Nanomaterials and Devices (SSPT-PROMAS-NANO), ENEA C. R. Portici, Piazzale Enrico Fermi 1, Località Granatello, Portici, Italy, [4] Institute for Polymers, Composites and Biomaterials (IPCB), CNR, Pozzuoli, Italy

Edited by:
Carlo Augusto Bortolotti,
University of Modena and Reggio Emilia, Italy

Reviewed by:
Vincent Ball,
Université de Strasbourg, France
Yingxin Deng,
California Institute of Technology, United States
Maria Grazia Bridelli,
University of Parma, Italy

***Correspondence:**
Paolo Tassini
paolo.tassini@enea.it
Alessandro Pezzella
alessandro.pezzella@unina.it

Specialty section:
This article was submitted to Organic Chemistry, a section of the journal Frontiers in Chemistry

Received: *10 January 2019*
Accepted: *04 March 2019*
Published: *26 March 2019*

Citation:
Migliaccio L, Manini P, Altamura D, Giannini C, Tassini P, Maglione MG, Minarini C and Pezzella A (2019) Evidence of Unprecedented High Electronic Conductivity in Mammalian Pigment Based Eumelanin Thin Films After Thermal Annealing in Vacuum. Front. Chem. 7:162. doi: 10.3389/fchem.2019.00162

Melanin denotes a variety of mammalian pigments, including the dark electrically conductive eumelanin and the reddish, sulfur-containing, pheomelanin. Organic (bio)electronics is showing increasing interests in eumelanin exploitation, e.g., for bio-interfaces, but the low conductivity of the material is limiting the development of eumelanin-based devices. Here, for the first time, we report an abrupt increase of the eumelanin electrical conductivity, revealing the highest value presented to date of 318 S/cm. This result, obtained via simple thermal annealing in vacuum of the material, designed on the base of the knowledge of the eumelanin chemical properties, also discloses the actual electronic nature of this material's conduction.

Keywords: charge transport, vacuum thermal treatment, electrical conductivity, organic (bio)electronics, eumelanin, melanins, molecular orientation

INTRODUCTION

In the 1974, McGinness et al. reported the first experimental evidence of the semiconducting behavior of the eumelanin (McGinness et al., 1974), the polyindolic pigment responsible, inter alia, of the dark-brown pigmentation of the mammalian (including human) skin, hair, and iris. The study followed a pioneering suggestion by Pullman and Pullman (1961) on the possible existence of energy bands associated with a non-localized empty molecular orbital within an infinite eumelanin polymer chain acting as an one-dimensional semiconductor.

Since then, the charge transport properties of this challenging materials class were extensively studied (d'Ischia et al., 2015), and particularly in the recent years, after the renewed interest in the topic, because of the prospect to exploit the eumelanin in organic (bio)electronics (Muskovich and Bettinger, 2012). Since the ′70 also the chemical characterization of eumelanin pigment witnessed a noteworthy development allowing to delineate a sound picture of the chemical structural signatures of the natural pigment and to design and fabricate valuable synthetic models (d'Ischia et al., 2015). Among these models the one involving oxidative polymerization of the 5,6-dihydroxyindole (DHI, **Figure S1**), the ultimate monomer precursor in the formation pathways of natural eumelanin, proved to be one of the most valuable for both its chemical structure and biocompatibility and is widely acknowledged (d'Ischia et al., 2015). To date, conductivity of synthetic as well as natural eumelanin is reported in the range (Osak et al., 1989; Meredith and Sarna, 2006) $10^{-13}-10^{-5}$ S/cm, largely depending on the measuring conditions, and especially on the presence of humidity in the measuring environment (Jastrzebska et al., 1995). For valuable applications, higher conductivity values are needed yet, thus several studies explored the integration of the eumelanin with other more conductive materials (Mihai et al., 2013; Gargiulo et al., 2015; Migliaccio et al., 2017), but strongly affecting its chemistry, or exploiting severe modifications of eumelanin-like materials to gain a graphene-like material, as for example by pyrolytic treatment of polydopamine under hydrogen or argon atmosphere (Kong et al., 2012; Li et al., 2013). Although the mechanisms of the charge transport in the eumelanin are still not fully clear, several evidences are concurring to sustain a hybrid ionic-electronic behavior (Mostert et al., 2012; Wünsche et al., 2015), where the electronic contribution depends on the presence, extent and the redox properties (Mostert et al., 2012) of the delocalized aromatic systems, while the ionic part is largely dictated by the hydration level of the material (Wünsche et al., 2015) (i.e., the humidity in the measuring environment).

Basing on the concurring evidences disclosing the correlation between the chemical-physical properties of the eumelanin and the polyindole π-system stacking, as well as the packing of molecular constituents within the material (Pezzella et al., 2009; Bonavolontà et al., 2017), we speculated about the modulation of the electronic conductivity (Noriega et al., 2013; Liu et al., 2017) by acting on the polyindole packing in eumelanin thin films. This is bringing us, here, for the first time in our knowledge, to report the preparation and characterization of eumelanin thin films showing the highest conductivity values of this material up to 318 S/cm.

Conductive eumelanin films were prepared via the preliminary oxidative polymerization of the solid state form of DHI (d'Ischia et al., 2013) and then by thermal annealing of the material films, at temperatures not higher than 600°C and under high vacuum conditions (order of 10^{-6} mbar). We name the obtained material as High Vacuum Annealed Eumelanin, HVAE.

EXPERIMENTAL PART

All the commercially available reagents and materials were used as received. All the solvents were analytical grade quality. The DHI was prepared according to a reported procedure (d'Ischia et al., 2013). The samples were prepared on quartz substrates (dimensions 15 mm × 6 mm × 1.2 mm), cleaned by sonication in a solution of detergent Borer Chemie AG Deconex 12PA® in deionized water (18 MΩ·cm) at 70°C for 30 min, and rinsed in deionized water, then in acetone and then in isopropanol for 15 min each sequentially. A concentrated solution of DHI in methanol-ethyl acetate (1:1 v/v) (50 mg/mL) was prepared, filtered through a 0.2 µm Whatman membrane before deposition; on each sample, 15 µL of this solution were applied. Thin films were obtained by spin coating, using a Laurell WS-650MZ23NPP/LITE coater, with the spinning recipe: acceleration 2,000 rpm/s, speed 3,500 rpm, duration 30 s. The resulting films were dried at 90°C for 30 min in oven in air. The thicknesses of the DHI films were 230 ± 10 nm, measured using a stylus profilometer KLA Tencor P-10. Thermogravimetric analysis (TGA) performed under not oxidizing atmosphere using a Perkin–Elmer Pyris thermogravimetric analyzer. Scanning electronic microscopy (SEM) was run using a SEM Zeiss Leo 1530 Gemini. UV-Vis spectra were recorded using a Perkin-Elmer Lambda 900 spectrophotometer. The electron paramagnetic resonance (EPR) spectra were measured using an X-band (9 GHz) Bruker Elexys E-500 spectrometer, equipped with a superhigh sensitivity probe head), the Raman spectra were reordered Renishaw inVia Raman microscope (532 nm), which uses a microscope to focus a laser source onto specific areas of a sample, then the light scattered off the surface of the sample is collected and directed to a Raman spectrometer), the FTIR analysis were run using a Thermo Fischer Scientific Nicolet 6700 FTIR to determine the attenuated total reflectance (ATR) spectra of the samples, with a resolution of 4 cm^{-1} and 16 scans averaged for each spectrum in a range between 4000 and 650 cm^{-1}), MALDI-MS analysis was done using a positive reflectron MALDI and LDI spectra were recorded on a Sciex 4800 MALDI ToF/ToF instrument. Grazing Incidence Wide Angle X-ray Scattering (GIWAXS) was run with a Fr-E+ SuperBright rotating anode microsource (CuKa, $\lambda = 0.154$ nm) equipped to a three-pinhole camera (Rigaku SMAX-3000) through a multilayer focusing optics (Confocal Max-Flux; CMF 15–105). Elemental composition (C, H, N wt.%) was estimated using a Perkin–Elmer 2400 CHNSO elemental analyzer. Measurements of electrical resistance vs. temperature were performed measuring the two-terminals devices of one type of the HVAE (600°C, 2 h, 10^{-6} mbar) in a probe station CASCADE Summit 11000B-M, featuring a closed chamber with thermal chuck, keeping the samples in constant flow (10 L/min) of pure dry Nitrogen, allowing the temperature to stabilize within ±1°C before each measurements run, and using a Keithley 4200 SCS Semiconductor Characterization System to acquire the electrical data.

The eumelanin formation was obtained by the oxidation of the DHI films thanks to the Ammonia-Induced Solid State Polymerization (AISSP) method, a recently developed solid state protocol (d'Ischia et al., 2013; Pezzella et al., 2015). Each sample was exposed for 12 h to an oxidizing atmosphere made of oxygen, water and ammonia vapors at controlled temperature (25°C), produced by the equilibrium of the air with an ammonia solution (5% NH_3 in H_2O) in a sealed chamber at 1 bar pressure. The material so obtained is here named DHI-eumelanin, to distinguish it from the starting DHI, and from the final HVAE. The thicknesses of the DHI-eumelanin films were 260 ± 6 nm. Films showed the typical dark brown color of the eumelanin (**Figure S2**), presenting flat surfaces (**Figure S3**, **Table S1**; surfaces roughness images were taken using a Taylor Hobson® CCI-HD non-contact 3D Optical Profilometer with thin & thick film measurement capability; films' roughness was estimated as a Root Mean Square (RMS) value from several scans on each sample).

The DHI-eumelanin films were finally turned into HVAE by annealing at different controlled temperatures (230, 300, 450, and 600°C, ±1°C for each value) in high vacuum conditions (10^{-6}

mbar); some samples were also annealed at various time lengths (from 30 min up to 6 h). The processes were performed in a dedicated high vacuum chamber using a turbomolecular pump to obtain the vacuum level, and doing preliminary leak detection and samples temperature verifications. The mean thickness of the HVAE films was dependent on the annealing conditions, with the smallest values down to 110 ± 2 nm for the processes at 600°C longer than 1 h (**Figure S5**).

RESULTS AND DISCUSSION

The chosen annealing temperatures were well below the values reported as the starting temperature for the degradation (Albano et al., 2016) and/or the carbonization processes in similar materials (Yu et al., 2014), but includes a significant part of the eumelanin mass loss region, as shown by thermogravimetric analysis (TGA). Moreover, applied temperatures include the complete loss of both weakly and strongly bound water (Albanese et al., 1984; Meredith and Sarna, 2006; Albano et al., 2016), as well as the loss of CO_2 from carboxyl groups in DHI-eumelanin (thermal decarboxylation) (Swan and Waggott, 1970). Indeed, TGA data under not oxidizing conditions indicate that mass loss is nearly completed at 800°C, suggesting that little or no modification of the molecular backbone occurs at 600°C. Instead, a complete different picture is obtained in presence of oxygen, which critically affects the stability of the material (**Figure S4**).

Morphology and surface analysis of the materials at the different stages of the process revealed a nearly unmodified roughness, passing from the starting DHI films to the HVAE films (**Figure S3**) (using the definition of the roughness according to the standard ISO 25178; DHI roughness = 6.45 nm; DHI-eumelanin roughness = 6.52 nm; HVAE roughness = 6.58 nm), while, as said, the thickness suffered a significant decrease in function of the annealing temperature from 260 to 109 nm in the case of the sample treated at 600°C (**Figure S5**). This was expected because of the said tendency of the eumelanin to loss labile carboxylic groups (Swan and Waggott, 1970; d'Ischia et al., 2013; Albano et al., 2016) and on the possible loss of low molecular weight components embedded in the material.

Scanning electronic microscopy (SEM) inspection confirmed the retaining of the high quality morphology of the HVAE films (**Figure S6**), showing an uniform surface of this material.

UV-Vis spectra, observed at the different process steps (**Figure 1**), show an evident increase in the absorption coefficients in nearly the entire UV-Vis range, passing from the DHI to the DHI-eumelanin and to the HVAE. This phenomenon is associated to the increase of both the delocalization of the aromatic systems and their π-stacking interactions (Pezzella et al., 2009; Bonavolontà et al., 2017), that suggest the actual increase of the extension and of the filling factor (Albanese et al., 1984; Bonavolontà et al., 2017) for the delocalized aromatic systems of the material backbone, in particular happening after the thermal annealing in vacuum: i.e., this reorganization results in an overlap of the π-electronic density of the adjacent packed chains and the delocalization of their electronic wave-functions (Koller et al., 2007).

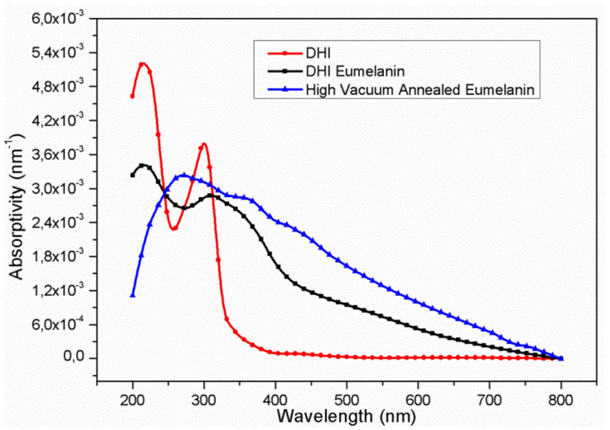

FIGURE 1 | UV-Vis absorptivity (percent absorbance/film thickness) of the films at the different process stages: (red, circles) DHI; (black, squares) DHI-eumelanin (film after AISSP); (blue, triangles) HVAE (film after thermal annealing in vacuum: 600°C; 2 h; 10^{-6} mbar).

Strong support to the picture of a structural reorganization and an enhanced packing order (Roncali and Thobie-Gautier, 1994; Roncali, 1997; Liu et al., 2016) of the molecular constituents within the HVAE films was further given by the retaining of the typical eumelanin signature observed using different characterization techniques (**Figures S7–S10**): (i) the electron paramagnetic resonance (EPR) spectrum (Meredith and Sarna, 2006; d'Ischia et al., 2013), (ii) the Raman spectroscopy (Capozzi et al., 2005; Albano et al., 2016), (iii) the FTIR analysis (Hyogo et al., 2011), and (iv) the MALDI-MS (Pezzella et al., 2015) analysis. A pictorial representation of this packing model, made possible by the concomitant loss of labile and low molecular weight components (Swan and Waggott, 1970) and by the clustering of the longer polyindole chains, is shown in **Figure 2**.

Although each of these techniques cannot be considered conclusive to confirm the nature of the molecular constituents within the films, the concurrence of data from different spectroscopies has to be considered decisive, basing on literature. Indeed, coherently with UV-Vis profiles, also ERP spectra of HVAE (**Figure S7**) were consistent with those reported in literature for eumelanin samples featuring a single, roughly symmetric signal at a B value in the range of 2.003 ± 0.004 G, a typical signature of the eumelanin pigment (Meredith and Sarna, 2006), associated to carbon-centered radicals formed in the 5,6-dihydroxyindole polymerization.

Without entering into the details of the Raman spectra (**Figure S8**), it is worth to note here how the comparison of the profiles before and after the annealing reveals, in agreement with the loss of carboxylic groups and possible pyrrolic acids, a relative reduction of the G band (the range of 1,600 cm^{-1}) following the reduction of O and N contribution. Consistent information is provided by the FTIR spectra of the DHI-eumelanin and the HVAE films (**Figure S9**) too, highlighting in particular the drastic decrease of the signals associated to the C=O stretching (1,620 cm^{-1}) and to the water (3,200 cm^{-1}) (Hyogo et al., 2011).

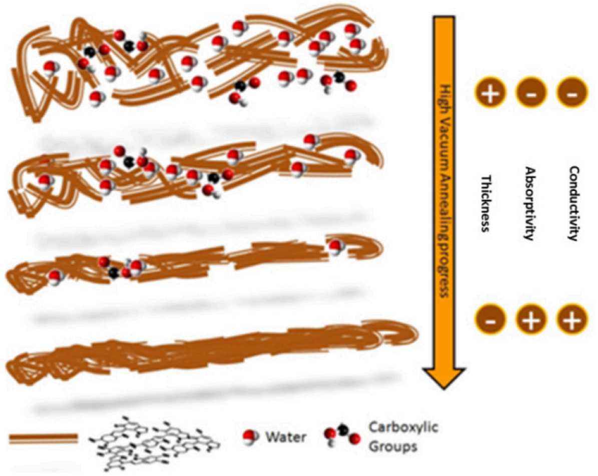

FIGURE 2 | Pictorial model of the polyindole packing evolution during the high vacuum annealing. Water molecules and carboxylic groups are evidenced, to show their reduction in the material as the process temperature increases.

Consistently with literature, MALDI profiles (**Figure S10**) of DHI-eumelanin and HVAE also share the recurring profile of masses of general formula *DHI oligomer*+mO_2-nCO_2 (Pezzella et al., 2015).

Finally, a direct support to the packing evolution hypothesis comes from 2D GIWAXS patterns (**Figure 3**). Diffraction data were collected from as-prepared films deposited on glass substrates in Grazing Incidence Wide Angle X-ray Scattering. The different anisotropy degree of the intensity distribution along the diffraction rings indicates an increased orientation degree after the vacuum thermal treatment is operated. In particular, the HVAE film (**Figure 3A**) features a diffraction intensity definitely concentrated along the Q_z axis, i.e., perpendicularly to the sample surface, denoting a preferred orientation of the diffracting planes parallel to the film surface. On the other hand, the DHI-eumelanin film (**Figure 3B**) features a weak diffraction intensity evenly distributed along the azimuth of a broad diffraction ring, indicating low crystallinity and random orientation of the molecules. The 1D radial cuts extracted from the GIWAXS maps along the out-of-plane (**Figure 3C**) and in-plane (**Figure 3D**) directions show indeed a clear difference between the two directions in the case of the HVAE film: a peak asymmetry in the out-of-plane direction reveals a diffraction contribution of the oriented molecules appearing as a shoulder at $q = 1.85$ Å, at the side of the main peak at $q = 1.56$ Å which is ascribed to the substrate and is in turn the only scattering contribution in the in-plane cut. The shoulder in the out-of-plane direction is a clear signature of the formation of a well oriented stack, compatible with the expected supramolecular structure with 3.4 Å periodicity (Zajac et al., 1994; Chen et al., 2013).

On the contrary, in the case of the DHI-eumelanin film no difference between the diffraction intensities in the two directions is recognized (so that a 5.5 additional scale factor has been applied in **Figure 3C** for the sake of clarity in the comparison).

The electrical properties of the materials were measured using two set-ups, because of the different conductivity values that samples presented. Between the various measurements runs, the samples were stored in mild vacuum (10^{-4} mbar), cleaning the storage chamber each time it was opened using pure dry nitrogen (oxygen and water vapor content below 5 ppm).

A four-point probes system (Schroder, 1986; Bothma et al., 2008) Napson RESISTAGE RG-80 was used, measuring the sheet resistance of each film, and assuming that input current flowed through the full thickness of each thin layer, in order to calculate the material conductivity thanks to the films thickness. In this measurement configuration, the contact resistance between the probes and the material can be disregarded, because (i) the input current is fixed and known by the instrument, and it could flow in the device regardless the presence of a contact resistance in this circuit branch, allowing to obtain the sheet resistance value, and (ii) virtually no current passes in the voltmeter circuit branch, so a contact resistance (if it were present) in this point gives no effect in the measurements.

For low conductivity samples, the four-point probes Napson instrument cannot be used, so two-terminal devices were prepared with the different films of the materials, using silver paste to prepare the devices contact pads and cutting away the film where it was not necessary, to avoid anomalous current paths. A power supply source meter Keithley 2410 was used in four-point probes configuration, and the devices resistance was derived through the alternating polarity method (Daire, 2001), and then the conductivity calculated.

In **Figure 4**, the samples conductivity vs. the annealing temperature and vs. the duration of the processes is shown. After the vacuum annealing, the conductivity of the films featured a remarkable increase, up to over 9 orders of magnitude, passing from around 10^{-7} S/cm for the DHI and DHI-eumelanin films, up to an unprecedented value of 318 S/cm for the material processed at 600°C for 2 h, and anyway obtaining values larger than 100 S/cm for all the samples processed at 600°C (**Figure 4** inset).

This unprecedented result is not a humidity response effect, as the data acquisitions were performed in few tens of seconds for each sample, with no variation of the ambient relative humidity, so suggesting that actual nature of the involved charge carriers is electronic. Nonetheless, at fixed temperature in air for longer time, the conductivity of the HVAE films appears pretty stable with time (**Figure S13**), allowing the material to sustain a constant current with a very low increase in the applied voltage along the time, as it can be expected for electronic conductive organics (Le et al., 2017). Even more, if the environmental humidity was being absorbed by the material films during the measurements, according to the current literature about eumelanin, its conductivity should be increased, which means that voltage should decrease during this type of measurement. Instead, here it can be observed the opposite effect: i.e., the sample resistance was increasing along the time. So, HVAE conduction can be considered largely independent from the presence of humidity in the material.

Current-voltage measurements performed before and after the exposition of the films to water or acidic conditions

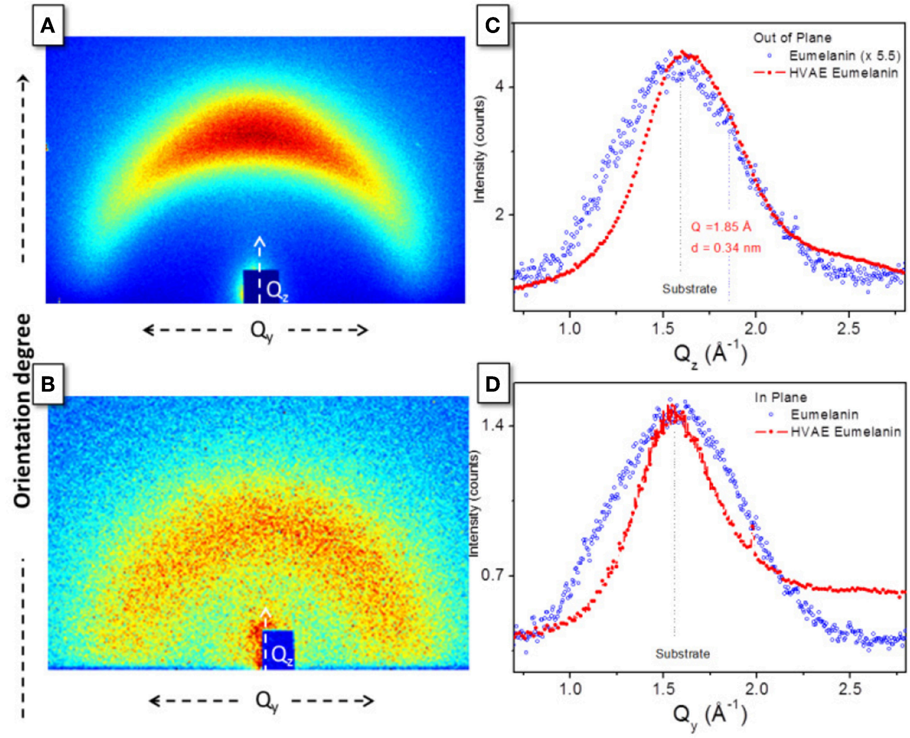

FIGURE 3 | GIWAXS 2D patterns of **(A)** HVAE film (processed at 600°C for 2 h) and **(B)** DHI-eumelanin film. 1D radial cuts along **(C)** the out-of-plane and **(D)** the in-plane directions, obtained from the 2D maps in **(A,B)**.

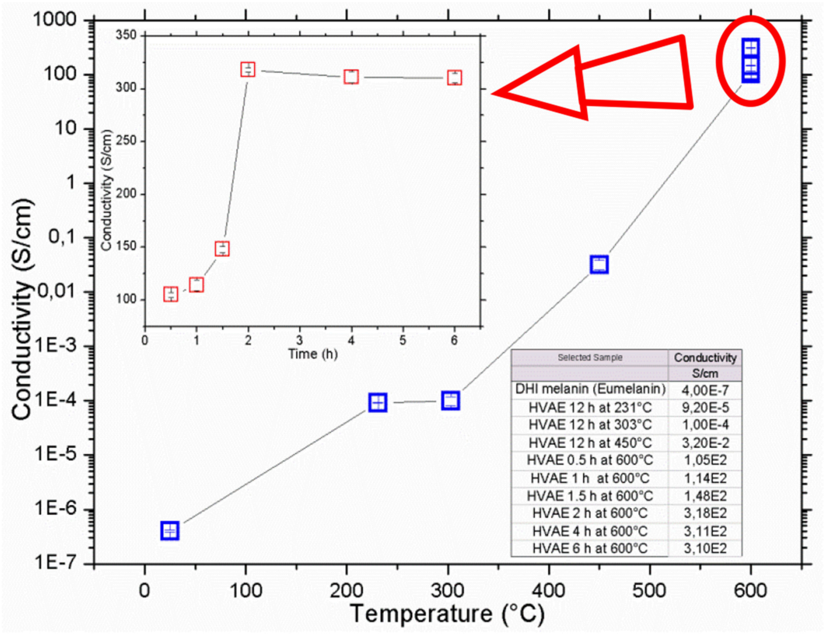

Selected Sample	Conductivity S/cm
DHI melanin (Eumelanin)	4,00E-7
HVAE 12 h at 231°C	9,20E-5
HVAE 12 h at 303°C	1,00E-4
HVAE 12 h at 450°C	3,20E-2
HVAE 0.5 h at 600°C	1,05E2
HVAE 1 h at 600°C	1,14E2
HVAE 1.5 h at 600°C	1,48E2
HVAE 2 h at 600°C	3,18E2
HVAE 4 h at 600°C	3,11E2
HVAE 6 h at 600°C	3,10E2

FIGURE 4 | Conductivity of vacuum annealed eumelanin thin films vs. the annealing temperature and (inset) vs. the annealing time at 600°C temperature. Data are listed in the table. All the measurements were performed in air at room temperature. Errors of each point are indicated inside the plots symbols.

conclusively ruled out any conductivity increase with the water content of the film. Immersion of the films in deionized water results in a marked decrease of the conductivity, also associated to a deterioration of the surface smoothness (**Figure S11** and **Table S2**). Reduction of the conductivity is even more pronounced when films are exposed to acidic solutions (d'Ischia et al., 2013) (**Figure S12** and **Table S3**). Notably, the films appear moderately stable under accelerated aging (**Table S4**), but stability is lost if the film was previously immersed in water (**Table S2**). In light of known literature (Bothma et al., 2008; Wünsche et al., 2015; Di Mauro et al., 2016), this behavior clearly suggests that contribution of the ionic effects in the charge transport can be considered negligible in HVAE. Moreover, the drastic effects induced by the exposition to soaking (Ito et al., 2011) water or acidic solutions witness the key role of packing of the aromatic polyindole systems in determining electrical properties of the films (Jastrzebska et al., 2002; Ito et al., 2011; Noriega et al., 2013; Liu et al., 2017).

The here observed increases in the conductivity cannot be ascribed to the formation of films akin to dense carbon black materials (Celzard et al., 2002; Jan et al., 2006), because the processes producing these materials operate high temperatures (1,000°C or more) when applied to eumelanin-like materials (Kong et al., 2012; Li et al., 2013), or anyway at temperatures above 600°C to obtain good conductivity values when applied to polypeptides rich in eumelanin precursors (phenylalanine) (Namgung et al., 2017). Instead, in this study it is observed a notably conductivity increase, from 3 to 5 orders of magnitude, even after annealing in the 200°C÷450°C range. This strongly suggests that conductivity rise has not to be ascribed to carbonization processes. Indeed, elemental analysis data (**Table S5**) do confirm the material does not present C/X ratios expectable for carbon black materials (Celzard et al., 2002).

Although the disordered eumelanin stuffs could suggest that the range of temperatures over which carbonization may take place is likely to be very broad, relevant literature addressing thermal evolution similar materials (Liu et al., 2007; Jin et al., 2016) (phenol and pyrrole polymers) do show no carbonization occurs below 850–900°C.

Moreover, the little observed increase in the C/X ratio is actually related to the loss of the labile CO_2 groups (see **Table S5** legend) as confirmed by the nearly constant C/N ratio.

On this basis, even the possible occurrence of a small amount of carbonization can be ruled out and, even more so, graphitization must be excluded as it requires even higher temperatures (Zajac et al., 1994; Li et al., 2013).

Measurements of electrical resistance vs. temperature were also performed (**Figure S14**), measuring the two-terminals devices of one type of the HVAE (600°C, 2 h, 10^{-6} mbar). The observed values of R and the trend of R vs. T reveal that not simple mechanisms are operating for the conductivity of the material: the small values of R indicate that it is a good electronic conductor (Le et al., 2017), while its trend in this range of temperatures cannot discriminate between a nature of semiconductor (decreasing R vs. T) or of conductor (increasing R vs. T), indeed a task beyond the scope of this paper.

CONCLUSIONS

Results here reported indicate a radical modification of the actual picture of the eumelanin charge transport properties, reversing the paradigm according to which eumelanin conductivity increases with the water content of the material. Indeed, if the eumelanin films are rearranged into conductive layers, thanks to a simple thermal annealing in vacuum which succeeds in inducing a structural reorganization of their molecular constituents, the contribution of the electronic current is here demonstrated to be largely preeminent with respect to the reported ionic one (Mostert et al., 2012; Di Mauro et al., 2016; Sheliakina et al., 2018). This allows to obtain unprecedented high conductivity values, up to 318 S/cm in this work, and the mammalian pigment model, the DHI eumelanin, can be considered as an actual conductor. The conductivity values here achieved and their fine tuning, allowed by the control of the process conditions, open to possible tailoring of *ad-hoc* eumelanin-based active layers for a wide range of applications in organic electronics and bioelectronics, deserving further extensive investigations to get a conclusive picture about the conductor vs. semiconductor behavior of the eumelanin and insights about the mobility of the charge carriers.

DATA AVAILABILITY

All datasets generated for this study are included in the manuscript and/or the **Supplementary Files**.

AUTHOR CONTRIBUTIONS

All authors conceived the experiments. LM and PM with contributions by AP, PT, and DA carried out the measurements. LM, AP, and PT processed and analyzed experimental data. LM fabricated all the samples. All the authors discussed the results and wrote the main manuscript. AP, PT, CG, MGM and CM contributed to refine the manuscript.

FUNDING

Italian Ministry for Education, University and Research—Project RELIGHT (PON02_00556_3306937); the Italian Ministry of Economic Development—PROG. No. E10/000798/02/E 17; the European Commission FP7-PEOPLE-2013-IRSES, Project Reference: 612538; Knowledge and Innovation Community (KIC) EIT RawMaterials—Network of Infrastructure OPTNEWOPT (P. A. 15065).

ACKNOWLEDGMENTS

Authors thank also Mr. Antonio Citarella, for his invaluable support in keeping the process systems running, Dr. Anna De Girolamo Del Mauro for the SEM images, and Dr. Carmela Tania Prontera for some of the UV-Vis acquisitions. R. Lassandro is acknowledged for his technical support in the X-ray lab.

SUPPLEMENTARY MATERIAL

The Supplementary Material for this article can be found online at: https://www.frontiersin.org/articles/10.3389/fchem.2019.00162/full#supplementary-material

REFERENCES

Albanese, G., Bridelli, M. G., and Deriu, A. (1984). Structural dynamics of melanin investigated by rayleigh scattering of mössbauer radiation. *Biopolymers.* 23, 1481–1498. doi: 10.1002/bip.360230805

Albano, L. G. S., Di Mauro, E., Kumar, P., Cicoira, F., Graeff, C. F. O., and Santato, C. (2016). Novel insights on the physicochemical properties of eumelanins and their dmso derivatives. *Polymer Int.* 65, 1315–1322. doi: 10.1002/pi.5167

Bonavolontà, C., Lisio, C., d'Ischia, M., Maddalena, P., Manini, P., Pezzella, A., et al. (2017). Anomalous evolution of broadband optical absorption reveals dynamic solid state reorganization during eumelanin build-up in thin films. *Sci. Rep.* 7:522. doi: 10.1038/s41598-017-00597-8

Bothma, J. P., de Boor, J., Divakar, U., Schwenn, P. E., and Meredith, P. (2008). Device-quality electrically conducting melanin thin films. *Adv. Mat.* 20, 3539. doi: 10.1002/adma.200703141

Capozzi, V., Perna, G., Gallone, A., Biagi, P. F., Carmone, P., Fratello, A., et al. (2005). Raman and optical spectroscopy of eumelanin films. *J. Mol. Struct.* 744–747, 717–721. doi: 10.1016/j.molstruc.2004.11.074

Celzard, A., Mareche, J. F., Payot, F., and Furdin, G. (2002). Electrical conductivity of carbonaceous powders. *Carbon.* 40, 2801–2815. doi: 10.1016/S0008-6223(02)00196-3

Chen, C. T., Ball, V., Gracio, J. J., Singh, M. K., Toniazzo, V., Ruch, D., et al. (2013). Self-assembly of tetramers of 5,6-dihydroxyindole explains the primary physical properties of eumelanin: Experiment, simulation, and design. *Acs Nano.* 7, 1524–1532. doi: 10.1021/nn305305d

Daire, A. (2001). *Improving the Repeatability of Ultra-High Resistance and Resistivity Measurements*. White Paper, Keithley Instruments, Inc., 1808.

Di Mauro, E., Carpentier, O., Yáñez Sánchez, S. I., Ignoumba, N., Lalancette-Jean, M., Lefebvre, J., et al. (2016). Resistive switching controlled by the hydration level in thin films of the biopigment eumelanin. *J. Mater. Chem.* C4, 9544–9553. doi: 10.1039/c6tc02793h

d'Ischia, M., Wakamatsu, K., Cicoira, F., Di Mauro, E., Garcia-Borron, J. C., Commo, S., et al. (2015). Melanins and melanogenesis: From pigment cells to human health and technological applications. *Pig. Cell Melanoma Res.* 28, 520–544. doi: 10.1111/pcmr.12393

d'Ischia, M., Wakamatsu, K., Napolitano, A., Briganti, S., Garcia-Borron, J. C., Kovacs, D., et al. (2013). Melanins and melanogenesis: methods, standards, protocols. *Pig. Cell Melanoma Res.* 26, 616–633. doi: 10.1111/pcmr.12121

Gargiulo, V., Alfè, M., Capua, R. D., Togna, A. R., Cammisotto, V., Fiorito, S., et al. (2015). Supplementing π-systems: eumelanin and graphene-like integration towards highly conductive materials for the mammalian cell culture bio-interface. *J. Mater. Chem. B* 3, 5070–5079. doi: 10.1039/c5tb00343a

Hyogo, R., Nakamura, A., Okuda, H., Wakamatsu, K., Ito, S., and Sota, T. (2011). Mid-infrared vibrational spectroscopic characterization of 5,6-dihydroxyindole and eumelanin derived from it. *Chem. Phys. Lett.* 517, 211–216. doi: 10.1016/j.cplett.2011.10.043

Ito, S., Wakamatsu, K., d'ischia, M., and Napolitano, A., Pezzella, A. (2011). "Structure of melanins," in *Melanins and Melanosomes: Biosynthesis, Biogenesis, Physiological, and Pathological Functions*, eds J. Borovanský and P. A. Riley (Weinheim: Wiley-VCH Verlag GmbH & Co. KGaA), 67–185. doi: 10.1002/9783527636150

Jan, C. J., Walton, M. D., McConnell, E. P., Jang, W. S., Kim, Y. S., and Grunlan, J. C. (2006). Carbon black thin films with tunable resistance and optical transparency. *Carbon.* 44, 1974–1981. doi: 10.1016/j.carbon.2006.01.021

Jastrzebska, M., Kocot, A., Vij, J. K., Zalewska-Rejdak, J., and Witecki, T. (2002). Dielectric studies on charge hopping in melanin polymer. *J. Mol. Struct.* 606, 205–210. doi: 10.1016/s0022-2860(01)00873-0

Jastrzebska, M. M., Isotalo, H., Paloheimo, J., and Stubb, H. (1995). Electrical conductivity of synthetic dopa-melanin polymer for different hydration states and temperatures. *J. Biomater. Sci.* 7, 577–586.

Jin, B., Gao, F., Zhu, Y. F., Lang, X. Y., Han, G. F., Gao, W., et al. (2016). Facile synthesis of non-graphitizable polypyrrole-derived carbon/carbon nanotubes for lithium-ion batteries. *Sci. Rep.* 6:19317. doi: 10.1038/srep19317

Koller, G., Berkebile, S., Oehzelt, M., Puschnig, P., Ambrosch-Draxl, C., Netzer, F. P., et al. (2007). Intra- and intermodular band dispersion in an organic crystal. *Science.* 317, 351–355. doi: 10.1126/science.1143239

Kong, J., Yee, W. A., Yang, L., Wei, Y., Phua, S. L., Ong, H. G., et al. (2012). Highly electrically conductive layered carbon derived from polydopamine and its functions in sno2-based lithium ion battery anodes. *Chem. Commun.* 48, 10316–10318. doi: 10.1039/c2cc35284b

Le, T. H., Kim, Y., and Yoon, H. (2017). Electrical and electrochemical properties of conducting polymers. *Polymers-Basel.* 9:150. doi: 10.3390/Polym9040150

Li, R. J., Parvez, K., Hinkel, F., Feng, X. L., and Mullen, K. (2013). Va bioinspired wafer-scale production of highly stretchable carbon films for transparent conductive electrodes. *Angew Chem Int Edit.* 52, 5535–5538. doi: 10.1002/anie.201300312

Liu, C., Huang, K., Park, W.-T., Li, M., Yang, T., Liu, X., et al. (2017). A unified understanding of charge transport in organic semiconductors: the importance of attenuated delocalization for the carriers. *Mater. Horiz.* 4, 608–618. doi: 10.1039/c7mh00091j

Liu, C., Wang, K., Gong, X., and Heeger, A. J. (2016). Low bandgap semiconducting polymers for polymeric photovoltaics. *Chem. Soc. Rev.* 45, 4825–4846. doi: 10.1039/c5cs00650c

Liu, C. L., Dong, W. S., Song, J. R., and Liu, L. (2007). Evolution of microstructure and properties of phenolic fibers during carbonization. *Mat. Sci. Eng. a-Struct* 459, 347–354. doi: 10.1016/j.msea.2007.02.067

McGinness, J., Corry, P., and Proctor, P. (1974). Amorphous semiconductor switching in melanins. *Science* 183, 853–855.

Meredith, P., and Sarna, T. (2006). The physical and chemical properties of eumelanin. *Pig. Cell Res.* 19, 572–594. doi: 10.1111/j.1600-0749.2006.00345.x

Migliaccio, L., Aprano, S., Iannuzzi, L., Maglione, M. G., Tassini, P., Minarini, C., et al. (2017). Eumelanin-pedot:Pss complementing en route to mammalian-pigment-based electrodes: design and fabrication of an ito-free organic light-emitting device. *Adv. Electr. Mater.* 3, 1600342. doi: 10.1002/aelm.201600342

Mihai, I., Addiégo, F., Del Frari, D., Bour, J., and Ball, V. (2013). Associating oriented polyaniline and eumelanin in a reactive layer-by-layer manner: Composites with high electrical conductivity. *Colloids Surf. Physicochem. Eng. Aspects.* 434, 118–125. doi: 10.1016/j.colsurfa.2013.05.028

Mostert, A. B., Powell, B. J., Pratt, F. L., Hanson, G. R., Sarna, T., Gentle, I. R., et al. (2012). Role of semiconductivity and ion transport in the electrical conduction of melanin. *Proc. Natl. Acad. Sci. U.S.A.* 109, 8943–8947. doi: 10.1073/pnas.1119948109

Muskovich, M., and Bettinger, C. J. (2012). Biomaterials-based electronics: Polymers and interfaces for biology and medicine. *Adv. Healthc. Mater.* 1, 248–266. doi: 10.1002/adhm.201200071

Namgung, S. D., Lee, J., Choe, I. R., Sung, T., Kim, Y. O., Lee, Y. S., et al. (2017). Increased electrical conductivity of peptides through annealing process. *Apl Mater.* 5:086109. doi: 10.1063/1.4997562

Noriega, R., Rivnay, J., Vandewal, K., Koch, F. P., Stingelin, N., Smith, P., et al. (2013). A general relationship between disorder, aggregation and charge transport in conjugated polymers. *Nat. Mater.* 12, 1038–1044. doi: 10.1038/nmat3722

Osak, W., Tkacz, K., Czternastek, H., and SłAwinski, J. (1989). I – v characteristics and electrical conductivity of synthetic melanin. *Biopolymers.* 28, 1885–1890. doi: 10.1002/bip.360281105

Pezzella, A., Barra, M., Musto, A., Navarra, A., Alfè, M., Manini, P., et al. (2015). Stem cell-compatible eumelanin biointerface fabricated by chemically controlled solid state polymerization. *Mater. Horizons.* 2, 212–220. doi: 10.1039/c4mh00097h

Pezzella, A., Iadonisi, A., Valerio, S., Panzella, L., Napolitano, A., Adinolfi, M., et al. (2009). Disentangling eumelanin "black chromophore": Visible absorption changes as signatures of oxidation state- and aggregation-dependent dynamic interactions in a model water-soluble 5,6-dihydroxyindole polymer. *J. Am. Chem. Soc.* 131, 15270–15275. doi: 10.1021/ja905162s

Pullman, A., and Pullman, B. (1961). The band structure of melanins. *Biochim. Biophys. Acta.* 54, 384–385. doi: 10.1016/0006-3002(61)90389-4

Roncali, J. (1997). Synthetic principles for bandgap control in linear π-conjugated systems. *Chem. Rev.* 97, 173–205.

Roncali, J., and Thobie-Gautier, C. (1994). An efficient strategy towards small bandgap polymers: the rigidification of the π-conjugated system. *Adv. Mater.* 6, 846–848. doi: 10.1002/adma.19940061108

Schroder, D. K. (1986). Electrical characterization of semiconductor-materials and devices. *Acs. Sym. Ser*. 295, 18–33.

Sheliakina, M., Mostert, A. B., and Meredith, P. (2018). Decoupling ionic and electronic currents in melanin. *Adv. Funct. Mater.* 28:1805514. doi: 10.1002/adfm.201805514

Swan, G. A., and Waggott, A. (1970). Studies related to the chemistry of melanins. Part x. Quantitative assessment of different types of units present in dopa-melanin. *J. Chem. Soc.* 1409–1418. doi: 10.1039/j39700001409

Wünsche, J., Deng, Y., Kumar, P., Di Mauro, E., Josberger, E., Sayago, J., et al. (2015). Protonic and electronic transport in hydrated thin films of the pigment eumelanin. *Chem. Mater.* 27, 436–442. doi: 10.1021/cm502939r

Yu, X., Fan, H., Liu, Y., Shi, Z., and Jin, Z. (2014). Characterization of carbonized polydopamine nanoparticles suggests ordered supramolecular structure of polydopamine. *Langmuir.* 30, 5497–5505. doi: 10.1021/la500225v

Zajac, G. W., Gallas, J. M., Cheng, J., Eisner, M., Moss, S. C., and Alvarado-Swaisgood, A. E. (1994). The fundamental unit of synthetic melanin: a verification by tunneling microscopy of x-ray scattering results. *BBA*. 1199, 271–278. doi: 10.1016/0304-4165(94)90006-x

Conflict of Interest Statement: The authors declare that the research was conducted in the absence of any commercial or financial relationships that could be construed as a potential conflict of interest.

frontiers
in Chemistry

ORIGINAL RESEARCH
published: 29 March 2019
doi: 10.3389/fchem.2019.00178

Facile Synthesis of a 3,4-Ethylene-Dioxythiophene (EDOT) Derivative for Ease of Bio-Functionalization of the Conducting Polymer PEDOT

Bingchen Wu[1,2]†, Bin Cao[1]†, Ian Mitch Taylor[1], Kevin Woeppel[1,2] and Xinyan Tracy Cui[1,2,3]*

[1] Department of Bioengineering, University of Pittsburgh, Pittsburgh, PA, United States, [2] Center for the Neural Basis of Cognition, University of Pittsburgh, Pittsburgh, PA, United States, [3] McGowan Institute for Regenerative Medicine, University of Pittsburgh, Pittsburgh, PA, United States

In the pursuit of conducting polymer based bio-functional devices, a cost-effective and high yield synthesis method for a versatile monomer is desired. We report here a new synthesis strategy for a versatile monomer 2-methylene-2,3-dihydrothieno (3,4-b) (1,4) dioxine, or 3,4-ethylenedioxythiophene with a exomethylene side group (EDOT-EM). Compared to the previously reported synthesis route, the new strategy uses less steps, with faster reaction rate, and higher yield. The presence of EM group opens up endless possibility for derivatization via either hydro-alkoxy addition or thiol-ene click chemistry. EDOT-EM could be polymerized into stable and low impedance PEDOT-EM polymer using electro-polymerization method on different conducting substrates at both macro and micro scales. Facile post-functionalization of PEDOT-EM with molecules of varying size and functionality (from small molecules to DNAs and proteins) was achieved. The new synthetic route of EDOT-EM and the ease of post-functionalization of PEDOT-EM will greatly accelerate the use of conducting polymer in a broad range of organic electronics and bioelectronics applications.

Keywords: thiol-ene, EDOT derivative, conducting polymer, bio-functionalization, organic electronics

OPEN ACCESS

Edited by:
Jae Young Lee,
Gwangju Institute of Science and Technology, South Korea

Reviewed by:
Won-Gun Koh,
Yonsei University, South Korea
John Forsythe,
Monash University, Australia

***Correspondence:**
Xinyan Tracy Cui
xic11@pitt.edu

†These authors have contributed equally to this work

Specialty section:
This article was submitted to Organic Chemistry, a section of the journal Frontiers in Chemistry

***Received:** 09 January 2019*
***Accepted:** 07 March 2019*
***Published:** 29 March 2019*

Citation:
Wu B, Cao B, Taylor IM, Woeppel K and Cui XT (2019) Facile Synthesis of a 3,4-Ethylene-Dioxythiophene (EDOT) Derivative for Ease of Bio-Functionalization of the Conducting Polymer PEDOT. Front. Chem. 7:178. doi: 10.3389/fchem.2019.00178

INTRODUCTION

Poly 3,4-ethylene dioxythiophene (PEDOT) is a widely used conductive polymer noted for its broad applicability, ranging from organic field-effect transistors, (Sirringhaus et al., 2000) solar cells, (Kim et al., 2011) and light emitting diodes (de Jong et al., 2000) to nanomedicine, (Karagkiozaki et al., 2013) biosensors and bioelectronics. (Cui and Martin, 2003; Martin, 2015) PEDOT have excellent conductivity, transparency, and processability, making it great candidates for fabrication of electrodes such as transparent organic solar cells or light emitting diodes (de Jong et al., 2000; Zhang et al., 2002; Sun et al., 2015). In particular, PEDOT has been widely utilized in the biomedical research front and is utilized for electrically controlled drug delivery, (Abidian et al., 2006; Luo and Cui, 2009; Chikar et al., 2012) conductive scaffolds for stimulation and tissue regeneration, (Bolin et al., 2009; Yazdimamaghani et al., 2015) and biosensors for chemical species such as dopamine, hydrogen peroxide, and acetylcholine (Istamboulie et al., 2010; Lin et al., 2010; Taylor et al., 2017b). Coating electrode with PEDOT is a commonly adopted strategy to enhance electrode performance due to high charge storage capacity, reversable redox activity, and extremely the high surface area of PEDOT films, which are highly desired properties for the applications of biosensing, recording, and stimulating devices (Luo et al., 2011; Lu et al., 2012; Taylor et al., 2017b). Within the contest of neural interfacing technology, PEDOT has been shown to be an excellent coating for neural electrodes due to its excellent biocompatibility and stability, and low impedance (Cui and Martin, 2003; Luo et al., 2008; Zhu et al., 2014; Kolarcik et al., 2015). Previous reports have demonstrated PEDOT based polymer coating can effectively improve sensitivity, stimulation and recording stability, and longevity of neural electrode *in vivo* (Schwartz et al., 2006; Luo et al., 2011; Du et al., 2015; Kolarcik et al., 2015; Vara and Collazos-Castro, 2015; Kozai et al., 2016; Taylor et al., 2017b).

In the pursuit of high efficiency and functional PEDOT based biomaterials and biomedical devices, it is highly desirable to incorporate readily available reactive groups in conducting polymers for surface modification and bioconjugation. Also, because of the requirement of tunability and processability in developing conducting polymers, electro-polymerization method has become a widely utilized convenient technique to precisely control polymerization process on conductive substrates. During the electro-polymerization, biomolecules may be incorporated in the polymer film as dopants, which is a convenient method for bio-functionalization (Stauffer and Cui, 2006; Boehler et al., 2017). The dopants are only physical entrapped in polymer film and can be released passively or actively, which is desirable in applications such as control drug delivery. However, there remains the need for a reliable and stable covalent functionalization method. Additionally, entrapped biomolecules have limited surface exposure, and if the bioactive sites of the molecule are blocked, the intended biological function will not be achieved. On the other hand, covalent attachment of biomolecules on the polymer surface can effectively overcome these limitations. Unfortunately, PEDOT lacks the necessary reactive sites for direct functionalization. This motivates the development of EDOT derivatives.

EDOT-OH is an EDOT derivative developed with the capability to undergo direct post-coating functionalization through reaction with a free hydroxymethyl group. EDOT-OH was first synthesized through the cyclization of diethyl 3,4-dihydroxythiophene-2,5-dicarboxylate through either a Williamson ether synthesis or Mitsunobu reaction pathway, followed by decarboxylation. This synthetic strategy was successful but resulted in poor overall yield. As a result, an alternative method was then developed to synthesize EDOT-OH from 3,4-dimethoxythiophene as the starting material, through an acid catalyzed transesterification pathway (Luo et al., 2008; Sekine et al., 2011). Electro-polymerization of PEDOT-OH and its application on neural electrode and biosensing were also demonstrated in literature (Xiao et al., 2006; Lu et al., 2012). However, the synthetic route of EDOT-OH involves complex synthesis and functionalization steps that are costly and with low yield. EDOT-acid is another EDOT derivative developed with the capability to covalently bind peptides on polymer surface. A number of researches have also showed successful functionalization of PEDOT-acid with biomolecules through EDC/NHS chemistry (Sirringhaus et al., 2000; Povlich et al., 2013). However, with the acid group, only a limited pool of molecules can be used for post-functionalization (Povlich et al., 2013). Another EDOT derivative EDOT-NH_2 been used to enhance adhesion of polymer to substrate, but no bioconjugation via the amine group has been demonstrated (Ouyang et al., 2017). Recently, functionalization through thiol-ene click chemistry has become increasingly popular due to its versatility, fast reaction rate and high yield (Hoyle et al., 2004; Kade et al., 2010). Using this chemistry for immobilization of biomolecules such as amino acids, peptides, and proteins are especially attractive due to the mild reaction condition and prevalence of thiol group in biological molecules (Jones et al., 2009; Zhang et al., 2016). Thiol-ene chemistry has also been used to functionalize conducting polymer poly (3,4-propylenedioxythiophene) (ProDOT) with hydrophobic and hydrophilic functional groups via single- or double-ene side groups, demonstrating the versatile and facile tuning options, although no direct bioconjugations have been reported so far (Hoyle et al., 2004; Kade et al., 2010; Feldman and Martin, 2012; Wei et al., 2015). EDOT with a single ene, i.e., exomethylene side group, referred to as EDOT-EM, has been reported by Beverina and co-workers (Sassi et al., 2013) in 2013. The synthesis route reported was complicated with only an overall yield around 50%, preventing the wide spread use of EDOT-EM. Beverina et al. further showed that various EDOT derivatives could be produced from EDOT-EM through thiol-ene chemistry demonstrating the versatility of this monomer. However, in their work, electro-polymerization of EDOT-EM was not successful.

In present work, we developed a novel synthesis route for EDOT-EM with one step, high conversion rate, and quantitative yield. We also optimized electro-polymerization method and produced stable and conductive PEDOT-EM film on macro and micro conductive surfaces. Furthermore, we demonstrated successful post-functionalization on PEDOT-EM polymer coatings with various molecules (**Scheme 1**).

MATERIALS AND METHODS

All reagents and solvents were used without further purification. 3,4-dimethoxythiophene was purchased from Matrix scientific. 3,4-Ethylenedioxythiophene (EDOT), 3-chloro-1,2-propanediol, p-toluene sulfonic acid monohydrate, toluene, tetrahydrofuran (THF), hexane, 3-mercaptopropionic acid (MPA), 2,2-Dimethoxy-2-phenylacetophenone (DMPA), Sodium Hydroxide (NaOH), Potassium hydroxide (KOH), Tris(2-carboxyethyl) phosphine hydrochloride (TCEP), Methanol (MeOH) and dichloromethane were purchased from Sigma. Potassium tert-butoxide (tBuOK) was purchased from ACROS. Ethanol (EtOH) was purchased through Fisher. Aptamer 5′-HS-(CH2)6-AGACAAGGAAAATCCTTCAATGAAGTGGGTCG-(CH2)7-MB-3′ with a 5′ thiol group as covalent linkage site and 3′ methylene blue (MB) as electrochemical reporter was purchased through Biosearch Technologies, Inc., Platinum/Iridium wires were purchased from A-M systems.

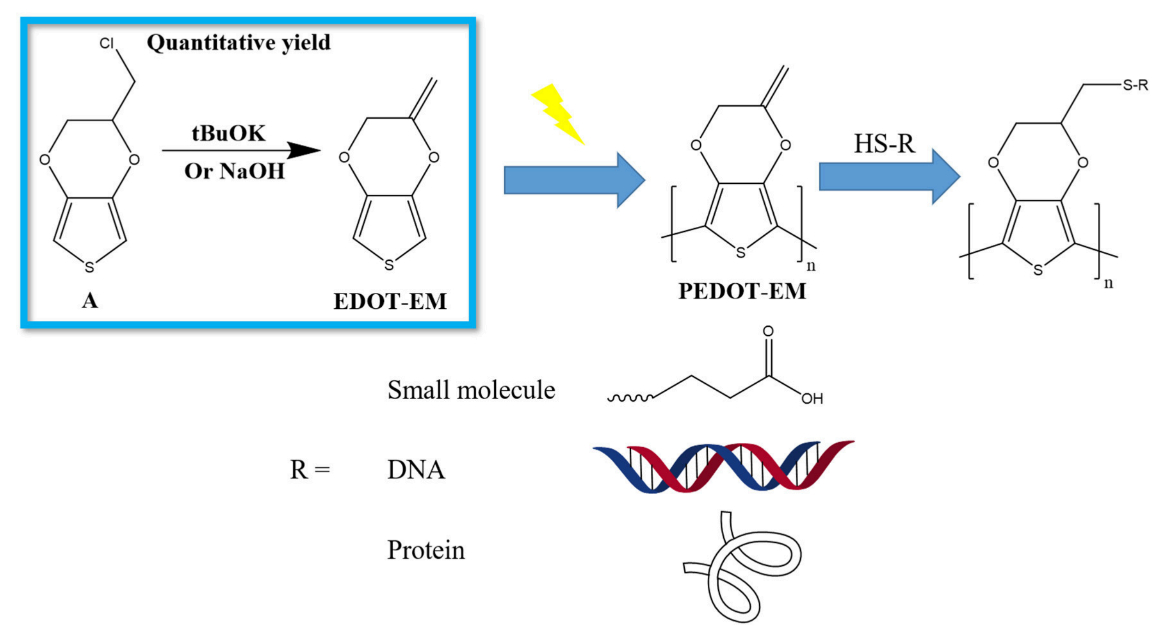

SCHEME 1 | Schematic demonstration of the work flow to produce functionalized PEDOT-EM devices. **(A)** EDOT-MeCl.

Synthesis of Monomers

2-Chloromethyl-2,3-dihydrothieno [3,4-b] [1,4] dioxine EDOT-MeCl

The monomer 2-Chloromethyl-2,3-dihydrothieno[3,4-b] [1,4] dioxine (EDOT-MeCl) was synthesized using a method similar to a published procedure (Segura et al., 2006). In brief, to a two-necked round bottom flask under nitrogen purge, 60 ml of dry toluene, 5 ml (39.5 mmol) of 3,4-dimethoxythiophene, 10 ml (120 mmol) of 3-chloro-1,2-propanediol, and 0.57 g (3 mmol) of *p*-toluene sulfonic acid monohydrate were added. Solution was heated at 90°C for 16 h with a reflux apparatus assembled on top. After this time, another 10 ml (120 mmol) of 3-chloro-1,2-propanediol was added, and the solution was heated at solvent, crude product was purified through gel. Chromatography (hexane/dichloromethane 4/1 v/v). The final product is a white solid.

2-Methylene-2,3-Dihydrothieno [3,4-b] [1,4] Dioxine EDOT-EM

tBuOK condition

To a single-necked round bottom flask, 0.7 g (3.67 mmol) of EDOT-MeCl dissolved in 5 ml of THF and 0.824 g (7.34 mmol) of tBuOK dissolved in 5 ml of THF were added. Flask was sealed with rubber plug and solution was kept at room temperature for 30 min with stirring. After removing solvent, the crude product was purified through silica gel chromatography (hexane/dichloromethane 9/1 v/v). After evaporating the solvent with a rotovap, final product was obtained as colorless liquid. H^1, NMR ($CDCl_3$, 400 MHz): δ [ppm]: 6.43 (d, $J = 3.6$ Hz, 1 H), 6.39 (d, $J = 3.6$ Hz, 1 H), 4.76 (d, $J = 2$ Hz, 1 H), 4.49 (d, $J = 0.4$ Hz, 2 H), 4.42 (d, $J = 2$ Hz, 1 H). C^{13}, NMR: $\delta = 149.57$, 141.09, 140.63, 100.5, 99.92, 92.64, 77.39, 77.07, 76.75, 65.29 ppm.

Diisopropylamine condition

To a single-necked round bottom flask, 0.7 g (3.67 mmol) of EDOT-MeCl dissolved in 5 ml of MeOH and 1.03 ml (7.34 mmol) of diisopropylamine were added. Flask was sealed with rubber plug and solution was heated to 90°C and left overnight with stirring. After removing solvent, crude product was purified through silica gel chromatography (hexane/dichloromethane = 9/1). After evaporating the solvent with a rotovap, no viable amount product was collected.

NaOH/KOH condition

To a single-necked round bottom flask, 0.22 g (1.16 mmol) of EDOT-MeCl dissolved in 2 ml of MeOH and 100 mg (1.81 mmol) of KOH or 80 mg (2 mmol) of NaOH dissolved in 2 ml of MeOH were added. Flask was sealed with rubber plug and solution was heated to 90°C and left overnight with stirring. After removing solvent, crude product was purified through silica gel chromatography (hexane/dichloromethane = 9/1). After evaporating the solvent with a rotovap, the final product was obtained as colorless liquid (yield 92%).

Characterization

NMR spectrum were measured on a Bruker ultra-shield 400 plus. ATR FT-IR spectra were measured using a Bruker Vertex-70LS spectrometer. SEM images were taken on a JSM 6335F SEM.

Electrochemistry

Instrument and Setup

All electrochemical experiments were performed using an Autolab potentiostat (Metrohm) in a three-electrode cell (1 ml) consisting of a working electrode (Au sputtered plastic/Au coated Si wafer/Pt-Ir wire), a platinum counter electrode, and an Ag/AgCl reference electrode.

Electro-Polymerization for PEDOT-EM

A solution of water/acetonitrile 1:1 (volume ratio) with 100 mM of monomer and 100 mM of $LiClO_4$ electrolyte was used as working solution. For galvanostatic (GS) method, a constant current ranging from 20 uA to 200 μA was applied and tested. The 200 μA conditions was determined as optimal current and utilized to coat Au sputter coated plastic with a surface area of 0.38 cm^2 for 45, 90, 180, and 360 s and Au coated Si wafer with a surface area of 0.385 cm^2 for 360 s. For potentiostatic (PS) method, a constant voltage of 1.1 V was applied with a charge cutoff at 0.009, 0.018, 0.036, and 0.072 C for Au-Si wafers with the same dimension, matching the amount of charge that was injected under optimal GS method. For coating Pt-Ir wires with a surface area of 0.00385 cm^2, a 2 μA current was applied for 120 s.

Aptamer Functionalization Detection

Square wave voltammetry was applied with a scan rate of 25 Hz from −0.1 to −0.6 V, with an amplitude of −0.025V and step size of −0.005V.

Post-functionalization of PEDOT-EM

MPA Functionalization

All PEDOT-EM and PEDOT coated Au-Si wafers were rinsed with EtOH three times before reaction. 64 mg (0.25 mmol) of DMPA, and 437 μl (5 mmol) of MPA were added into 5 ml EtOH solution in a Petri dish. PEDOT-EM and PEDOT coated Au plastic substrates were then immersed into solution and the petri dish was covered with a quartz glass lid and placed under UV lamp (100 w, Series 1000 Omni Cure^{TM}) for 1 h. All Samples were rinsed with EtOH three times after reaction to remove MPA residues.

Aptamer Functionalization

10 μL of 50 mM TCEP were first added into 5 μL of 100 μM aptamer solution, and solution was kept at room temperature for 30 min in order to reduce the disulfide bond. Then aptamer solution was diluted to 10 μM with PBS. 25 μL of diluted aptamer solution were dropped on PEDOT-EM and PEDOT coated Au plastic substrates, covered with aluminum foil, and left at room temperature overnight. PEDOT-EM coated wires were immersed into the solution left at room temperature overnight. All samples were rinsed with PBS 3 times and stored in PBS before characterization.

Protein Functionalization

100 μl of 0.04 g/ml laminin solution was dropped on PEDOT-EM and PEDOT films on Au-Si wafer and allow protein to bind for 2 h at ambient temperature. Sample were then washed with PBS and incubated for 30 min at 37°C. After incubation, half of the samples were washed by 1% tween 20 (1 to 100 in PBS) to remove physically adsorbed laminin protein and rinsed with PBS extensively (15 times per sample). All other samples were submerged in PBS during the washing procedure. PBS was drained before plating the cells.

Cell Culture and Immunostaining

Elution Test in Fibroblast Culture

3T3 fibroblast cells were plated in a 96-well plate at a density of 10^4 cells/well in 100 μL of culture medium—DMEM/F-12, HEPES medium (Gibco) supplemented with 10% Fetal Bovine Serum (FBS) (Gibco) and 1% PenStrep (Life Technologies)—for 24 hr before use. Polymer films were immersed in 2 ml serum free and phenol red free culture medium incubated at 37°C for 72 h, after which 10% FBS was added back to medium before extraction. Elution solutions were made by mixing extractions with phenol red free medium at volume/volume ratio of 25, 50, 75, and 100%. Plating medium was then replaced with elution solutions and cells were then incubated at 37°C for 24 h after which a standard XTT assay was performed to text cytotoxicity of the elution.

Primary Neuron Cell Assay

All procedures followed NIH and federal guidelines and were approved by the University of Pittsburgh, the Institutional Animal Care & Use Committee. Primary neurons were isolated from E18 rat fetus (Taconic). In brief, E18 pregnant rats were euthanized by CO_2 and the rat pups extracted. Pup brains were removed, and cortices were dissociated by Trypsin/EDTA solution (0.05%) followed by mechanical trituration with a fire-polished Pasteur pipette. Dissociated cells were collected by centrifuge (200 g, 5 min) and resuspended in NeuroBasal media (Gibco) supplemented with 2% B27 (Gibco) 1% GlutiMax (Gibco) and 1% PenStrep (Life Technologies). Cells were counted by taking a small aliquot of cell suspension and mixing 1:1 in Trypan blue solution (0.4%, BioWhittaker), following which cells were plated at a density of 2.5×10^5 cells/cm^2.

Immunostaining Procedure

Cells were cultured for 48 h and fixed with 4% para-formaldehyde for 30 min. Membranes were permeabilized with 0.2% Triton-X in PBS/Goat Serum (5%, Gibco). Mouse beta-3-tubulin primary antibody (Invitrogen) was introduced at 1:1,000 in PBS/Goat Serum and incubated for 2 h. Following washing with PBS, AlexaFluor-488 Rat-Anti-Mouse secondary antibody was introduced at 1:1,000 in PBS/Goat Serum incubated at 37°C for 45 min. Samples were washed again with PBS, and nuclei were labeled by Hoechst stain (Invitrogen), mixed at 1:1,000 in PBS and incubated for 10 min at 37°C. After staining, cells were washed twice with PBS and imaged by a fluorescence microscope (Leica DMI4000b).

RESULTS AND DISCUSSION

One Step Synthesis of Edot-Em With Quantitative Yield

Previously EDOT-EM was synthesized using a 2 steps process by starting from EDOT-OH (**Scheme 2**) (Sassi et al., 2013). The first tosylation step of EDOT-OH has a 65% yield, which then followed by elimination of tosylate group with 80% yield. EDOT-EM was obtained with an overall yield around 52 % (**Scheme 2**). We made a discovery in the

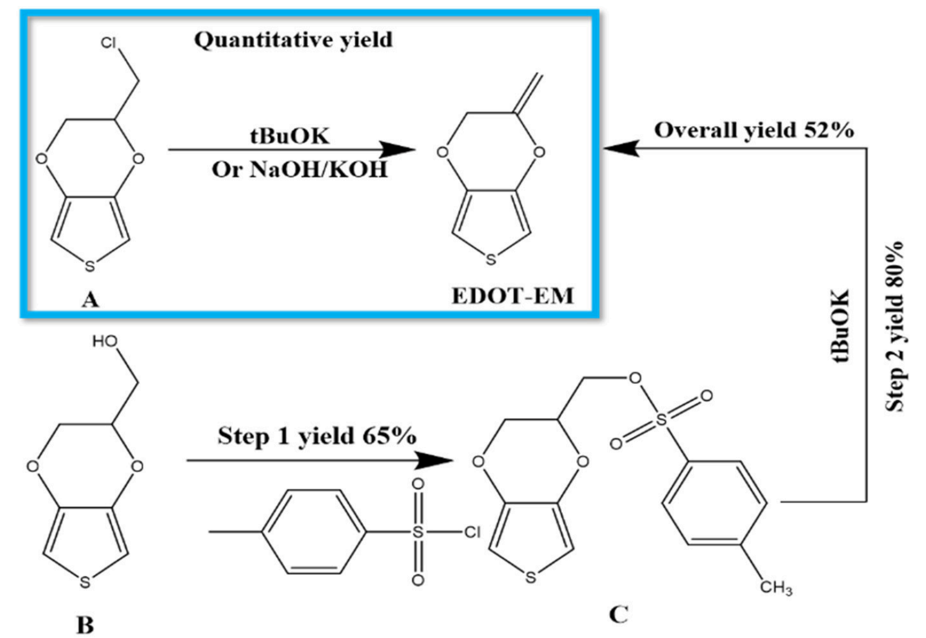

SCHEME 2 | Synthesis of EDOT-EM. Our novel approach is highlighted in the blue box, which requires only 1 step with fast reaction rate, quantitative conversion, and extremely high yield, while the previously published route (outside of the box) showed more steps and lower yield (Sassi et al., 2013). **(A)** EDOT-MeCl, **(B)** EDOT-OH, **(C)** EDOT-Acid.

TABLE 1 | Reaction conditions tested to synthesize EDOT-EM.

Reagent	Reaction Time	Solvent	Temperature	Yield
tBuOK	30 min	Dry THF	RT	>95%
NaOH/KOH	Overnight	Methanol	90°C (sealed)	92%
Diisopropylamine	Overnight	Methanol	90°C (sealed)	–

process of synthesizing EDOT-OH (compound **B**). During the reaction of EDOT-MeCl (compound **A**) with sodium acetate to make (2,3-Dihydrothieno[3,4-b] [1,4] dioxin-2-yl) methyl acetate (EDOT-Acid) at 120°C in DMSO, although the reactant was completely consumed, the conversion rate to targeting compound was found to be lower than expected. However, a side product was discovered with even lower polarity than the EDOT-MeCl. After isolation and purification, the obtained side product was examined by NMR spectrum and based on ^{1}H, ^{13}C spectra, and DEPT135 NMR spectrum (**Figures S1**, **S2**). We determined that the compound is a product from dehalogenation reaction upon heating at high temperature. Detailed atomic connectivity from two-dimensional NMR HSQC (**Figure S3**) and HMBC (**Figure S4**) confirmed the EDOT-EM structure. We propose that after elimination of HCl, the product converted into an EDOT-EM, and the newly-formed double bond could extend the conjugation thus stabilize the overall molecular structure.

Different reaction conditions were tested as shown in **Table 1**, three different types of reagents were tested to optimize the dehalogenation reaction conditions to produce EDOT-EM. Firstly, a non-nucleophilic strong base potassium tert-butoxide (tBuOK) was applied. Dehydrohalogenation was completed within 30 min with above 95 % isolation yield after washing and purification with silica gel chromatography. Secondly, reactions were attempted with milder bases either sodium hydroxide or potassium hydroxide. Conversion rate was slow at room temperature but could be completed upon heating at 90°C in a sealed reaction vessel overnight with a yield of 92%. This slightly lower yield was probably due to small amount of oligomerization or polymerization of EDOT-EM during heating. Lastly, a weak non-nucleophilic base, diisopropylamine, was tested at both room temperature and heated condition. Reaction conversion was very low, and no product was isolated. In conclusion, using this dehalogenation route and strong bases, the synthesis of EDOT-EM can be completed in one single step from EDOT-MeCl. Compared with the previously reported route for EDOT-EM synthesis, our approach takes fewer steps, with faster reaction rate, quantitative conversion, and quantitative yield. The presence of EM group opens up endless possibility for derivatization by either hydro-alkoxy addition or thiol-ene click chemistry (Sassi et al., 2013). In the previous report, (Sassi et al., 2013) it was demonstrated that EDOT-EM monomer can be functionalized and produce variety of monomer derivatives. Some of these derivatives, however, may not be amenable for electro-polymerization. The alternative might be more attractive and practical, in which EDOT-EM can be polymerized first and then undergoes post-functionalization via the ene group. Theoretically any molecules in the "tool-box" equipped with free thiol (SH) units could be directly attached to the polymer PEDOT-EM through the click chemistry.

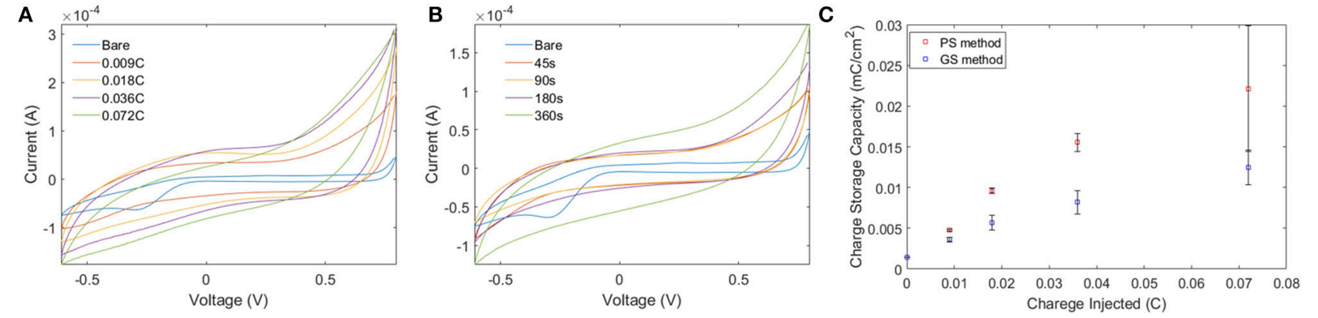

FIGURE 1 | (A,B) Comparison of CV of PEDOT-EM acquired by GS method **(A)** and PS method. **(C)** Quantification of CSC for PS and GS methods. Both methods showed increased charge storage capacity proportional to amount of charge injected, with PS producing higher CSC than GS.

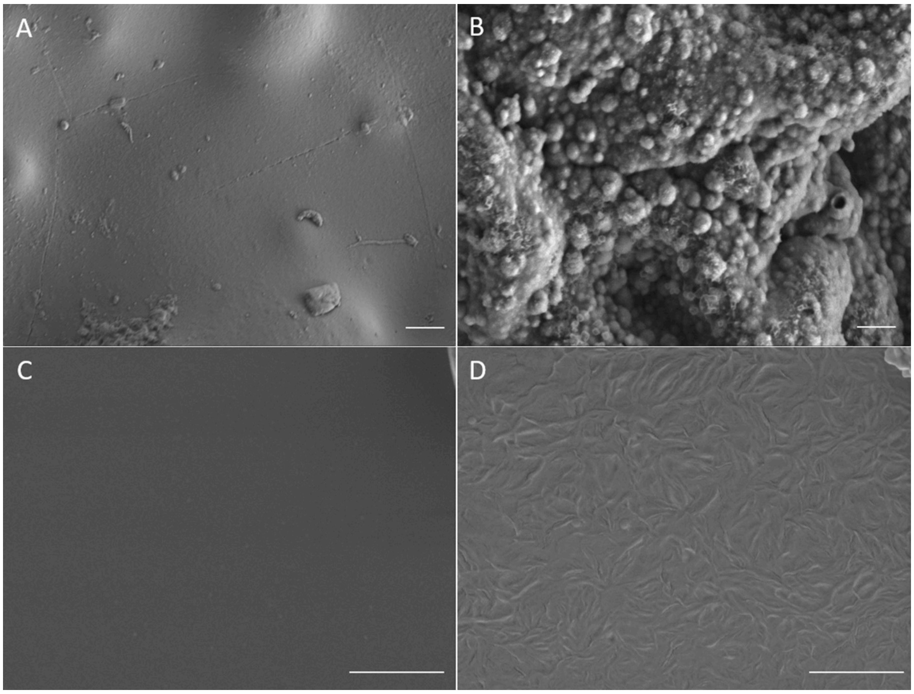

FIGURE 2 | SEM images of **(A)** Bare gold surface on gold plastic electrode, **(B)** PEDOT-EM film coated gold plastic electrode surface (deposition charge 249.4 mC/cm^2) **(C)**, Bare Pt/Ir wire and **(D)**, Pt/Ir wire coated with thin layer of PEDOT-EM (deposition charge 62.3 mC/cm^2). Scale bar: 1 µm.

Electro-Polymerization of PEDOT-EM

Electro-polymerization method was employed to deposit conjugated PEDOT-EM onto different surfaces, such as iridium-platinum microwire (Pt-Ir), gold coated silicon wafers (Au-Si), and gold coated plastic. The electro-polymerization process could be monitored and processed in a precisely controlled manner by simply adjusting the potential/current and polymerization time (Cui and Martin, 2003). Previous work by Sassi et. al. only tested cyclic voltammetry method, which didn't successfully produce the polymer PEDOT-EM (Sassi et al., 2013). With the large quantity and high purity of EDOT-EM easily yielded using our new synthesis route, we were able to extensively test and optimize the electro-polymerization protocol. As indicated by previous research that deposition method affects polymer film properties, two different electrochemical methods were tested including the GS method that supplies a constant current and PS method that supplies a constant voltage (Cui and Martin, 2003). The amount of charge injected in both electro-polymerization methods were controlled and matched. The cyclic voltammetry of PEDOT-EM made by both methods were compared and the charge storage capacity (CSC) was calculated for each condition (**Figure 1**). Under both methods, the acquired PEDOT-EM films showed increased CSC proportional to the amount the charge that was injected (**Figure 1C**). Interestingly, although the total amount of charge injected in GS and PS method was matched, the CSC of polymer films are different. At the deposition charges of 0.018, 0.036 and 0.072 C, the CSCs of PEDOT-EM produced via the PS method are 9.6 ± 0.32, 15.5 ± 1.1, and 22.2 ± 7.7 mC/cm^2, respectively, which are higher than the CSCs of

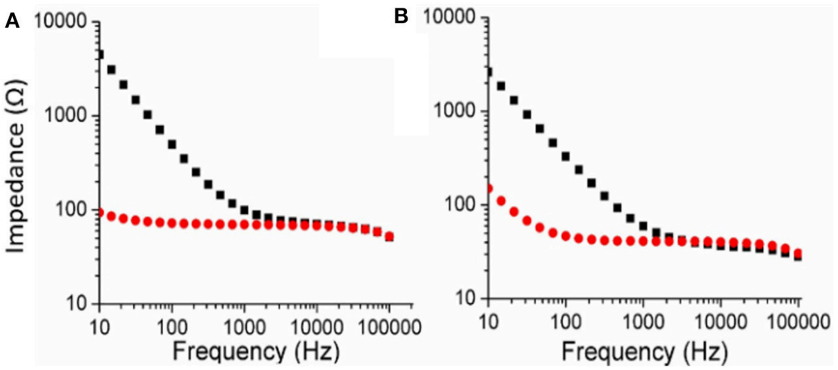

FIGURE 3 | Comparison of EIS (Bode plots) for PEDOT **(A)** and PEDOT-EM **(B)** samples. EIS of bare Au-Si substrate was shown in black squares and polymer coated Au-Si substrate was shown in red dots. Deposition charge for both coating was 249.4 mC/cm^2.

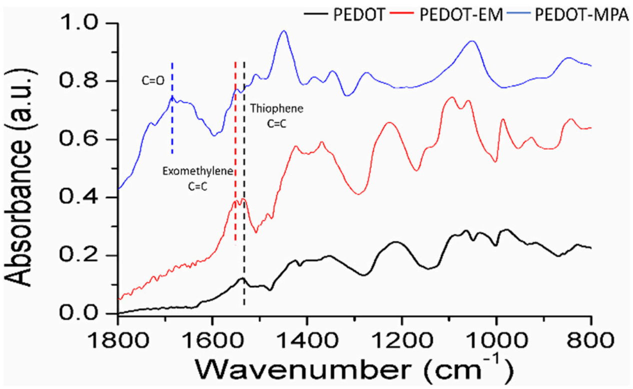

FIGURE 4 | FTIR spectra comparison of PEDOT film treated with MPA, PEDOT-EM film before, and after functionalized with MPA. All films were obtained from electrochemical polymerization on Au-Si. Deposition charge for both coating was 249.4 mC/cm^2.

polymer produced via GS method (5.7 ± 0.89, 8.2 ± 1.4, and 12.4 ± 2.1 mC/cm^2, respectively). Such difference might be a result of different electro-polymerization voltages between the two methods. Under the GS method the voltage initially increased to around 0.9 V then stabilized around 0.85 V (data not shown), which is lower than the constant 1.1 V voltage applied under PS method. For the remaining experiments EDOT-EM were polymerized using GS method since GS provided a more stable and reliable polymerization control and previous research also indicated GS method produced more homogenous polymer film (Cui and Martin, 2003). We then examined the surface morphology of the PEDOT-EM polymer film grown on different substrates at different deposition charges by SEM (**Figure 2**). A rougher PEDOT-EM film with a cauliflower morphology typical of electrodeposited conducting polymer (**Figure 2B**) was produced comparing to bare gold surface (**Figure 2A**). On the other hand, a smoother surface was observed on PEDOT-EM coated Pt/Ir wires, where a thin film of PEDOT-EM produced wavelike structure features (**Figure 2D**). Minimum surface morphology changes were observed comparing to bare Pt/Ir wires (**Figure 2C**).

The Electrochemical Impedance Spectroscopy (EIS) of both PEDOT-EM and PEDOT polymerized on Au-Si wafers were characterized and compared (**Figure 3**). The impedance of the PEDOT-EM coated substrate was about over one order of magnitude lower than that of the uncoated gold at a broad range of low frequencies (**Figure 3B**), which can be explained by the increased surface area (**Figure 2B**). The reduction of impedance is comparable to that of PEDOT films (**Figure 3A**). Low impedance of PEDOT film has been shown to significantly improve microelectrode performances by decreasing recording noise and increasing charge injection limit (Cui and Martin, 2003; Abidian and Martin, 2008; Abidian et al., 2010; Harris et al., 2013; Castagnola et al., 2015; Du et al., 2015; Kolarcik et al., 2015; Charkhkhar et al., 2016; Kozai et al., 2016). The EIS result indicates that the PEDOT-EM can exhibit similar impedance benefit as PEDOT, which is highly desired for applications such as neural electrode coatings.

PEDOT-EM Post-functionalization

To investigate whether the exomethylene group on PEDOT-EM was preserved after electro-polymerization process and can be further used for post-functionalization, we attempted to covalently attach molecules of different sizes to PEDOT-EM. We first post-functionalized the PEDOT-EM film with a small molecule, 3-mercaptopropionic acid (MPA) with the aid of a photo initiator (DMPA). Attenuated Total Reflectance-Fourier Transform Infrared (ATR FT-IR) spectroscopy was taken before and after functionalization of the PEDOT-EM films. For comparison, a PEDOT film was also treated with MPA and characterized with FTIR. The FTIR spectrum of the MPA treated PEDOT and PEDOT-EM slightly differs from each other. For PEDOT-EM, a peak at 1549 cm^{-1} can be attributed to the EM group, which was not seen in the spectrum of PEDOT. After thiol-ene functionalization of PEDOT-EM with MPA, appearance of the peaks of carbonyl C=O stretching, between 1600 and 1800 cm^{-1}, and decreased signal intensity of EM group at 1,549 cm^{-1} confirmed the successful post-functionalization (**Figure 4**).

For biosensors and bioelectrode applications, surface modifications with functional biological molecules that

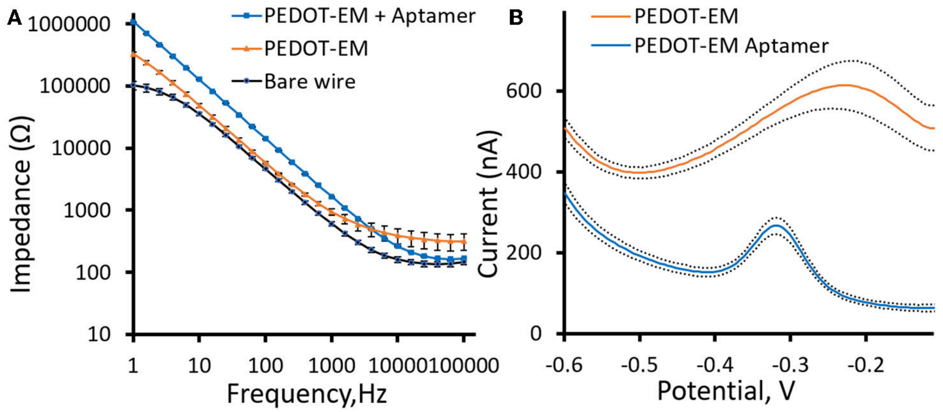

FIGURE 5 | Aptamer functionalization **(A)**, Comparison of electrochemical impedance spectra (Bode plots) for PEDOT-EM functionalized with aptamer, PEDOT-EM, and bare Pt-Ir wires. **(B)**, Comparison of Square wave voltammetry scan before and after post-functionalization of PEDOT-EM, $n = 5$, Mean ± standard error.

can recognize specific analytes are highly desirable. Pt-Ir microwires were coated with a thin layer of PEDOT-EM and post-functionalized with a DNA aptamer previously used for cocaine sensing (Baker et al., 2006; Taylor et al., 2017a). The aptamer contains a thiol group on 5′ that can be used as anchoring site and a methylene-blue group on 3′ that serves as electrochemical reporters. The impedance of Pt-Ir wires slightly increased with the deposition of a thin layer PEDOT-EM coating (**Figure 5A**). Here the polymerization condition was adjusted to obtain thin PEDOT-EM film with minimum surface area increase (**Figure 2D**) and impedance reduction, with the goal of minimizing background current in voltammetry sensing. Impedance further increased after aptamers were attached to PEDOT-EM polymer film, which is to be expected when nonconductive molecules are added to the electrode surface. Square wave voltammetry (SWV) was taken before and after post-functionalization of PEDOT-EM to detect successful immobilization of aptamer (**Figure 5B**). A methylene blue oxidation peak was clearly observed after PEDOT-EM was functionalized with aptamer, while no peaks were observed at the same voltage range for unfunctionalized PEDOT-EM film (**Figure 5B**). The observed peak position is consistent with previous literatures utilizing the same type of aptamers (Baker et al., 2006; Taylor et al., 2017a). Overall, PEDOT-EM functionalized with aptamer has a lower background current than PEDOT-EM alone. This observation is consistent with the EIS data, where PEDOT-EM has lower impedance than aptamer functionalized PEDOT-EM (**Figure 5A**). Additionally, FTIR spectroscopy verified the presence of aptamer on PEDOT-EM, while the PEDOT control showed minimum physical adsorption of aptamers (**Figure S5**). Together, the observed clearly resolved reduction peak at −0.3 V of methylene blue, the increased impedance after aptamer immobilization, and FTIR spectrum confirmed that the aptamer was successfully immobilized on the PEDOT-EM polymer surface. This opens the door for various aptamer based biosensing.

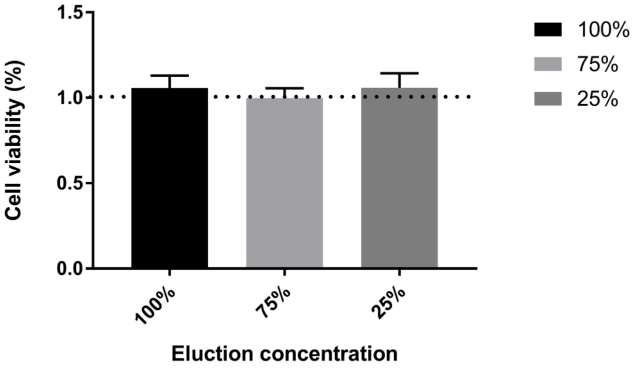

FIGURE 6 | Cell viability test through XTT assay for different elution concentration. $n = 12$, no significant difference was found between groups, One-wat ANOVA, $p = 0.7944$.

For PEDOT-EM to be utilized in biomedical devices, it is important to confirm that it is non-toxic to human body. Cytotoxicity of PEDOT-EM was tested by the elution test followed by a standard XTT assay that tests the viability of cells using 3T3 fibroblast cells (**Figure 6**). No loss in cell viability was observed for cells grown in different concentrations of eluted solutions up to 100%. All experimental groups resulted in a cell viability around 100%, confirming PEDOT-EM is non-cytotoxic and safe to be utilized in biological applications.

Often in biomedical applications, interactions between biological tissue and biomaterial surfaces need to be tailored based on the specific application. Peptides and proteins are commonly utilized biomolecules that serve as ligands and adhesion molecules to modulate device-tissue interactions. These biomolecules need to be attached to the biomaterial surface robustly to maintain device functionality and promote device integration within human body (Lauer et al., 2001; Luo and Shoichet, 2004; Azemi et al., 2008; Xu et al., 2009; Cheong et al., 2014; Hassarati et al., 2016). For this purpose, we further demonstrate the feasibility of post-functionalizing PEDOT-EM with larger biomolecule such as proteins. Laminin, an extracellular matrix protein known to promote neuron attachment and neurite outgrowth (Lander et al., 1985), were added to PEDOT and PEDOT-EM surfaces respectively and allowed to react with the surface for 2 h followed by PBS washes. Both surfaces were then treated with Tween 20 to

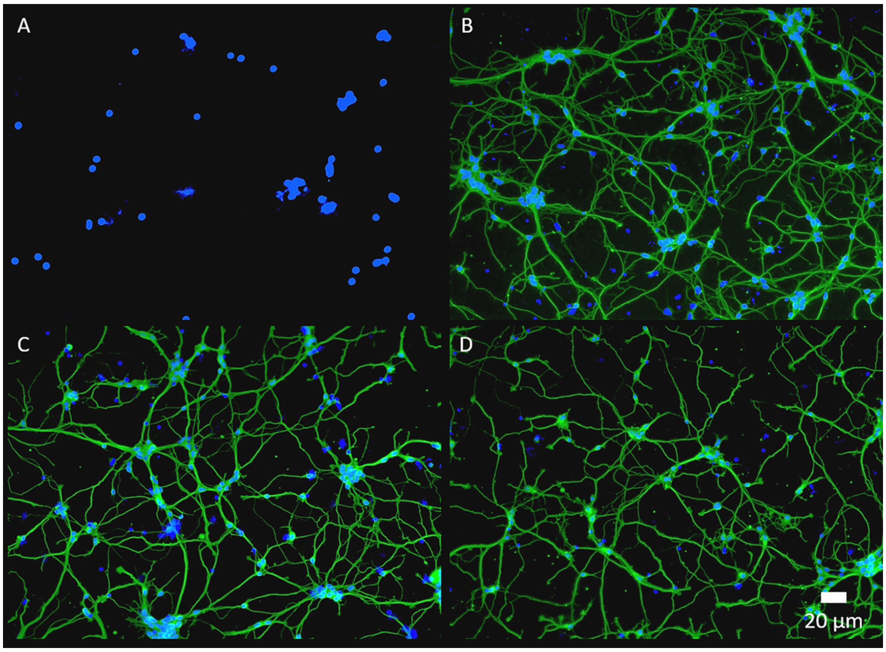

FIGURE 7 | Fluorescence images of primary neuron culture on different surfaces. **(A)**, PEDOT-EM. **(B)**, NC-Laminin. **(C)**, PEDOT-EM-Laminin without tween-20 wash. **(D)**, PEDOT-EM-Laminin after tween-20 wash. ß tubulin (green) and cell nuclei (blue).

remove the physically adsorbed laminin. FTIR spectroscopy showed that laminin on PEDOT was successfully removed by Tween 20 wash because the protein was physically adsorbed (**Figure S6A**) (Nosworthy et al., 2009). On the other hand, PEDOT-EM surface showed sustained and strong laminin signal after Tween 20 wash indicating a covalent binding (**Figure S6B**). Laminin functionalized PEDOT-EM (**Figure 7C**) shows neuron cell attachment and neurite outgrowth as good as the laminin coated nitrocellulose (a standard neural adhesive substrate for primary neuron culture) (**Figure 7B**), whereas PEDOT-EM alone does not support neuron attachment and growth due to lack of adhesion sites (**Figure 7A**). The laminin functionalized PEDOT-EM surface after Tween 20 wash (**Figure 7D**) showed similar neuronal growth as the surfaces without Tween 20 wash (**Figure 7C**), which confirms that laminin is firmly attached to the PEDOT-EM with covalent binding and remains bioactive.

CONCLUSION

In conclusion, we have developed a novel approach to synthesize the versatile EDOT-EM, with fewer steps than the previously reported method, fast and quantitative conversion, and extremely high yield. EDOT-EM can be facilely and reproducibly polymerized into PEDOT-EM through electro-polymerization. The resulting PEDOT-EM films exhibit comparable conductivity to PEDOT, no cytotoxicity, and the capability of post-functionalization with small molecules, DNA aptamers, and large proteins. This monomer shows great promises for applications in organic electronics and bioelectronics. The ease of synthesis, polymerization and post-functionalization are expected to greatly accelerate the research and development of PEDOT based bio-functional devices in a broad range of applications.

DATA AVAILABILITY

The raw datasets for this study will be available upon request.

AUTHOR CONTRIBUTIONS

BW designed the experiments, collected and analyzed all data, drafted up manuscript, and led the revision of manuscript. BC designed the experiments, collected preliminary data and participated in drafting manuscript. IT involved in polymerization condition optimization and aptamer sensor. KW involved in neuron cell culture experiments. PI XC supervised the entire project and edited the draft.

FUNDING

This project was supported by NIH R01NS062019, R01NS089688 and R21DA043817 and US Army W81XWH-13-C-0157 and the University of Pittsburgh library open access authors fee fund.

ACKNOWLEDGMENTS

We greatly appreciated PINSE of University of Pittsburgh for providing FTIR instruments, CBI of University of Pittsburgh for providing SEM instruments, and Chemistry department of University of Pittsburgh for providing NMR instruments.

SUPPLEMENTARY MATERIAL

The Supplementary Material for this article can be found online at: https://www.frontiersin.org/articles/10.3389/fchem.2019.00178/full#supplementary-material

REFERENCES

Abidian, M. R., Corey, J. M., Kipke, D. R., and Martin, D. C. (2010). Conducting-polymer nanotubes improve electrical properties, mechanical adhesion, neural attachment, and neurite outgrowth of neural electrodes. *Small* 6, 421–429. doi: 10.1002/smll.200901868

Abidian, M. R., Kim, D. H., and Martin, D. C. (2006). Conducting-polymer nanotubes for controlled drug release. *Adv. Mater. Weinheim.* 18, 405–409. doi: 10.1002/adma.200501726

Abidian, M. R., and Martin, D. C. (2008). Experimental and theoretical characterization of implantable neural microelectrodes modified with conducting polymer nanotubes. *Biomaterials* 29, 1273–1283. doi: 10.1016/j.biomaterials.2007.11.022

Azemi, E., Stauffer, W. R., Gostock, M. S., Lagenaur, C. F., and Cui, X. T. (2008). Surface immobilization of neural adhesion molecule L1 for improving the biocompatibility of chronic neural probes: *in vitro* characterization. *Acta Biomater.* 4, 1208–1217. doi: 10.1016/j.actbio.2008.02.028

Baker, B. R., Lai, R. Y., Wood, M. S., Doctor, E. H., Heeger, A. J., and Plaxco, K. W. (2006). An electronic, aptamer-based small-molecule sensor for the rapid, label-free detection of cocaine in adulterated samples and biological fluids. *J. Am. Chem. Soc.* 128, 3138–3139. doi: 10.1021/ja056957p

Boehler, C., Kleber, C., Martini, N., Xie, Y., Dryg, I., Stieglitz, T., et al. (2017). Actively controlled release of Dexamethasone from neural microelectrodes in a chronic *in vivo* study. *Biomaterials* 129, 176–187. doi: 10.1016/j.biomaterials.2017.03.019

Bolin, M. H., Svennersten, K., Wang, X. J., Chronakis, I. S., Richter-Dahlfors, A., Jager, E. W. H., et al. (2009). Nano-fiber scaffold electrodes based on PEDOT for cell stimulation. *Sensors Actuat. B-Chem.* 142, 451–456. doi: 10.1016/j.snb.2009.04.062

Castagnola, V., Descamps, E., Lecestre, A., Dahan, L., Remaud, J., Nowak, L. G., et al. (2015). Parylene-based flexible neural probes with PEDOT coated surface for brain stimulation and recording. *Biosens. Bioelectron.* 67, 450–457. doi: 10.1016/j.bios.2014.09.004

Charkhkar, H., Knaack, G. L., McHail, D. G., Mandal, H. S., Peixoto, N., Rubinson, J. F., et al. (2016). Chronic intracortical neural recordings using microelectrode arrays coated with PEDOT-TFB. *Acta Biomater.* 32, 57–67. doi: 10.1016/j.actbio.2015.12.022

Cheong, G. L. M., Lim, K. S., Jakubowicz, A., Martens, P. J., Poole-Warren, L. A., and Green, R. A. (2014). Conductive hydrogels with tailored bioactivity for implantable electrode coatings. *Acta Biomater.* 10, 1216–1226. doi: 10.1016/j.actbio.2013.12.032

Chikar, J. A., Hendricks, J. L., Richardson-Burns, S. M., Raphael, Y., Pfingst, B. E., and Martin, D. C. (2012). The use of a dual PEDOT and RGD-functionalized alginate hydrogel coating to provide sustained drug delivery and improved cochlear implant function. *Biomaterials* 33, 1982–1990. doi: 10.1016/j.biomaterials.2011.11.052

Cui, X., and Martin, D. C. (2003). Electrochemical deposition and characterization of poly(3,4-ethylenedioxythiophene) on neural microelectrode arrays. *Sensor Actuat. B Chem.* 89, 92–102. doi: 10.1016/S0925-4005(02)00448-3

de Jong, M. P., van IJzendoorn, L. J., and de Voigt, M. J. A. (2000). Stability of the interface between indium-tin-oxide and poly(3,4-ethylenedioxythiophene)/poly(styrenesulfonate) in polymer light-emitting diodes. *Appl. Phys. Lett.* 77, 2255–2257. doi: 10.1063/1.1315344

Du, Z. J., Luo, X., Weaver, C., and Cui, X. T. (2015). Poly (3, 4-ethylenedioxythiophene)-ionic liquid coating improves neural recording and stimulation functionality of MEAs. *J. Mater. Chem. C Mater. Opt. Electron Devices* 3, 6515–6524. doi: 10.1039/C5TC00145E

Feldman, K. E., and Martin, D. C. (2012). Functional conducting polymers via thiol-ene chemistry. *Biosensors* 2, 305–317. doi: 10.3390/bios2030305

Harris, A. R., Morgan, S. J., Chen, J., Kapsa, R. M., Wallace, G. G., and Paolini, A. G. (2013). Conducting polymer coated neural recording electrodes. *J. Neural Eng.* 10:016004. doi: 10.1088/1741-2560/10/1/016004

Hassarati, R. T., Marcal, H., John, L., Foster, R., and Green, R. A. (2016). Biofunctionalization of conductive hydrogel coatings to support olfactory ensheathing cells at implantable electrode interfaces. *J. Biomed. Mater. Res. Part B Appl. Biomater.* 104, 712–722. doi: 10.1002/jbm.b.33497

Hoyle, C. E., Lee, T. Y., and Roper, T. (2004). Thiol-enes: chemistry of the past with promise for the future. *J. Polymer Sci. Part A-Polymer Chem.* 42, 5301–5338. doi: 10.1002/pola.20366

Istamboulie, G., Sikora, T., Jubete, E., Ochoteco, E., Marty, J. L., and Noguer, T. (2010). Screen-printed poly(3,4-ethylenedioxythiophene) (PEDOT): a new electrochemical mediator for acetylcholinesterase-based biosensors. *Talanta* 82, 957–961. doi: 10.1016/j.talanta.2010.05.070

Jones, M. W., Mantovani, G., Ryan, S. M., Wang, X., Brayden, D. J., and Haddleton, D. M. (2009). Phosphine-mediated one-pot thiol-ene "click" approach to polymer-protein conjugates. *Chem. Commun.* 5272–5274. doi: 10.1039/b906865a

Kade, M. J., Burke, D. J., and Hawker, C. J. (2010). The power of thiol-ene chemistry. *J. Poly. Sci. Part A-Poly. Chem.* 48, 743–750. doi: 10.1002/pola.23824

Karagkiozaki, V., Karagiannidis, P. G., Gioti, M., Kavatzikidou, P., Georgiou, D., Georgaraki, E., et al. (2013). Bioelectronics meets nanomedicine for cardiovascular implants: PEDOT-based nanocoatings for tissue regeneration. *Biochim. Biophys. Acta* 1830, 4294–4304. doi: 10.1016/j.bbagen.2012.12.019

Kim, Y. H., Sachse, C., Machala, M. L., May, C., Müller-Meskamp, L., and Leo, K. (2011). Highly conductive PEDOT:PSS electrode with optimized solvent and thermal post-treatment for ITO-free organic solar cells. *Adv. Funct. Mater.* 21, 1076–1081. doi: 10.1002/adfm.201002290

Kolarcik, C. L., Catt, K., Rost, E., Albrecht, I. N., Bourbeau, D., Du, Z., et al. (2015). Evaluation of poly(3,4-ethylenedioxythiophene)/carbon nanotube neural electrode coatings for stimulation in the dorsal root ganglion. *J. Neural Eng.* 12:016008. doi: 10.1088/1741-2560/12/1/016008

Kozai, T. D., Catt, K., Du, Z., Na, K., Srivannavit, O., Haque, R. U., et al. (2016). Chronic *in vivo* evaluation of PEDOT/CNT for stable neural recordings. *IEEE Trans. Biomed. Eng.* 63, 111–119. doi: 10.1109/TBME.2015.2445713

Lander, A. D., Fujii, D. K., and Reichardt, L. F. (1985). Laminin is associated with the neurite outgrowth-promoting factors found in conditioned media. *Proc. Natl. Acad. Sci. U.S.A.* 82, 2183–2187. doi: 10.1073/pnas.82.7.2183

Lauer, L., Ingebrandt, S., Scholl, M., and Offenhausser, A. (2001). Aligned microcontact printing of biomolecules on microelectronic device surfaces. *IEEE Trans. Biomed. Eng.* 48, 838–842. doi: 10.1109/10.930910

Lin, K. C., Tsai, T. H., and Chen, S. M. (2010). Performing enzyme-free H2O2 biosensor and simultaneous determination for AA, DA, and UA by MWCNT-PEDOT film. *Biosens. Bioelectron.* 26, 608–614. doi: 10.1016/j.bios.2010.07.019

Lu, Y., Wen, Y. -P., Lu, B. -Y., Duan, X. -M., Xu, J. -K., Zhang, L., et al. (2012). Electrosynthesis and characterization of poly(hydroxy-methylated-3,4-ethylenedioxythiophene) film in aqueous micellar solution and its biosensing application. *Chin. J. Poly. Sci.* 30, 824–836. doi: 10.1007/s10118-012-1195-2

Luo, S. -C., Mohamed Ali, E., Tansil, N. C., Yu, H. -H., Gao, S., Kantchev, E. A. B., et al. (2008). Poly(3,4-ethylenedioxythiophene) (PEDOT) nanobiointerfaces: thin, ultrasmooth, and functionalized PEDOT Films with *in vitro* and *in vivo* biocompatibility. *Langmuir* 24, 8071–8077. doi: 10.1021/la800333g

Luo, X., and Cui, X. T. (2009). Electrochemically controlled release based on nanoporous conducting polymers. *Electrochem. Commun.* 11, 402–404. doi: 10.1016/j.elecom.2008.11.052

Luo, X., Weaver, C. L., Zhou, D. D., Greenberg, R., and Cui, X. T. (2011). Highly stable carbon nanotube doped poly(3,4-ethylenedioxythiophene) for chronic neural stimulation. *Biomaterials* 32, 5551–5557. doi: 10.1016/j.biomaterials.2011.04.051

Luo, Y., and Shoichet, M. S. (2004). Light-activated immobilization of biomolecules to agarose hydrogels for controlled cellular response. *Biomacromolecules* 5, 2315–2323. doi: 10.1021/bm0495811

Martin, D. C. (2015). Molecular design, synthesis, and characterization of conjugated polymers for interfacing electronic biomedical devices with living tissue. *MRS Comm.* 5, 131–153. doi: 10.1557/mrc.2015.17

Nosworthy, N. J., McKenzie, D. R., and Bilek, M. M. (2009). A new surface for immobilizing and maintaining the function of enzymes in a freeze-dried state. *Biomacromolecules* 10, 2577–2583. doi: 10.1021/bm900523m

Ouyang, L., Wei, B., Kuo, C. C., Pathak, S., Farrell, B., and Martin, D. C. (2017). Enhanced PEDOT adhesion on solid substrates with electrografted P(EDOT-NH2). *Sci. Adv.* 3:e1600448. doi: 10.1126/sciadv.1600448

Povlich, L. K., Cho, J. C., Leach, M. K., Corey, J. M., Kim, J., and Martin, D. C. (2013). Synthesis, copolymerization and peptide-modification of carboxylic acid-functionalized 3,4-ethylenedioxythiophene (EDOTacid) for neural electrode interfaces. *Biochim. Biophys. Acta* 1830, 4288–4293. doi: 10.1016/j.bbagen.2012.10.017

Sassi, M., Mascheroni, L., Ruffo, R., Salamone, M. M., Pagani, G. A., Mari, C. M., et al. (2013). Exomethylene-3,4-ethylenedioxythiophene (emEDOT): a new versatile building block for functionalized electropolymerized poly(3,4-ethylenedioxythiophenes) (PEDOTs). *Org. Lett.* 15, 3502–3505. doi: 10.1021/ol401008s

Schwartz, A. B., Cui, X. T., Weber, D. J., and Moran, D. W. (2006). Brain-controlled interfaces: movement restoration with neural prosthetics. *Neuron* 52, 205–220. doi: 10.1016/j.neuron.2006.09.019

Segura, J. L., Gomez, R., Blanco, R., Reinold, E., and Bauerle, P. (2006). Synthesis and electronic properties of anthraquinone-, tetracyanoanthraquinodimethane-, and perylenetetracarboxylic diimide-functionalized poly(3,4-ethylenedioxythiophenes). *Chem. Mater.* 18, 2834–2847. doi: 10.1021/cm0602085

Sekine, J., Luo, S. -C., Wang, S., Zhu, B., Tseng, H. -R., and Yu, H. -H. (2011). Functionalized conducting polymer nanodots for enhanced cell capturing: the synergistic effect of capture agents and nanostructures. *Adv. Mater.* 23, 4788–4792. doi: 10.1002/adma.201102151

Sirringhaus, H., Kawase, T., Friend, R. H., Shimoda, T., Inbasekaran, M., Wu, W., et al. (2000). High-resolution inkjet printing of all-polymer transistor circuits. *Science* 290, 2123–2126. doi: 10.1126/science.290.5499.2123

Stauffer, W. R., and Cui, X. T. (2006). Polypyrrole doped with 2 peptide sequences from laminin. *Biomaterials* 27, 2405–2413. doi: 10.1016/j.biomaterials.2005.10.024

Sun, K., Zhang, S. P., Li, P. C., Xia, Y. J., Zhang, X., Du, D. H., et al. (2015). Review on application of PEDOTs and PEDOT: PSS in energy conversion and storage devices. *J. Mater. Sci.* 26, 4438–4462. doi: 10.1007/s10854-015-2895-5

Taylor, I. M., Du, Z., Bigelow, E. T., Eles, J. R., Horner, A. R., Catt, K. A., et al. (2017a). Aptamer-functionalized neural recording electrodes for the direct measurement of cocaine *in vivo*. *J. Mater. Chem. B* 5, 2445–2458. doi: 10.1039/C7TB00095B

Taylor, I. M., Robbins, E. M., Catt, K. A., Cody, P. A., Happe, C. L., and Cui, X. T. (2017b). Enhanced dopamine detection sensitivity by PEDOT/graphene oxide coating on *in vivo* carbon fiber electrodes. *Biosens. Bioelectron.* 89(Pt. 1), 400–410. doi: 10.1016/j.bios.2016.05.084

Vara, H., and Collazos-Castro, J. E. (2015). Biofunctionalized conducting polymer/carbon microfiber electrodes for ultrasensitive neural recordings. *ACS Appl. Mater. Interfaces* 7, 27016–27026. doi: 10.1021/acsami.5b09594

Wei, B., Ouyang, L. Q., Liu, J. L., and Martin, D. C. (2015). Post-polymerization functionalization of poly(3,4-propylenedioxythiophene) (PProDOT) via thiol-ene "click" chemistry. *J. Mater. Chem. B* 3, 5028–5034. doi: 10.1039/C4TB02033B

Xiao, Y., Martin, D. C., Cui, X., and Shenai, M. (2006). Surface modification of neural probes with conducting polymer poly(hydroxymethylated-3,4- ethylenedioxythiophene) and its biocompatibility. *Appl. Biochem. Biotechnol.* 128, 117–130. doi: 10.1385/ABAB:128:2:117

Xu, F. J., Neoh, K. G., and Kang, E. T. (2009). Bioactive surfaces and biomaterials via atom transfer radical polymerization. *Prog. Polym. Sci.* 34, 719–761. doi: 10.1016/j.progpolymsci.2009.04.005

Yazdimamaghani, M., Razavi, M., Mozafari, M., Vashaee, D., Kotturi, H., and Tayebi, L. (2015). Biomineralization and biocompatibility studies of bone conductive scaffolds containing poly(3,4-ethylenedioxythiophene):poly(4-styrene sulfonate) (PEDOT:PSS). *J. Mater. Sci. Mater. Med*. 26:274. doi: 10.1007/s10856-015-5599-8

Zhang, F. L., Johansson, M., Andersson, M. R., Hummelen, J. C., and Inganas, O. (2002). Polymer photovoltaic cells with conducting polymer anodes. *Adv. Mater.* 14, 662–665. doi: 10.1002/1521-4095(20020503)14:9<662::AID-ADMA662>3.0.CO;2-N

Zhang, L., Vila, N., Klein, T., Kohring, G. W., Mazurenko, I., Walcarius, A., et al. (2016). Immobilization of cysteine-tagged proteins on electrode surfaces by thiol-ene click chemistry. *ACS Appl. Mater. Interfaces* 8, 17591–17598. doi: 10.1021/acsami.6b02364

Zhu, B., Luo, S. C., Zhao, H., Lin, H. A., Sekine, J., Nakao, A., et al. (2014). Large enhancement in neurite outgrowth on a cell membrane-mimicking conducting polymer. *Nat. Commun.* 5:4523. doi: 10.1038/ncomms5523

Conflict of Interest Statement: The authors declare that the research was conducted in the absence of any commercial or financial relationships that could be construed as a potential conflict of interest.

frontiers in Chemistry

ORIGINAL RESEARCH
published: 16 April 2019
doi: 10.3389/fchem.2019.00234

Impedimetric Biosensors for Detecting Vascular Endothelial Growth Factor (VEGF) Based on Poly(3,4-ethylene dioxythiophene) (PEDOT)/Gold Nanoparticle (Au NP) Composites

Minsoo Kim[1], *Raymond Iezzi Jr.*[2], *Bong Sup Shim*[1,3] *and David C. Martin*[1]*

[1] Department of Materials Science and Engineering, University of Delaware, Newark, DE, United States, [2] Department of Ophthalmology, Mayo Clinic, Rochester, MN, United States, [3] Department of Chemical Engineering, Inha University, Incheon, South Korea

OPEN ACCESS

Edited by:
Carlo Augusto Bortolotti,
University of Modena and Reggio Emilia, Italy

Reviewed by:
Basem Moosa,
KAUST Catalysis Center (KCC), Saudi Arabia
Mindy Levine,
University of Rhode Island, United States
Stefano Casalini,
UMR7006 Institut de Science et d'Ingénierie Supramoléculaires (ISIS), France

***Correspondence:**
David C. Martin
milty@udel.edu

Specialty section:
This article was submitted to Organic Chemistry, a section of the journal Frontiers in Chemistry

Received: *20 December 2018*
Accepted: *25 March 2019*
Published: *16 April 2019*

Citation:
Kim M, Iezzi R Jr, Shim BS and Martin DC (2019) Impedimetric Biosensors for Detecting Vascular Endothelial Growth Factor (VEGF) Based on Poly(3,4-ethylene dioxythiophene) (PEDOT)/Gold Nanoparticle (Au NP) Composites. Front. Chem. 7:234. doi: 10.3389/fchem.2019.00234

In advanced forms of diabetic retinopathy, retinal vascular occlusive disease and exudative age-related macular degeneration, vision loss is associated with elevated levels or extravasation of vascular endothelial-derived growth factor (VEGF) into the retina, vitreous, and anterior chamber of the eye. We hypothesize that point-of-care biosensors, capable of rapidly and precisely measuring VEGF levels within the eye will assist clinicians in assessing disease severity, and in establishing individualized dosing intervals for intraocular anti-VEGF injection therapy. An impedance biosensor based on a poly(3,4-ethylenedioxythiophene) (PEDOT)/gold nanoparticle (Au NP) composite was developed for detecting VEGF. PEDOT with Au NP was electrochemically deposited on three different medical electrode sensor designs: free-standing pads, screen printed dots, and interdigitated micro-strip electrodes. Anti-VEGF antibody was covalently immobilized on the surface of the polymer films through attachment to citrate-functionalized Au NPs, and the resulting composites were used to detect VEGF-165 by electrochemical impedance spectroscopy (EIS). The PEDOT-Au NP composite materials were characterized using optical microscopy, SEM/EDS, FIB, TEM, and STEM techniques. Among the different micro-electrodes, the interdigitated strip shape showed the best overall film stability and reproducibility. A linear relationship was established between the charge transfer resistance (R_{ct}) and VEGF concentration. The detection limit of VEGF was found to be 0.5 pg/mL, with a correlation coefficient of 0.99 ± 0.064%. These results indicate that the proposed PEDOT/Au NP composites can be used in designing low-cost and accurate VEGF biosensors for applications such as clinical diagnosis of VEGF-mediated eye disease.

Keywords: VEGF (Vascular Endotelial Growth Factor), PEDOT (poly(3, 4-ethylenedioxythiophene)), biosensor, electrochemical deposition, impedance spectroscopy

INTRODUCTION

VEGF-mediated eye disease is associated with several causes of severe vision loss due to exudative Age-related Macular Degeneration (AMD), advanced diabetic retinopathy, and retinal vascular occlusive disease. These three disease groups may often be successfully treated or controlled with long-term intravitreous injection therapy using anti-VEGF drugs such as bevacizumab, an engineered antibody to VEGF-165, ranibizumab, and engineered antibody fragment with enhanced binding affinity to VEGF-165, and aflibercept, an anti-VEGF fusion protein (Hernandez et al., 2018). These drugs are aimed at reducing intraocular levels of biologically-active VEGF, a signaling protein important in vasculogenesis and angiogenesis that promotes the growth and survival of vascular endothelial cells. VEGF is known to exist in five different isoforms containing 121, 145, 165, 189, and 206 amino acids, respectively (Ferrara, 2004). Both VEGF-121 and VEGF-165 are found in neovascular membranes in patients with AMD (Rakic et al., 2003). VEGF-165 is the predominant isoform associated with increased vascular permeability and retinal vascular proliferation (Adamis and Shima, 2005). The aqueous concentration of VEGF in the eyes of the AMD patients ranged from 74.5 to 521.6 pg/mL (Cabral et al., 2017). However, anti-VEGF treatments using anti-angiogenic drugs require repetitive and costly intravitreal injections for patients (Maguire, 2012). Thus, the precise amount of anti-VEGF drug that should be injected and the total number of treatments required could be better controlled by detecting the VEGF concentration in patient's retina. This potential ability to accurately measure VEGF concentrations should substantially reduce the financial burden for patients as well the potential over/under-dose side effects by the anti-VEGF drug treatments. While an implantable biosensor would be highly desirable for continuous *in situ* monitoring during the treatment, components of biosensor technologies still need to be developed including a non-cytotoxic and conductive coating material with a large surface area, an ability to be coated onto a needle-shaped electrode, and the capability of stable, non-destructive measuring.

Biosensors selectively detect the presence or concentrations of a specific biological target by mechanisms such as optical, electrochemical, thermometric, piezoelectric, or magnetic transductions (Potyrailo and Mirsky, 2009). Electrochemical biosensors measure a biochemical interaction between a bioactive substance on a sensor and a biomarker, making it possible to convert the concentrations of VEGF to a quantifiable electrochemical signal. The change of electrochemical signals is coupled to immobilized VEGF on the surface of the sensor. Impedimetric biosensors measure the changes in charge conductance and capacitance at the sensor surface as the selective binding of the target occurs. Here, we used Electrochemical Impedance Spectroscopy (EIS) to measure the impedance changes associated with varying VEGF concentrations in the analyte. EIS has been previously used for monitoring the healthy conditions of animal tissues *in vivo* (Dean et al., 2008) as well as for detecting a wide variety of biomolecules such as proteins (Smiechowski et al., 2006), DNA (Park and Park, 2009), small molecules (Kara et al., 2010), and direct cell-based assays (Mishra et al., 2005). While EIS sensors for VEGF detection have been introduced by utilizing a series of anti-VEGF aptamers (Qureshi et al., 2015; Shamsipur et al., 2015), there are still serious limitations of previous designs for intraocular AMD treatment. Remaining issues include the ability to measure VEGF over a wide range of concentrations, the ability to have an implantable electrode design, and chemical and biological stability.

Conjugated polymers are a unique set of polymeric materials that have intriguing combinations of properties such as electronic and ionic conductivities, and biocompatibility. Conjugated conducting polymers can be polymerized either chemically or electrochemically (Inzelt, 2012). One of the most well-studied of these materials is poly(3,4-ethylenedioxythiophene) (PEDOT)/polystyrene sulfonate (PSS), which is currently used in a variety of organic electronic and bioelectronic applications. PEDOT can be doped and entangled by anionic molecules or polymers because conjugated polymers including PEDOT are p-type semiconductors. While neighboring anionic dopants could not ionize PEDOT, they draw electronic clouds so that PEDOT hold increased concentration of delocalized mobile hole conductors along the conjugated structures. These dopants can be replaced by any form of anions during the polymerization process of EDOT. In this case, citric acid has been used to dope PEDOT as well as to stabilize Au NPs on the composite of PEDOT with improved biofunctionality compared to PSS. Commercially available PEDOT/PSS is polymerized chemically with an oxidizing agent (Elschner et al., 2010). Another method is electrochemical polymerization. An applied electrical current causes irreversible oxidation of the monomer through series of reactions, and resulting in deposition of the polymers on an electrode (El-Abdallah, 2014). A nano- or micro-scale thin polymer film can be deposited on an electrode surface by varying amount of monomers, processing time, and applied electrical charge (Olowu et al., 2010). This conformable deposition is also applicable to coat non-flat electrodes. In designing materials for an EIS biosensor, conjugated polymers can improve the sensitivity and selectivity by which bioactive recognition elements are immobilized on the electrode. The conducting polymers may act as a molecular cable for the direct electron transfer processes between the recognition elements and the electrode surface (Bard et al., 2012). Combined with all these unique properties, a few selected conducting polymers are also biocompatible. Recently, Miriani et al. (2008) reported that PEDOT is not cytotoxic to cells and successfully supports cellular proliferation and differentiation. In addition to its non-cytotoxicity, the rough surface morphology, and charge conduction properties of PEDOT would also be beneficial as a bio-electrode coating *in vivo* system. We have designed a PEDOT-based impedimetric VEGF biosensor via electropolymerization. To improve its binding to the antibody by overcoming the inherent lack of surface functionality of PEDOT, we synthesized a PEDOT/citrate-capped Au nanoparticle (NP) composite. We hypothesized that the PEDOT would interact strongly with Au NPs (Häkkinen, 2012), entrapping them into the PEDOT polymer film during the elctropolymerization (Pan et al., 2015). The citrate-capped Au

NPs would enable the resulting film to bind to the antibody of interest with covalent surface reactions. As a proof of principle, we have investigated three types of medical grade electrode designs including three-dimensional freestanding metal pads, screen-printed dots, and inter-digitated micro-strip electrodes. We confirmed the conformable electrochemical deposition of polymer/Au NP composites onto these various electrodes and their functionalization with the VEGF antibody. We used EIS techniques to examine the response of the sensors to solutions with variations of VEGF concentration, and fit the data to three-element equivalent circuit models. We found that the charge-transfer resistance (R_{ct}) could be directly correlated with VEGF concentration in the analyte. Finally, we conclude with the implications and future directions for this work.

EXPERIMENTAL

Materials

3,4-ethylenedioxylthiophene (EDOT, >97%) monomer was obtained from Sigma–Aldrich (St. Louis, MO, USA). Citrate-capped Au NPs with an average diameter of 10 nm and concentration of 40–50 µg/mL were obtained from NN-Labs (Fayetteville, AR, USA). Ranibizumab (Trade name: Lucentis, MW: 48 kDa), a monoclonal VEGF antibody without a fragment crystallized (Fc) region was obtained from the Mayo Clinic (Rochester, MN., USA). Human recombinant VEGF-165 was purchased from Sigma–Aldrich (St. Louis, MO, USA). The contents of anti-VEGF antibody and VEGF-165 were reconstituted using ultrapure water. Anti-VEGF antibody and VEGF-165 were stored at 4°C and at −20°C, respectively, prior to use. Potassium hexacyanoferrate (III) ($K_3Fe(CN)_6$, >99%), potassium hexacyanoferrate (II) trihydrate ($K_4Fe(CN)_6$, 98.5–102.0%), and potassium chloride (KCl, >99%) were purchased from Sigma–Aldrich (St. Louis, MO, USA). A redox probe solution for electrochemical measurements was prepared from an aqueous solution of 0.005 M $[Fe(CN)_6]^{-3/-4}$ in 0.1 M KCl at pH 7. 2-(N-morpholino)ethanesulfonic acid (MES) buffered saline packs were purchased from Thermo Fisher (San Jose, CA, USA). Cross-linkers including 1-ethyl-3-(3-dimethylaminopropyl)carbodiimide (EDC) and N-hydroxysuccinimide (NHS) were purchased from Pierce, Germany. Water was purified to a resistance of 18 MΩ/cm (Academic Milli-Q Water System; EMD Millipore, Billerica, MA, USA) and filtered through a 0.22 µm membrane filter prior to use.

As working electrodes, four types of electrodes were used; stainless steel free-standing pad electrodes for morphological characterization and biosensing, gold transmission electron microscopy (TEM) grids for TEM characterization, gold screen printed dot electrodes (Au SPEs), and gold interdigitated micro-stripe electrodes (Au IDEs). Stainless steel pad electrodes were purchased from Plastics One (Roanoke, VA, USA) and gold TEM grids were purchased from Electron Microscopy Sciences (Hatfield, PA, USA). Au SPEs with a working diameter of 1.6 mm (gold as a working electrode and a counter electrode, and Ag/AgCl as a reference electrode) and Au IDEs (two gold working and counter channels, each channel: 125 bands, dimension of bands/gaps: 10 µm) were purchased from Metrohm AG (Riverview, FL, USA). Platinum foil (99.999%) was used as an external counter electrode and a reference electrode was purchased from Alfa Aesar (Word Hill, MA, USA). An Ag/AgCl reference electrode (4 M KCl) was obtained from Fisher Scientific Accumet (Pittsburgh, PA, USA).

Electrochemical Polymerization

All electrochemical experiments were carried out with an Autolab PGSTAT12 (Metrohm Autolab, Utrecht, The Netherlands) potentiostat/galvanostat with a frequency response analyzer (FRA) module. 0.005 M of EDOT was mixed with an equal volume of a commercial aqueous solution of Au NPs and the mixture was stirred for 5 min. The ratio of EDOT to Au solution was adjusted to 1:2 by volume. The polymerization was performed in a two-electrode cell with a diameter of 3 cm, where one of three types of electrodes was used as a working electrode, and an external platinum foil or a gold counter channel on an IDE was used as a counter and reference electrode. After the electrochemical polymerization was completed, the residual EDOT monomer and Au NPs were removed by gentle washing with deionized water. To prepare samples for scanning electron microscopy (SEM), electrochemical polymerization of PEDOT/Au NP composite on the stainless-steel electrode was carried out under galvanostatic conditions in a mixture of EDOT and Au NPs at a current density of 1 mA/cm^2 for 30 min. To prepare samples for TEM, electrochemical polymerization of PEDOT/Au NP composite on the gold TEM grid was carried out under galvanostatic conditions in a mixture of EDOT and Au NPs at a current density of 0.1 mA/cm^2 for 20 s. To perform biosensing, electrochemical polymerization of PEDOT/Au NP composite on the stainless-steel pad electrode, Au SPEs, and Au IDEs were carried out under galvanostatic conditions in a mixture of EDOT and Au NPs at a current density of 0.1–1 mA/cm^2 for 1–30 min, 0.1–5 mA/cm^2 for 1–10 min, and 0.1–0.2 mA/cm^2 for 3–5 min, respectively.

Morphological Characterization

Optical microscopy was conducted on a Nikon SMZ800 (Mager Scientific, Dexter, Michigan, USA). Digital images were acquired with a OMAX A3590U digital camera. For SEM and focused ion beam (FIB*)* measurements, an Auriga 60 crossbeam FIB-SEM instrument (Carl Zeiss, Oberkochen, Germany) was used. Augria 60 crossbeam FIB-SEM using an electron beam at the acceleration voltage of 3 kV and a gallium ion beam with a current of 4 nA and the acceleration voltage of 30 kV for ion beam milling to enable cross-sectional analysis was performed. FIB images were recorded at an incident angle of 52°. X-ray energy dispersive spectroscopy (XEDS) was performed on the SEM using Oxford Synergy X-MAX80 & EBSD. For TEM/Scanning Transmission Electron Microscopy (STEM), the samples were studied by a JEOL JEM-3010 transmission electron microscope with a 300 kV field emission gun.

Anti-VEGF Immobilization and VEGF Binding

Two different strategies for the immobilization of antibodies were used for stainless steel electrodes and IDEs: electrostatic interaction for stainless steel electrodes and covalent binding for IDEs. 0.1 M MES solution with 0.9% sodium chloride at pH 4.7 was prepared by dissolving the saline powder to deionized water for physical immobilization of antibodies. It was performed by dipping the stainless-steel electrode in tubes containing 200 μL of 0.1 M MES solution with the anti-VEGF antibody and then the electrodes were incubated at room temperature for 2 h. EDC/NHS coupling agents were used for covalent immobilization of antibody on the electrode surface of IDEs. The terminal—COOH group of citrated stabilized Au NPs was activated using EDC/NHS. The PEDOT coated electrode was immersed in a solution of 0.4 M EDC and 0.1 M NHS for 1 h at room temperature. The resulting electrode was allowed to wash with deionized water and purge under a stream of argon gently. Fifty microliters of anti-VEGF antibody was dropped on the surface of Au IDEs with a pipette and the electrodes were incubated at room temperature for 2 h. All electrodes were then gently rinsed with deionized water to remove unreacted anti-VEGF antibodies on the electrode surface. Finally, 50 μL of VEGF at 0–500 pg/mL was dropped on the surface of electrodes and was incubated at room temperature in a closed container to prevent evaporation for 1 h. All electrodes were gently washed with deionized water again to remove unreacted VEGF.

Electrochemical Measurements

Cyclic Voltammetry (CV) was carried out in 0.1 M KCl solution containing 5 mM ferry/ferrocyanide (1:1) as a redox component to characterize the deposition of polymer/metal composites on an IDE. Voltage was applied from −400 to 800 mV in a step size of 2 mV at a scan rate of 120 mV/s. EIS measurements for VEGF sensing were performed with an alternating sinusoidal signal of 10 mV amplitude and direct current (DC) potential was set to 0 mV. Impedance spectra were collected by scanning the frequency range from 1 to 10 kHz. The same redox couple was also used for impedance measurements. All impedance measurements were carried out in a Faraday cage to minimize external interference on the system. Both CV and EIS measurements were performed in a three-electrode configuration. The stainless-steel electrodes or IDEs coated PEDOT/Au NP composite were used as a working electrode while an external platinum foil was used as a counter electrode and an Ag/AgCl (in 4 M KCl) electrode was used as a reference electrode. The experimental spectra of EIS were fitted to an equivalent circuit using the Windows software ZView v3.4e (Scribner Associates).

RESULTS AND DISCUSSION

Structural Characterization of Electrochemical PEDOT/Au NP Composite

Schematics of electrochemical preparation of PEDOT/Au NP composites and selective detection VEGF 165 by anti-body binding are presented in **Figure 1**. The mediating Au NPs were also characterized by UV-visible spectroscopy and TEM as shown in **Figure S1**. The surface plasmon absorption band of Au NPs was observed at 525 nm. The average diameter of Au NPs was determined to be 10.6 ± 0.7 nm using TEM. The synthesis of PEDOT/Au NP composites was carried out on three different micro-electrodes by electrochemical polymerization; three-dimensional freestanding pad, screen-printed dot, and inter-digitated strip electrodes. The as-prepared sensor with 200 nm thickness of PEDOT/Au NP composite had poor sensitivity to detect tens to hundreds pg/mL of VEGF concentration accurately, which is required for treating average AMD patients clinically. To improve the sensitivity, aggregated Au NPs, on which antibodies were bound to citrate-capped surface via covalent bonding, were deposited on PEDOT binders. For achieving this complex material structure in a one pot synthesis, an excess amount of Au NP solution was mixed with EDOT solution prior to the electrochemical polymerization (1:1 to 1:3 volume ratio). The EDOT and Au NPs were polymerized together on the electrode as a composite and then excess Au NPs were still aggregated. This aggregated structure provides additional sensitivity, presumably due to electrical charge transfer through antigen/ antibody complex formation. We investigated a wide range of volume ratios of Au NP solutions to EDOT solutions during the electrochemical polymerization but the biosensors without aggregated gold layers showed a poor sensitivity to detect VEGF.

Figure 2 shows the surface morphology and cross-sectional analysis of a PEDOT/Au NP composite, characterized using SEM/FIB and optical microscopy. An increase in surface roughness with larger grains was observed due to aggregation of Au NPs. A yellowish, rather than reddish color in **Figure 2** (a-1) indicated that Au NPs were mostly aggregated inside the film. The thickness of the PEDOT/Au NP composite layers was directly measured from the FIB-SEM images, resulting in an estimated thickness of 700 nm. Interestingly, the size of the aggregated Au NPs was much <100 nm which was barely observable by SEM analysis. The dispersion of Au NPs in the PEDOT matrix was characterized using EDS, TEM, and STEM. In **Figure 2c**, colored EDS element maps indicate that the aggregated Au NPs were distributed evenly throughout the PEDOT layer and also confirms the presence of primary elements C, O, S, and Au, corresponding to PEDOT and Au NPs, as expected. High magnification images by TEM and STEM (**Figure 3D**) indicated that the diameter of Au NPs was about 10 nm, again consistent with analysis of the Au NP solution (**Figure S1**).

VEGF Sensing Performance of PEDOT/Au NP Composites on a Free-Standing Pad Electrode

AC impedance measurements were carried out over a range of frequencies from 1 Hz to 10 kHz, in the presence of a redox-active electrolyte following each modification step. The first measurements were performed on the free-standing pad electrodes coated with a PEDOT/Au NP composite. These same

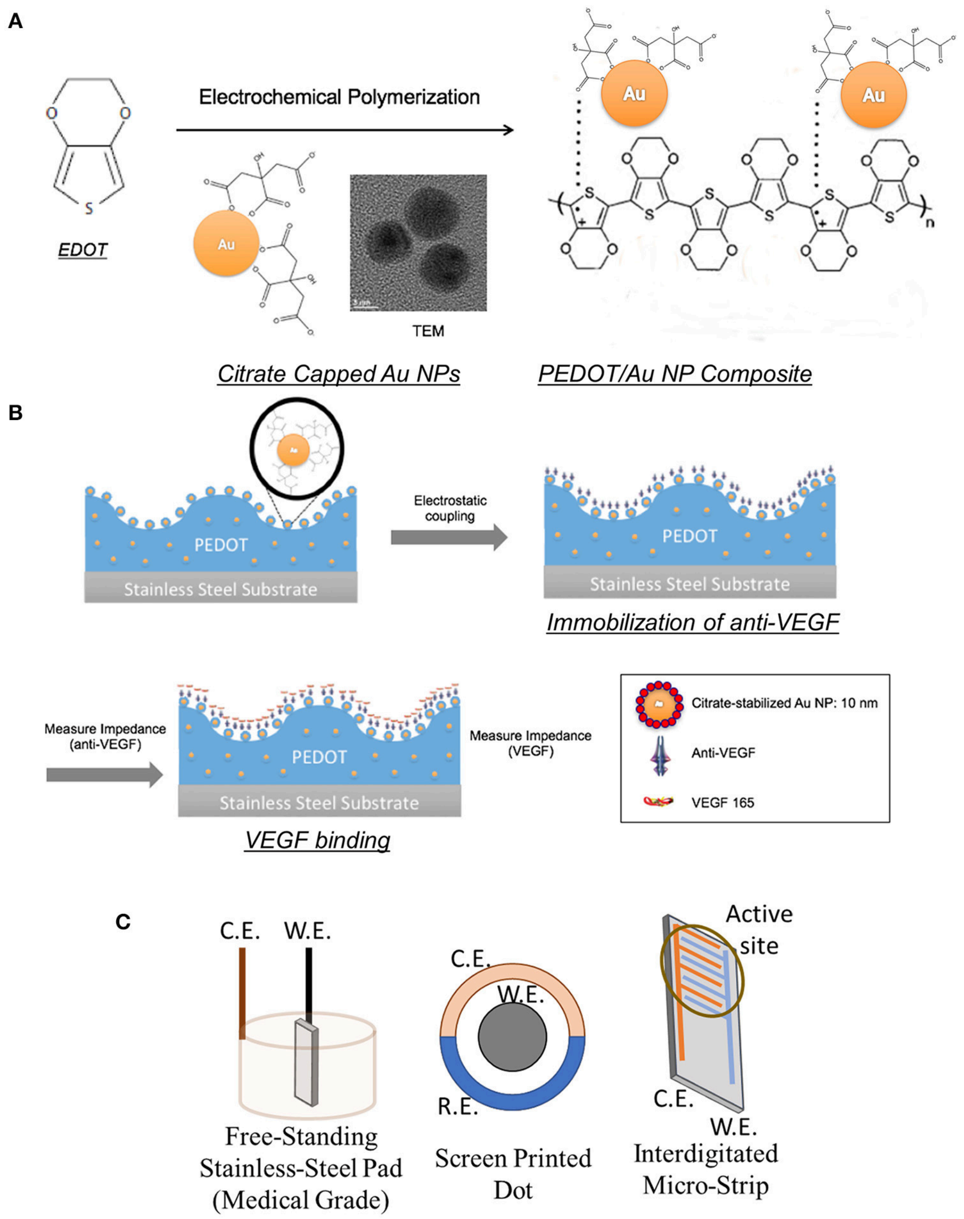

FIGURE 1 | Schematics of PEDOT/Au NP composites for VEGF sensors: **(A)** Electrochemical polymerization of PEDOT/Au NP composites **(B)** Anti-VEGF immobilization and VEGF binding **(C)** Configurations of working (W.E.), counter (C.E.), and reference (R.E.) electrodes.

electrodes were also measured after VEGF incubation followed by anti-VEGF immobilization. **Figure 3A** shows Nyquist impedance plots after each step. The obtained impedance spectra were fit to an equivalent circuit model using an electrochemical modeling and analysis software ZView, as shown in **Figure 3E**, where the solution resistance, R_s represents the electrical resistance of the solution bulk between the electrodes, the constant phase element (CPE) is related to a double-layer capacitance, and the charge transfer resistance, R_{ct} is related to the charge transfer rate of the redox reaction at the biofunctionalized electrode (Braiek et al., 2012). We found that a CPE was a better fit to the experimental results, was used instead of a pure capacitor presumably due to anomalous diffusion from the porous surface of a PEDOT/Au NP composite (Sharifi-Viand et al., 2012). The impedance value of R_{ct} was obtained from each step. The resistive, capacitive, and inductive processes occur in the electrochemical cell during AC impedance measurements (Daniels and Pourmand, 2007). The negative imaginary component of impedance (Z_{im}) can be plotted against the real impedance component (Z_{re}) at each excitation frequency in what is known as a Nyquist, Cole-Cole, or complex impedance plane plot (Spichiger-Keller, 1998). Nyquist plots of all impedance

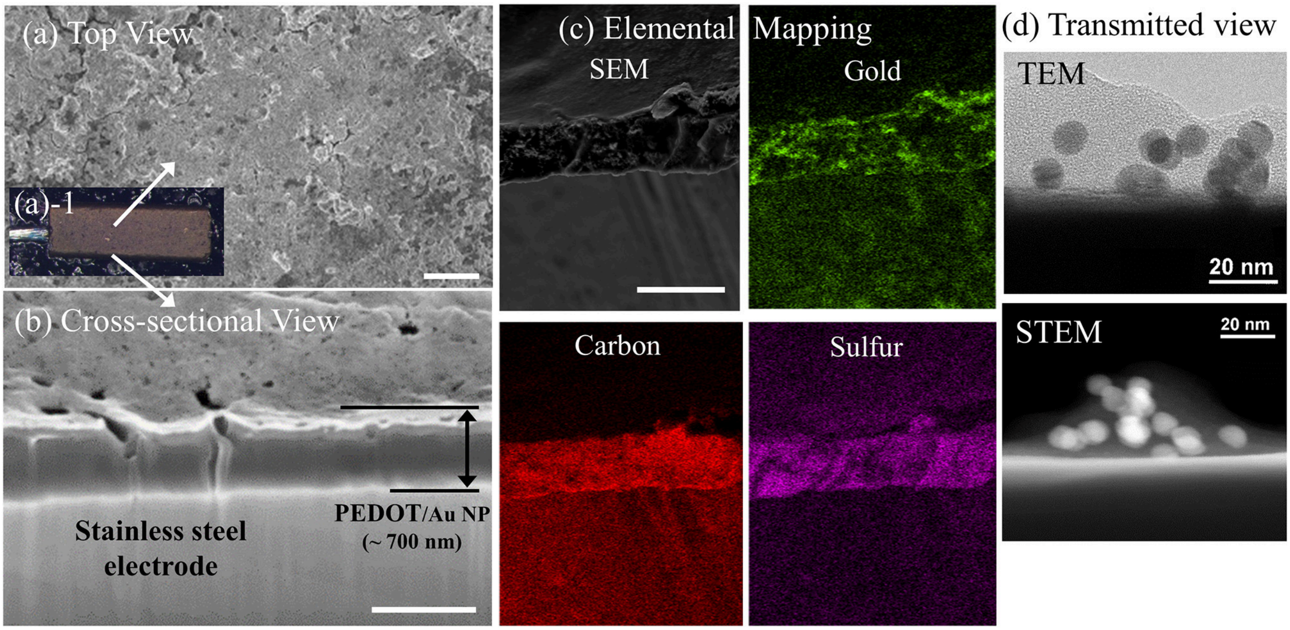

FIGURE 2 | Images of PEDOT/Au NP composites on a free-standing pad electrode. **(a)** Top view, (a-1) **(a)** SEM (scale bar 1 μm) **(b)** optical microscopy **(c)** cross-sectional SEM images of PEDOT/Au NP composite and aggregated Au NPs on a pad electrode (scale bar 500 nm) **(d)** Transmitted images of a PEDOT/Au NP composite by TEM and STEM.

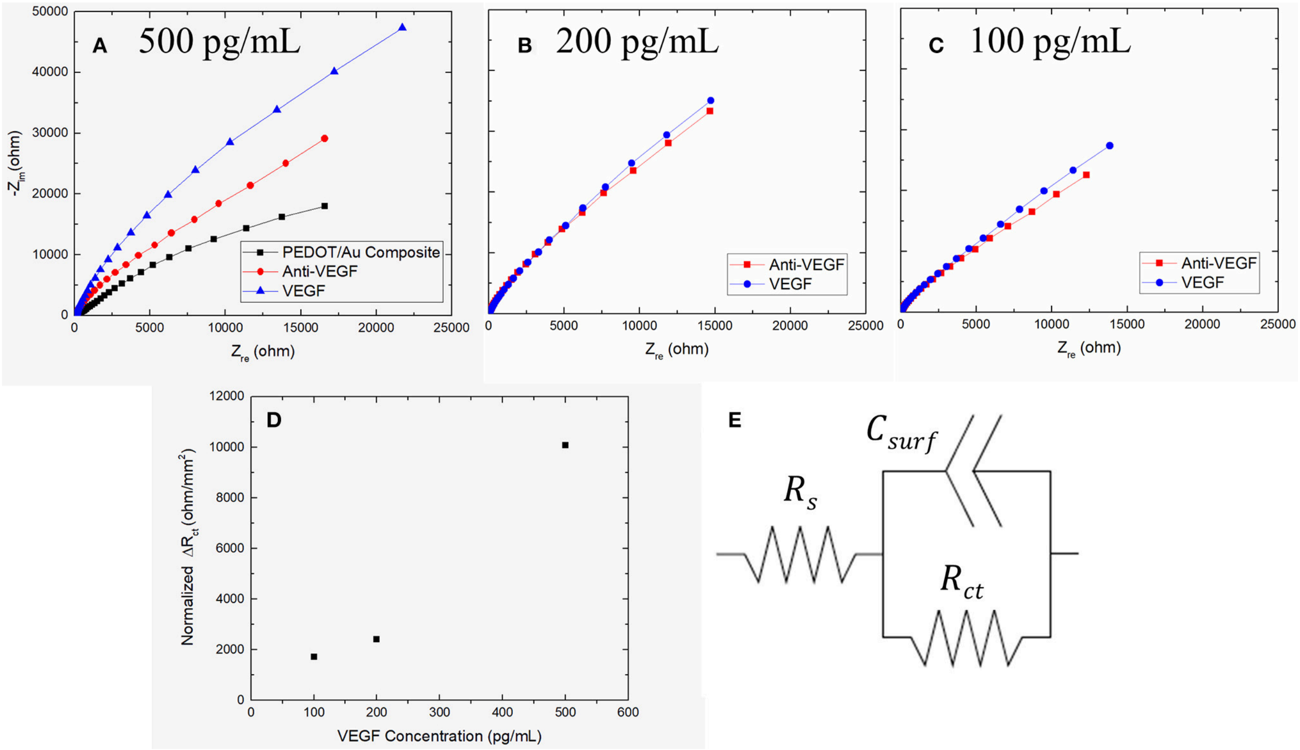

FIGURE 3 | Nyquist plots of impedance spectra obtained from the increasing concentration of VEGF of **(A)** 500 pg/mL **(B)** 200 pg/mL **(C)** 100 pg/mL on three stainless steel electrodes and **(D)** Plot of ΔR_{ct} as a function of VEGF concentration **(E)** Schematic diagram of an equivalent circuit model.

data consist of depressed semi-circles at the high and middle frequency region and straight lines in the low frequency region. A Warburg impedance exists when the electrochemical reaction rate is limited by the mass transport of redox probes to the electrode surface (Suni, 2008). This is generally observed at relatively low frequencies by an interfacial line at 45 degrees to the real axis. The distinct semicircle at high frequencies and a Warburg impedance at sufficiently low frequencies (e.g., 0.1 Hz) in Nyquist plot indicates that the impedance is controlled by the interfacial electron transfer and by diffusion of the redox probe. The incomplete semi-circle at given frequency range in in **Figure 3A** indicates a highly resistive surface and high-frequency domain characteristic of an interfacial charge-transfer mechanism due to a typical impedance response for a free-standing pad electrode. The best matching of experimental impedance spectra with Randall's model was obtained in the frequency range from 1 Hz to 10 kHz. The semicircle at the high frequency region has been reported to correspond to the charge-transfer process at the electrode/electrolyte interface (Dutta et al., 2005). Since the diameter of the semi-circle is proportional to R_{ct}, the EIS semi-circle in **Figure 3A** represents qualitative characteristic of insufficient charge transfer on the surface of stainless steel electrode. The larger diameter of the semi-circle in the presence of biological materials indicates that anti-VEGF and VEGF complexes create an electrostatic barrier to the negatively charged redox couple in solution and effectively hinder the transfer of electrical charges toward the electrode surface (Kharitonov et al., 2000). After anti-VEGF molecules were bound to the electrode modified with a PEDOT-Au NP composite, $R_{ct}$was significantly increased compared to the previously modified electrode surfaces, apparently due to a surface coverage with an additional insulating layer to hinder the redox reaction of $[Fe(CN)_6]^{3-/4-}$. The increase in R_{ct} indicates a successful immobilization of anti-VEGF on the PEDOT/Au NP composite electrode modified with a carboxylic group of Au NPs. Following the incubation of 500 pg/mL of VEGF on the surface of biosensor, $R_{ct}$was further increased, which confirms that the surface was covered with an extra layer derived from binding of VEGF to anti-VEGF. **Figures 3B,C** shows Nyquist plots of 100 and 200 pg/mL as a function of VEGF concentration.

Three different samples were tested with increasing VEGF concentrations. The average R_{ct} from three electrodes after PEDOT/Au NP composite were deposited was 104,000 Ω with a relative standard deviation of 12% shown in **Table 1**. To construct a calibration curve for the biosensor, the R_{ct}variation was calculated against the value of R_{ct} of antibody immobilization using equation 1.

$$\Delta R_{ct} = R_{ct}\left(\frac{antiVEGF}{VEGF}\right) - R_{ct}\,(antiVEGF) \tag{1}$$

where $R_{ct}\left(\frac{antiVEGF}{VEGF}\right)$ is the value of $R_{ct}$when VEGF was bound to anti-VEGF and $R_{ct}\,(antiVEGF)$ is the value of R_{ct} when anti-VEGF antibody was immobilized on the surface of the electrode. All the values of ΔR_{ct} summarized in **Table 2** were normalized by dividing by the value (11.88 mm^2) of electrode surface area. It was noted that the slope of Nyquist plots increased with increasing VEGF concentration. **Figure 3D** shows a linear relationship between $R_{ct}$and VEGF concentration at 100–500 pg/mL, which is applicable to the average VEGF concentrations required for AMD treatment.

As discussed above, the aggregated layer of Au NPs improved sensitivity to impedance. The thickness of PEDOT/Au NP layer was significantly increased with the addition of excess Au solution, which tended to cause delamination of PEDOT/Au film shown in **Figure S2** and to decrease the reproducibility of measurements. Previously, Zhou et al. (2010) reported that the thickness of the PEDOT coating was approximately proportional to deposition time and had a direct effect on the mechanical failure observed. Similarly, we observed that more mechanical failures such as cracking and delamination occurred with thicker films, presumably due to a higher stress imposed on the film. Under electrical stimulation conditions, a thick film was observed to form cracks, and delamination, which would limit the use of the same sample for a multiple EIS test. We found that the exposure time to the solution for immobilization of anti-VEGF and VEGF binding had a significant impact on the delamination of PEDOT. When the exposure time was longer than 4 h, there was a significant decrease in the reproducibility of the EIS measurements.

PEDOT/Au NP Composites on Dot Electrodes

Next, screen-printed dot electrodes (SPEs) were tested in order to improve the sensitivity and homogeneity of the polymer/metal coating. SPEs are low-cost, disposable devices (Hayat and Marty, 2014). The Au SPE design we used consisted of three electrodes, including an Au working, an Au counter, and an Ag reference electrodes. This configuration is ideal for examining small sample volumes as low as 50 μL. The PEDOT/Au NP composites were electrochemically polymerized on the Au SPE electrode under galvanostatic conditions in a mixture of EDOT and Au NPs at a current density of 2 mA/cm^2. **Figure S3** shows inhomogeneous structures of PEDOT/Au NP composite on the working electrode. The thickness varied significantly from the center to the peripheral region. A polymer layer with a thickness of 600 nm was deposited in a peripheral region whereas the thickness of polymer/metal composite coating in the central region was only several nanometers. Similar inhomogeneities of surface roughness were also observed at different current densities, which is presumably related to a non-uniform surface charge distribution. Therefore, we have concluded that SPEs cannot be reliably used for our biosensor.

VEGF Sensing Performance of PEDOT/Au NP Composite on Interdigitated Micro-Strip Electrodes

Finally, experiments with Au IDEs consisting of two interdigitated micro-strip electrodes with two connection tracks were performed. The interdigitated configuration enhances sensitivity and detection limits of sensors due to the maximized contact area between the sensing layer and a chemical analyte. IDEs have been developed for various sensor

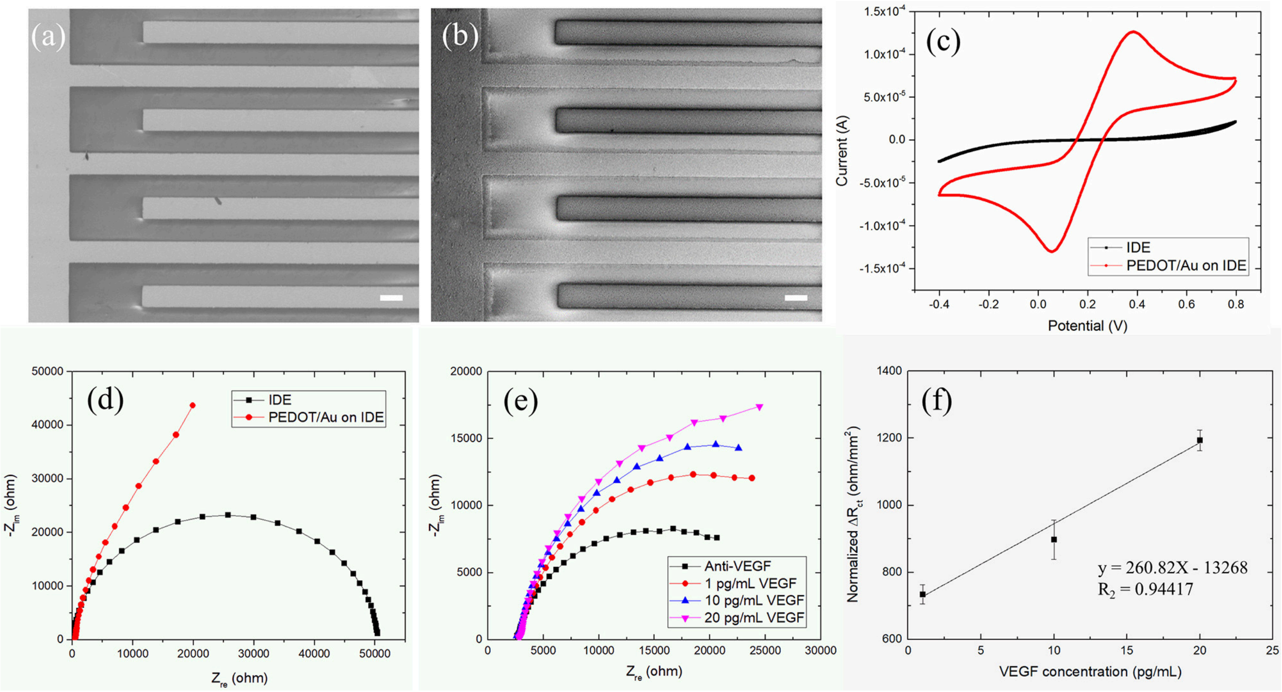

FIGURE 4 | (a,b) SEM images (scale bar 10 μm) of a PEDOT/Au NP composite deposited on an IDE, **(c)** Nyquist plots, **(d)** cyclic voltammograms (or CVs) for a bare Au SPE and a PEDOT/Au NP composite-coated IDE **(e)** Nyquist Plot of impedance spectra obtained from the increasing concentration of VEGF from 1 to 20 pg/mL on a Au IDE **(f)** Linear plot of ΔR_{ct} as a function of VEGF concentration.

applications such as bio sensors (Singh et al., 2011), chemical sensors (Li et al., 2006), and acoustic sensors (Wang et al., 2005). The IDE design including geometrical parameters has been optimized for improved sensitivity of sensors. Min and Baeumner (2004) found that the gap size and finger width of IDE had a significant effect on the signals obtained. Radke et al. (2004) reported that through simulations, the optimal IDE electrode finger width and spacing were 3 and 4 μm, respectively, for enhanced detection of bacteria. Here, commercial IDEs with 10 μm dimensions for bandgaps were tested. The PEDOT/Au NP composites were electrochemically polymerized on Au SPE electrodes under galvanostatic conditions in a mixture solution of EDOT and Au NPs at a current density of 0.1–0.2 mA/cm^2. The thickness of the thin film was controlled by adjusting the deposition time and the applied electrical charges. The resulting thin films were highly homogenous with an overall thickness of 100–200 nm, as shown in **Figures 4a,b**. This film showed smooth surfaces with a reduced grain size on the sub-micron scale.

We have tested different current density for three different commercial electrodes since they have different layouts and dimensions. We have limited the maximum deposition time to 1 h for the practical use. Thick PEDOT/Au NP layers seems to be delaminating under prolonged steps but the thin or porous gold layer on the top of sensor deposited at a low current density showed a poor sensitivity to detect VEGF. The applied current density in this paper was chosen to provide denser gold layer and improved sensitivity. It is noted that sensitivity to detect VEGT would likely be improved by further optimization of current density as well as robust surface of electrode. We are planning to investigate further with a needle type electrode.

TABLE 1 | The fitted result of the impedance spectra in **Figure 3** obtained from ZView software.

	$R_S(\Omega)$	$R_{ct}(\Omega)$	*CPE–T*	*CPE–P*
PEDOT/Au	79.0	37,900	6.68E-06	0.848
Anti-VEGF	78.9	88,900	6.08E-06	0.878
500 pg/mL VEGF	73.0	208,600	4.32E-06	0.876
Anti-VEGF	59.2	102,110	4.24E-06	0.856
200 pg/mL VEGF	60.9	130,800	3.56E-06	0.897
Anti-VEGF	63.0	121,450	4.63E-06	0.881
100 pg/mL VEGF	70.0	141,920	4.55E-06	0.875

TABLE 2 | The normalized ΔR_{ct} as a function of VEGF concentration.

	ΔR_{ct}
100 pg/mL VEGF–Anti VEGF	1723
200 pg/mL VEGF–Anti VEGF	2415
500 pg/mL VEGF–Anti VEGF	10078

The electrochemical characteristics before and after the deposition of a PEDOT/Au NP composite on an IDE were characterized by EIS and CV. The change in the diameter of semi-circles in Nyquist plots in **Figure 4d** can be explained as follows. The qualitatively similar capacitive behaviors were

TABLE 3 | The fitted result of the impedance spectra in **Figure 4e** obtained from ZView software.

	R_s(Ω)	R_{ct}(Ω)	*CPE–T*	*CPE–P*
Anti-VEGF	2,579	23,805	6.31E-06	0.776
1 pg/mL VEGF	2,704	33,151	6.89E-06	0.820
10 pg/mL VEGF	2,727	34,379	7.71E-06	0.882
20 pg/mL VEGF	2,889	38,771	7.16E-06	0.900

TABLE 4 | The normalized ΔR_{ct} a function of VEGF concentration.

	1st	2nd	3rd
ΔR_{ct} (1 pg/mL VEGF–Anti VEGF)	733.02	763.14	705.88
ΔR_{ct} (10 pg/mL VEGF–Anti VEGF)	829.34	930.03	931.76
ΔR_{ct} (20 pg/mL VEGF–Anti VEGF)	1173.80	1228.31	1177.09

normally obtained from conductive porous structures with 45° inclined line at higher frequencies in the impedance spectra of IDE coated by PEDOT/Au NP composite (Park et al., 2013). The single semi-circle representing the process is controlled by the interfacial electron transfer which was obtained in the impedance spectra of a bare IDE. **Figure 4c** shows CV obtained with a bare Au IDE (black line) and Au IDE coated with a PEDOT/Au NP composite (red line). The bare Au IDE exhibits a sigmoidal CV curve for the oxidation and reduction of $[Fe(CN)_6]^{-3/-4}$ whereas a peak-shaped CV with a PEDOT/Au NP composite. This behavior attributes to enhanced mass transport by redox species toward the electrode surface given by geometry characteristic of IDE allowing the current to go to a steady-state value (Yang and Zhang, 2007). The redox potential was measured at +0.06 and +0.38 V for a PEDOT/Au NP composite-coated Au IDE. Compared to a bare IDE, a PEDOT/Au NP composite-coated IDE led to a significant increase in the area within the curve, indicating a larger charge capacity characteristic. Both EIS and CV data demonstrated that a PEDOT/Au NP composite was successfully deposited on the electrode, which is consistent with SEM images in **Figure 4b**.

Figure 4e shows the complex impedance spectra of the PEDOT/Au NP composite-modified Au IDE as a function of VEGF concentration. The uniform thin single layer of a PEDOT/Au NP composite on an Au IDE allowed for a multiple test on the same sample unlike non-uniform layers on the stainless steel electrode, as discussed earlier. EIS data were fitted to the equivalent circuit model in **Figure 4e** in the frequency from 0.5 Hz to 1 kHz shown in **Table 3**. All the values of ΔR_{ct} were normalized by dividing by the value (12.75 mm^2) of electrode surface area summarized in **Table 4**. **Figure 4f** shows a calibration line of the impedance biosensor encompassing the desired range of detection. It was found that R_{ct} variation and the logarithmic value of VEGF concentrations have a linear correlation within a range of 1–20 pg/mL which is applicable for VEGF concentrations of average AMD patients. The linear correlation led to a slope of 24.1 and a correlation coefficient of 0.99, and the limit of detection (LOD) was 0.5 pg/mL. To validate the reproducibility of the biosensor, three different electrode samples were measured under the same conditions. The relative standard deviation for three electrodes was 6.5% indicating reasonably good reproducibility of the biosensor. The correlation coefficient in this study is 0.99 ± 0.064. The increase in R_{ct} with increasing VEGF concentration was discussed earlier. Increased thickness of the bio layers due to binding of VEGF onto the immobilized anti-VEGF resulted in an increase in R_{ct} to hinder the electron transfer process of redox couples.

In this paper, we have used commercial Au NPs with a diameter of 10 nm. Piletsk et al. investigated the correlation between the size of biotinylated nanoparticles and their affinity in relation to interactions with the solid surface (Piletska and Piletsky, 2010). It was shown that the increase in the particle size from 50 to 200 nm reduced the affinity of biotin–streptavidin interactions so that sensitivity decreased from 1.2×10^{-12} to 1.2×10^{-10} M (Piletska and Piletsky, 2010). Similarly, we expect that biofunctional Au NPs of smaller sizes increase the active sites for anti-VEGF immobilization at the gold surface and the higher concentrations of immobilized anti-VEGF result in stronger binding with VEGF.

We have focused on detecting VEGF-165 as a biomarker of AMD, which could also be applied to detect other VEGF isoforms. To immobilize VEGF-165, we have used ranibizumab which was produced using recombinant antibody technology. Ranibizumab also bounds all isoforms of VEGF-A but markedly low affinity (Papadopoulos et al., 2012). Aflibercept is another VEGF antibody which has a higher all isoforms of VEGF-A binding affinity as well as its ability to bind VEGF-B and PlGF (Mantione et al., 2017). However, Aflibercept is larger molecules than Ranibizumab, which might result steric hindrances during immobilizing on the sensor surface.

CONCLUSIONS

We have designed and characterized a label-free impedance biosensor using PEDOT/Au NP composites for detecting VEGF-165. As a proof of principle, PEDOT/Au NP composites were galvanostatically electropolymerized onto the three types of electrodes including stainless steel free-standing pads, Au SPEs, and Au IDEs. Thin films of a PEDOT Au NP composites with uniform thickness were successfully deposited on Au IDEs whereas inhomogeneous layers with the potential to delaminate were found on both on stainless steel electrodes and Au SPEs, resulting in a low reproducibility of the resulting biosensors. Nyquist plots obtained from the use of IDEs showed a significant change in R_{ct} due to anti-VEGF immobilization and its specific binding to VEGF. For a biosensor with IDEs, R_{ct} was found to have a linear relationship with VEGF over a concentration range of 1–20 pg/mL. The performance of the biosensor was further investigated in terms of limit of detection and reproducibility. A detection limit of 0.5 pg/mL and correlation coefficient of 0.987 were obtained with a relative standard deviation of 0.99 ± 0.064 were obtained. Our work demonstrates the potential of PEDOT/Au NP composites as effective materials for reproducible and sensitive measurements of VEGF concentration. Future experiments will seek to further extend this biosensor technology to *in-vivo* testing, perhaps using needle type electrodes.

AUTHOR CONTRIBUTIONS

DM and Rl conceived of the idea to use conjugated polymers as the basis for VEGF sensors. The development of specific methods, in particular including the use of metal NPs and the experimental work, were done by MK. The paper was written by MK, with editorial input and final editing by all co-authors. The final draft was prepared and uploaded by DM.

FUNDING

This research was supported in part by funding from University of Delaware and the National Science Foundation (DMR-1505144 and DMR-1808048). BS acknowledges funding support from NRF-2017R1A2B4012736.

ACKNOWLEDGMENTS

The authors thank Dr. Fei Deng in Keck Lab at UD for supporting SEM/FIB and TEM measurements and Dr. Whirang Cho and Chin-Chen Kuo for helpful discussions.

SUPPLEMENTARY MATERIAL

The Supplementary Material for this article can be found online at: https://www.frontiersin.org/articles/10.3389/fchem.2019.00234/full#supplementary-material

REFERENCES

Adamis, A. P., and Shima, D. T. (2005). The role of vascular endothelial growth factor in ocular health and disease. *Retina* 25, 111–118. doi: 10.1097/00006982-200502000-00001

Bard, A. J., Inzelt, G., and Scholz, F. (eds). (2012). *Electrochemical Dictionary*, *2nd rev.extended Edn*. Heidelberg: Springer. doi: 10.1007/978-3-642-29551-5

Braiek, M., Rokbani, K. B., Chrouda, A., Mrabet, B., Bakhrouf, A., Maaref, A., et al. (2012). An electrochemical immunosensor for detection of *Staphylococcus aureus* bacteria based on immobilization of antibodies on self-assembled monolayers-functionalized gold electrode. *Biosensors* 2, 417–426. doi: 10.3390/bios2040417

Cabral, T., Luiz, H. L., Julia, P., Jimmy, D., Erika, O., Akiyoshi, O., et al. (2017). Aqueous vascular endothelial growth factor and clinical outcomes correlation after single intravitreal injection of bevacizumab in patients with neovascular age-related macular degeneration. *Int. J. Retina Vitreous* 3:6. doi: 10.1186/s40942-017-0066-y

Daniels, J. S., and Pourmand, N. (2007). Label-free impedance biosensors: opportunities and challenges. *Electroanalysis* 19, 1239–1257. doi: 10.1002/elan.200603855

Dean, D. A., Ramanathan, T., Machado, D., and Sundararajan, R. (2008). Electrical impedance spectroscopy study of biological tissues. *J. Electrostat.* 66, 165–77. doi: 10.1016/j.elstat.2007.11.005

Dutta, S., Choudhary, R. N. P., and Sinha, P. K. (2005). Impedance spectroscopy studies on Ga-Ion-modified PLZT ceramics. *Phys. Status Solidi* 202, 1172–1181. doi: 10.1002/pssa.200406932

El-Abdallah, G. M. (2014). Electrochemical characterization of poly 3-thiopheneacetonitrile: technique, solvent and relaxation effects. *J. Saudi Chem. Soc.* 18, 825–834. doi: 10.1016/j.jscs.2011.10.001

Elschner, A., Kirchmeyer, S., Lovenich, W., Merker, U., and Reuter, K. (2010). *PEDOT: Principles and Applications of an Intrinsically Conductive Polymer*. Boca Raton, FL: CRC Press. doi: 10.1201/b10318

Ferrara, N. (2004). Vascular endothelial growth factor: basic science and clinical progress. *Endocr. Rev.* 25, 581–611. doi: 10.1210/er.2003-0027

Häkkinen, H. (2012). The gold-sulfur interface at the nanoscale. *Nat. Chem.* 4, 443–455. doi: 10.1038/nchem.1352

Hayat, A., and Marty, J. L. (2014). Disposable screen printed electrochemical sensors: tools for environmental monitoring. *Sensors* 14, 10432–10453. doi: 10.3390/s140610432

Hernandez, L., Tereza, L., Clifford, C., Hector, T., Andrea, G., and Andreas, K. (2018). Intravitreal aflibercept versus ranibizumab for wet age-related macular degeneration: a cost-effectiveness analysis. *J. Manag. Care Spec. Pharm.* 24, 608–616. doi: 10.18553/jmcp.2018.24.7.608

Inzelt, G. (2012). *Conducting Polymers: A New Era in Electrochemistry*, *2nd Edn.* Monographs in Electrochemistry. Heidelberg ; New York, NY: Springer. doi: 10.1007/978-3-642-27621-7

Kara, P., de la Escosura-Muñiz, A., Maltez-da Costa, M., Guix, M., Ozsoz, M., and Merkoçi, A. (2010). Aptamers based electrochemical biosensor for protein detection using carbon nanotubes platforms. *Biosens. Bioelectron.* 26, 1715–1718. doi: 10.1016/j.bios.2010.07.090

Kharitonov, A. B., Alfonta, L., Katz, E., and Willner, I. (2000). Probing of bioaffinity interactions at interfaces using impedance spectroscopy and chronopotentiometry. *J. Electroanal. Chem.* 487, 133–41. doi: 10.1016/S0022-0728(00)00178-9

Li, J., Lu, Y., and Meyyappan, M. (2006). Nano chemical sensors with polymer-coated carbon nanotubes. *IEEE Sens. J.* 6, 1047–1051. doi: 10.1109/JSEN.2006.881018

Maguire, M. G. (2012). Comparing treatments for age-related macular degeneration: safety, effectiveness, and cost. *LDI Issue Brief* 17, 1–4. doi: 10.2147/OPTH.S1485

Mantione, D., del Aqua, I., Sanchez-Sanchez, A., and Mecerreyes, D. (2017). Poly(3,4-ethylenedioxythiophene) (PEDOT) derivatives: innovative conductive polymers for bioelectronics. *Polymers* 9:354. doi: 10.3390/polym9080354

Min, J., and Baeumner, A. J. (2004). Characterization and optimization of interdigitated ultramicroelectrode arrays as electrochemical biosensor transducers. *Electroanalysis* 16, 724–729. doi: 10.1002/elan.2003 02872

Miriani, R. M., Abidian, M. R., and Kipke, D. R. (2008). Cytotoxic analysis of the conducting polymer PEDOT using myocytes. *Conf. Proc. IEEE Eng. Med. Biol. Soc*. 2008, 1841–1844. doi: 10.1109/IEMBS.2008.4649538

Mishra, N. N., Retterer, S., Zieziulewicz, T. J., Isaacson, M., Szarowski, D., Mousseau, D. E., et al. (2005). On-chip micro-biosensor for the detection of human CD4+ cells based on ac impedance and optical analysis. *Biosens. Bioelectron*. 21, 696–704. doi: 10.1016/j.bios.2005.01.011

Olowu, R. A., Arotiba, O., Mailu, S. N., Waryo, T. T., Baker, P., and Iwuoha, E. (2010). Electrochemical aptasensor for endocrine disrupting 17β-estradiol based on a poly(3,4-Ethylenedioxylthiopene)-gold nanocomposite platform. *Sensors.* 10, 9872–9890. doi: 10.3390/s101109872

Pan, Y., Zhao, F., and Zeng, B. (2015). Electrochemical sensors of octylphenol based on molecularly imprinted poly(3,4-Ethylenedioxythiophene) and poly(3,4-ethylenedioxythiophene-gold nanoparticles). *RSC Adv.* 5, 57671–57677. doi: 10.1039/C5RA08094K

Papadopoulos, N., Martin, J., Ruan, Q., Rafique, A., Rosconi, M. P., Shi, E., et al. (2012). Binding and neutralization of vascular endothelial growth factor (VEGF) and related ligands by VEGF Trap, ranibizumab and bevacizumab. *Angiogenesis* 15, 171–185. doi: 10.1007/s10456-011-9249-6

Park, H. S., Ko, S. J., Park, J. S., Kim, J. Y., and Song, H. K. (2013). Redox-active charge carriers of conducting polymers as a tuner of conductivity and its potential window. *Sci. Rep.* 3:2454. doi: 10.1038/srep02454

Park, J.-Y., and Park, S.-M. (2009). DNA hybridization sensors based on electrochemical impedance spectroscopy as a detection tool. *Sensors* 9, 9513–9532. doi: 10.3390/s91209513

Piletska, E. V., and Piletsky, S. A. (2010). Size matters: influence of the size of nanoparticles on their interactions with ligands immobilized on the solid surface. *Langmuir* 26, 3783–3785. doi: 10.1021/la904834y

Potyrailo, R. A., and Mirsky, V. M. (2009). Introduction to combinatorial methods for chemical and biological sensors, in *Combinatorial Methods for Chemical and Biological Sensors*. Integrated analytical systems, eds R. A. Potyrailo and V. M. Mirsky (New York, NY: Springer), 3–24.

Qureshi, A., Gurbuz, Y., and Niazi, J. H. (2015). Capacitive aptamer–antibody based sandwich assay for the detection of VEGF cancer biomarker in serum. *Sens. Actuat. B Chem.* 209, 645–51. doi: 10.1016/j.snb.2014.12.040

Radke, S. M., Alocilja, E. C., Radke, S. M., and Alocilja, E. C. (2004). Design and fabrication of a microimpedance biosensor for bacterial detection. *IEEE Sens. J.* 4, 434–440. doi: 10.1109/JSEN.2004.830300

Rakic, J. M., Lambert, V., Devy, L., Luttun, A., Carmeliet, P., Claes, C., et al. (2003). Placental growth factor, a member of the VEGF family, contributes to the development of choroidal neovascularization. *Invest. Opthalmol. Visual Sci.* 44, 3186–3193. doi: 10.1167/iovs.02-1092

Shamsipur, M., Farzin, L., Amouzadeh Tabrizi, M., and Molaabasi, F. (2015). Highly sensitive label free electrochemical detection of VGEF165 tumor marker based on 'signal off' and 'signal on' strategies using an Anti-VEGF165 aptamer immobilized BSA-gold nanoclusters/ionic liquid/glassy carbon electrode. *Biosens. Bioelectron.* 74, 369–375. doi: 10.1016/j.bios.2015.06.079

Sharifi-Viand, A., Mahjani, M. G., and Jafarian, M. (2012). Investigation of anomalous diffusion and multifractal dimensions in polypyrrole film. *J. Electroanal. Chem.* 671, 51–57. doi: 10.1016/j.jelechem.2012.02.014

Singh, K. V., Bhura, D. K., Nandamuri, G., Whited, A. M., Evans, D., King, J., et al. (2011). Nanoparticle-enhanced sensitivity of a nanogap-interdigitated electrode array impedimetric biosensor. *Langmuir* 27, 13931–13939. doi: 10.1021/la202546a

Smiechowski, M. F., Lvovich, V. F., Roy, S., Fleischman, A., Fissell, W. H., and Riga, A. T. (2006). Electrochemical detection and characterization of proteins. *Biosens. Bioelectron.* 22, 670–677. doi: 10.1016/j.bios.2006.02.008

Spichiger-Keller, U. E. (1998). *Chemical Sensors and Biosensors for Medical and Biological Applications*. Weinheim ; New York, NY ; Chichester ; Brisbane, QLD ; Singapore ; Toronto, ON: Wiley-VCH.

Suni, I. I. (2008). Impedance methods for electrochemical sensors using nanomaterials. *TrAC Trends Anal. Chem.* 27, 604–611. doi: 10.1016/j.trac.2008.03.012

Wang, Z., Wang, C., and Liu, L. (2005). Design and analysis of a PZT-based micromachined acoustic sensor with increased sensitivity. *IEEE Trans. Ultrasonics Ferroelectr. Frequency Control* 52, 1840–1850. doi: 10.1109/TUFFC.2005.1561640

Yang, X., and Zhang, G. (2007). The voltammetric performance of interdigitated electrodes with different electron-transfer rate constants. *Sens. Actuators B Chem.* 126, 624–631. doi: 10.1016/j.snb.2007.04.013

Zhou, D. D., Cui, T. X., Hines, A., and Greenberg, R. J. (2010). Conducting polymers in neural stimulation applications, in *Implantable Neural Prostheses 2: Techniques and Engineering Approaches*. Biological and medical physics, biomedical engineering, eds D. Zhou and E. Greenbaum (New York, NY: Springer), 217–52.

Conflict of Interest Statement: The authors declare that the research was conducted in the absence of any commercial or financial relationships that could be construed as a potential conflict of interest.

frontiers in Chemistry

MINI REVIEW
published: 18 April 2019
doi: 10.3389/fchem.2019.00265

Conjugated Oligo- and Polymers for Bacterial Sensing

Susanne Löffler[1]*, Haris Antypas[1], Ferdinand X. Choong[1], K. Peter R. Nilsson[2] and Agneta Richter-Dahlfors[1]*

[1] Department of Neuroscience, Swedish Medical Nanoscience Center, Karolinska Institutet, Stockholm, Sweden,
[2] Department of Chemistry, IFM, Linköping University, Linköping, Sweden

Fast and accurate detection of bacteria and differentiation between pathogenic and commensal colonization are important keys in preventing the emergence and spread of bacterial resistance toward antibiotics. As bacteria undergo major lifestyle changes during colonization, bacterial sensing needs to be achieved on different levels. In this review, we describe how conjugated oligo- and polymers are used to detect bacterial colonization. We summarize how oligothiophene derivatives have been tailor-made for detection of biopolymers produced by a wide range of bacteria upon entering the biofilm lifestyle. We further describe how these findings are translated into diagnostic approaches for biofilm-related infections. Collectively, this provides an overview on how synthetic biorecognition elements can be used to produce fast and easy diagnostic tools and new methods for infection control.

Keywords: conjugated polymers, conjugated oligoelectrolytes, luminescent conjugated oligothiophenes, bacterial sensing, biofilms, curli, cellulose

OPEN ACCESS

Edited by:
Jae Young Lee,
Gwangju Institute of Science and Technology, South Korea

Reviewed by:
Francesca Di Maria,
Istituto di Nanotecnologia (NANOTEC), Italy
Florenci Vicent González,
University of Jaume I, Spain

Correspondence:
Susanne Löffler
susanne.loffler@ki.se
Agneta Richter-Dahlfors
agneta.richter.dahlfors@ki.se

Specialty section:
This article was submitted to Organic Chemistry, a section of the journal Frontiers in Chemistry

Received: *01 February 2019*
Accepted: *01 April 2019*
Published: *18 April 2019*

Citation:
Löffler S, Antypas H, Choong FX, Nilsson KPR and Richter-Dahlfors A (2019) Conjugated Oligo- and Polymers for Bacterial Sensing. Front. Chem. 7:265. doi: 10.3389/fchem.2019.00265

INTRODUCTION

Detection of bacterial pathogens in clinical settings is often based on slow and outdated technology (O'Neill, 2016). Bacterial culturing on solid nutrient media in Petri dishes has remained the golden standard for detection since the 1880s despite lengthy incubation times. Light microscopy and Gram staining are routinely used methods but their specificity and sensitivity are low (Bursle and Robson, 2016). With bacterial infections re-emerging as a global health threat, there is an urgent need to implement new technologies with rapid delivery of results (O'Neill, 2016). Currently, the long diagnostic turnaround times often leave the clinician with no choice but to empirically prescribe antibiotics to secure a patient's life. With no information at hand on the presence and identity of bacteria, this approach may result in suboptimal therapy or unnecessary prescription of antibiotics that may negatively affect the patient's bacterial microflora and select for resistant bacteria (Cantón and Morosini, 2011). New technologies with reduced diagnostic turnaround times should also account for the high complexity of bacterial pathogenesis. Contrary to the planktonic, single-cell lifestyle, bacteria can form multicellular colonies called biofilms. Characteristic of the biofilm lifestyle is that bacteria embed themselves in a self-secreted extracellular matrix (ECM). This matrix, which consists of proteins, extracellular DNA, and polysaccharides, provides spatial organization, and mechanical support to the community (Flemming and Wingender, 2010). The aggregation of proteins and polysaccharides acts as a molecular glue that adheres the bacterial cells to each other and to both biotic and abiotic surfaces. Biofilms thus become extremely resilient toward mechanical or chemical cleaning as well as antibiotic treatment (Hall-Stoodley et al., 2004). Despite evidence for the importance of biofilms for bacterial virulence and the establishment of chronic infections, which are difficult to treat, no diagnostic methods exist to identify a biofilm infection (Phillips and Schultz, 2012; Koo et al., 2017).

In an effort to achieve rapid detection of pathogens, several new approaches have been implemented. These include amplification or hybridization of pathogen-associated nucleic acids, antibody-based immunological detection of bacterial antigens, and various forms of biosensors (Law et al., 2014). While nucleic acid-based and immunological detection methods are highly specific and can detect as few as 10 colony-forming units (CFU/ml), sample processing can be time-consuming, require experienced personnel as well as expensive equipment (Min and Baeumner, 2002; Mollasalehi and Yazdanparast, 2013; Huang et al., 2014). Biosensor-based approaches have a higher detection limit ($\geq 10^3$ CFU/ml) but deliver the result within an hour (Wei et al., 2007). Biosensors for bacterial detection are generally based on an optical or electronic transducer combined with a biological recognition element, such as receptors, nucleic acids, or antibodies (Ivnitski et al., 1999).

Conjugated polymers (CPs), conjugated polyelectrolytes (CPEs), and soluble conjugated oligoelectrolytes (COEs) recently emerged as interesting materials interfacing biological systems. Among important features, these materials show optoelectronic properties, redox activities as well as tunable electronic conductivity (Löffler et al., 2015a,b). CPs and CPEs have been successfully used as actuators and modulators of biological systems and as transducer materials in various biosensors as well as in neuronal interfaces (Gerard et al., 2002; Wang et al., 2002; Svennersten et al., 2009, 2011; Larsson et al., 2013; Simon et al., 2015). This review highlights specifically the use of CPs, CPEs, and COEs for detection of bacteria and bacterial biofilms.

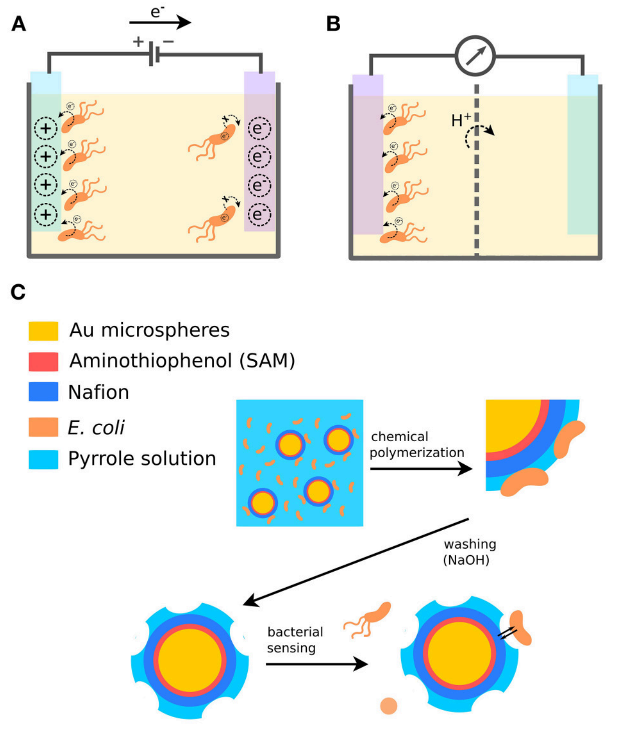

FIGURE 1 | Bacterial sensing using conjugated polymers. **(A)** Modulation of bacterial biofilm formation based on the availability of electron acceptors in the PEDOT surface. **(B)** Detection of bacteria by sensing bacterial electron transfer to a PEDOT electrode. **(C)** Detection of bacteria by fabrication of cell-imprinted microspheres using the conjugated polymer PPy.

BACTERIAL SENSING USING CONJUGATED POLYMER SURFACES

Detection of Bacteria Based on CP Redox Properties

CPs such as poly(3,4-ethylenedioxythiophene) (PEDOT), polypyrrole (PPY), polydiacetylene (PDA), and polyaniline (PANI), are characterized by a π-conjugated backbone. The π-electron system at the backbone confers optical and semiconducting properties. Electrically conducting polymers can be created by charge injection to the conjugated backbone (doping) and by fabrication of thin films or other microstructures to allow for electronic coupling between the polymer chains. Anionic dopants (counter anions) are embedded into CP films during electrochemical or chemical oxidation to neutralize the positive charges in the CP backbones (Le et al., 2017; Inal et al., 2018). The most well-known CP counter anions are tosylate (Tos), poly(styrenesulfonate) (PSS), and dodecyl benzene sulfonate (DBS). Several other small and biologically relevant anions have also been used, such as heparin, DNA and dexamethasone (Herland et al., 2011; Gomez-Carretero et al., 2017; Shah et al., 2018).

Successful modulation of the formation of *Salmonella* biofilm has been demonstrated using electropolymerized PEDOT doped with heparin, DBS, or chloride (Gomez-Carretero et al., 2017). Fabrication of polymer surfaces was performed under conditions that maintained comparable charge storage capacity and hydrophobicity irrespective of counter ion. The electrochemical redox state and exposed chemical functional groups were therefore the sole factors affecting biofilm formation. To investigate whether the redox state of PEDOT, i.e., the amount of available electron acceptors, influences biofilm formation, surfaces integrated into a custom-made culturing device were electronically addressed to generate oxidized, reduced or unswitched (pristine) PEDOT during static culturing of *Salmonella* for 24 h. Macroscopic analysis of the amount of surface-attached biomass revealed a decrease of 52–58% in the reduced state and 39–58% in the unswitched state compared to the oxidized state (**Figure 1A**). The same effect was observed irrespective of counter ion. Moreover, bacteria themselves were shown capable to reduce the PEDOT (**Figure 1B**). This work is the first demonstration of a bidirectional mode of redox control, where an intimate interplay between bacteria and the electroactive material defines the bacterial physiology based on the availability of electron acceptors in the PEDOT.

In a similar study, the electrochromic properties of a graphene-PEDOT composite were used to observe electron transfer from *Pseudomonas aeruginosa* (*P. aeruginosa*) to the material (Webb et al., 2015). High conductivity graphene-PEDOT composites are ideal to observe electron transfer occurring between bacteria and substrate, owing to their robust mechanical and enhanced electrocatalytic properties. The color of graphene-PEDOT composite films exposed for 2 weeks to *P. aeruginosa* appeared darker and showed a significant increase in sheet resistance compared to control surfaces. The reduction of the graphene–PEDOT was likely due to the exposure to bacteria. A simple sensor for detection of bacteria on or near the substrate was proposed based on the monitoring of electrical resistance and/or optical absorbance of the graphene–PEDOT.

The mechanism of PEDOT redox control was used for creating a high-throughput, rapid, and highly sensitive test array to evaluate the electrogenic properties of newly discovered and/or genetically engineered bacterial species (Gao et al., 2017). By applying a recent method for co-fabrication of electrofluidic structures on paper (Hamedi et al., 2016), Gao et al. integrated a three-dimensional microbial fuel cell (MFC) device within paper. PEDOT:PSS conductive ink patterned on paper was used as anode reservoir, which was separated from a metal cathode by a wax membrane that allowed for ion exchange. An 8-channel MFC array was fabricated to assay the electrogenicity of wild type *P. aeruginosa* and isogenic strains with mutations in metabolic and signaling pathways as well as in surface structures expected to affect the electrochemical activity of the bacterial cells. Generally, minor differences were detected between the wild type and mutant strains. A hyperpiliated *pilT* mutant, known to show increased cell-to-cell and cell-to-surface adhesion, exhibited increased electrogenicity (Chiang and Burrows, 2003). In contrast, a deletion in the *pmpR* gene, known to inhibit the type III secretion system, generated less current than the wild type (Liang et al., 2012). Collectively, this work presents an important milestone toward redox-based sensing of bacteria using conducting polymers.

Detection of Bacteria by Cellular Imprinting in Conjugated Polymer Surface

Introduction of recognition sites to the transducer matrix in a biosensor allows for sensitive and specific sensor operation. The most relevant biological recognition elements are protein and DNA receptors. Physical recognition by size and shape is based on the creation of an analyte-shaped mold in the transduction matrix, a technique referred to as molecular imprinting. The technique allows rapid formation of cavities forming receptors for various targets (Haupt et al., 2012). A variety of molecular imprinting applications using conducting polymers have been presented (Hayden et al., 2006; Schillinger et al., 2012; Canfarotta et al., 2018; Parlak et al., 2018).

One example demonstrates a bacterial biosensing application, where a cell-imprinting technique has been used to generate specific binding sites for bacteria, thereby enabling their detection and differentiation (**Figure 1C**) (Shan et al., 2017). This involves the detection of *Escherichia coli* (*E.coli*) strain O157:H7 in aqueous medium. Cell-imprinted microspheres were fabricated based on a gold-coated plastic microbead core (5 nm) and a polymer complex shell. The beads were pre-treated by depositing a self-assembled aminothiophenol monolayer and coating with Nafion through electrostatic interactions. Finally, in the presence of bacterial cells, Polypyrrole (PPy) was deposited on the pre-treated surface by chemical oxidation. This generated microspheres with bacterial cells entrapped in a conjugated polymer matrix. To remove the bacterial cells and expose bacilli-like surfaces complementary to *E. coli*, the microspheres were treated with 0.1 M NaOH, which also overoxidized PPy through curing and de-doping. When *E. coli* O157:H7 subsequently were incubated with the microspheres, bacterial cells were found specifically captured in the complementary cavities. When other strains were tested, such as *E. coli* O157:HNM, *E. coli* O26:H11, *E. coli* O26:HNM, *E. coli* O rough as well as *P. aeruginosa*, *Serratia marcescens*, and *Acinetobacter calcoaceticus*, the cross-reactivity of the cell-imprinted microspheres was lower than 10%. The specificity of the imprinted material likely arises from multiple interactions with chemical groups in the cavity as well as from shape and size complementarity to the imprinted bacterial cell. The same basic technique was later used to fabricate cell-imprinted microplates used as biorecognition elements in an ELISA detection assay (Shan et al., 2018). The assay showed high selectivity and sensitivity for the imprinted bacterial cells, demonstrating that CPs as cell-imprinted matrices can complement or even replace biological receptors as superior recognition elements in biosensor applications.

BACTERIAL SENSING USING CP VESICLES

The CP polydiacetylene (PDA) has a lipid-like amphiphilic structure. The hydrophobic tail and hydrophilic head group drive self-assembly into sheets or vesicles in aqueous solution (**Figure 2A**). When aligned, adjacent molecules can be crosslinked using UV irradiation (254 nm), thereby generating a robust polymerized structure. The polymerized, conjugated framework shows increased absorption at 650 nm, appearing as deep blue color. Perturbations of the conjugated framework and conformational changes of the polymeric backbone cause a typical blue to red color transition. Environmental stimuli such as pH, temperature, and pressure, are known to induce such perturbations as well as analytes binding to recognition elements embedded in the vesicle structure (Kaganove et al., 2005; Kim et al., 2012). As the colorimetric transition initiated by analyte binding is visible with the naked eye, rapid sensing platforms can be created based on the PDA liposomes.

The PDA liposome system has been used to detect and differentiate *E. coli* O26:B6, *P. aeruginosa*, *Salmonella Enteritidis*, and *Salmonella Minessota* based on the specific lipopolysaccharide (LPS) expressed by each strain (Rangin and Basu, 2004). LPS are complex glycolipids anchored within the outer membrane of gram-negative bacteria by the lipidated disaccharide Lipid A. Attached to Lipid A is a core oligosaccharide fragment, which extends the serotype-specific polysaccharide called O-antigen. When carbohydrate binding proteins make contact with sugars, it frequently occurs via tryptophan and tyrosine residues (Weis and Drickamer, 1996). These residues were therefore added as anchors on the PDA liposomes through functionalization of the hydrophilic headgroup. The functionalized PDA liposomes were then self-assembled and crosslinked. Upon exposure of the functionalized PDA liposomes to bacterial LPS, a visible color change from blue to red was observed, consistent

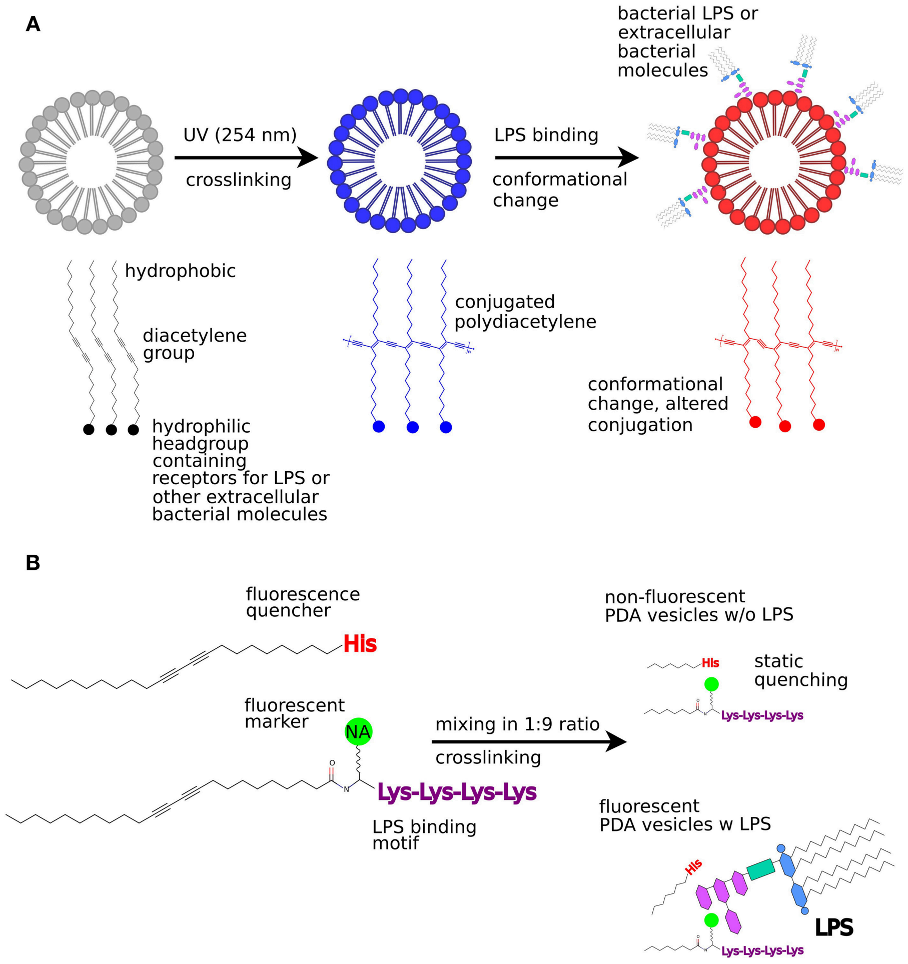

FIGURE 2 | Bacterial sensing using PDA vesicles. **(A)** Colorimetric sensing utilizing absorption change due to conformational change in PDA structures when bacterial LPS binds to the PDA vesicle. **(B)** Fluorescence turn-on sensor for bacterial LPS. This figure was partly reproduced from Kim et al. (2012), licenced under CC BY 3.0 (http://creativecommons.org/licenses/by/3.0/).

with an increase in absorbance at 550 nm. Using a similar approach, PDA liposomes were functionalized with dioctadecyl glyceryl ether-β-glucosides (DGG) as anchor molecules, which enabled detection of *E. coli* observed by a change in peak absorbance from 650 nm (blue) to 550 nm (red) (Ma et al., 1998).

In a different approach, PDA liposomes were used for bacterial detection by means of their secreted compounds. Surfactin is a cyclic lipopeptide that is secreted from gram-positive spore-forming *Bacillus subtilis* (*B. subtilis*) as a natural antibiotic. An amine-functionalized PDA liposome was generated and added to the Luria Bertani (LB) growth medium in agar plates. When comparing the growth of a *B. subtilis* surfactin-producing strain (NCIB3610) to a non-producing strain (SSB466) on the PDA-LB-agar, different phenotypes were clearly distinguished as the color changed from blue to red, in correspondence to an absorbance shift from 645 to 550 nm (Park et al., 2016).

Interestingly, peptide-functionalized PDA liposomes can also act as a fluorescent turn-on sensor for bacterial LPS (Wu et al., 2011). In this approach, the naturally occurring LPS-binding antibiotic polymyxin B (PMB) was used as a template to synthesize an LPS-binding anchor molecule. To mimic the LPS-binding region of PMB, an amphiphilic PDA lipid was synthesized that carried a pentalysine oligopeptide as headgroup, with a naphthalic acid fluorophore linked to the N-terminal lysine. On another amphiphilic PDA lipid, a single histidine residue was added as headgroup. Both amphiphiles were mixed, self-assembled into liposomes and crosslinked so that the histidine group of one component quenched the naphthalic acid fluorescence of the other (**Figure 2B**). When LPS was added to these mixed PDA liposomes, increased fluorescence from the naphthalic acid was observed. This is most likely because the close contact between the fluorescent unit and the quencher was disrupted when the LPS interacted with exposed pentalysine residues. Despite some cross-reactivity with bovine serum albumin (BSA), these PDA liposomes were successfully used to detect *E. coli* strain DH5α as spectrophotometric recordings as well as confocal microscopy revealed an on-switch of fluorescence from the naphthalic acid.

SOLUBLE CONJUGATED POLY- AND OLIGOELECTROLYTES FOR BACTERIAL SENSING

Characteristic for CPEs are the π-conjugated backbone and ionic pendant groups, which enable electrostatic interaction with oppositely charged counterions and effectively create a conjugated polyelectrolyte. The π-conjugated backbone enables excitation of electrons from the highest occupied molecule orbital (HOMO) in the π-band to the lowest unoccupied molecule orbital (LUMO) in the π* band. Energy in the range of the UV-vis spectrum is required for π-π* transitions. After excitation, electrons relax via rapid emission as photons give rise to fluorescence, or non-radiative decay via heat or energy transfer to acceptors. Thus, conjugated systems have interesting optical properties that can be interpreted using UV-vis spectroscopy. The ionic side chains confer water solubility and the charged pendant groups allow formation of electrostatic interactions with oppositely charged macromolecules (Mcquade et al., 2000).

The number of repeating units in the backbone of CPEs is generally not well-defined. In contrast, conjugated oligoelectrolytes (COEs) contain chemically defined structures as well as a defined number of repeat units. This makes COEs more versatile, reliable, and selective compared to their polymeric counterparts. The conjugated backbone and hydrophilic-charged side chains can easily be modified to tune the optoelectronic properties. Batch variability is minimized due to the defined structure and the limited number of repeat units creates weaker interactions between the COEs and their targets, thereby increasing specificity (Bunz, 2000; Liu and Bazan, 2004).

Detection of Bacteria Based on Fluorescence Quenching in COE Complexes

Fluorescence quenching can lead to formation of a non-fluorescent complex between the COE and a quencher molecule (static quenching) or to exchange of resonance energy between a donor and acceptor molecule (dynamic quenching). The most common dynamic quenching mechanism is Förster Resonance Energy Transfer (FRET) in which the donor fluorophore transmits energy to the acceptor fluorophore without coming into direct contact. This process is extremely dependent on the donor-acceptor distance, which can be used to detect changes in the distance between them. This allows FRET to be used for detection of the presence of an analyte based on its interaction with a COE complex.

A bacterial detection system based on static quenching was demonstrated using cationic Au nanoparticles (NPs) and the anionic conjugated polymer poly(para-phenyleneethynylene) (PPE) featuring a branched oligo(ethyleneglycol) side chain (Phillips et al., 2008). Free PPE is excited at 400 nm and exhibits maximum emission at 463 nm. When the anionic PPE is complexed with cationic ammonium-functionalized Au-NPs, PPE fluorescence is quenched by the formation of supramolecular complexes (**Figure 3A**). Three different Au-NPs were used exhibiting various hydrophobic anchors close to the ammonium moiety. When the PPE/Au-NP complexes were exposed to bacteria, PPE fluorescence was recovered, indicating that functionalized Au-NPs interact with the bacterial surface (**Figure 3B**). Exposure of the PPE/Au-NP complexes to a total of 12 different gram-positive, gram-negative, and spore-forming bacteria induced distinct fluorescence changes for each bacterial strain. This indicated that differentiation in the fluorophore displacement could be applied for bacterial identification. Analyzing the fluorescence recovery for each of the three PPE/Au-NP complexes with each bacterial strain, a unique interaction pattern was established. As a dedicated machine-learning algorithm was fed with learning data from all interaction patterns, bacterial identification with an accuracy of >95% was achieved in a second, double-blind experiment using unknown bacterial samples.

A method for bacterial detection based on dynamic quenching was presented using a tetracationic COE based on a fluorene phenylene fluorene (FPF) framework with hexylammonium side chains. FPF was complexed with single-stranded DNA (ssDNA) labeled with fluorescein (FAM). The FPF/ssDNA-FAM complexes were used to detect and differentiate between bacterial strains of *E. coli* K12, *E. coli* FAD-1, *Lactobacillus acidophilus*, *Rhodopseudomonas palustris* CGA009, *Sporomusa* DMG58, and *Streptococcus mutans* (Duarte et al., 2010). This bacterial sensor is based on resonance energy transfer, where FPF acts as a resonance energy donor and ssDNA-FAM as acceptor. Five different ssDNA sequences containing 20 nucleotides each were labeled with FAM at the 5' end. Mixing each ssDNA-FAM with FPF in phosphate buffer generated five different FPF/ssDNA-FAM composites. When the FPF/ssDNA-FAM composites were excited at 336 nm (Ex_{max} FPF), the optical spectrum showed a small peak at 365–480 nm characteristic for FPF emission, and a larger peak at 490–600 nm characteristic for FAM emission. The presence of these peaks indicated resonance energy transfer from the FPF donor to the FAM acceptor (**Figure 3C**). Upon mixing with a diluted bacterial culture, the intensity of the FPF peak increased, whereas the intensity of the FAM peak decreased. This suggested an increase in the average distance between the FRET donor-acceptor pair when bacteria interact with each FPF/ssDNA-FAM complex (**Figure 3D**). Next, diluted cultures of each bacterial strain were mixed with the five different FPF/ssDNA-FAM complexes, and emission spectra were recorded. Comparison of optical spectra from FPF/ssDNA-FAM in the presence vs. absence of bacteria generated a parameter δ, derived from the increase in FPF fluorescence and decrease in FAM fluorescence. As δ differed slightly for each of the five different FPF/ssDNA-FAM complexes, a consistent and distinct pattern was established for each complex interacting with each bacterial strain. To classify the interaction patterns, a discriminant analysis workflow was used, which provided a basis for bacterial identification based on FPF/ssDNA-FAM complexes. In a follow-up study using advanced data modeling (Duarte et al., 2012), the feasibility of this method was extended to discriminate not only between different bacterial strains, but also between bacteria cultured under different conditions. This

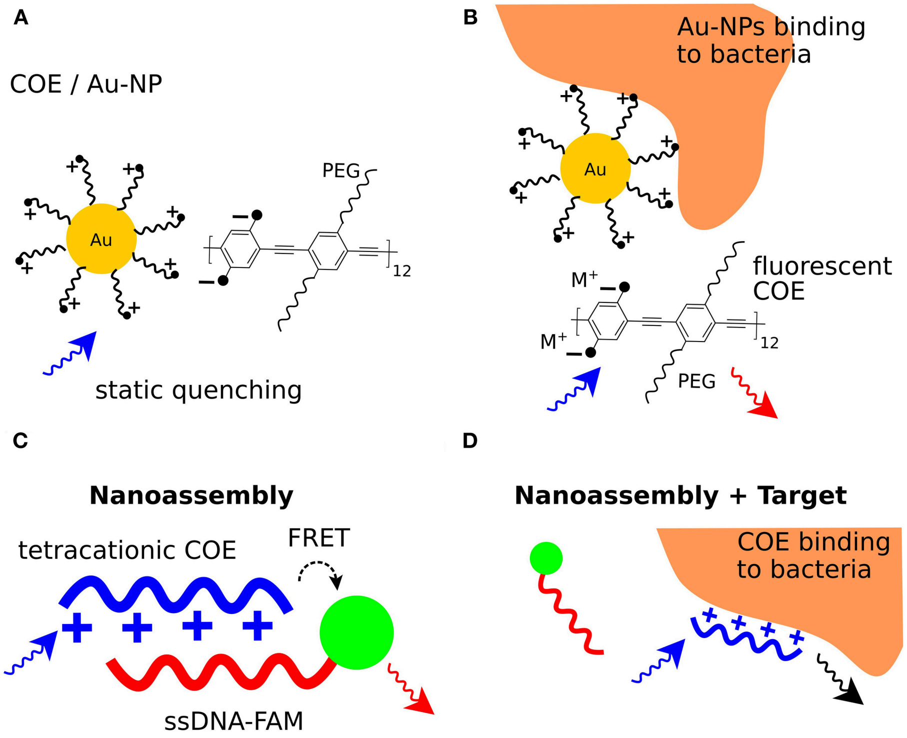

FIGURE 3 | Bacterial sensing using conjugated poly- and oligoelectrolytes. **(A)** Formation of a non-fluorescent complex between ammonium functionalized Au-NPs and the anionic COE (COE/Au-NP). **(B)** Binding of bacteria to the ammonium functionalized Au-NPs frees the fluorescent COE and leads to fluorescence emission at 463 nm. **(C)** Resonance energy transfers from a tetracationic COE donor to the FAM acceptor in a COE/ssDNA-FAM complex. Excitation of the COE leads to FAM fluorescence emission. **(D)** Interaction of bacteria with the tetracationic COE frees the ssDNA-FAM so that excitation of the COE mainly leads to COE fluorescence emission.

highly sensitive technique for bacterial differentiation represents an innovative method, equally applicable to microbiologists in the basic research, and clinical laboratories alike.

Optotracing Based on the Intrinsic Optical Characteristics of COEs for Bacterial Detection

The optoelectronic properties of COEs have shown to be excellently suited as a sensing mechanism for large analytes. The multivalent interactions that govern binding of a COE, via its conjugated backbone and/or the pendant side chains, to a range of biomacromolecules lead to a conformational change in the COEs. Since the conformation is inherently linked to the molecules optoelectronic properties, alteration of the intensity and/or wavelength of the absorbed/emitted light is induced. This conformation-dependent optical detection principle has been vividly explored for optical detection of biomacromolecules (Herrmann et al., 2015; Shirani et al., 2015; Nyström et al., 2017).

Luminescent conjugated oligothiophenes (LCO) represent a class of COEs. Their superior capability for detection of protein aggregates has been utilized for early detection of amyloids in degenerative diseases (Aslund et al., 2009; Klingstedt et al., 2011, 2013; Shirani et al., 2015) (**Figure 4A**). Upon binding to a target molecule, the flexible conjugated thiophene backbone distorts in response to non-covalent electrostatic interactions. This generates a conformation-based, target-specific spectral signature, which in contrast to conventional fluorophores exhibits ON/OFF fluorescence. Interactions with amyloid proteins characteristically lead to the flattening of the molecular backbone and a more effective conjugation. These changes can be observed as a red-shift in the fluorescence excitation as well as increased fluorescence emission intensity (**Figure 4B**).

Amyloid proteins are not only relevant in degenerative diseases, but are also produced by bacteria growing biofilm. Amyloid proteins constitute a major component of the extracellular matrix (ECM), in which bacteria embed themselves during the biofilm lifestyle. Key constituents of biofilms produced by *E. coli* and *Salmonella* are the amyloid curli protein and structural polysaccharides. The first sensing platform enabling specific reporting of the presence of biofilm was recently developed (Choong et al., 2016a). The method, termed optotracing, takes advantage of the specific optical signatures generated from heptameric LCOs when bound to curli and cellulose. A selection of isogenic strains of *S. Enteritidis* was used, whose curli and cellulose production is genetically well-defined. Bacterial strains included the wild type *Salmonella* 3934 able to produce both curli and cellulose (curli+/cellulose+), and the mutants Δ*csgA* producing cellulose but no curli

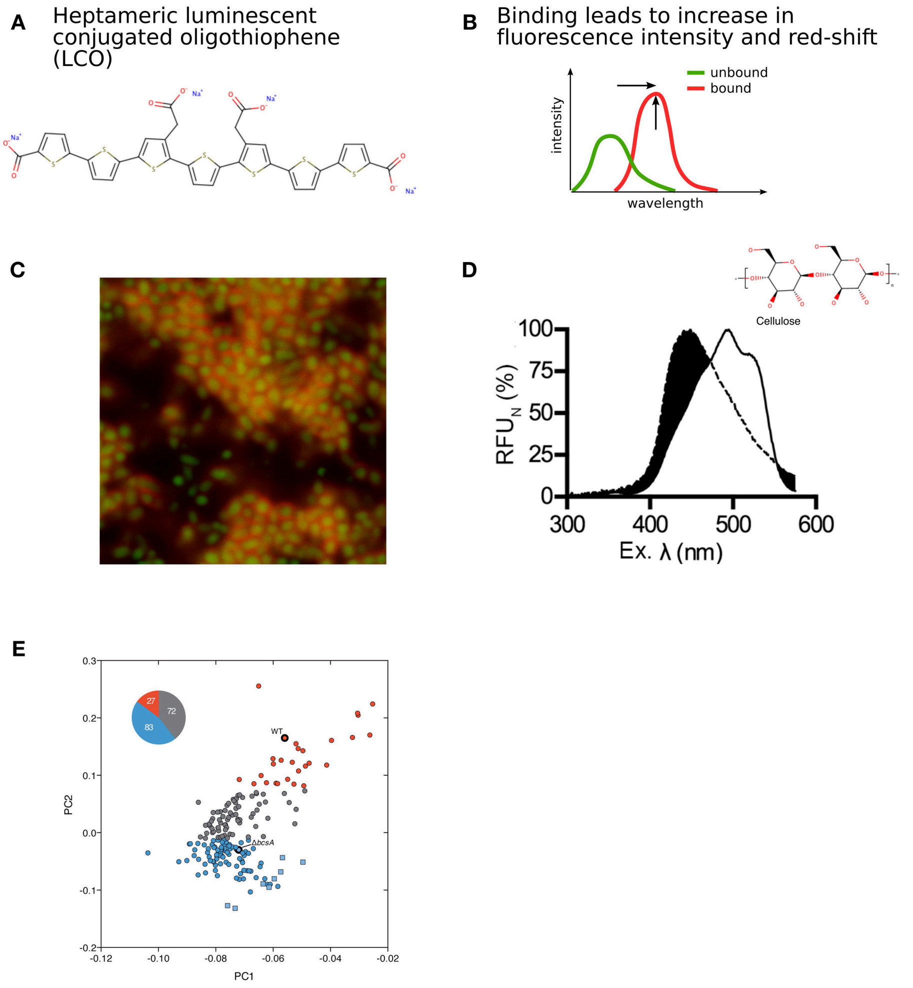

FIGURE 4 | Detection of bacterial biofilm based on modulation of intrinsic optical characteristics of LCOs. **(A)** Structure of a heptameric LCO (h-FTAA). **(B)** Changes in fluorescence intensity and red-shift of the spectrum depending on LCO backbone conformation. **(C)** Confocal imaging revealing large communities of distinct rod-shaped GFP-expressing bacteria (green) surrounded by bacterial biofilm marked by h-FTAA (red). **(D)** Characteristic optical signature of h-FTAA bound to cellulose. **(E)** PCA and k-means clustering of optical spectra from UTI and healthy urine samples screened with LCOs. This analysis identified 27 cellulose-positive (red circles) and 83 cellulose-negative (blue circles) urine samples from UTI patients, as well as 72 UTI urine samples with insufficient discriminatory performance (gray circles). Healthy urine samples (blue squares) were also differentiated from infected samples. Cellulose-positive (WT) and cellulose-negative (△bcsA) biofilm controls are also indicated. Panel **(C)** was reproduced from Choong et al. (2016a), Panel **(D)** was reproduced from Choong et al. (2018) and Panel **(E)** was reproduced from Antypas et al. (2018), licensed under CC BY 4.0 (http://creativecommons.org/licenses/by/4.0/).

(curli–/cellulose+), Δ*bcsA* producing curli but no cellulose (curli+/cellulose–), and Δ*csgD* which is unable to produce either component of the biofilm matrix (curli–/cellulose–) and therefore cannot grow biofilm. As a first step, LCOs in aqueous solution were added onto pre-formed *Salmonella* biofilm grown on glass surfaces. Confocal fluorescence microscopy revealed distinct labeling of the biofilm formed by curli and/or cellulose producing strains, thus demonstrating a novel use of the LCOs for visualization of the distinct biofilm morphology.

To widen the applicability of the method to live studies, the toxicity of LCOs was tested. No effects were observed on bacterial growth rates in liquid culture. This corroborates previous studies on eukaryotic cells and intravital mouse models, showing a non-toxic nature of the LCO family of molecules (Aslund et al., 2009). This opened for the use of LCOs as optical sensors enabling kinetic recordings of biofilm production in live bacterial cultures. To test this concept, LCOs were added directly to the culture medium. Spectrophotometric recordings of the growing culture identified one LCO, whose distinct red-shift in excitation clearly differentiated biofilm-forming and non-forming strains based on their production of curli and cellulose. Moreover, a peak appearing at 480 nm could be specifically linked to the cellulose-producing strains. By comparing the signal-structure relationships of the tested LCOs vs. the different bacterial strains, it was found that bi-directional projection of carboxylic side chains along the conjugated thiophene backbone is required for curli and cellulose detection.

Bacterial expression of the curli- and cellulose-encoding genes is under strict regulatory control. When the optotracing method was applied to liquid cultures of wild type *Salmonella*, a progressive increase of fluorescence intensity was observed around 15 h. The increase in fluorescence reflects that at this time point, bacteria have synthesized curli and cellulose, and cells are now in the process of secreting these biomacromolecules into the extracellular environment. When present in the medium, curli and cellulose become available as binding targets for the LCO, which produces biofilm-specific fluorescent signals when bound. Interestingly, the timing coincides with the time point when the bacterial culture transitions from late logarithmic to stationary phase, when a lifestyle-shift from single planktonic cells to the sessile state of biofilm occurs. This was confirmed by confocal imaging. Large communities of distinct rod-shaped GFP-expressing bacteria were observed, surrounded by dense mesh-like structures that were visualized by LCOs bound to curli and cellulose in the ECM (**Figure 4C**). The optotracing sensing platform thus provides the first method for kinetic recordings of biofilm formation under live conditions.

Sensing of cellulose in the bacterial biofilm was the first report on LCO binding to polysaccharides. In a series of follow-up studies, the molecular details of the interaction between LCO, cellulose and related glucans have been studied (Choong et al., 2016b, 2018). Using the cellulose fragments cellopentaose, celloheptaose, and cellooctaose, a minimum of 8 $\beta(1–4)$ linked glucose monomers was defined for LCO to bind and give rise to the characteristic cellulose peak at 480 nm (**Figure 4D**). This interaction provides resolution at the molecular level and discriminates cellulose from highly similar stereoisomers and other glucans. This study opens a new field in which the optotracing technology is used for determination of purity and localization of cellulose in plant and organic biomass of other origins.

The optical sensing platform for bacterial biofilms has also found clinical application, since bacterial biofilm formation is of great clinical significance (Flores-Mireles et al., 2015). Uropathogenic *E. coli* (UPEC) is the main causative agent of urinary tract infections (UTI), where biofilm is considered a main contributor to chronic and recurrent infections. Similar to *Salmonella*, the ECM of UPEC biofilms is mainly composed of cellulose and curli. This inspired Antypas et al. to investigate whether cellulose can be detected in urine by optotracing, as a diagnostic biomarker for UTI (Antypas et al., 2018). Analysis of spectra from LCOs interacting with relevant control strains showed the ability of the LCO to identify cellulose in UPEC biofilms. This was observed as a distinct spectral signature with a primary peak at 464 nm and a secondary at 484 nm. Following successful detection of cellulose in UPEC biofilm *in vitro*, optotracing was applied to urine samples from 182 patients presented with UTI and 8 healthy volunteers. A workflow was developed, where the spectral information from each sample was analyzed by principal component analysis (PCA) and k-means clustering (**Figure 4E**). This study classified 27 urine samples as positive for cellulose, providing the first, direct evidence that bacteria can form biofilm within the urinary tract and establishing that UTI can be biofilm-related. Interestingly, the method was also able to differentiate healthy from infected urine. Optotracing by LCOs thus represents the first method able to detect biofilm in clinical samples, which may be of high clinical value when selecting for optimal antibiotic treatment.

CONCLUSION

This review summarizes recent efforts in which conjugated polymers and conjugated poly-/oligoelectrolytes have been applied for detection and differentiation of bacteria, their secreted compounds as well as the different lifestyles. The variety of applications clearly demonstrates the versatility of these materials to produce simple, sensitive, and fast detection systems to monitor the presence of bacteria, also under clinical conditions. Modulation of bacterial metabolism using the redox state of electroactive surfaces is an unexplored method, which promises great potential for the development of anti-bacterial and anti-biofilm surfaces. Likewise, these materials provide the possibility to read-out bacterial electron transfer processes, which is a field that only recently has been recognized and is likely to gain in importance as extracellular electron transfer mechanisms are described for an increasing number of bacterial species. The specificity of bacterial cell-imprinted matrices made from conjugated polymers highlights how these materials can compete with DNA and antibodies as biological recognition elements, possibly leading to cheaper and more robust biosensing applications in the future. While the tunable optical properties of conjugated polymers can be applied to obtain visible optical information, conjugated oligoelectrolytes often provide extremely sensitive fluorescence readouts. As a wide variety of anchor molecules or counter ions can be used that generate slightly different patterns for each bacterial species, these systems are excellently suited to develop systems like the electronic nose or tongue for bacterial determination. With the use of advanced machine learning techniques, which are more and more easy to use and apply, these systems may also find importance in clinical settings. As the first technology to specifically detect bacterial biofilm and differentiate between different biofilm components, the optotracing technology sets a milestone for detection of sporadic and chronic infections using an optical biosensor approach. Taken together, the availability of all these technologies promises that point-of-care bacterial diagnosis and targeted antibiotic treatment will soon become a clinical reality.

AUTHOR CONTRIBUTIONS

All authors listed have made a substantial, direct and intellectual contribution to the work, and approved it for publication.

ACKNOWLEDGMENTS

We thank the Erling-Persson Family Foundation, the Swedish Foundation for Strategic Research, the Swedish Research Council as well as Getinge Group AB for financial support.

REFERENCES

Antypas, H., Choong, F. X., Libberton, B., Brauner, A., and Richter-Dahlfors, A. (2018). Rapid diagnostic assay for detection of cellulose in urine as biomarker for biofilm-related urinary tract infections. *npj Biof. Microb.* 4:26. doi: 10.1038/s41522-018-0069-y

Aslund, A., Sigurdson, C. J., Klingstedt, T., Grathwohl, S., Bolmont, T., Dickstein, D. L., et al. (2009). Novel pentameric thiophene derivatives for in vitro and in vivo optical imaging of a plethora of protein aggregates in cerebral amyloidoses. *ACS Chem. Biol.* 4, 673–684. doi: 10.1021/cb900112v

Bunz, U. H. (2000). Poly(aryleneethynylene)s: syntheses, properties, structures, and applications. *Chem. Rev.* 100, 1605–1644. doi: 10.1021/cr990257j

Bursle, E., and Robson, J. (2016). Non-culture methods for detecting infection. *Aust. Prescr.* 39, 171–175. doi: 10.18773/austprescr.2016.059

Canfarotta, F., Czulak, J., Guerreiro, A., Cruz, A. G., Piletsky, S., Bergdahl, G. E., et al. (2018). A novel capacitive sensor based on molecularly imprinted nanoparticles as recognition elements. *Biosensors Bioelectron.* 120, 108–114. doi: 10.1016/j.bios.2018.07.070

Cantón, R., and Morosini, M. I. (2011). Emergence and spread of antibiotic resistance following exposure to antibiotics. *FEMS Microbiol. Rev.* 35, 977–991. doi: 10.1111/j.1574-6976.2011.00295.x

Chiang, P., and Burrows, L. L. (2003). Biofilm Formation by hyperpiliated mutants of *Pseudomonas aeruginosa*. *J. Bacteriol.* 185, 2374–2378. doi: 10.1128/JB.185.7.2374-2378.2003

Choong, F. X., Bäck, M., Fahlén, S., Johansson, L. B., Melican, K., Rhen, M., et al. (2016a). Real-time optotracing of curli and cellulose in live Salmonella biofilms using luminescent oligothiophenes. *npj Biof. Microb.* 2:16024. doi: 10.1038/npjbiofilms.2016.24

Choong, F. X., Bäck, M., Schulz, A., Nilsson, K. P. R., Edlund, U., and Richter-Dahlfors, A. (2018). Stereochemical identification of glucans by oligothiophenes enables cellulose anatomical mapping in plant tissues. *Sci. Rep.* 8:3108. doi: 10.1038/s41598-018-21466-y

Choong, F. X., Bäck, M., Steiner, S. E., Melican, K., Nilsson, K. P., Edlund, U., et al. (2016b). Nondestructive, real-time determination and visualization of cellulose, hemicellulose and lignin by luminescent oligothiophenes. *Sci. Rep.* 6:35578. doi: 10.1038/srep35578

Duarte, A., Chworos, A., Flagan, S. F., Hanrahan, G., and Bazan, G. C. (2010). Identification of bacteria by conjugated oligoelectrolyte/single-stranded DNA electrostatic complexes. *J. Am. Chem. Soc.* 132, 12562–12564. doi: 10.1021/ja105747b

Duarte, A., Slutsky, M., Hanrahan, G., Mello, C. M., and Bazan, G. C. (2012). Supramolecular electrostatic nanoassemblies for bacterial *Forensics* 18, 756–759. doi: 10.1002/chem.201103237

Flemming, H. C., and Wingender, J. (2010). The biofilm matrix. *Nat. Rev. Microbiol.* 8, 623–633. doi: 10.1038/nrmicro2415

Flores-Mireles, A. L., Walker, J. N., Caparon, M., and Hultgren, S. J. (2015). Urinary tract infections: epidemiology, mechanisms of infection and treatment options. *Nat. Rev. Microbiol.* 13, 269–284. doi: 10.1038/nrmicro3432

Gao, Y., Hassett, D. J., and Choi, S. (2017). Rapid characterization of bacterial electrogenicity using a single-sheet paper-based electrofluidic array. *Front. Bioeng. Biotechnol.* 5:44. doi: 10.3389/fbioe.2017.00044

Gerard, M., Chaubey, A., and Malhotra, B. D. (2002). Application of conducting polymers to biosensors. *Biosensors Bioelectron.* 17, 345–359. doi: 10.1016/S0956-5663(01)00312-8

Gomez-Carretero, S., Libberton, B., Rhen, M., Richter-Dahlfors, A., et al. (2017). Redox-active conducting polymers modulate Salmonella biofilm formation by controlling availability of electron acceptors. *npj Biof. Microb.* 3:19. doi: 10.1038/s41522-017-0027-0

Hall-Stoodley, L., Costerton, J. W., and Stoodley, P. (2004). Bacterial biofilms: from the natural environment to infectious diseases. *Nat. Rev. Microbiol.* 2, 95–108. doi: 10.1038/nrmicro821

Hamedi, M. M., Campbell, V. E., Rothemund, P., Güder, F., Christodouleas, D. C., Bloch, J.-F., et al. (2016). Electrically activated paper actuators. *Adv. Funct. Mater.* 26, 2446–2453. doi: 10.1002/adfm.201505123

Haupt, K., Linares, A. V., Bompart, M., and Bui, B. T. (2012). Molecularly imprinted polymers. *Top. Curr. Chem.* 325, 1–28. doi: 10.1007/978-3-642-28421-2

Hayden, O., Lieberzeit, P. A., Blaas, D., and Dickert, F. L. (2006). Artificial antibodies for bioanalyte detection—sensing viruses and proteins. *Adv. Funct. Mater.* 16, 1269–1278. doi: 10.1002/adfm.200500626

Herland, A., Persson, K. M., Lundin, V., Fahlman, M., Berggren, M., Jager, E. W., et al. (2011). Electrochemical Control of growth factor presentation to steer neural stem cell differentiation. *Angew. Chem. Int. Ed. Engl.* 50, 12529–12533. doi: 10.1002/anie.201103728

Herrmann, U. S., Schütz, A. K., Shirani, H., Huang, D., Saban, D., Nuvolone, M., et al. (2015). Structure-based drug design identifies polythiophenes as antiprion compounds. *Sci. Transl. Med.* 7:299ra123. doi: 10.1126/scitranslmed.aab1923

Huang, A., Qiu, Z., Jin, M., Shen, Z., Chen, Z., Wang, X., et al. (2014). High-throughput detection of food-borne pathogenic bacteria using oligonucleotide microarray with quantum dots as fluorescent labels. *Int. J. Food Microbiol.* 185, 27–32. doi: 10.1016/j.ijfoodmicro.2014.05.012

Inal, S., Rivnay, J., Suiu, A. O., Malliaras, G. G., and Mcculloch, I. (2018). Conjugated polymers in bioelectronics. *Acc. Chem. Res.* 51, 1368–1376. doi: 10.1021/acs.accounts.7b00624

Ivnitski, D., Abdel-Hamid, I., Atanasov, P., and Wilkins, E. (1999). Biosensors for detection of pathogenic bacteria. *Biosensors Bioelectron.* 14, 599–624. doi: 10.1016/S0956-5663(99)00039-1

Kaganove, S. N., Dvornic, P. R., and Satoh, P. S. (2005). Colorimetric biosensors based on polydiacetylene (PDA) and polyamidoamine (PAMAM) dendrimers AU - sarkar, Abhijit. *Polym. News* 30, 370–377. doi: 10.1080/00323910500402714

Kim, Y. R., Jung, S., Ryu, H., Yoo, Y. E., Kim, S. M., and Jeon, T. J. (2012). Synthetic biomimetic membranes and their sensor applications. *Sensors* 12, 9530–9550. doi: 10.3390/s120709530

Klingstedt, T., Aslund, A., Simon, R. A., Johansson, L. B., Mason, J. J., Nyström, S., et al. (2011). Synthesis of a library of oligothiophenes and their utilization as fluorescent ligands for spectral assignment of protein aggregates. *Org. Biomol. Chem.* 9, 8356–8370. doi: 10.1039/c1ob05637a

Klingstedt, T., Shirani, H., Åslund, K. O., Cairns, N. J., Sigurdson, C. J., Goedert, M., et al. (2013). The structural basis for optimal performance of oligothiophene-based fluorescent amyloid ligands: conformational flexibility is essential for spectral assignment of a diversity of protein aggregates. *Chemistry* 19, 10179–10192. doi: 10.1002/chem.201301463

Koo, H., Allan, R. N., Howlin, R. P., Stoodley, P., and Hall-Stoodley, L. (2017). Targeting microbial biofilms: current and prospective therapeutic strategies. *Nat. Rev. Microbiol.* 15, 740–755. doi: 10.1038/nrmicro.2017.99

Larsson, K. C., Kjäll, P., and Richter-Dahlfors, A. (2013). Organic bioelectronics for electronic-to-chemical translation in modulation of neuronal signaling and machine-to-brain interfacing. *Biochim. Biophys. Acta* 1830, 4334–4344. doi: 10.1016/j.bbagen.2012.11.024

Law, J. W., Ab Mutalib, N. S., Chan, K. G., and Lee, L. H. (2014). Rapid methods for the detection of foodborne bacterial pathogens: principles, applications, advantages and limitations. *Front. Microbiol.* 5:770. doi: 10.3389/fmicb.2014.00770

Le, T.-H., Kim, Y., and Yoon, H. (2017). Electrical and electrochemical properties of conducting polymers. *Polymers* 9:150. doi: 10.3390/polym9040150

Liang, H., Kong, W., Shen, T., Duan, J., and Duan, K. J. C. S.B. (2012). The effect of pmpR on the type III secretion system in *Pseudomonas aeruginosa*. *Chinese Sci. Bull.* 57, 2413–2418. doi: 10.1007/s11434-011-4941-x

Liu, B., and Bazan, G. C. (2004). Interpolyelectrolyte complexes of conjugated copolymers and DNA: platforms for multicolor biosensors. *J. Am. Chem. Soc.* 126, 1942–1943. doi: 10.1021/ja038667j

Löffler, S., Libberton, B., and Richter-Dahlfors, A. (2015a). Organic bioelectronic tools for biomedical applications. *Electronics* 4, 879–908. doi: 10.3390/electronics4040879

Löffler, S., Libberton, B., and Richter-Dahlfors, A. (2015b). Organic bioelectronics in infection. *J. Mater. Chem. B* 3, 4979–4992. doi: 10.1039/C5TB00382B

Ma, Z., Li, J., Liu, M., Cao, J., Zou, Z., Tu, J., et al. (1998). Colorimetric detection of *Escherichia coli* by polydiacetylene vesicles functionalized with glycolipid. *J. Am. Chem. Soc.* 120, 12678–12679. doi: 10.1021/ja982663a

Mcquade, D. T., Pullen, A. E., and Swager, T. M. (2000). Conjugated polymer-based chemical sensors. *Chem. Rev.* 100, 2537–2574. doi: 10.1021/cr9801014

Min, J., and Baeumner, A. J. (2002). Highly sensitive and specific detection of viable *Escherichia coli* in drinking water. *Anal. Biochem.* 303, 186–193. doi: 10.1006/abio.2002.5593

Mollasalehi, H., and Yazdanparast, R. (2013). Development and evaluation of a novel nucleic acid sequence-based amplification method using one specific primer and one degenerate primer for simultaneous detection of *Salmonella Enteritidis* and *Salmonella Typhimurium*. *Anal. Chim. Acta* 770, 169–174. doi: 10.1016/j.aca.2013.01.053

Nyström, S., Bäck, M., Nilsson, K. P. R., and Hammarström, P. (2017). Imaging amyloid tissues stained with luminescent conjugated oligothiophenes by hyperspectral confocal microscopy and fluorescence lifetime imaging. *J. Vis. Exp.* e56279. doi: 10.3791/56279

O'Neill, J. (2016). *Tackling Drug-Resistant Infections Globally: Final Report and Recommendations.* (amr-review.org/sites/default/files/160518_Final paper_with cover.pdf: The Review on Antimicrobial Resistance).

Park, J., Ku, S. K., Seo, D., Hur, K., Jeon, H., Shvartsman, D., et al. (2016). Label-free bacterial detection using polydiacetylene liposomes. *Chem. Commun.* 52, 10346–10349. doi: 10.1039/C6CC03116A

Parlak, O., Keene, S. T., Marais, A., Curto, V. F., and Salleo, A. (2018). Molecularly selective nanoporous membrane-based wearable organic electrochemical device for noninvasive cortisol sensing. *Sci. Adv.* 4:eaar2904. doi: 10.1126/sciadv.aar2904

Phillips, P. L., and Schultz, G. S. (2012). Molecular mechanisms of biofilm infection: biofilm virulence factors. *Adv. Wound Care* 1, 109–114. doi: 10.1089/wound.2011.0301

Phillips, R. L., Miranda, O. R., You, C. C., Rotello, V. M., and Bunz, U. H. (2008). Rapid and efficient identification of bacteria using gold-nanoparticle-poly(para-phenyleneethynylene) constructs. *Angew. Chem. Int. Ed. Engl.* 47, 2590–2594. doi: 10.1002/anie.200703369

Rangin, M., and Basu, A. (2004). Lipopolysaccharide identification with functionalized polydiacetylene liposome sensors. *J. Am. Chem. Soc.* 126, 5038–5039. doi: 10.1021/ja039822x

Schillinger, E., Möder, M., Olsson, G. D., Nicholls, I. A., and Sellergren, B. (2012). An artificial estrogen receptor through combinatorial imprinting. *Chemistry* 18, 14773–14783. doi: 10.1002/chem.201201428

Shah, S. A. A., Firlak, M., Berrow, S. R., Halcovitch, N. R., Baldock, S. J., Yousafzai, B. M., et al. (2018). Electrochemically enhanced drug delivery using polypyrrole films. *Materials* 11:E1123. doi: 10.3390/ma11071123

Shan, X., Yamauchi, T., Yamamoto, Y., Niyomdecha, S., Ishiki, K., Le, D. Q., et al. (2017). Spontaneous and specific binding of enterohemorrhagic *Escherichia coli* to overoxidized polypyrrole-coated microspheres. *Chem. Commun.* 53, 3890–3893. doi: 10.1039/C7CC00244K

Shan, X., Yamauchi, T., Yamamoto, Y., Shiigi, H., and Nagaoka, T. (2018). A rapid and specific bacterial detection method based on cell-imprinted microplates. *Analyst* 143, 1568–1574. doi: 10.1039/C7AN02057K

Shirani, H., Linares, M., Sigurdson, C. J., Lindgren, M., Norman, P., and Nilsson, K. P. (2015). A palette of fluorescent thiophene-based ligands for the identification of protein aggregates. *Chemistry* 21, 15133–15137. doi: 10.1002/chem.201502999

Simon, D. T., Larsson, K. C., Nilsson, D., Burström, G., Galter, D., Berggren, M., et al. (2015). An organic electronic biomimetic neuron enables auto-regulated neuromodulation. *Biosensors Bioelectron.* 71, 359–364. doi: 10.1016/j.bios.2015.04.058

Svennersten, K., Berggren, M., Richter-Dahlfors, A., and Jager, E. W. (2011). Mechanical stimulation of epithelial cells using polypyrrole microactuators. *Lab. Chip* 11, 3287–3293. doi: 10.1039/c1lc20436j

Svennersten, K., Bolin, M. H., Jager, E. W., Berggren, M., and Richter-Dahlfors, A. (2009). Electrochemical modulation of epithelia formation using conducting polymers. *Biomaterials* 30, 6257–6264. doi: 10.1016/j.biomaterials.2009.07.059

Wang, D., Gong, X., Heeger, P. S., Rininsland, F., Bazan, G. C., and Heeger, A. J. (2002). Biosensors from conjugated polyelectrolyte complexes. *Proc. Natl. Acad. Sci. U.S.A.* 99, 49–53. doi: 10.1073/pnas.012581399

Webb, H. K., Notley, S. M., and Evans, D. R. (2015). Observation of electron transfer between bacteria and high conductivity graphene–PEDOT composites. *RSC Adv.* 5, 45642–45645. doi: 10.1039/C5RA08720A

Wei, D., Oyarzabal, O. A., Huang, T. S., Balasubramanian, S., Sista, S., and Simonian, A. L. (2007). Development of a surface plasmon resonance biosensor for the identification of *Campylobacter jejuni*. *J. Microbiol. Methods* 69, 78–85. doi: 10.1016/j.mimet.2006.12.002

Weis, W. I., and Drickamer, K. (1996). Structural basis of lectin-carbohydrate recognition. *Annu. Rev. Biochem.* 65, 441–473. doi: 10.1146/annurev.bi.65.070196.002301

Wu, J., Zawistowski, A., Ehrmann, M., Yi, T., and Schmuck, C. (2011). Peptide functionalized polydiacetylene liposomes act as a fluorescent turn-on sensor for bacterial lipopolysaccharide. *J. Am. Chem. Soc.* 133, 9720–9723. doi: 10.1021/ja204013u

Conflict of Interest Statement: All authors are co-inventors of patents (granted and pending) relevant to this work. Intellectual properties are owned by Richter Life Science Development AB founded by AR-D. SL, FC, and KPRN are shareholders of Furcifer AB.

frontiers in Chemistry

ORIGINAL RESEARCH
published: 26 April 2019
doi: 10.3389/fchem.2019.00281

Organic Electrochemical Transistors/SERS-Active Hybrid Biosensors Featuring Gold Nanoparticles Immobilized on Thiol-Functionalized PEDOT Films

Jia-An Chou [1]†, Chieh-Lin Chung [1]†, Po-Cheng Ho [1,2]†, Chun-Hao Luo [2], Yu-Han Tsai [2], Chung-Kuan Wu [3], Chiung-Wen Kuo [4], Yu-Sheng Hsiao [1], Hsiao-hua Yu [2]* and Peilin Chen [4]**

[1] Department of Materials Engineering, Ming Chi University of Technology, New Taipei City, Taiwan, [2] Institute of Chemistry, Academia Sinica, Taipei, Taiwan, [3] Division of Nephrology, Department of Internal Medicine, Shin-Kong Wu Ho-Su Memorial Hospital, Taipei, Taiwan, [4] Research Center for Applied Sciences, Academia Sinica, Taipei, Taiwan

Edited by:
Carlo Augusto Bortolotti,
University of Modena and Reggio Emilia, Italy

Reviewed by:
Basem Moosa,
KAUST Catalysis Center (KCC), Saudi Arabia
Mindy Levine,
University of Rhode Island, United States

***Correspondence:**
Yu-Sheng Hsiao
yshsiao@mail.mcut.edu.tw
Hsiao-hua Yu
bruceyu@gate.sinica.edu.tw
Peilin Chen
peilin@gate.sinica.edu.tw

† These authors have contributed equally to this work

Specialty section:
This article was submitted to Organic Chemistry, a section of the journal Frontiers in Chemistry

Received: 27 December 2018
Accepted: 05 April 2019
Published: 26 April 2019

Citation:
Chou J-A, Chung C-L, Ho P-C, Luo C-H, Tsai Y-H, Wu C-K, Kuo C-W, Hsiao Y-S, Yu H and Chen P (2019) Organic Electrochemical Transistors/SERS-Active Hybrid Biosensors Featuring Gold Nanoparticles Immobilized on Thiol-Functionalized PEDOT Films. Front. Chem. 7:281. doi: 10.3389/fchem.2019.00281

In this study we immobilized gold nanoparticles (AuNPs) onto thiol-functionalized poly(3,4-ethylenedioxythiophene) (PEDOT) films as bioelectronic interfaces (BEIs) to be integrated into organic electrochemical transistors (OECTs) for effective detection of dopamine (DA) and also as surface-enhanced Raman scattering (SERS)—active substrates for the selective detection of *p*-cresol (PC) in the presence of multiple interferers. This novel PEDOT-based BEI device platform combined (i) an underlying layer of polystyrenesulfonate-doped PEDOT (PEDOT:PSS), which greatly enhanced the transconductance and sensitivity of OECTs for electrochemical sensing of DA in the presence of other ascorbic acid and uric acid metabolites, as well as amperometric response toward DA with a detection limit (S/N = 3) of 37 nM in the linear range from 50 nM to 100 μM; with (ii) a top interfacial layer of AuNP-immobilized three-dimensional (3D) thiol-functionalized PEDOT, which not only improved the performance of OECTs for detecting DA, due to the signal amplification effect of the AuNPs with high catalytic activity, but also enabled downstream analysis (SERS detection) of PC on the same chip. We demonstrate that PEDOT-based 3D OECT devices decorated with a high-density of AuNPs can display new versatility for the design of next-generation biosensors for point-of-care diagnostics.

Keywords: gold nanoparticles, poly(3, 4-ethylenedioxythiophene), bioelectronic interfaces, organic electrochemical transistors, surface-enhanced Raman scattering

INTRODUCTION

Dopamine (DA), a neurotransmitter, plays important physiological roles in movement, motivation, memory, and other functions. Dysfunction of dopaminergic neurons is associated with, for example, Parkinson's disease, Alzheimer's disease, bipolar disorder, and restless leg syndrome (Coyle et al., 1983; Paulus and Trenkwalder, 2006; Ziemssen and Reichmann, 2007). Moreover, determining the levels of DA in biological systems can provide valuable information for the diagnosis, treatment, and prognosis of these neurological diseases. *p*-Cresol (PC), which is highly conjugated with proteins, is a product of the intestinal bacterium metabolism of tyrosine and phenylalanine and can be excreted by the kidneys. Serum PC levels are correlated with chronic kidney disease and uremic symptoms (Bammens et al., 2003, 2006). In addition, serum PC levels also correlate with the prognosis of cardiovascular diseases. Therefore, the detection of serum PC can influence disease treatment and prevention. Furthermore, PC can inhibit dopamine-β-hydroxylase (DBH), which converts DA to norepinephrine, a small-molecule neurotransmitter. The presence of PC in the central nervous system can lead to excesses of DA and its metabolites, which are possibly associated with neurological disorders. Nevertheless, the effects of DA and PC in most diseases remain unclear, especially in neurological disorders and their presentation in chronic kidney disease. Therefore, a challenge remains to develop methods for the rapid, sensitive, and selective detection of DA and PC in biological samples, thereby enabling assessments, during routine clinical diagnoses, of the complex relationships among the expression levels of secretions, the effects of uremic toxins, and the neurological disorders.

In addition to high-performance liquid chromatography (HPLC) method, several promising analytical assays exhibiting high sensitivity and selectivity have been developed for the detection of DA and PC (Yoshitake et al., 2006; Zhou et al., 2013; Ferry et al., 2014; Pandikumar et al., 2014; Mercante et al., 2015; Yusoff et al., 2015; Sajid et al., 2016). For example, the fluorescence method, the surface-enhanced Raman scattering (SERS) detection assay, passive component measurement methods (based on electrochemical electrodes), and active component measurement methods (based on field effect transistors) have been explored widely for biosensing in the presence of ascorbic acid (AA) and uric acid (UA) metabolites. In particular, poly(3,4-ethylenedioxythiophene):polystyrenesulfonate (PEDOT:PSS)—based organic electrochemical transistors (OECTs) have recently attracted attention for their high electrochemical identification capabilities, easy operation (driven at voltages below 1 V), low cost (prepared using vacuum-free fabrication processes), and stable performance (operated under aqueous conditions) (Tang et al., 2011; Gualandi et al., 2016, 2018; Wang et al., 2018a). In addition, SERS-active substrates have been investigated thoroughly for their tremendous potential to detect complex biomaterials, due to their high chemical identification capabilities, high sensitivity, low cost, ready implementation, and less time consuming operation. Nevertheless, we are unaware of any previous reports of OECT/SERS hybrid biosensors designed specifically for investigations of the correlations between DA and PC in biological samples, although such device concepts would presumably be viable alternatives to other sensing platforms.

In the last decade, nanoparticles (NPs) have been exploited widely in electrochemical sensors to enlarge their surface areas, promote catalyzed electrochemical reactions, and enhance electron transfer at their electrode–electrolyte interfaces (Kim et al., 2010; Huang et al., 2014; Ali et al., 2018). Gold nanoparticles (AuNPs) are particularly attractive nanomaterials for electrochemical biosensing because of their efficient signal amplification, good stability, and outstanding biocompatibility in electrolyte solutions. Although AuNPs can ensure SERS detection with improved signal reproducibility and lower toxicity, AuNP-based SERS-active substrates have lower enhancement factors (EFs) than do those incorporating silver nanoparticles (AgNPs) (Ou et al., 2014; Chiang et al., 2017). To reverse the gap between the SERS signals of AuNP- and AgNP-active substrates, electromagnetic hot spots can be further created through well-controlled AuNP aggregation, resulting in greater EFs from SERS-active substrates (Guerrini and Graham, 2012; Ou et al., 2014; Yang et al., 2016; Chiang et al., 2017). The efficiency of the hot spots of SERS-active substrates can be modulated through variation of the sizes of the AuNPs and the compositions of their colloidal solutions. Nevertheless, manipulation of the uniform aggregation of AuNPs over large areas remains a key challenge when creating hot spots on SERS-active substrates (Shiohara et al., 2014). In fact, three-dimensional (3D) SERS-active substrates have recently be found to create high-density hot spots under laser illumination; because they possess large specific surface areas for the immobilization of more AuNPs and the absorption of more target analytes, such systems might solve the problem of intrinsically weak Raman signals (Lee et al., 2012; Liu et al., 2014; Chiang et al., 2017).

In this present study, we prepared an integrated 3D-OECT device featuring a AuNP-immobilized bilayer PEDOT film as the active channel; we fabricated it from a high-conductivity PEDOT:PSS underlying layer and a nanostructured thiol-functionalized PEDOT upper layer presenting AuNPs on top. We have used these OECTs for the effective detection of DA and for the preparation of SERS-active substrates for the selective detection of PC in the presence of multiple metabolites. To the best of our knowledge, this paper is the first to demonstrate OECT/SERS hybrid biosensors for the efficient detection of DA (using OECTs) with the additional capability of sensing PC (using SERS spectroscopy).

MATERIALS AND METHODS

Chemicals and Materials

Hydroxymethyl EDOT (EDOT-OH, 95%), sodium hydride (NaH, 60% dispersion in mineral oil), trityl chloride (97%), magnesium sulfate ($MgSO_4$), potassium carbonate (K_2CO_3), triphenylphosphine (PPh_3), Amberlite IR-120 resin, sodium methoxide (NaOMe), iron(III) *p*-toluenesulfonate hexahydrate (technical grade), imidazole (IM, 99%), dimethyl sulfoxide (DMSO), (3-glycidoxypropyl)trimethoxysilane (GOPS, $\geq$98%), hydrogen tetrachloroaurate(III) hydrate ($HAuCl_4$), trisodium citrate dihydrate (TSC, 99%), DA, AA, UA, and PC were purchased from Sigma–Aldrich. The aqueous PEDOT:PSS solution (Clevios PH1000, PEDOT:PSS ratio = 1:2.5) was purchased from Heraeus with a solid concentration 1.0–1.3 wt%. Tetrahydrofuran (THF), ethyl acetate (EA), hexane, acetone, carbon tetrabromide (CBr_4), potassium thioacetate (KSAc), hydrochloric acid (HCl, 37%), and nitric acid (HNO_3, 70%) were purchased from Acros Organics. All materials and reagents were used as received without further purification. The aqueous solutions were prepared with deionized (DI) water from a Millipore Milli-Q water treatment system (18.2 MΩ cm^{-1}).

AuNPs

Briefly, the citrate-capped AuNPs were synthesized using trisodium citrate dehydrate (TSC) and a modified version of a method reported previously (Hsiao et al., 2012). To ensure that no other metal ions were present during the synthesis of the AuNPs, all glassware and magnetic stir bars were cleaned with freshly prepared aqua regia (3:1 HCl:HNO_3, vol/vol), washed with copious amounts of DI water, and dried prior to use. The synthesis was performed as follows: (1) individual aqueous solutions of 0.5 wt % $HAuCl_4$, 1 wt % TSC, and 0.1 wt % $AgNO_3$ were stored at 4°C for at least 30 min; (2) the $HAuCl_4$ (2 mL) and $AgNO_3$ (85 µL) solutions were mixed, and then the TSC solution (1.8 mL) was added; (3) this mixed solution was further diluted with DI water to a total volume of 5 mL, and then boiling deionized (DI) water (95 mL) was added into the 250-mL two-neck flask under stirring.

OECTs

Device Fabrication

The single-layer of PEDOT:PSS (with the GOPS crosslinker) and thiol-functionalized PEDOT films were individually prepared as the active layer channel materials, and denoted as **P** and **P-SH** films, respectively; the bi-layer conducting polymer film, including **P** as underlying layer and **P-SH** as top interfacial layer, was prepared as the active layer channel materials, and denoted as **PP-SH** film. The spin coating parameters were (5000 rpm, 60 s), (2000 rpm, 60 s), and (800 rpm, 180 s) for obtaining three different thicknesses (100, 200, and 400 nm, respectively) of **P** thin films; **P-SH** thin films at a thickness of approximately 90 nm were prepared by the chemical oxidative polymerization process (see **Supplementary Material** for detail preparation). The active layer channel of the OECTs [width (W): 1.5 mm; length (L): 5 mm] was first prepared through a sequence of coating processes (**Figures 1a–c**) and then by patterning **P** and **PP-SH** films using a commercial CO_2 laser engraving system (Universal VLS2.30, Universal laser System, AZ, USA) with high-power density focusing optics (HPDFO). The device assembled from the **PP-SH**–based OECT featured a cylindrical PDMS chamber (volume: ca. 50 µL) that was used to confine the channel area of the OECT device. To prepare the OECT/SERS hybrid biosensors, the device was treated with the as-prepared aqueous AuNP solution [optical density (OD) = 0.4; 150 µL] for at least 6 h, and then washed with DI water thoroughly (five times) to remove any non-immobilized AuNPs. The resulting OECT (**AuNPs@PP-SH**) was a ready-to-use system for the detection of analytes by measuring the electrical signals and SERS spectra (see **Figures 1c–f**).

Materials and Device Characterization

Details of the characterization of the materials are provided in the Supporting Information. For three-terminal OECT electrical measurements, the integrated measurement system consisted of two source meters (Keysight B1500A and Agilent B2912A) and a switching matrix (Agilent E5250A), controlled by a personal

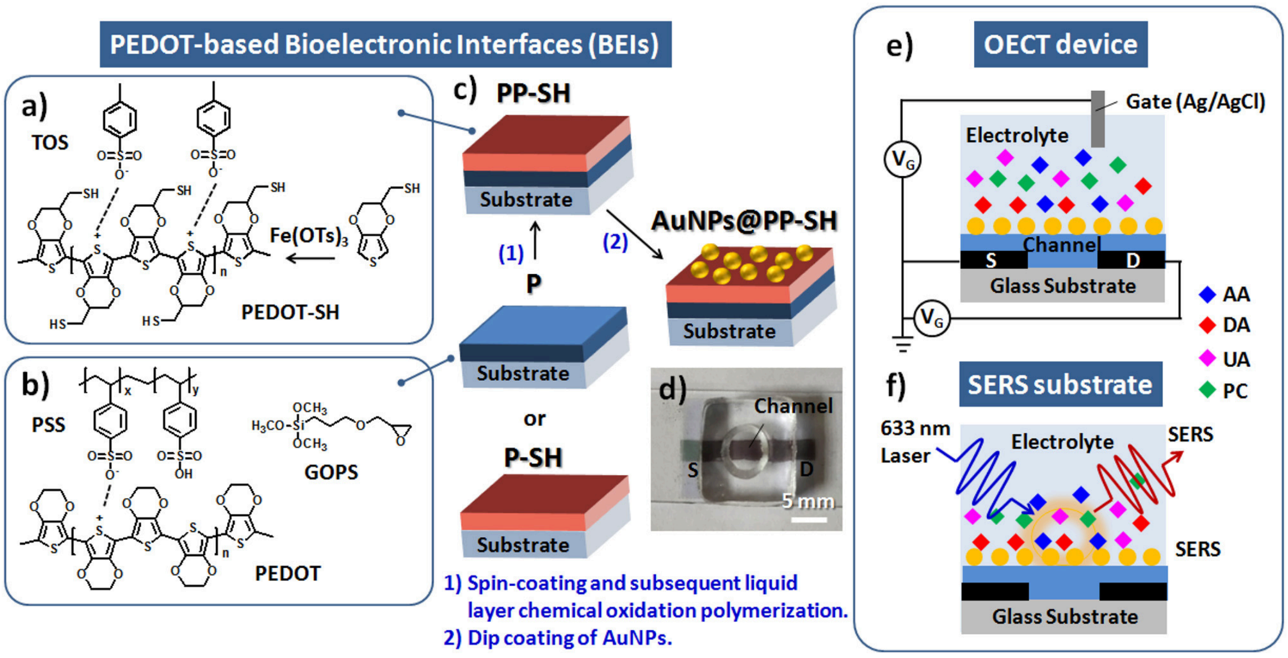

FIGURE 1 | (a) Chemical oxidative polymerization of EDOT-SH monomers by $Fe(OTs)_3$ for the fabrication of **P-SH** films. **(b)** Chemical structures in the PEDOT:PSS solution with the GOPS crosslinker for the fabrication of **P** films. **(c)** Schematic representation of four different architectures of PEDOT films (**P**, **P-SH**, **PP-SH**, **AuNPs@PP-SH**) as BEIs. **(d)** Photograph of a **AuNPs@PP-SH**–based OECT/SERS hybrid biosensor featuring a cylindrical PDMS chamber. **(e,f)** Schematic representation of a PEDOT-based OECT/SERS hybrid biosensor for OECT sensing of DA and SERS detection of PC.

computer through customized LabVIEW software; the electrical signals of as-prepared OECT device were measured in 1× PBS (pH 7.4) buffer with Ag/AgCl wire as the gate electrode. The drain current (I_d; scan rate: 12.5 mV s^{-1}) was obtained by applying different source-gate voltages (V_g: from −0.8 to +0.8 V) and a fixed source-drain potentials (V_d: −0.4 or −0.01 V). Transconductance (g_m) curves were obtained by deriving the transfer curves and the definition given in Equation (1).

$$g_m = \frac{\partial I_d}{\partial V_g} \qquad (1)$$

The electrochemical response toward DA was investigated from the (g_m–V_g) curves and the amperometric (I_d–t) curve. All of the as-prepared OECT devices were stored in PBS buffer for at least 30 min prior to each testing.

For SERS measurements, Raman spectroscopy (HR800, HORIBA, Japan) was used to measure the Raman spectra of PC in the range 200–3600 cm^{-1} using a 17-mW-output helium–neon (He–Ne) laser operated at a wavelength of 633 nm. The Raman signals were collected under the conditions of a fixed 5-s exposure and accumulation four times. A constant amount of PC solution (10 μL) was placed on the as-prepared **AuNPs@P-SH** devices (area: 0.196 cm^2) for SERS detection.

RESULTS AND DISCUSSION

Characterization and Surface Morphology of PEDOT Films

Prior to device fabrication, we studied the optical transparency and surface morphology of the PEDOT-based bioelectronic interfaces (BEIs). **Figure 2** presents photographs and SEM and AFM images of the P and P-SH films. **Figures 2a,b** reveal that the P and P-SH films had thicknesses of 200 and 90 nm, respectively, with both exhibiting high transparency. The oxidized polymerization process of the P-SH film, however, led to the ready formation of a 3D porous-like nanostructure, thereby giving a surface roughness (Ra = 29.1 nm) higher than that of the P films (Ra = 1.42 nm) (**Figures 2c–f**). Such a high surface area of the BEI could possibly improve the performance through signal enhancements in the electrochemical and SERS detections.

Characterization of AuNPs and PEDOT Films

To synthesize AuNPs for use in the OECT/SERS hybrid detection system, we employed a modified version of a procedure reported previously for fabricating quasi-spherical gold nanostructures (Hsiao et al., 2012). TEM analysis confirmed that the Au spheres were highly monodisperse, with a uniform size of ∼14.5 ± 1.4 nm (**Figures 3a–c**); the UV–Vis absorption spectrum of the aqueous AuNP solution featured a strong absorption peak near 519 nm, arising from surface plasmon resonance, with a relatively narrow of full width at half maximum (FWHM), suggesting a narrow size distribution for the AuNPs (**Figure S1**, see Supplementary Material). After immobilizing the citrate-capped AuNPs and washing with copious amounts of DI water, SEM revealed a highly dense coating of uniformly distributed AuNPs on the P-SH film, presumably because of strong covalent bonding between the Au NPs and the thiol-functionalized P-SH films. We suspected that the surface of the AuNPs@P-SH film, with large-scale aggregation or an interconnected network of AuNPs, would provide a large electroactive surface area and more hot-spot resonance effects, thereby substantially enhancing the electrochemical and Raman signals, respectively of analytes on such chips (**Figures 3d,e**). Nevertheless, the electrical conductivity of the P-SH film after AuNP treatment (AuNPs@P-SH) was enhanced only slightly relative to that of the pristine P-SH film (**Figure 3f**). We suspect that the presence of citrate units, used for capping the AuNPs and thereby achieving a densely packed monolayer of AuNPs on the thiol-functionalized surfaces, may have led to the insignificant improvement in conductivity, due to a nonlinear I–V response, as measured using the standard four-point probe method.

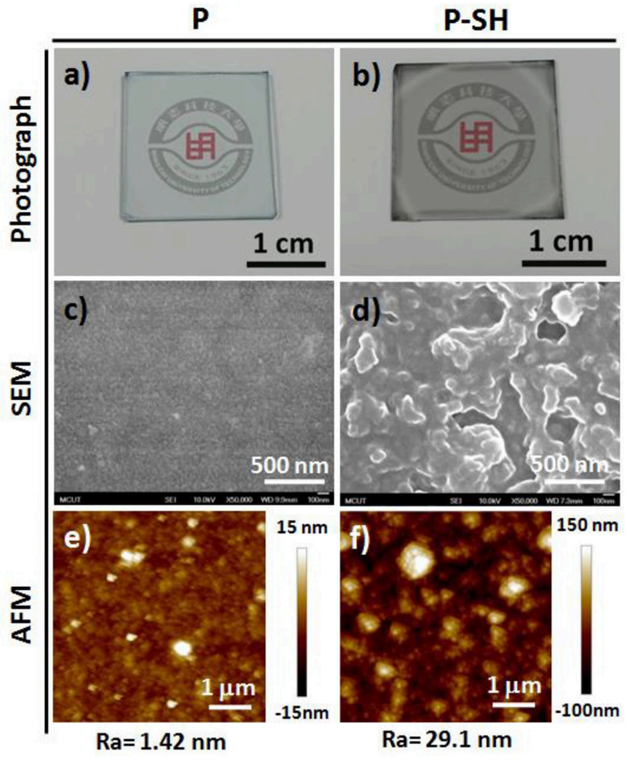

FIGURE 2 | Photographs and SEM and AFM images, with mean average roughnesses (R_a), of **(a,c,e) P** and **(b,d,f) P-SH** films on glass substrates.

Zeta-Potentials and Electrochemical Properties of PEDOT Films

According to the design rule of BEIs for electrochemical sensing, the presence of more negative surface charges on electrodes can be used to resolve the problem of interference from overlapping signals of DA, AA, and UA metabolites (Wang et al., 2009; Huang et al., 2014). Therefore, if the BEI is designed to favor cationic exchange—that is, to attract cationic DA and repel anionic AA

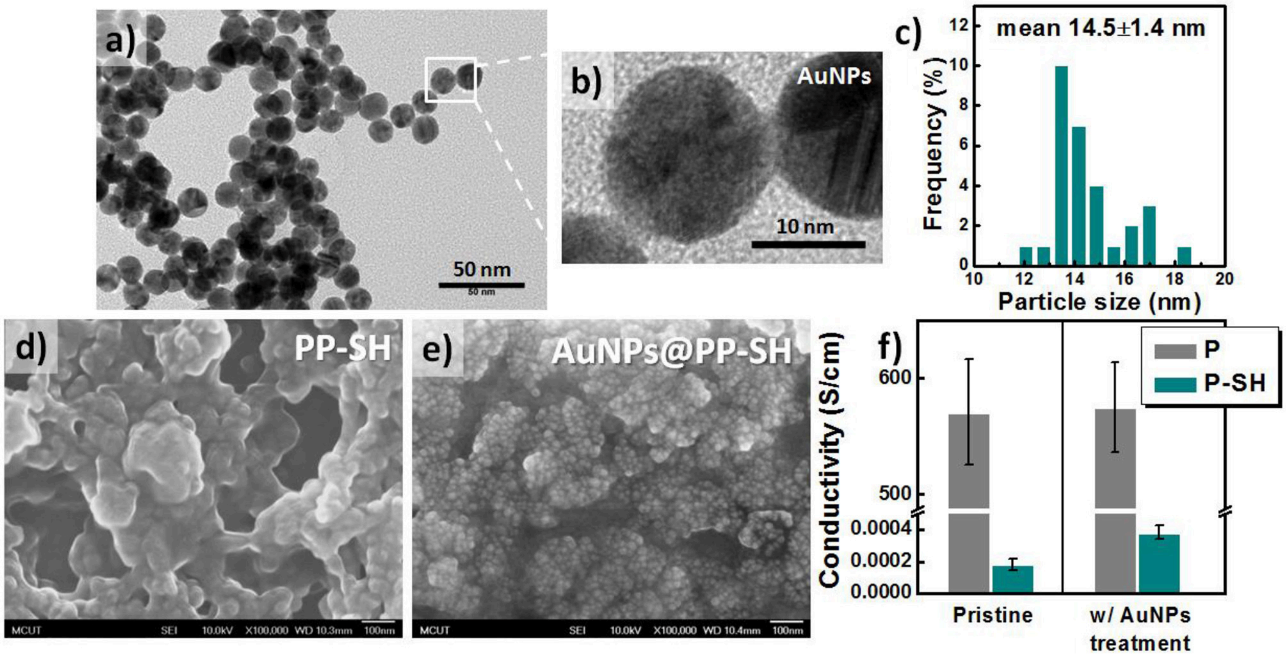

FIGURE 3 | Characteristics of citrate-capped AuNPs. **(a–c)** TEM images and corresponding size distributions of citrate-capped AuNPs. **(d, e)** SEM images of **(d)** **PP-SH** and **(e) AuNPs@PP-SH** electrodes (with AuNPs immobilized on **PP-SH** electrodes) on glass substrates. **(f)** Electrical conductivity of **P** and **P-SH** electrodes prepared with and without AuNP treatment. The thicknesses of the **P** and **P-SH** films were ∼200 and 90 nm, respectively.

and UA—it will thereby allow the selective detection of DA in the presence of AA and DA. **Figure 4a** presents a schematic representation of **AuNPs@PP-SH** films, which we suspected would be more suitable for preventing negatively charged AA and UA from reaching the surface, due to the presence of a surface of negatively charged citrate ions on the AuNPs. The pristine **P** and **P-SH** films both exhibited similar zeta potentials, ∼-4.3 and −7.2 mV, respectively; in contrast, the **P-SH** film treated with citrate-capped AuNPs (**AuNPs@P-SH**) had a much more negative surface charge (zeta potential: −17.1 mV). In addition, a less-changed zeta potential appeared for **P** after AuNP treatment, due to no binding sites being available for AuNP immobilization (**Figure 4b**), consistent with the SEM results of less AuNPs on the surface of P in **Figure S2** (see Supplementary Material). Prior to studying the electrochemical responses of all of the OECT devices for the selective sensing of DA in the presence of AA and UA, we used cyclic voltammetry (CV) to examine the electrochemical properties of **P**, **PP-SH**, and **AuNPs@PP-SH** electrodes in 1× PBS buffer (pH 7.4). As displayed in **Figure 4c**, the experimental cyclic voltammograms of all of the electrodes featured no obvious electrochemical responses at a scan rate of 100 mV s^{-1} when the voltage was swept from −0.8 to +0.8 V in the 1× PBS (pH 7.4) buffer solution. The areas enveloped by the sweep of the CV curves decreased in the order **P** > **PP-SH** > **AuNPs@PP-SH**, revealing that decoration with the citrate-capped AuNPs decreased the negative charge capacity density of the **AuNPs@PP-SH** electrode. Moreover, electrochemical impedance spectroscopy (EIS) revealed a decrease in impedance that followed the order **AuNPs@PP-SH** > **PP-SH** ≈ **P** in the low frequency range from 10^{-1} to 2×10^2 Hz; in contrast, the decrease in impedance followed the order **PP-SH ≈ P** > **AuNPs@PP-SH** in the high frequency range from 2×10^2 to 10^5 Hz (**Figure 4d**). These experimental results suggested that **AuNPs@PP-SH** was the candidate BEI material for preventing negatively charged AA and UA from reaching the PEDOT electrode, with no obvious loss in ionic conductivity, thereby allowing highly selective detection of DA during electrochemical operation.

DPV Measurements of the Selective Detection of DA

We employed more sensitive differential pulse voltammetry (DPV) measurements to explore the ability of PEDOT-based BEIs to selectively detect DA in the presence of AA and UA (**Figures 5a–f**). The interference effect of AA at a concentration of 1 mM on all of the PEDOT-based electrodes would be negligible during the determination of DA, because AA caused no obvious changes in the current response; the oxidation peak potential for AA appeared at ∼-0.1 V. **Figure 5a** reveals that the DPV curves of the **P** electrode could be used for the determination of DA at various concentrations (0.5, 1, 5, 10, 50, 100, 500, and 1000 μM), with two linear regions in the plot of the DPV peak current (I_{DA}) observed for DA oxidation with respect to the DA concentration (C_{DA}) in the presence of other AA and UA metabolites, the concentrations of which were fixed at 1 mM. The DPV responses obtained from the **P** electrodes was represented by the linear regression function $I_{DA} = 24.37 +$

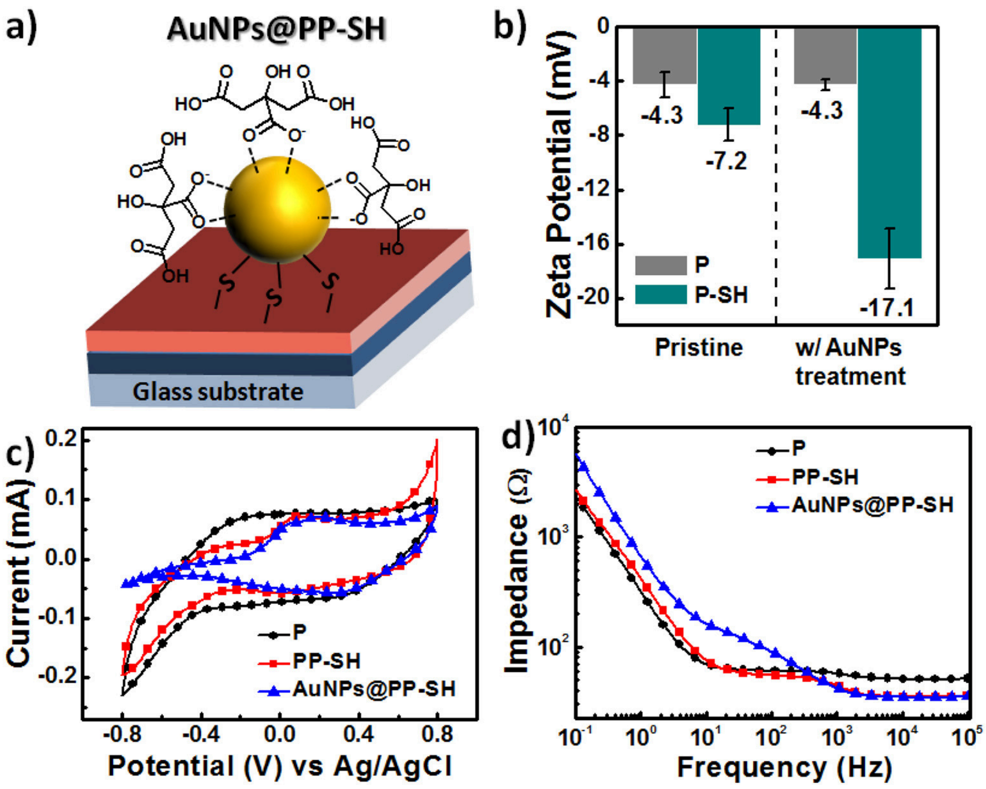

FIGURE 4 | (a) Schematic representation of a single citrate-capped AuNP immobilized on the PP-SH film (**AuNPs@PP-SH**). **(b)** Surface charge, measured through electrokinetic analyses, on the pristine and AuNP-treated PEDOT films (**P** and **P-SH**, respectively). **(c,d)** Electrical properties of **P**, **PP-SH**, and **AuNPs@PP-SH** films in 1× PBS (pH 7.4): **(c)** CV curves (potential swept from −0.8 to 0.8 V at a scan rate of 100 mV s^{-1}) and **(d)** EIS spectra (frequency range: from 10^{-1} to 10^5 Hz).

$0.17C_{DA}$ with a correlation coefficient (R^2) of 0.9862 in the low-concentration region of DA, and by the linear regression function $I_{DA} = 32.73 + 0.07C_{DA}$ with a correlation coefficient (R^2) of 0.9583 in the high-concentration region of DA (**Figure 5d**). Similar trends—of two slopes in all calibration curves—have appeared in previous reports of DA adsorption on electrode surfaces (Yue et al., 2014; Su et al., 2017). This feature can be explained by considering that a monolayer adsorption would first result in higher sensitivity in the low-concentration region, due to the unsaturated active sites of the PEDOT-based BEIs; multilayer adsorption of analytes would, however, limit the availability of active sites and, therefore, result in decreased sensitivity in the high-concentration region. Unfortunately, the interference effect was much more prominent at lower concentrations of DA, potentially bringing about misjudgment of the UA concentration. Although the **PP-SH** electrode provided a DPV peak current similar to that of the **P** electrode, UA had a greater interference effect, with the correlation coefficient ($R^2 = 0.4678$) in the low-concentration region being much lower than that for the **P** electrode ($R^2 = 0.9862$) (**Figures 5b,e**). This observation suggests that the addition of UA might influence the adsorption or oxidation of DA and, therefore, fail to precisely detect DA in the low-concentration region. Notably, however, the DPV curves of the **AuNPs@PP-SH** electrode were not affected by the interference of UA and could be used to precisely determine various DA concentrations, presumably because the high specific area of the citrate-capped AuNPs (presenting carboxyl groups) prevented UA from reaching the electrode surface—in addition to the thiol-functionalized PEDOT materials exhibiting superior electron transfer properties (Ali et al., 2018). The **AuNPs@PP-SH** electrodes also exhibited two linear regression equations for the DA concentrations in the presence of AA and UA (**Figure 5f**): for low concentrations of DA it was $I_{DA} = 20.91 + 0.3029C_{DA}$ ($R^2 = 0.9502$) with a detection limit of 79 nM (S/N = 3); for high concentrations of DA it was $I_{DA} = 37.00 + 0.04C_{DA}$ ($R^2 = 0.8573$). To prove that this **AuNPs@PP-SH** electrode could also exhibit good selectivity against a broad range of other analytes, we further selected other protein-bound uremic toxins, such as p-cresol (PC), indoxyl sulfate (IS), and hippuric acid (HA), in the preparation of three different kinds of quaternary mixtures containing [PC (1 mM) + DA (1 mM) + UA (1 mM) + AA (1 mM)], [IS (1 mM) + DA (1 mM) + UA (1 mM) + AA (1 mM)], and [HA (1 mM) + DA (1 mM) + UA (1 mM) + AA (1 mM)] in PBS buffer solution and tested them on the chips using the DPV measurement, indicating that there were no additional peaks (originated from PC, IS, and HA) observed in the range from −0.5 to 0.8 V (**Figure S3**, see Supplementary Material). Therefore, this biosensor have a good selectivity toward DA against a broad range of AA, UA, PC, IS, and HA analytes through the electrochemical approach.

Output Characteristics and Transfer Curves of OECT/SERS Hybrid Biosensors

To explore the enhancement effect of the AuNPs on the OECT device performance, we measured the I_d-V_d output characteristics, I_d-V_g transfer curves, and g_m-V_g curves to determine the differences in the electrical conductivities and electrochemical properties of the various PEDOT-based active layer channels (featuring the **P**, **PP-SH**, and **AuNPs@PP-SH** films) at the level of realistic devices (**Figure 6**). Because the transconductance (g_m) depends strongly on the channel

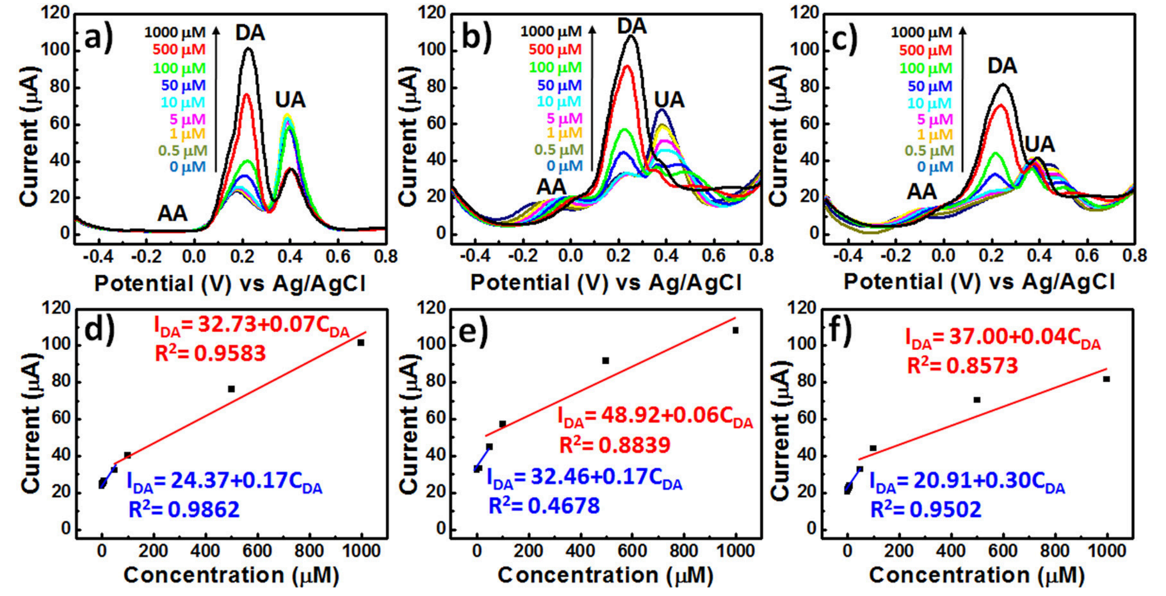

FIGURE 5 | DPV curves of various PEDOT films in 1× PBS (pH 7.4) containing AA, DA, and UA (1 mM AA; 0.5–1000 μM DA; 1 mM UA): **(a) P**, **(b) PP-SH**, and **(c) AuNPs@PP-SH**. **(d–f)** Oxidation DPV peak currents of DA (I_DA) plotted with respect to the DA concentration (C_DA) for **(a–c)**, respectively.

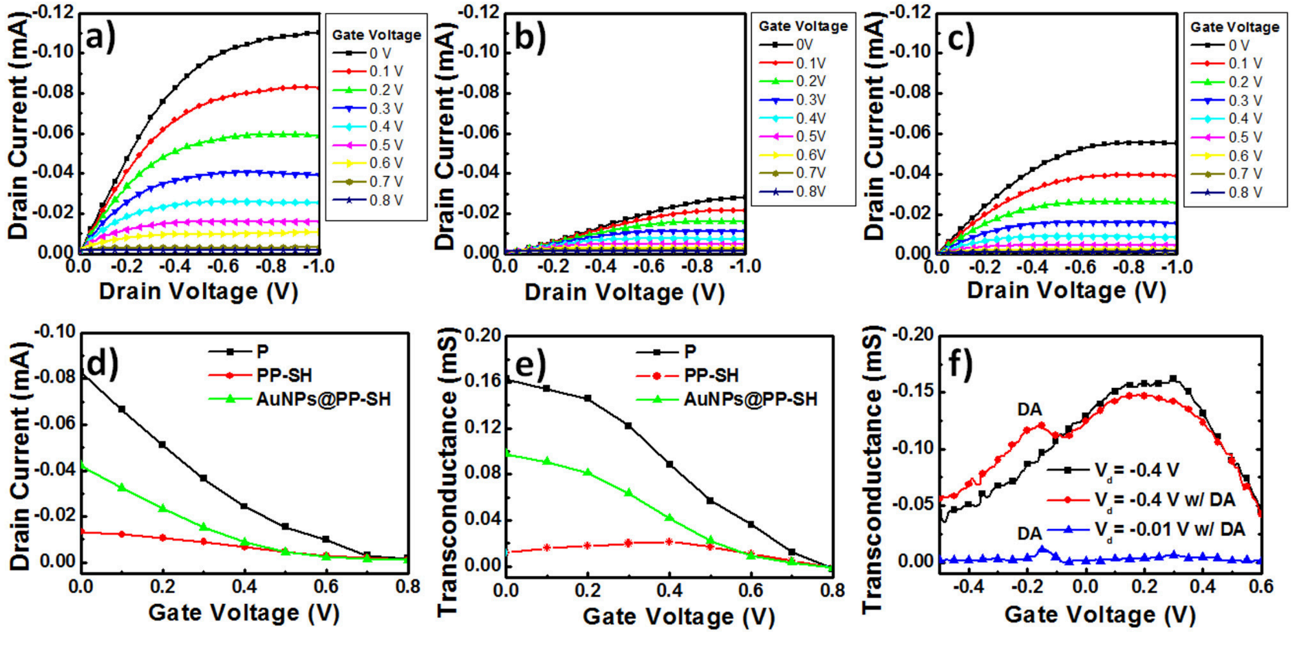

FIGURE 6 | (a–c) Output curves for PEDOT-based OECT devices: **(a)** the **P** OECT, **(b)** the **PP-SH** OECT, and **(c)** the **AuNPs@PP-SH** OECT. **(d)** Transfer curves for PEDOT-based OECT devices (**P**, **PP-SH**, and **AuNPs@PP-SH** OECTs). **(e)** Transconductance plotted with respect to V_g for PEDOT-based OECT devices (**P**, **PP-SH**, and **AuNPs@PP-SH** OECTs): potential swept from 0 to 0.8 V. **(f)** Transconductance plotted with respect to V_g for **AuNPs@PP-SH** OECTs, and recorded in 1× PBS (pH 7.4) with 1 mM DA at various values of V_d: potential swept from −0.5 to +0.6 V.

geometry, it is necessary to compensate for the device geometries (channel length, channel width, film thickness) when comparing the performances of different OECT channel materials. It has been studied that the OECT transconductance of PEDOT:PSS-based devices at saturation is proportional to ($W \times d/L$), where the channel geometry of PEDOT:PSS thin film was designed in OECTs [width (W); length (L); thickness (d)] (Rivnay et al., 2015). More importantly, the previous report suggested that the use of large-area thin film would result in maximizing the signal-to-noise (SNR) for biochemical sensing applications (Stoop et al., 2017). Therefore, in this study, we have used three different thicknesses (100, 200, and 400 nm) of PEDOT:PSS thin films [width (W): 1.5 mm; length (L): 5 mm] to study the effect of membrane thickness on the **P** OECT behaviors. Although the 400 nm-thickness sample exhibited higher transconductance than others, a higher turn-off gate voltage (∼0.8 V) and a shifted transconductance peak (∼0.35 V) were also obtained, thereby faring away from the sweeping potential range of DA (between −0.5 and +0.6 V) (**Figure S4**, see Supplementary Material). Accordingly, taking the factors influencing device performance together, it can be concluded that the 200 nm-thickness of **P** underlying layer displayed the optimized OECT performance and could possibly be used for DA detection in the presence of AA and UA. For this study, we controlled the thickness of the **P**, **PP-SH**, and **AuNPs@PP-SH** active layer channels of the OECTs at ∼290 nm (through spin-coating) and confined the same channel length and width (through the use of a CO_2 laser engraving system). For example, the thickness of the PEDOT:PSS film for **P** device was approximately 290 nm; the thicknesses of the PEDOT:PSS underlying layer (**P**) and the thiol-functionalized PEDOT top layer (**P-SH**) were ∼200 and 90 nm, respectively, in both the **PP-SH** and **AuNPs@PP-SH** devices. **Figures 6a–c** present the output characteristics of OECTs prepared with **P**, **PP-SH**, and **AuNPs@PP-SH** as active layer channels, measured under a negative sweeping bias (from 0 to −1.0 V) on the drain and stepped gate voltages varied from 0 to 0.8 V (using the Ag/AgCl gate electrode). Briefly, all of the devices, featuring the three different kinds of active layers, exhibited the depletion regime of an OECT under typical low-voltage operation, with the drain current decreasing as the applied gate voltage increased. A comparison of the electrical conductivities and output characteristics of the three different kinds of active layers in the OECTs (**Figures 3f**, **6**), revealed that the drain current of the OECTs was strongly correlated to the electrical conductivity of the PEDOT-based active layer and the electrocatalytic activity of the AuNP coating. For example, when the values of V_g and V_d were fixed at 0 and −1 V, respectively, all of the channels exhibited their highest drain currents; a decrease in the on-current was found, however, to follow the order **AuNPs@PP-SH** > **PP-SH**, suggesting that the high specific area of the AuNP coating may have enhanced the electrical conductivity of **PP-SH**; a decrease in the off-current followed the order **P** > **AuNPs@PP-SH**, suggesting that the AuNP-decorated **PP-SH** channel could boost the electrochemical process in the active layer channels to switch the transistor off efficiently, according to the de-doping phenomenon in the channel (**Figure 6d**).

OECT devices can amplify an input signal and lead to an increase in current modulation in the presence of analyte oxidation; therefore, they might be represent excellent candidates for biosensing. In particular, a pivotal parameter for OECTs is the transconductance (g_m), which can be obtained from the derivative of the I_d-V_g transfer curve ($g_m = \partial I_d/\partial V_g$) (**Figure 6d**). When applying a constant value of V_d (−0.4 V) and varying the value of V_g (from 0 to 0.8 V) applied to the OECTs, the resulting g_m-V_g curves of the **P**, **PP-SH**, and **AuNPs@PP-SH** devices provided their maximum values of g_m near values of V_g of 0, 0, and 0.4 V, respectively (**Figure 6e**). The experimentally measured transconductances plotted with respect to V_g in the range from −0.5 to +0.6 V confirmed the background signal of the **AuNPs@PP-SH** OECTs, as well as the location of the DA signal in the g_m-V_g curves (**Figure 6f**). The **AuNPs@PP-SH** OECTs operated at a value of V_d of −0.4 V would result in a broad background signal with a maximum value of g_m located near 0.2 V, with an additional peak appearing near a gate voltage of −0.15 V in the presence of DA (1 mM) in 1× PBS (pH 7.4) buffer solution. Notably, operating the OECT at a value of V_d of −0.01 V minimized the background signal of the PEDOT film in the **AuNPs@PP-SH** device, potentially providing a more accurate determination of DA.

Response of OECTs to the Addition of DA

Our goal for this study was to demonstrate that the developed **AuNPs@PP-SH** OECTs could be employed for the highly selective determination of DA in the presence of AA and UA as interfering agents. **Figure 7a** displays the transconductance (g_m) responses of **AuNPs@PP-SH** OECTs measured at various DA concentrations (0, 0.5, 1, 10, 50, 100, 500, and 1000 μM) in 1× PBS (pH 7.4) buffer solution, in the presence of AA and UA, at a constant value of V_d of −0.01 V. The generated Faradic current appears to be the main working mechanism underlying the effect of DA electro-oxidation on the gate electrode upon increasing the concentration of DA. Therefore, the transfer characteristic curves shifted to more negative gate voltages, due to the increase in the effective gate voltage applied on the transistor; the greater values of g_m were due to the decrease in the potential drop at the electrolyte–gate interface (Gualandi et al., 2018). For these measurements, the **AuNPs@PP-SH** OECT provided sensitivity similar to that of the DPV method (**Figure 5f**) for the determination of DA, with less interference from AA and UA. The **AuNPs@PP-SH** devices functioned with two linear regression equations for the determination of the DA concentrations (**Figure 7c**): for low concentrations of DA it was $I_{DA} = 2.30 + 0.12C_{DA}$ ($R^2 = 0.9348$) with a detection limit of ∼33 nM (S/N = 3); for high concentrations of DA, it was $I_{DA} = 12.96 + 0.01C_{DA}$ ($R^2 = 0.9987$). Gualandi et al. (2018) found that a maximum amplification of PEDOT:PSS OECTs operated at a value of V_g close to 0 V would provide higher sensitivity for biosensing, while values of V_g lower than 0 V would result in higher electrochemical potentials for the channels and higher rates of hole regeneration, providing higher rates of charge-transfer for real-time monitoring of targeted analyte concentrations. Therefore, for our present measurements, we applied values of

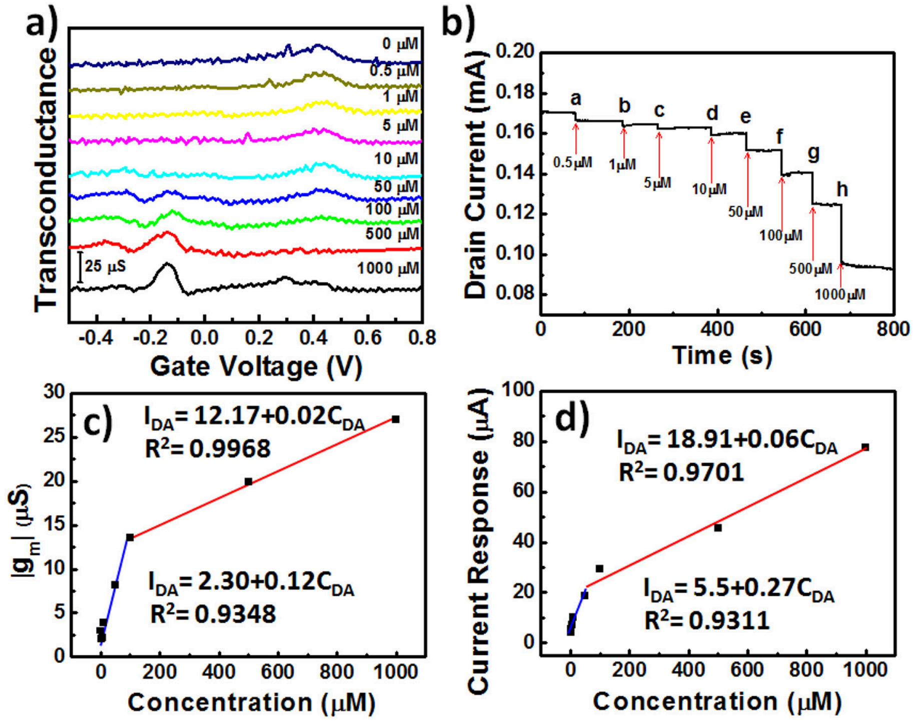

FIGURE 7 | (a) Transconductance (g_m) plotted with respect to V_g for **AuNPs@PP-SH** OECTs, and recorded in 1× PBS (pH 7.4) containing AA, DA, and UA (1 mM AA; 0.5–1000 μM DA; 1 mM UA) at a value of V_d of −0.01 V: potential swept from −0.5 to +0.8 V. **(b)** Amperometric response (I_d plotted with respect to time) recorded with incremental additions of DA in the presence of 1 mM AA and 1 mM UA. **(c)** Transconductance (g_m) plotted with respect to DA concentration (C_{DA}) for **(a)**. **(d)** Drain current response plotted with respect to DA concentration (C_{DA}) for **(b)**.

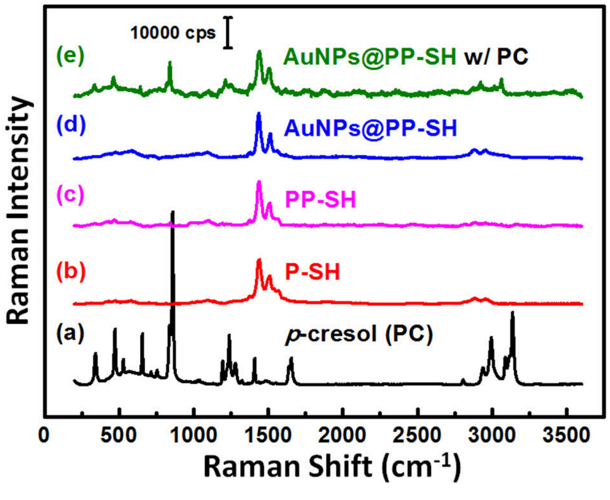

FIGURE 8 | (a–d) Raman spectra of PC, **P-SH**, **PP-SH**, and **AuNPs@PP-SH**. **(e)** SERS spectrum of the **AuNPs@PP-SH** device in the presence of 1 mM PC, recorded at an excitation laser wavelength of 633 nm.

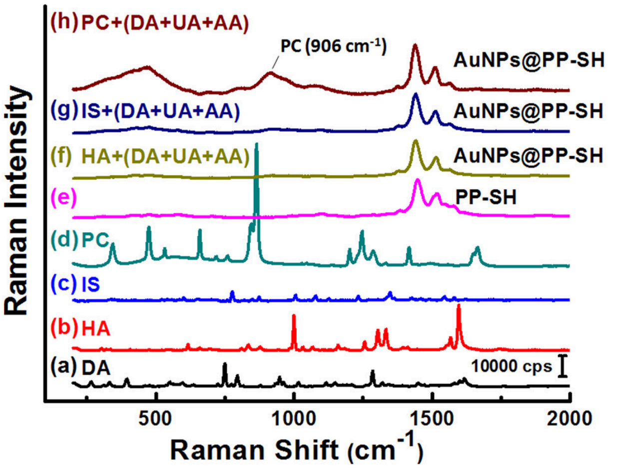

FIGURE 9 | (a–e) Raman spectra of DA, HA, IS, PC, and **PP-SH**. SERS spectra of the **AuNPs@PP-SH** device, recorded in 1× PBS (pH 7.4) in the presence of a quaternary mixture containing **(f)** HA (1 mM), DA (1 mM), UA (1 mM), and AA (1 mM); **(g)** IS (1 mM), DA (1 mM), UA (1 mM), and AA (1 mM); **(h)** PC (1 mM), DA (1 mM), UA (1 mM), and AA (1 mM) at an excitation laser wavelength of 633 nm.

V_d and V_g of −0.4 and −0.01 V, respectively, to the **AuNPs@PP-SH** OECTs to ensure detections with high sensitivity and rapid responses, and measured the amperometric response of the drain current (I_d-time curve) upon the continuous addition of DA (**Figure 7b**). When greater degrees of DA oxidation occurred in the **AuNPs@PP-SH** active layer channel, it consumed more cationic species and, thereby, led to a decrease in the value of

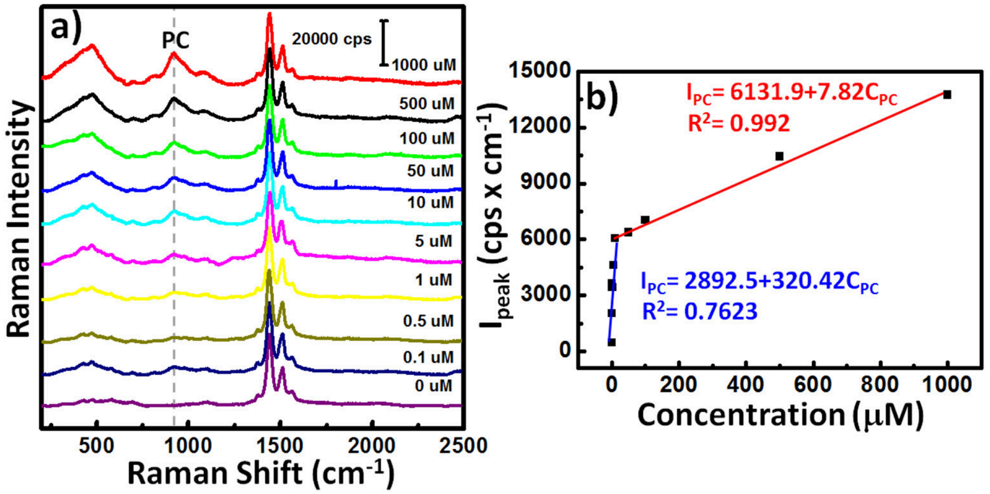

FIGURE 10 | (a) SERS spectra of the **AuNPs@PP-SH** device in the presence of various concentrations of PC and 1 mM DA, 1 mM AA, and 1 mM UA. **(b)** SERS signal intensity (I_{PC}) at 906 cm^{-1} plotted with respect to PC concentration (C_{PC}) for **(a)**.

I_{d}, characterized by two empirical equations (**Figure 7d**): a linear regression equation for low concentrations (0.5–100 μM) of DA of $I_{\mathrm{DA}} = 5.5 + 0.27C_{\mathrm{DA}}$ ($R^2 = 0.9311$) with a detection limit (S/N = 3) of 37 nM; for high concentrations (100–1000 μM) of DA, the corresponding linear regression equation was $I_{\mathrm{DA}} = 18.91 + 0.06C_{\mathrm{DA}}$ ($R^2 = 0.9701$).

SERS Experiments for Selective Detection of PC

To explore the possibility of using the same OECT device for the detection of PC in biological fluids through SERS spectroscopy, we recorded the Raman spectra of liquid-phase pure PC and studied its SERS spectra recorded on the **PP-SH** and **AuNPs@PP-SH** devices (**Figure 8**). Very strong Raman bands of pure PC appear near 850 and 830 cm^{-1}, assigned to the canonical Fermi doublet (Takahashi and Noguchi, 2007) (**Figure 8a**). As displayed in **Figures 8b–d**, the Raman fingerprints of the **P-SH**, **PP-SH**, and **AuNPs@PP-SH** devices were similar to those previous reported for commercial PEDOT:PSS materials (Wang et al., 2018b), with the vibration peaks of PEDOT at 1374, 1437, and 1513 cm^{-1} assigned to C_β-C_β stretching, $C_\alpha = C_\beta$ symmetrical, and $C_\alpha = C_\beta$ symmetrical vibrations, respectively. The Raman signal at 860 cm^{-1} from the liquid-phase PC appeared for our **AuNPs@PP-SH** device; therefore, it could be used for the quantitative detection of PC (**Figure 8e**). To evaluate the SERS enhancement effect of the **AuNPs@PP-SH** devices for the detection of PC in aqueous fluids, we prepared a quaternary mixture containing PC (1 mM), DA (1 mM), UA (1 mM), and AA (1 mM) in PBS buffer solution and tested it on the chips using SERS spectroscopy with comparison to the mixture solutions of [HA (1 mM) + DA (1mM) + UA (1 mM) + AA (1 mM)] and [IS (1 mM) + DA (1mM) + UA (1 mM) + AA (1 mM)] (**Figure 9**). Previous reports have shown that the strongest peak at 1331, 1386, and 1567 cm^{-1} can be chosen to estimate the correlation between the Raman intensity and the concentration of DA, AA, and UA, respectively (Pucetaite et al., 2016; Cholula-Díaz et al., 2018; Phung et al., 2018). The **AuNPs@PP-SH** devices provided a higher-intensity Raman signal for PC, due to its greater SERS activity (SERS hot spots), in the presence of DA, UA, and AA than did the **PP-SH** devices; nevertheless, discrimination of the overlapping region of signals from the DA, AA, and UA analytes from the background signals of **AuNPs@PP-SH** devices remained a major challenge in the fingerprint region (1300–1600 cm^{-1}) (**Figure 9h**).

Because the serum concentrations of PC in healthy control and hemodialysis patients are 8.6 ± 3.0 and 88.7 ± 49.3 μM (De Smet et al., 1998), we varied the concentration of PC (C_{PC}) in a predictable manner (0.1, 0.5, 1, 5, 10, 50, 100, 500, and 1000 μM) and then used our **AuNPs@PP-SH** device to quantify the SERS signal responses in the presence of 1 mM DA, 1 mM UA, and 1 mM AA (**Figure 10a**). The SERS intensity (I_{PC}) of the band at 906 cm^{-1} (assigned to a large red-shift of the canonical Fermi doublet) could be expressed quantitatively using two empirical equations (**Figure 10b**): for low concentrations (0.1–50 μM) of PC it was $I_{\mathrm{PC}} = 2892.5 + 320.42C_{\mathrm{PC}}$ ($R^2 = 0.7623$); for high concentrations (50–1000 μM) of PC it was $I_{\mathrm{PC}} = 6131.9 + 7.82C_{\mathrm{PC}}$ ($R^2 = 0.992$). The sensitivity of SERS in the region of high PC concentration (50–1000 μM) was much lower than that in the region of low PC concentration (0.1–50 μM) because of the hotspot effect decreases dramatically—indeed, exponentially—with the distance between the SERS-active substrates. In total, all of these SERS-active demonstrations have reveal that the **AuNPs@PP-SH** device was capable of detecting PC over a wide concentration range, with high specificity when using a ternary aqueous solution of DA, UA, and AA.

CONCLUSION

We have developed a PEDOT-based 3D-OECT device decorated with a high density of AuNPs for the effective detection of DA in the presence of multiple interferers, and as SERS-active substrates for the selective detection of PC on the same chip. This novel OECT/SERS hybrid biosensor platform featured a highly conductive PEDOT:PSS film as the underlying layer, which greatly enhanced the transconductance and sensitivity of the OECTs for the electrochemical sensing of DA in the presence of AA and UA, and provided an amperometric response to DA with a detection limit of 37 nM in the linear range 50 nM−100 μM. The AuNP-immobilized thiol-functionalized PEDOT film as the top interfacial layer not only improved the performance of the OECTs for the selective detection of DA, due to the signal amplification effect of AuNPs with high catalytic activity, but also enabled downstream detection of PC in biological fluids, due to the outstanding enhancement effect of SERS hotspots. Such OECT/SERS hybrid biosensors decorated with high densities of AuNPs display new versatility, encouraging the design of next-generation biosensors for point-of-care diagnostics.

AUTHOR CONTRIBUTIONS

P-CH and C-LC contributed to the fabrication of the OECT/SERS hybrid biosensors, as well as to the DPV and OECT measurements. C-HL and Y-HT contributed to the synthesis of EDOT-SH. J-AC performed the experiments involving SERS detection. C-KW, C-WK, HY, and PC supervised the experiments, critically reviewed and edited the manuscript. Y-SH contributed to the experimental design and wrote the main manuscript text. All authors have reviewed the manuscript and approved its final version.

ACKNOWLEDGMENTS

This study was supported by the Ministry of Science and Technology (MOST) of Taiwan (grant nos.: MOST 107-2221-E-131-009-MY3, MOST 107-2119-M-001-007-) and by the Academia Sinica Research Project on Thematic Project (grant no.: AS-107-TP-A09).

SUPPLEMENTARY MATERIAL

The Supplementary Material for this article can be found online at: https://www.frontiersin.org/articles/10.3389/fchem.2019.00281/full#supplementary-material

REFERENCES

Ali, A., Abdiryim, T., Huang, X., Jamal, R., and Simayi, R. (2018). Hollow, spherical, poly(3,4-ethylenedioxythiophene)-bearing methanethiol as a gold stabilizer for high-efficiency electrochemical sensors. *J. Electrochem. Soc.* 165, B335–B343. doi: 10.1149/2.0211809jes

Bammens, B., Evenepoel, P., Keuleers, H., Verbeke, K., and Vanrenterghem, Y. (2006). Free serum concentrations of the protein-bound retention solute p-cresol predict mortality in hemodialysis patients. *Kidney Int.* 69, 1081–1087. doi: 10.1038/sj.ki.5000115

Bammens, B., Evenepoel, P., Verbeke, K., and Vanrenterghem, Y. (2003). Removal of middle molecules and protein-bound solutes by peritoneal dialysis and relation with uremic symptoms. *Kidney Int.* 64, 2238–2243. doi: 10.1046/j.1523-1755.2003.00310.x

Chiang, C.-Y., Liu, T.-Y., Su, Y.-A., Wu, C.-H., Cheng, Y.-W., Cheng, H.-W., et al. (2017). Au nanoparticles immobilized on honeycomb-like polymeric films for surface-enhanced Raman scattering (SERS) detection. *Polymers* 9:93. doi: 10.3390/polym9030093

Cholula-Díaz, J. L., Lomelí-Marroquín, D., Pramanick, B., Nieto-Argüello, A., Cantú-Castillo, L. A., Hwang, H. (2018). Synthesis of colloidal silver nanoparticle clusters and their application in ascorbic acid detection by SERS. *Colloids Surface B* 163, 329–335. doi: 10.1016/j.colsurfb.2017.12.051

Coyle, J. T., Price, D. L., and Delong, M. R. (1983). Alzheimer's disease: a disorder of cortical cholinergic innervation. *Science* 219, 1184–1190. doi: 10.1126/science.6338589

De Smet, R., David, F., Sandra, P., Van Kaer, J., Lesaffer, G., Dhondt, A., et al. (1998). A sensitive HPLC method for the quantification of free and total p-cresol in patients with chronic. *Clin. Chim. Acta* 278, 1–21. doi: 10.1016/S0009-8981(98)00124-7

Ferry, B., Gifu, E. P., Sandu, I., Denoroy, L., and Parrot, S. (2014). Analysis of microdialysate monoamines, including noradrenaline, dopamine and serotonin, using capillary ultra-high performance liquid chromatography and electrochemical detection. *J. Chromatogr. B* 951–952, 52–57. doi: 10.1016/j.jchromb.2014.01.023

Gualandi, I., Scavetta, E., Mariani, F., Tonelli, D., Tessarolo, M., Fraboni, B. (2018). All poly(3,4-ethylenedioxythiophene) organic electrochemical transistor to amplify amperometric signals. *Electrochim. Acta* 268, 476–483. doi: 10.1016/j.electacta.2018.02.091

Gualandi, I., Tonelli, D., Mariani, F., Scavetta, E., Marzocchi, M., Fraboni, B. (2016). Selective detection of dopamine with an all PEDOT:PSS organic electrochemical transistor. *Sci. Rep.* 6:35419. doi: 10.1038/srep35419

Guerrini, L., and Graham, D. (2012). Molecularly-mediated assemblies of plasmonic nanoparticles for surface-enhanced raman spectroscopy applications. *Chem. Soc. Rev.* 41, 7085–7107. doi: 10.1039/c2cs35118h

Hsiao, Y.-S., Charan, S., Wu, F.-Y., Chien, F.-C., Chu, C.-W., Chen, P., et al. (2012). Improving the light trapping efficiency of plasmonic polymer solar cells through photon management. *J. Phys. Chem. C* 116, 20731–20737. doi: 10.1021/jp306124n

Huang, Q., Zhang, H., Hu, S., Li, F., Weng, W., Chen, J., et al. (2014). A sensitive and reliable dopamine biosensor was developed based on the Au@carbon dots-chitosan composite film. *Biosens. Bioelectron.* 52, 277–280. doi: 10.1016/j.bios.2013.09.003

Kim, D. J., Lee, N. E., Park, J. S., Park, I. J., Kim, J. G., Cho, H. J. (2010). Organic electrochemical transistor based immunosensor for prostate specific antigen (PSA) detection using gold nanoparticles for signal amplification. *Biosens. Bioelectron.* 25, 2477–2482. doi: 10.1016/j.bios.2010.04.013

Lee, S., Hahm, M. G., Vajtai, R., Hashim, D. P., Thurakitseree, T., Chipara, A. C., et al. (2012). Utilizing 3D SERS active volumes in aligned carbon nanotube scaffold substrates. *Adv. Mater.* 24, 5261–5266. doi: 10.1002/adma.201200645

Liu, T.-Y., Ho, J.-Y., Wei, J.-C., Cheng, W.-C., Chen, I.-H., Shiue, J., et al. (2014). Label-free and culture-free microbe detection by three dimensional hot-junctions of flexible Raman-enhancing nanohybrid platelets. *J. Mater. Chem. B* 2, 1136–1143. doi: 10.1039/C3TB21469A

Mercante, L. A., Pavinatto, A., Iwaki, L. E., Scagion, V. P., Zucolotto, V., Oliveira, O. N. Jr., et al. (2015). Electrospun polyamide 6/poly(allylamine hydrochloride) nanofibers functionalized with carbon nanotubes for electrochemical detection of dopamine. *ACS Appl. Mater. Interfaces* 7, 4784–4790. doi: 10.1021/am508709c

Ou, Y., Wang, L.-Y., Zhu, L.-W., Wan, L.-S., and Xu, Z.-K. (2014). In-situ immobilization of silver nanoparticles on self-assembled honeycomb-patterned films enables surface-enhanced Raman scattering (SERS) substrates. *J. Phys. Chem. C* 118, 11478–11484. doi: 10.1021/jp503166g

Pandikumar, A., How, G. T. S., See, T. P., Omar, F. S., Jayabal, S., Kamali, K. Z., et al. (2014). Graphene and its nanocomposite material based electrochemical sensor platform for dopamine. *RSC Adv.* 4, 63296–63323. doi: 10.1039/C4RA13777A

Paulus, W., and Trenkwalder, C. (2006). Less is more: Pathophysiology of dopaminergic-therapy-related augmentation in restless legs syndrome. *Lancet Neurol.* 5, 878–886. doi: 10.1016/S1474-4422(06)70576-2

Phung, V.-D., Jung, W.-S., Kim, J.-H., and Lee, S.-W. (2018). Gold nanostructures electrodeposited on graphene oxide-modified indium tin oxide glass as a surface-enhanced Raman scattering-active substrate for ultrasensitive detection of dopamine neurotransmitter. *Jpn. J. Appl. Phys.* 57:08PF02. doi: 10.7567/JJAP.57.08PF02

Pucetaite, M., Velicka, M., Pilipavicius, J., Beganskiene, A., Ceponkus, J., Sablinskas, V., et al. (2016). Uric acid detection by means of SERS spectroscopy on dried Ag colloidal drops. *J. Raman Spectrosc*. 47, 681–686. doi: 10.1002/jrs.4875

Rivnay, J., Leleux, P., Ferro, M., Sessolo, M., Williamson, A., Koutsouras, D. A., et al. (2015). High-performance transistors for bioelectronics through tuning of channel thickness. *Sci. Adv*. 1:e1400251. doi: 10.1126/sciadv.1400251

Sajid, M., Nazal, M. K., Mansha, M., Alsharaa, A., Jillani, S. M. S., Basheer, C., et al. (2016). Chemically modified electrodes for electrochemical detection of dopamine in the presence of uric acid and ascorbic acid: a review. *TrAC Trend. Anal. Chem*. 76, 15–29. doi: 10.1016/j.trac.2015.09.006

Shiohara, A., Langer, J., Polavarapu, L., and Liz-Marzán, L. M. (2014). Solution processed polydimethylsiloxane/gold nanostar flexible substrates for plasmonic sensing. *Nanoscale* 6, 9817–9823. doi: 10.1039/C4NR02648A

Stoop, R. L., Thodkar, K., Sessolo, M., Bolink, H. J., Schönenberger, C., Calame, M. (2017). Charge noise in organic electrochemical transistors. *Phys. Rev. Appl.* 7:014009. doi: 10.1103/PhysRevApplied.7.014009

Su, C. H., Sun, C. L., and Liao, Y. C. (2017). Printed combinatorial sensors for simultaneous detection of ascorbic acid, uric acid, dopamine, and nitrite. *ACS Omega* 2, 4245–4252. doi: 10.1021/acsomega.7b00681

Takahashi, R., and Noguchi, T. (2007). Criteria for determining the hydrogen-bond structures of a tyrosine side chain by Fourier transform infrared spectroscopy: density functional theory analyses of model hydrogen-bonded complexes of p-cresol. *J. Phys. Chem. B* 111, 13833–13844. doi: 10.1021/jp0760556

Tang, H., Lin, P., Chan, H. L., and Yan, F. (2011). Highly sensitive dopamine biosensors based on organic electrochemical transistors. *Biosens. Bioelectron*. 26, 4559–4563. doi: 10.1016/j.bios.2011.05.025

Wang, N., Liu, Y., Fu, Y., and Yan, F. (2018a). AC measurements using organic electrochemical transistors for accurate sensing. *ACS Appl. Mater. Interfaces* 10, 25834–25840. doi: 10.1021/acsami.7b07668

Wang, X., Meng, F., Wang, T., Li, C., Tang, H., Gao, Z., et al. (2018b). High performance of PEDOT: PSS/SiC-NWs hybrid thermoelectric thin film for energy harvesting. *J. Alloy. Compd*. 734, 121–129. doi: 10.1016/j.jallcom.2017.11.013

Wang, Y., Li, Y., Tang, L., Lu, J., and Li, J. (2009). Application of graphene-modified electrode for selective detection of dopamine. *Electrochem. Commun*. 11, 889–892. doi: 10.1016/j.elecom.2009.02.013

Yang, S., Dai, X., Stogin, B. B., and Wong, T.-S. (2016). Ultrasensitive surface-enhanced Raman scattering detection in common fluids. *Proc. Nati. Acad. Sci. U.S.A.* 113, 268–273. doi: 10.1073/pnas.1518980113

Yoshitake, T., Kehr, J., Todoroki, K., Nohta, H., and Yamaguchi, M. (2006). Derivatization chemistries for determination of serotonin, norepinephrine and dopamine in brain microdialysis samples by liquid chromatography with fluorescence detection. *Biomed. Chromatogr*. 20, 267–281. doi: 10.1002/bmc.560

Yue, H. Y., Huang, S., Chang, J., Heo, C., Yao, F., Adhikari, S., et al. (2014). ZnO nanowire arrays on 3D hierachical graphene foam: biomarker detection of Parkinson’s disease. *ACS Nano* 8, 1639–1646. doi: 10.1021/nn405961p

Yusoff, N., Pandikumar, A., Ramaraj, R., Lim, H. N., and Huang, N. M. (2015). Gold nanoparticle based optical and electrochemical sensing of dopamine. *Microchim. Acta* 182, 2091–2114. doi: 10.1007/s00604-015-1609-2

Zhou, Y., Yan, H., Xie, Q., Huang, S., Liu, J., Li, Z., et al. (2013). Simultaneous analysis of dopamine and homovanillic acid by high-performance liquid chromatography with wall-jet/thin-layer electrochemical detection. *Analyst* 138, 7246–7253. doi: 10.1039/c3an01437a

Ziemssen, T., and Reichmann, H. (2007). Non-motor dysfunction in Parkinson’s disease. *Parkinsonism Relat. D*. 13, 323–332. doi: 10.1016/j.parkreldis.2006.12.014

Conflict of Interest Statement: The authors declare that the research was conducted in the absence of any commercial or financial relationships that could be construed as a potential conflict of interest.

frontiers in Chemistry

ORIGINAL RESEARCH
published: 30 April 2019
doi: 10.3389/fchem.2019.00262

Electrochemical Co-deposition of Polydopamine/Hyaluronic Acid for Anti-biofouling Bioelectrodes

Semin Kim [1†], Sanghun Lee [1†], Junggeon Park [1] and Jae Young Lee [1,2]*

[1] *School of Materials Science and Engineering, Gwangju Institute of Science and Technology, Gwangju, South Korea,*
[2] *Department of Biomedical Science and Engineering, Gwangju Institute of Science and Technology, Gwangju, South Korea*

Bioelectrodes are key components of electronic devices that efficiently mediate electrical signals in biological systems. However, conventional bioelectrodes often undergo biofouling associated with non-specific proteins and cell adhesion on the electrode surfaces, which leads to seriously degraded electrical and/or electrochemical properties. Hence, a facile and effective method to modify the surface of bioelectrodes is required to introduce anti-biofouling properties and improve performance. Here, we report an electrochemical surface modification of a bioelectrode via co-deposition of hyaluronic acid (HA) and polydopamine (PDA). The electrochemical polymerization and deposition of PDA offered simple and effective incorporation of highly hydrophilic and anti-fouling HA to the electrode surfaces, with no substantial increase in impedance. HA-incorporated PDA (PDA/HA)-modified electrodes displayed significant resistance to non-specific protein adsorption and the adhesion of fibroblasts. In addition, 4-week subcutaneous implantation studies revealed that the modified electrodes attenuated scar tissue formation compared with that induced by unmodified bare electrodes. This simple and effective electrochemical surface modification could be further employed for various implantable bioelectrodes (e.g., prosthetics and biosensors) and could extend their bioelectronic applications.

Keywords: polydopamine, hyaluronic acid, electrochemical, bioelectrodes, anti-fouling

Edited by:
Greta Varchi,
Consiglio Nazionale delle Ricerche (Bologna), Italy

Reviewed by:
Jun Wang,
University of Arizona, United States
Josef Alexander Goding,
Imperial College London, United Kingdom

Correspondence:
Jae Young Lee
jaeyounglee@gist.ac.kr

† These authors have contributed equally to this work

Specialty section:
This article was submitted to Organic Chemistry, a section of the journal Frontiers in Chemistry

Received: *12 January 2019*
Accepted: *01 April 2019*
Published: *30 April 2019*

Citation:
Kim S, Lee S, Park J and Lee JY (2019) Electrochemical Co-deposition of Polydopamine/Hyaluronic Acid for Anti-biofouling Bioelectrodes. Front. Chem. 7:262. doi: 10.3389/fchem.2019.00262

INTRODUCTION

Recently, biomedical electronic devices have been developed for various applications, such as cardiac pacemakers, implantable prosthetic devices, and neural electrodes (Xu et al., 2014; Choi et al., 2016; Feiner et al., 2016; Park et al., 2018). In these devices, a bioelectrode plays an important role because it directly receives and/or transmits biological signals in contact with cells and tissues; therefore, its performance and biocompatibility are generally considered essential features for bioelectrode design and development (Fattahi et al., 2014; Kleber et al., 2017). However, for conventional implanted bioelectrodes, scar tissue is frequently formed around the electrodes, which eventually impedes their electrical and/or electrochemical properties, and thus limits their practical uses (Lin et al., 2013; Hu et al., 2016). This phenomenon is known as a typical foreign body response (FBR), which occurs as a host defense mechanism when foreign biomaterials are implanted into the body. The initial FBR involves non-specific protein adsorption onto the material surfaces, followed by attachment of various cells (e.g., macrophages and fibroblasts), and eventual scar tissue formation around the biomaterial implants (Grainger, 2013; KyungáKim, 2016). Therefore, a simple and effective strategy to develop anti-biofouling bioelectrodes is required to suppress scarring associated with the bioelectrodes and thus improve their functions in a biological milieu.

Several studies have reported the surface modification of electrodes using hydrophilic polymers to reduce the FBR. Hydrophilic polymers [e.g., hyaluronic acid (HA) and poly(ethylene glycol) (PEG)] on material surfaces hold a large amount of water and form hydration layers that can resist protein adsorption and/or denaturation and cell adhesion (Banerjee et al., 2011; Liu et al., 2016). To tether these polymers on the electrodes, chemical covalent modification is typically employed. However, most conductive electrode materials (e.g., metals and metal oxides) do not possess chemical functional groups to form covalent bonds with polymers (except for certain specific reactions, e.g., the thiol-gold reaction). For example, Brash's group coated gold electrodes with thiolated poly(ethylene glycol) by chemisorption and demonstrated the anti-fouling nature of the resultant surfaces (Unsworth et al., 2005). In addition, chemical reactions between electrodes and polymers for coating are difficult to be controlled precisely in term of the reaction degree and location. Plasma treatment has been utilized to generate functional groups on the surfaces for further coupling with various polymers; however, it possesses some disadvantages, such as the requirement of a complicated process, difficulties in controlling the coating degree and selective modification, and importantly, damage to whole devices (Cao et al., 2007; Chittrakarn et al., 2016; Park et al., 2019). By contrast, an electrochemical method for electrode passivation could be a good option because of the relatively easy control over the modification reaction, the lack of a requirement for toxic chemicals, and possibility of selective electrode coatings (Lee and Schmidt, 2010; Kim et al., 2017).

Hyaluronic acid (HA) is an anionic polysaccharide present in the body that has excellent hydrophilicity and biocompatibility (Highley et al., 2016). In particular, HA-based materials have been recognized as attractive anti-biofouling materials because of their excellent moisture-retention and lubrication ability, which properties are attributed to the amide (CO-NH) or carboxyl (-COOH) groups present in HA (Huang et al., 2015; Ye et al., 2016). However, HA cannot be directly employed for electrochemical deposition because it does not inherently contain electrochemically active groups. Moreover, HA binding with metallic substrates is generally poor. Consequently, a simple and effective method for the electrochemical immobilization of HA onto conductive electrode materials is required. Dopamine (DA) is a mussel-derived bio-adhesive molecule. In particular, its polymeric form [polydopamine (PDA)] exhibits strong adhesion to various substrates and thus has been explored extensively to tether various molecules (e.g., proteins and peptides) on various substrates (Lee et al., 2007; Ryu et al., 2018). PDA is usually obtained via a chemical oxidation reaction through self-polymerization in alkaline solution. The catechol group in DA moieties is oxidized to quinone, which can interact with various molecules via hydrogen bonding, hydrophobic interactions, and chemical reactions (e.g., Michael addition and Schiff base reactions) (Rai and Perry, 2012; Rodriguez-Emmenegger et al., 2013; Salazar et al., 2016). Importantly, a DA moiety is an electroactive molecule that can be oxidized and/or polymerized to PDA by applying oxidative potentials (Stöckle et al., 2014). Previously, we reported the electrochemical surface modification of electrodes using DA-HA conjugates (DA-HA) (Kim et al., 2017). Electrodes electrochemically coated with DA-HA exhibited non-fouling properties (resistance to non-specific serum protein adsorption and cell attachment) with no impairment of the electrodes' original electrochemical properties; however, that procedure required additional steps for DA-HA conjugation and purification.

In the present study, we aimed to develop a simple and effective method to create anti-fouling electrode surfaces via electrochemical coating of HA and PDA. Specifically, PDA was electrochemically deposited on the electrode surface in the presence of HA. We expected that HA would be incorporated into the PDA layer via entrapment during PDA deposition and/or its strong molecular interactions with PDA, displaying stable functions for biofouling resistance (**Figure 1**). The deposition of PDA and HA was studied using a quartz crystal microbalance (QCM). The PDA and PDA/HA-coated electrode surfaces were characterized by HA immunostaining, water contact angle (WCA) measurements, atomic force microscopy (AFM), and electrochemical impedance spectroscopy (EIS). Subsequently, we evaluated the electrode anti-fouling properties via a serum protein adsorption test, *in vitro* cell adhesion, and *in vivo* compatibility test.

MATERIALS AND METHODS

Materials

Dopamine hydrochloride (DA), potassium ferrocyanide ($K_4Fe(CN)_6$), and fluorescein-isothiocyanate-labeled bovine serum albumin (BSA-FITC) were purchased from Sigma Aldrich (St. Louis, MO, USA). Hyaluronic acid (1.5×10^6 Da) was obtained from LG Chem (Daejeon, Republic of Korea). Dulbecco's modified Eagle's medium, Dulbecco's phosphate buffered saline, and fetal bovine serum (FBS) were purchased from Gibco (Grand Island, NY, USA). An FITC-labeled HA binding peptide (FITC-HABP) was purchased from ChinaPeptides (Shanghai, China).

Electrochemical Coating of HA-Incorporated PDA on Electrodes

Indium tin oxide-coated slides (ITO electrodes; AMG, Gwangju, Republic of Korea) were washed by successive sonications in acetone and methanol for 10 min each. The polymerization solution [10 mM DA and 2 mg/mL of HA in phosphate-buffered saline (PBS, pH 6)] was freshly prepared. For electrochemical deposition, a potentiostat (VersaSTAT3 electrochemical working station, Princeton Applied Research, Oak Ridge, TN, USA) was used in a three-electrode system with a Pt wire as the counter electrode and a standard calomel electrode (SCE) as the reference electrode. PDA/HA deposition was performed on the ITO electrodes by applying a constant potential of 1 V for 30 or 60 min. The mass change profile and current profile were monitored during electrochemical deposition using a quartz

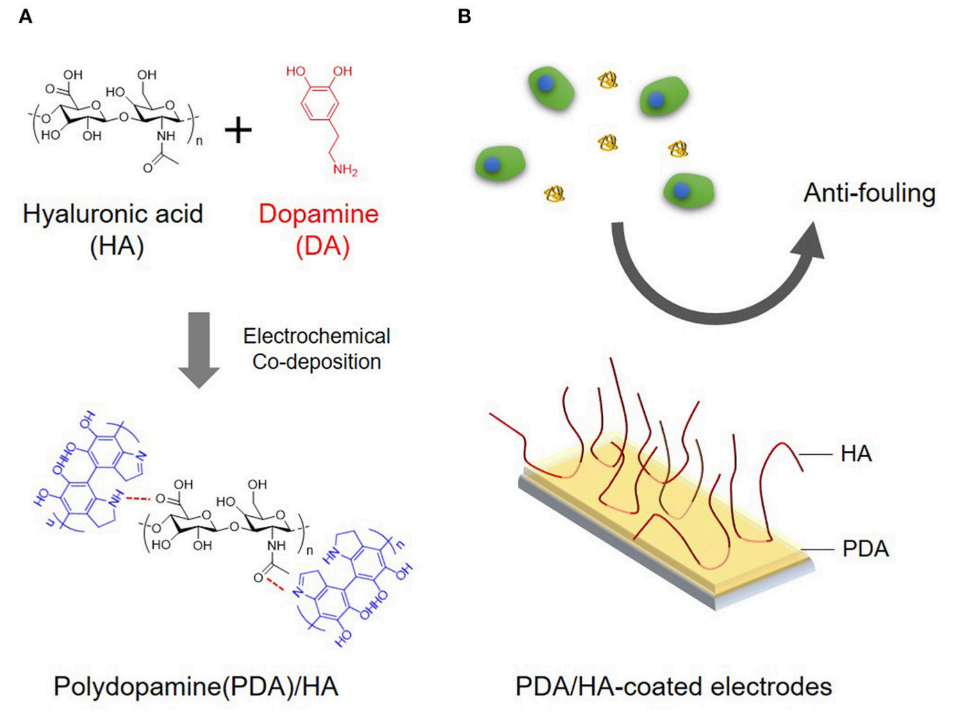

FIGURE 1 | (A) Schematic illustration for electrochemical co-deposition of PDA/HA. **(B)** Scheme showing the use of anti-fouling of PDA/HA-coated electrodes.

crystal microbalance (QCM; QCM922A, SEIKO EG&G, Tokyo, Japan). After coating, the samples were washed with double de-ionized (DDI) water and then stored in PBS (pH 7.4). For comparison, PDA was also deposited on ITO electrodes in a HA-free polymerization solution [10 mM DA in PBS (pH 6)] under the same electrochemical conditions as the PDA/HA deposition.

Florescence and Image Analysis

The presence of HA on the modified electrode surfaces was studied by immunostaining with the FITC-HABP. Samples were incubated in blocking solution [1% BSA in PBS (pH 7.4)] at room temperature for 30 min, followed by incubation in FITC-HABP [5 µg/mL in PBS (pH 7.4)] at room temperature for 45 min. The samples were washed with PBS, and fluorescence images were acquired using a ChemiDoc MP image system (Bio-Rad, Hercules, CA, USA) with the same exposure time for all samples.

Atomic Force Microscopy

An atomic force microscope (AFM; XE-100, PARK System, Suwon, Republic of Korea) was used to characterize the surface morphology and thickness of the coated films. Substrates were scanned in a tapping mode using a non-contact, high resonance tip (Nanoworld, Neuchâtel, Switzerland) at a scan rate of 0.3 Hz. The thicknesses of the PDA and PDA/HA films was measured using a DEKTAK-XT stylus profiler (Bruker, Karlsruhe, Germany).

Water Contact Angle Measurement

Static water contact angles of the samples were measured using a contact angle analyzer (Phoenix 300, Surface Electro Optics Co., Suwon, Republic of Korea). A 10-µL DDI water droplet was dropped onto the sample at room temperature.

Electrochemical Impedance Spectroscopy

Electrochemical impedance spectroscopy (EIS) was performed on bare ITO and PDA/HA-modified ITO electrodes. For EIS analysis, ITO electrodes were covered with a tape having a circular hole (6 mm in diameter) before electrochemical deposition to ensure a constant electrode area (0.2829 cm^2). The same three-electrode system as described in section Electrochemical Coating of HA-Incorporated PDA on Electrodes was employed, using a VersaSTAT3 electrochemical working station. An alternative sinusoidal potential of 10 mV and a DC potential of 0 V (vs. open circuit voltage) was applied in a range of 10^{-1}-10^5 Hz and the measurements were performed in PBS with 5 mM $[Fe(CN)_6]^{3-/4-}$.

Protein Adsorption Test

A QCM was used to monitor the protein adsorption onto the bare, PDA- and PDA/HA modified ITO electrodes. The electrodes were exposed to the solutions pumped at 100 mL/min for 1 h in a QCM flow cell. In the order of PBS, 10% FBS, and PBS, individual solutions were flowed over the electrodes. The frequency changes were observed using the WinQCM software. The effects of protein adsorption onto the electrode samples in terms of electrochemical impedance were studied. Bare and modified electrodes were incubated in 10% FBS in PBS (pH 7.4) at 37°C for 1 h. The impedance spectra from the electrodes before and after protein adsorption were obtained in frequency ranges of 1–10^5 Hz, with an amplitude of 5 mV. Nyquist plots of the impedance data were fitted with an equivalent circuit using the ZsimpWin 3.21 software package (Princeton Applied Research). The charge transfer resistance (R_{ct}) was calculated from fitting the impedance data and then compared among the electrodes.

In vitro Cell Culture

To study the ability of PDA/HA-modified substrates to resist cell attachment, mouse NIH3T3 fibroblasts were seeded and cultured on bare, PDA-, PDA/HA-coated ITO electrodes, respectively. Fibroblasts were maintained in a tissue culture plate with 5% CO_2 at 37°C in a culture medium consisting of Dulbecco's modified Eagle's medium (Gibco), 10% heat-inactivated FBS, and 1% antibiotic/antimycotic solution. Before cell seeding, the samples were sterilized by exposure to ultraviolet light for 1 h. Fibroblasts were seeded at a density of 3×10^4 cells per cm^2 and incubated in a humidified incubator with 5% CO_2 at 37°C for 3 days.

In vivo Tissue Compatibility

All animal experiments were performed with permission from the committee on animal research and ethics in Gwangju Institute of Science and Technology, Republic of Korea (Approval number: GIST-2017-044). *In vivo* animal experiments were conducted with BALB/c mice (6 weeks old) to assess the tissue compatibility of PDA/HA-modified electrodes. The PDA/HA-coated electrodes were first immersed in 70% ethanol for sterilization for 1 h, and then thoroughly washed with sterile Dulbecco's PBS. The back of each mouse was shaved and the shaved area was disinfected. The mice were anesthetized using 2% isoflurane. It should be noted that gold-coated epoxy electrodes were used for the *in vivo* study. In brief, SU-8 100 (MicroChem, Westborough, MA, USA) was spin-coated on a clean glass substrate at 1,500 rpm, followed by pre-curing (30 min at 65°C and 30 min at 95°C), ultraviolet light exposure (1 min), baking (90 min at 95°C), and developing (60 min in isopropyl alcohol). Then, a 50 nm-thick gold layer was coated on the fabricated epoxy probe using a sputter technique. The gold-coated epoxy electrode was peeled-off from the glass substrate and electrochemically deposited with PDA or PDA/HA. Samples were implanted in subcutaneous pockets made to the right and left sides of a midline incision on the mouse's back, and the skin was sutured using silk thread. Four mice were used for each sample—bare, PDA, PDA/HA. At 4 weeks after implantation, the mice were sacrificed. Skin and muscle tissues surrounding the samples were fixed in 3.7% formaldehyde and embedded in paraffin. The tissue blocks were sectioned to 5-μm-thick slides

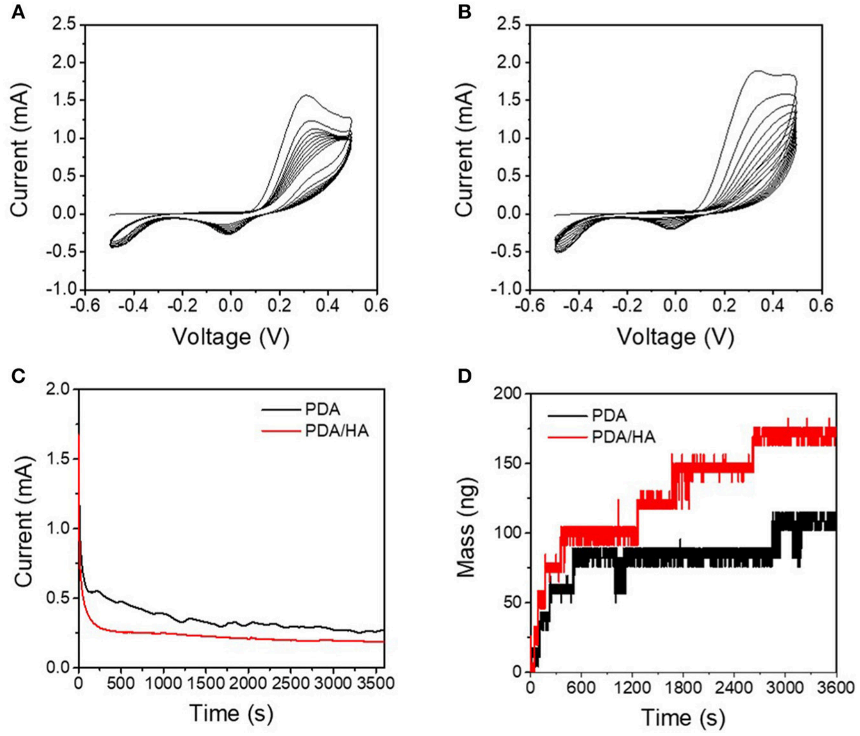

FIGURE 2 | (A) Cyclic voltammograms of DA solution [10 mM DA in phosphate-buffered saline (PBS) (pH 6)] at a scan rate of 0.02 V s^{-1}. **(B)** Cyclic voltammograms of DA/HA solution [10 mM DA and 2 mg/mL HA in PBS (pH 6)] at a scan rate of 0.02 V s^{-1}. **(C)** Chronoamperograms of the DA solution and DA/HA solution at 1 V vs. standard calomel electrode (SCE). **(D)** Electrochemical quartz crystal microbalance (QCM) profiles during chronoamperometry (at 1 V *vs.* SCE) of the DA solution and the DA/HA solution.

using a microtome. For histological analyses, hematoxylin and eosin staining and Masson's trichrome staining were performed according to the manufacturer's protocol (Sigma Aldrich, St. Louis, MO, USA). Images of stained tissues were acquired under an optical microscope.

Statistical Evaluation

All tests were performed at least in triplicate and the results are reported as the mean ± standard deviation (SD) unless otherwise noted. Results between groups were analyzed by one-way ANOVA analysis using Origin software (Microcal Software, Inc., Northampoton, MA, USA), with appropriate corrections, such as Tukey's *post hoc* tests, for comparisons.

RESULTS AND DISCUSSION

Electrochemical Deposition of PDA/HA

The redox properties of DA and DA/HA were first examined to study the electrochemical deposition of PDA/HA by cyclic voltammetry in the voltage range from −0.5 V to 0.5 V vs. SCE (**Figures 2A,B**), before electrochemical deposition. DA and DA/HA exhibited distinct oxidation peaks at 0.2–0.4 V and reduction peaks at around 0 V, indicating the redox couples of DA/dopaquinone, and oxidation peaks at −0.1 V and reduction peaks around −0.5 V, indicating the redox couples of leucodopaminechrome/dopaminechrome. In particular, the DA/dopaquinone intermediate state is known to play an important role in adhesion to various material surfaces because of its ability of form bidentate and binuclear complexes on substrates. As the polymerization proceeded during multiple cyclic voltammetry scans, the currents for both PDA and PDA/HA polymerization steadily decreased, which indicated the part formation of insulating PDA domains on the electrode surfaces and deposition of insulating bulky HA molecules with PDA domains on the electrodes. We further investigated the electrochemical deposition of PDA and PDA/HA in the galvanostatic mode by applying a constant potential of 1 V (vs. SCE) for 1 h (**Figure 2C**). The current decreased over time

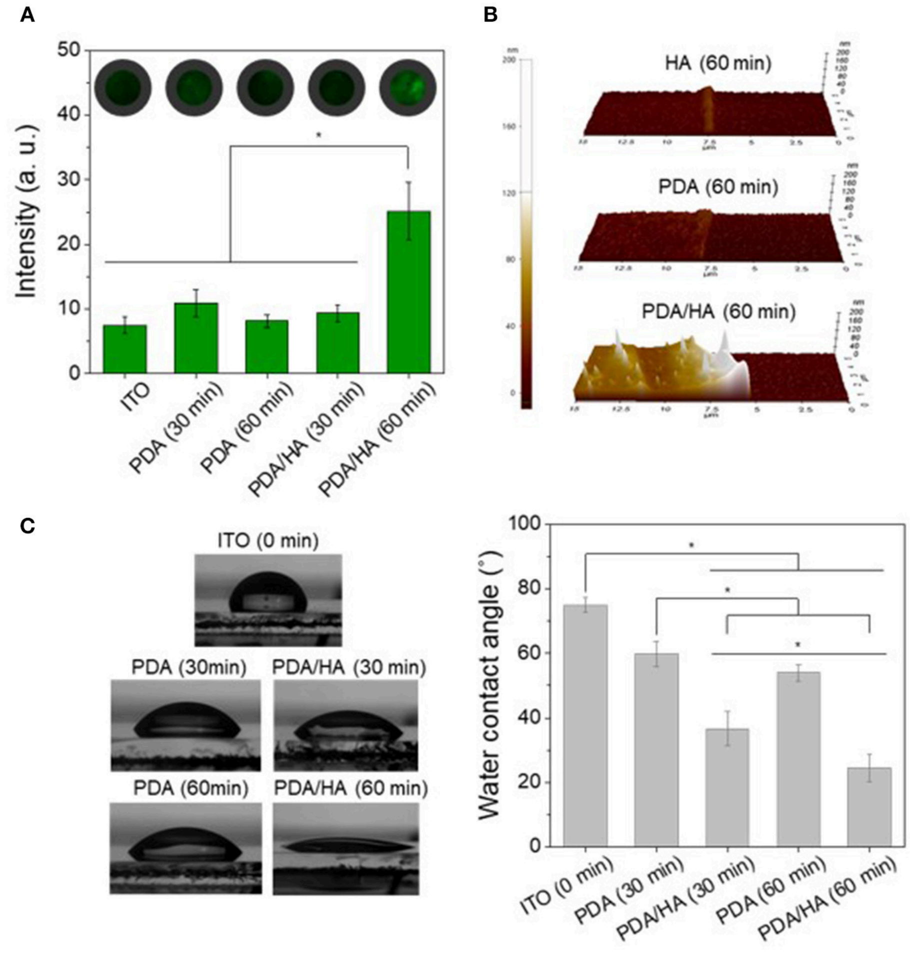

FIGURE 3 | (A) Immunofluorescence images and fluorescence intensities of the various electrodes modified with PDA or PDA/HA. FITC-HABP (fluorescein isothiocyanate labeled hyaluronic acid binding peptide) was used for HA staining. Fluorescence images for each condition were randomly selected ($n > 3$) and intensities were calculated. **(B)** AFM images of HA (60 min), PDA (60 min), and PDA/HA (60 min)-coated electrodes. **(C)** Water contact angles of bare ITO, PDA (30 min, 60 min), and PDA/HA (30 min, 60 min)-coated ITO. Asterisks indicate statistical significance ($p < 0.05$).

during electrochemical deposition, likely caused by the gradual formation of the PDA and PDA/HA layer and the local depletion of DA and HA in the vicinity of electrode surfaces. Interestingly, PDA/HA showed a lower current than PDA, which indicated that the HA was entrapped in the PDA and acted as a barrier on the electrode surface. Furthermore, the QCM results indicated that the mass increased steadily for both PDA and PDA/HA during electrodeposition (**Figure 2D**). The mass of PDA/HA increased more than that of PDA, confirming that bulky HA was well entrapped in PDA. Thus, the results indicated successful electrochemical deposition of PDA/HA onto the electrodes.

Characterization of PDA/HA-Coated Electrodes

The Electrodes electrochemically modified with PDA/HA were characterized by multiple techniques, such as immunostaining of HA, AFM, and WCA measurement. First, FITC-HABP conjugates were employed for immunostaining of HA to confirm the presence of HA on the various modified electrodes, including bare ITO, PDA, and PDA/HA with deposition times of 30 min or 60 min (**Figure 3A**). Bare ITO, PDA (30 min), PDA (60 min), and PDA/HA (30 min) had similar fluorescence intensity values. By contrast, PDA/HA (60 min) showed an approximately 3.4-fold higher fluorescence intensity than the bare ITO, indicating the successful introduction of HA chains between the PDA layers during electrochemical deposition. In addition, a high amount of free HA was deposited onto the PDA/HA surfaces, apparently via electrochemical co-deposition with PDA.

AFM was employed to assess of the film thicknesses and topographies of the various prepared coatings (**Figure 3B**). The average thicknesses of HA (60 min), PDA (60 min), and PDA/HA (60 min) were 5.9, 10.7, and 51 nm, respectively (**Figure S1**). The increased thickness of PDA/HA compared with PDA can be attributed to the incorporation of HA chains. Furthermore, the measured average roughness (Ra) of PDA and PDA/HA-coated ITO were 3.4 and 8 nm, respectively. The PDA/HA coated surface was slightly rougher than the PDA-coated surface, probably because of the entrapment of HA. Thus, it is possible to obtain a PDA/HA coated electrode, which is expected to be more efficient for proteins and cell resistance than bare and PDA-coated electrodes.

The hydrophilicity of the PDA/HA-coated electrode surface was evaluated by measuring the WCA (**Figure 3C**). The bare ITO surface was relatively hydrophobic, with a WCA of 74.9 ± 2.2° compared with the PDA and PDA/HA-coated electrodes. The PDA-coated ITO electrodes were more hydrophilic than ITO, displaying a WCA of 59.8 ± 3.9° for PDA (30 min) and 53.9 ± 2.7° for PDA (60 min). Compared with the bare and PDA-coated ITOs, electrochemical deposition of PDA/HA significantly decreased the WCA to 46.7 ± 9.7° and 24.5 ± 4.4° for PDA/HA (30 min) and PDA/HA (60 min)-coated electrodes, respectively. The increased electrochemical deposition time of PDA/HA resulted in slight increases in surface hydrophilicity of the PDA/HA-modified electrodes. The significantly hydrophilic surfaces of the PDA/HA-modified electrodes could be explained by successful incorporation of highly hydrophilic HA molecules into the coating. Highly hydrated and dynamic HA moieties immobilized on the coated layer were expected to play a key role in preventing the access and non-specific adsorption of proteins and cells by forming a hydration layer on the electrode surfaces. One-week incubation of the PDA/HA-modified electrodes in PBS revealed no significant changes in WCA, suggesting the HA component in the layer appeared to stably remain on the surfaces (**Figure S2**).

Electrochemical Characterization of PDA/HA-Coated Electrodes

Electrochemical impedances were analyzed as an important factor for the functions of the modified electrodes of biomedical applications (**Figure 4**). Impedance at low frequency (10^{-1}-10^3 Hz) was slightly decreased after PDA/HA coating; however, the difference between the unmodified bare ITO and the PDA/HA-modified ITO was not significant. This result might be attributed to the contribution of anionic HA at the interfaces and that the coverage by PDA/HA would not be too

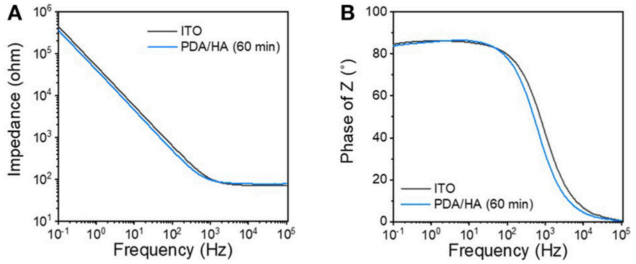

FIGURE 4 | (A) Bode and **(B)** Nyquist plots of the bare ITO and the PDA/HA (60 min)-coated ITO electrodes.

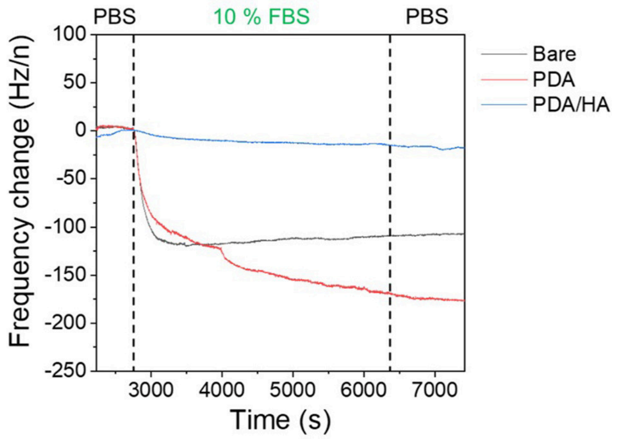

FIGURE 5 | Protein adsorption on bare ITO, PDA (60 min), and PDA/HA (60 min)-coated ITO electrodes using a quartz crystal microbalance (QCM). Frequency change profiles of bare ITO, PDA (60 min), and PDA/HA (60 min)-coated electrodes during incubation in 10% fetal bovine serum (FBS) solution. Electrodes were flowed with phosphate-buffered saline (PBS), followed by 10% FBS solution for 3,000 s and rinsing with PBS.

dense to prevent electron transfer reactions at the interfaces. Previously, we found that electrochemical deposition of DA-HA conjugates on ITO electrodes did not affect their impedances while displaying resistance to cell attachment (Kim et al., 2017). Moreover, we examined the stability of the modified electrodes while incubating them in PBS for 7 days. Impedances were not significantly altered during the incubation, implying that the PDA/HA modified electrodes would be stable under physiological conditions (**Figure S3**).

Protein Adsorption Test

Protein adsorption prompts cell attachment and is the initial event that causes an eventual FBR of implanted biomaterials, including bioelectrodes. A QCM flow cell was used to explore non-specific protein adsorption onto the surfaces of the bare, PDA-, and PDA/HA-coated electrodes in the 10% FBS-containing PBS. Before exposure to FBS, PBS was flowed on the electrode surfaces until a stable frequency was observed. As shown in **Figure 5**, bare and PDA-coated electrodes showed significant mass increases when the FBS solution began to flow across the samples. Especially, the serum proteins were remarkably adsorbed onto the PDA-coated electrodes, likely because of strong molecular interactions between PDA and various substances, including proteins. In our previous report, we found a similar trend of higher protein adsorption to PDA/polypyrrole-modified gold electrodes than to polypyrrole alone (Kim et al., 2018a). By contrast, the PDA/HA-coated electrodes did not show significant mass changes. The reduced protein adsorption onto the PDA/HA-coated materials could be accounted for by the presence of HA chains that may hinder the access and interactions of proteins with the electrode surfaces. Furthermore, we performed electrochemical analyzes using redox probes, as a model for electrochemical sensing, to investigate the effects of non-specific protein adsorption on the electrical properties of the electrodes. Specifically, after the samples were incubated in 10% FBS solution for 1 h at 37°C, their electrical properties were analyzed in the presence of 5 mM $[Fe(CN)_6]^{3-/4-}$. Non-specific protein adsorption typically inhibits the current flow of the redox probe at the electrode/electrolyte interface, resulting in increased charge transfer resistance (R_{ct}) of the electrodes and inconsistent signals, which is critically related to the practical applicability of bioelectrodes and biosensors. As shown **Figure 6**, most samples showed significant increases in R_{ct} values after incubation with

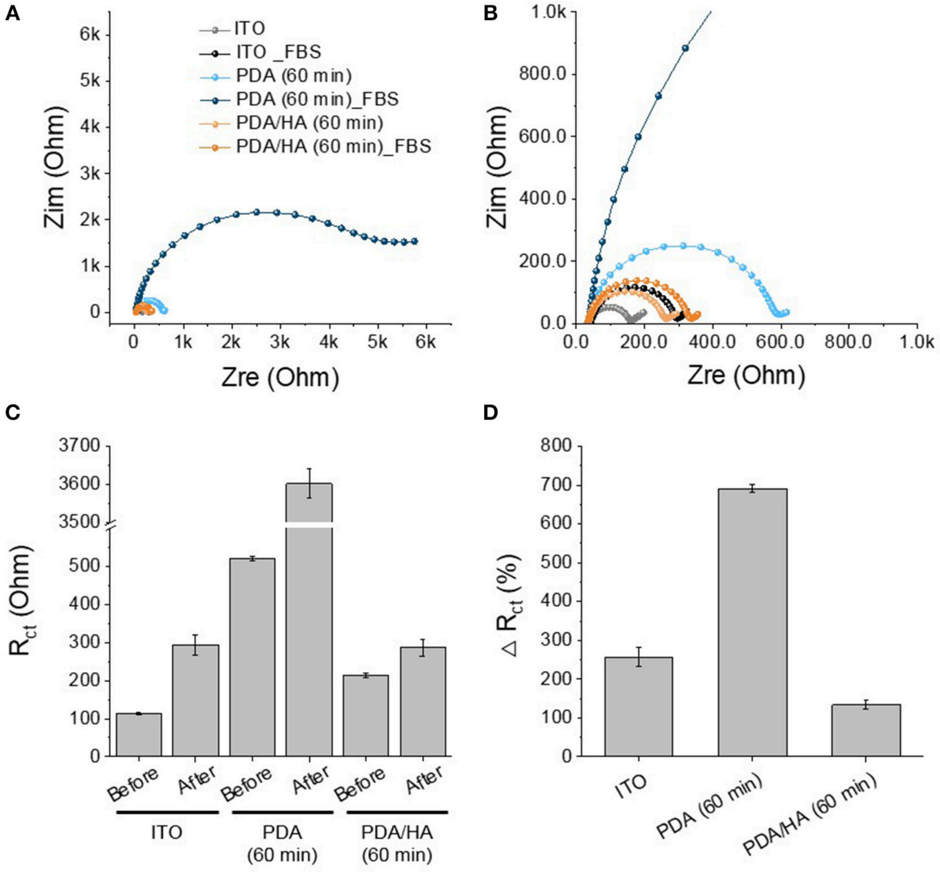

FIGURE 6 | Protein adsorption test of PDA (60 min)-modified, PDA/HA (60 min)-modified, and bare ITO. **(A)** The Nyquist plot of the electrodes after incubation in 10% FBS solution for 1 h. **(B)** Magnified plot of **(A)**. **(C)** R_{ct} values of the electrodes before and after the incubation in 10% FBS solution. **(D)** Relative increases in R_{ct} values after incubation.

serum proteins. The R_{ct} values of the bare ITO, PDA (60 min), and PDA/HA (60 min) electrodes increased from 114, 521, and 214, to 293, 3,602, and 286, respectively. Importantly, the PDA/HA-modified electrode showed a lower increase in R_{ct} than the bare and PDA-modified electrodes. The relative increases in R_{ct} values between before and after protein adsorption were 258 ± 23.9%, 692 ± 10.3%, and 134 ± 11% for bare ITO, PDA (60 min), and PDA/HA (60 min)-modified electrodes, respectively. For the PDA (60 min)-modified samples, which showed the highest protein adsorption, the R_{ct} increased by approximately 43 times post incubation compared with that of PDA/HA. These results are consistent with previous studies that PDA promotes protein adsorption (Hecker et al., 2018). The resistance changes of the PDA/HA (60 min)-modified electrode was relatively small compared with those of the other samples. These EIS results suggested that HA entrapped in the PDA layer could prevent fouling and improve the functions of implantable bioelectrodes. The result, as mentioned above, suggests that the PDA/HA coating does not cause any changes in electrochemical properties of the bioelectrodes, and in this respect, the PDA/HA-modification can be widely used in bioelectronics applications.

In vitro Cell Culture Studies

Fibrous scar tissue encapsulation of the implanted electrodes can be caused by attachment of non-specific proteins and cells, such as macrophages and fibroblasts. To observe cell adhesion, fibroblasts were cultured *in vitro* on bare, PDA-, and PDA/HA-coated ITO electrodes. As shown in **Figure 7**, no fibroblasts were found on the PDA/HA-modified substrates, regardless of the deposition time (30 or 60 min); however, cells adhered well and grew on the bare ITO or PDA-modified substrates. The deposition time for PDA/HA did not influence their ability to resist cell adhesion. In addition, the cells on the patterned substrates did not migrate from an ITO area to the PDA/HA-coated area (border lines are marked with dashed lines). These results indicated that the PDA/HA modification effectively hinders cell attachment, likely because the PDA/HA coating does not allow access of small protein molecules and large objects, such as cells. By contrast, fibroblasts adhered to the PDA-coated electrodes in both samples, regardless of the deposition time, showing no differences compared with the bare ITO surface. Higher cell attachment onto PDA could be explained in a similar context as the protein adsorption test with QCM in section Protein Adsorption Test, which was also consistent with the findings of previous reports that protein adsorption and cell adhesion were markedly promoted on PDA (Ku et al., 2010; Ding et al., 2014; Chuah et al., 2015; Kim et al., 2018a). The hydrophilic HA component on the PDA/HA appeared to contribute non-fouling properties (e.g., resistance to non-specific protein adsorption and cell attachment). Likewise, direct hydrogel coating on bioelectrodes can improve the antifouling property. However, in many cases, the electrical characteristics of hydrogel-coated electrodes were greatly deteriorated because the hydrogel acted as an electrical insulator and a diffusion barrier (Jung et al., 2017; Tavakoli and Tang, 2017). This issue can be partly addressed by conductive polymer-based hydrogel for electrode modification. Although modification with conductive hydrogels can lead to improved electrical properties, their antifouling property was greatly diminished (Cheong

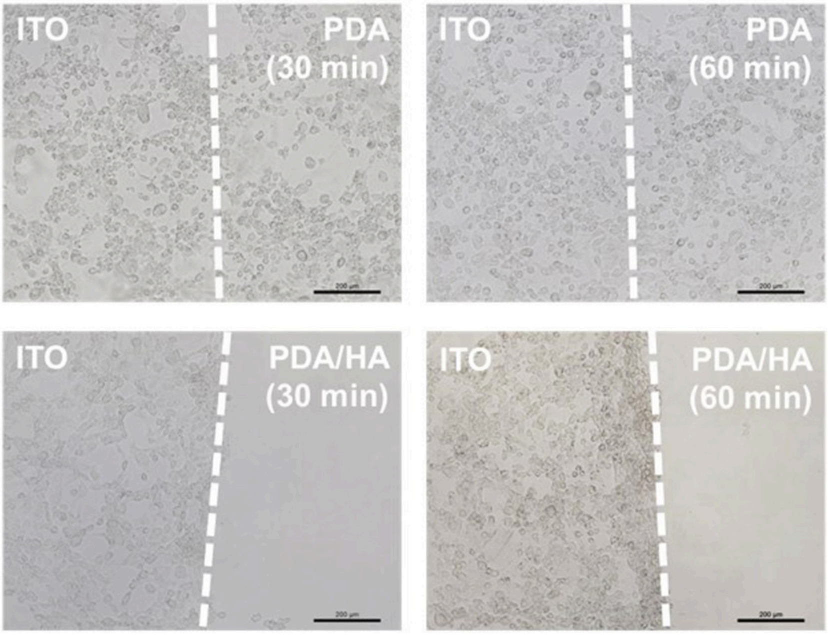

FIGURE 7 | Optical micrographs of fibroblasts cultured on the various electrodes electrochemically modified with PDA or PDA/HA for different times. Dashed lines indicate the borders between unmodified ITO and modified areas on in individual electrodes. Scale bars are 200 μm.

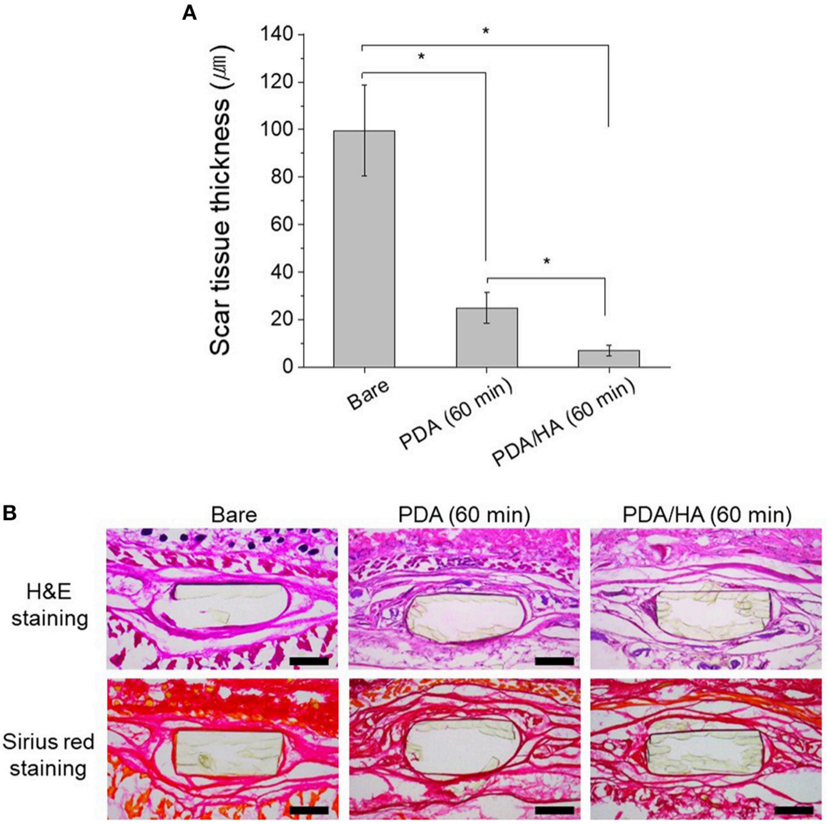

FIGURE 8 | (A) Scar tissue thickness in the tissues implanted with bare, PDA (60 min), and PDA/HA (60 min)-modified electrodes. Asterisks indicate statistical significance ($p < 0.05$). **(B)** H&E and Sirius red staining images of the tissues after 4 weeks of subcutaneous implantation of bare, PDA (60 min), and PDA/HA (60 min)-modified electrodes. Scale bars represents 200 μm.

et al., 2014; Naveen et al., 2017). In contrast, our PDA/HA-modified electrodes present both good electrical characteristics and an excellent antifouling ability; in this respect, the PDA/HA-modification can be widely used in bioelectronics applications.

In vivo Tissue Compatibility

The tissue compatibility of PDA/HA was assessed using subcutaneous implantation of the samples for 4 weeks (**Figure 8**). No symptoms of severe tissue inflammation, such as redness or yellow fluids, were observed in all the tissues implanted with these samples. In the PDA/HA-coated electrode, the scar tissue thickness was significantly reduced compared with that measured for the bare and PDA-coated electrode. The scar tissue thicknesses were 99.5 ± 19.1, 25.1 ± 6.4, and 7.1 ± 2.3 μm for the bare, PDA-coated, and PDA/HA-coated samples, respectively. HA immobilization onto biomaterials was reported to mitigate inflammatory responses (Kim et al., 2018b). HA moieties could attenuate the non-specific adsorption of proteins and cells by passivating foreign materials, and the anti-inflammatory properties might further contribute the lack of activation of inflammatory responses to the PDA/HA-modified samples. Accordingly, PDA/HA-modified electrodes can be widely applied as biocompatible implant materials for various uses.

CONCLUSIONS

To create anti-biofouling bioelectrodes, we developed and demonstrated a facile and effective method for direct electrochemical coating of PDA/HA onto electrodes. HA can be incorporated during the electrochemical deposition of PDA on the electrode surface. Characterization of the PDA/HA-modified substrates revealed the successful deposition of HA, creating a highly hydrophilic surface. Importantly, the electrochemical properties of the PDA/HA-modified electrode remained intact. Furthermore, the use of a PDA/HA coating significantly decreased the non-specific adsorption of serum proteins, cell attachment, and scar tissue formation *in vivo*. We believe that this simple and effective electrochemical method for electrode surface modification could benefit biocompatible biomaterials and thus could be used in diverse applications, including implantable bioelectrodes, biosensors, and prosthetics.

ETHICS STATEMENT

All animal experiments were performed with permission from the committee on animal research and ethics in Gwangju

Institute of Science and Technology, Republic of Korea (Approval number: GIST-2017-044).

AUTHOR CONTRIBUTIONS

SK, SL, and JL designed the study. SK and SL performed the study. JP assisted *in vivo* study. All authors participated in development and discussions.

ACKNOWLEDGMENTS

This research was supported by the Pioneer Research Center Program (2014M3C1A3053029) through the National Research Foundation of Korea (NRF) funded by the Ministry of Science, ICT and Future Planning and Korea Health Technology R&D Project through the Korea Health Industry Development Institute (KHIDI), funded by the Ministry of Health and Welfare (HI14C3484), South Korea. This work was also supported by GIST Research Institute(GRI) grant funded by the GIST in 2018.

SUPPLEMENTARY MATERIAL

The Supplementary Material for this article can be found online at: https://www.frontiersin.org/articles/10.3389/fchem.2019.00262/full#supplementary-material

REFERENCES

Banerjee, I., Pangule, R. C., and Kane, R. S. (2011). Antifouling coatings: recent developments in the design of surfaces that prevent fouling by proteins, bacteria, and marine organisms. *Adv. Mater*. 23, 690–718. doi: 10.1002/adma.201001215

Cao, L., Chang, M., Lee, C., Castner, D. G., Sukavaneshvar, S., Ratner, B. D., et al. (2007). Plasma-deposited tetraglyme surfaces greatly reduce total blood protein adsorption, contact activation, platelet adhesion, platelet procoagulant activity, and *in vitro* thrombus deposition. *J. Biomed. Mater. Res. A* 81, 827–837. doi: 10.1002/jbm.a.31091

Cheong, G. M., Lim, K. S., Jakubowicz, A., Martens, P. J., Poole-Warren, L. A., and Green, R. A. (2014). Conductive hydrogels with tailored bioactivity for implantable electrode coatings. *Acta Biomater*. 10, 1216–1226. doi: 10.1016/j.actbio.2013.12.032

Chittrakarn, T., Tirawanichakul, Y., Sirijarukul, S., and Yuenyao, C. (2016). Plasma induced graft polymerization of hydrophilic monomers on polysulfone gas separation membrane surfaces. *Surf. Coat. Technol*. 296, 157–163. doi: 10.1016/j.surfcoat.2016.04.018

Choi, S., Lee, H., Ghaffari, R., Hyeon, T., and Kim, D. (2016). Recent advances in flexible and stretchable bio-electronic devices integrated with nanomaterials. *Adv. Mater*. 28, 4203–4218. doi: 10.1002/adma.201504150

Chuah, Y. J., Koh, Y. T., Lim, K., Menon, N. V., Wu, Y., and Kang, Y. (2015). Simple surface engineering of polydimethylsiloxane with polydopamine for stabilized mesenchymal stem cell adhesion and multipotency. *Sci. Rep*. 5:18162. doi: 10.1038/srep18162

Ding, Y., Yang, Z., Bi, C. W., Yang, M., Zhang, J., Xu, S. L., et al. (2014). Modulation of protein adsorption, vascular cell selectivity and platelet adhesion by mussel-inspired surface functionalization. *J. Mater. Chem. B* 2, 3819–3829. doi: 10.1039/C4TB00386A

Fattahi, P., Yang, G., Kim, G., and Abidian, M. R. (2014). A review of organic and inorganic biomaterials for neural interfaces. *Adv. Mater*. 26, 1846–1885. doi: 10.1002/adma.201304496

Feiner, R., Engel, L., Fleischer, S., Malki, M., Gal, I., Shapira, A., et al. (2016). Engineered hybrid cardiac patches with multifunctional electronics for online monitoring and regulation of tissue function. *Nat. Mater*. 15, 679–685. doi: 10.1038/nmat4590

Grainger, D. W. (2013). All charged up about implanted biomaterials. *Nat. Biotechnol*. 31, 507–509. doi: 10.1038/nbt.2600

Hecker, M., Ting, M. S. H., and Malmström, J. (2018). Simple coatings to render polystyrene protein resistant. *Coatings* 8:55. doi: 10.3390/coatings8020055

Highley, C. B., Prestwich, G. D., and Burdick, J. A. (2016). Recent advances in hyaluronic acid hydrogels for biomedical applications. *Curr. Opin. Biotechnol*. 40, 35–40. doi: 10.1016/j.copbio.2016.02.008

Hu, Y., Liang, B., Fang, L., Ma, G., Yang, G., Zhu, Q., et al. (2016). Antifouling zwitterionic coating via electrochemically mediated atom transfer radical polymerization on enzyme-based glucose sensors for long-time stability in 37 C serum. *Langmuir* 32, 11763–11770. doi: 10.1021/acs.langmuir.6b03016

Huang, R., Liu, X., Ye, H., Su, R., Qi, W., Wang, L., et al. (2015). Conjugation of hyaluronic acid onto surfaces via the interfacial polymerization of dopamine to prevent protein adsorption. *Langmuir* 31, 12061–12070. doi: 10.1021/acs.langmuir.5b02320

Jung, I. Y., Kim, J. S., Choi, B. R., Lee, K., and Lee, H. (2017). Hydrogel based biosensors for *in vitro* diagnostics of biochemicals, proteins, and genes. *Adv. Healthc. Mater*. 6:1601475. doi: 10.1002/adhm.201601475

Kim, S., Jang, L. K., Jang, M., Lee, S., Hardy, J. G., and Lee, J. Y. (2018a). Electrically conductive polydopamine–polypyrrole as high performance biomaterials for cell stimulation *in vitro* and electrical signal recording *in vivo*. *ACS Appl. Mater. Interfaces* 10, 33032–33042. doi: 10.1021/acsami.8b11546

Kim, S., Jang, Y., Jang, L. K., Sunwoo, S. H., Kim, T., Cho, S.-W., et al. (2017). Electrochemical deposition of dopamine–hyaluronic acid conjugates for anti-biofouling bioelectrodes. *J. Mater. Chem. B* 5, 4507–4513. doi: 10.1039/C7TB00028F

Kim, S., Jang, Y., Jang, M., Lim, A., Hardy, J. G., Park, H. S., et al. (2018b). Versatile biomimetic conductive polypyrrole films doped with hyaluronic acid of different molecular weights. *Acta Biomater*. 80, 258–268. doi: 10.1016/j.actbio.2018.09.035

Kleber, C., Bruns, M., Lienkamp, K., Rühe, J., and Asplund, M. (2017). An interpenetrating, microstructurable and covalently attached conducting polymer hydrogel for neural interfaces. *Acta Biomater*. 58, 365–375. doi: 10.1016/j.actbio.2017.05.056

Ku, S. H., Ryu, J., Hong, S. K., Lee, H., and Park, C. B. (2010). General functionalization route for cell adhesion on non-wetting surfaces. *Biomaterials* 31, 2535–2541. doi: 10.1016/j.biomaterials.2009.12.020

KyungáKim, Y. (2016). Biomolecular strategies to modulate the macrophage response to implanted materials. *J. Mater. Chem. B* 4, 1600–1609. doi: 10.1039/C5TB01605C

Lee, H., Dellatore, S. M., Miller, W. M., and Messersmith, P. B. (2007). Mussel-inspired surface chemistry for multifunctional coatings. *Science* 318, 426–430. doi: 10.1126/science.1147241

Lee, J. Y., and Schmidt, C. E. (2010). Pyrrole–hyaluronic acid conjugates for decreasing cell binding to metals and conducting polymers. *Acta Biomater*. 6, 4396–4404. doi: 10.1016/j.actbio.2010.06.011

Lin, P., Lin, C.-W., Mansour, R., and Gu, F. (2013). Improving biocompatibility by surface modification techniques on implantable bioelectronics. *Biosens. Bioelectron*. 47, 451–460. doi: 10.1016/j.bios.2013.01.071

Liu, B., Liu, X., Shi, S., Huang, R., Su, R., Qi, W., et al. (2016). Design and mechanisms of antifouling materials for surface plasmon resonance sensors. *Acta Biomater*. 40, 100–118. doi: 10.1016/j.actbio.2016.02.035

Naveen, M. H., Gurudatt, N. G., and Shim, Y.-B. (2017). Applications of conducting polymer composites to electrochemical sensors: a review. *Appl. Mater. Today* 9, 419–433. doi: 10.1016/j.apmt.2017.09.001

Park, D.-W., Ness, J. P., Brodnick, S. K., Esquibel, C., Novello, J., Atry, F., et al. (2018). Electrical neural stimulation and simultaneous *in vivo* monitoring with transparent graphene electrode arrays implanted in GCaMP6f mice. *ACS Nano* 12, 148–157. doi: 10.1021/acsnano.7b04321

Park, J., Kim, G. B., Lippitz, A., Kim, Y. M., Jung, D., Unger, W. E., et al. (2019). Plasma-polymerized antifouling biochips for label-free measurement of protease activity in cell culture media. *Sens. Actuators B Chem.* 281, 527–534. doi: 10.1016/j.snb.2018.10.123

Rai, A., and Perry, C. C. (2012). Mussel adhesive protein inspired coatings: a versatile method to fabricate silica films on various surfaces. *J. Mater. Chem.* 22, 4790–4796. doi: 10.1039/c2jm15810h

Rodriguez-Emmenegger, C., Preuss, C. M., Yameen, B., Pop-Georgievski, O., Bachmann, M., Mueller, J. O., et al. (2013). Controlled cell adhesion on poly (dopamine) interfaces photopatterned with non-fouling brushes. *Adv. Mater.* 25, 6123–6127. doi: 10.1002/adma.201302492

Ryu, J. H., Messersmith, P. B., and Lee, H. (2018). Polydopamine surface chemistry: a decade of discovery. *ACS Appl. Mater. Interfaces* 10, 7523–7540. doi: 10.1021/acsami.7b19865

Salazar, P., Martín, M., and Gonzalez-Mora, J. (2016). "Polydopamine-modified surfaces in biosensor applications," in *Polymer Science: Research Advances, Practical Applications and Educational Aspects.* (Sevilla: FORMATEX RESEARCH CENTER), 385–396.

Stöckle, B., Ng, D. Y. W., Meier, C., Paust, T., Bischoff, F., Diemant, T., et al. (2014). Precise control of polydopamine film formation by electropolymerization. *Macromol. Symp.* 346, 73–81. doi: 10.1002/masy.201400130

Tavakoli, J., and Tang, Y. (2017). Hydrogel based sensors for biomedical applications: an updated review. *Polymers* 9:364. doi: 10.3390/polym9080364

Unsworth, L. D., Sheardown, H., and Brash, J. L. (2005). Protein resistance of surfaces prepared by sorption of end-thiolated poly (ethylene glycol) to gold: effect of surface chain density. *Langmuir* 21, 1036–1041. doi: 10.1021/la047672d

Xu, L., Gutbrod, S. R., Bonifas, A. P., Su, Y., Sulkin, M. S., Lu, N., et al. (2014). 3D multifunctional integumentary membranes for spatiotemporal cardiac measurements and stimulation across the entire epicardium. *Nat. Commun.* 5:3329. doi: 10.1038/ncomms4329

Ye, H., Xia, Y., Liu, Z., Huang, R., Su, R., Qi, W., et al. (2016). Dopamine-assisted deposition and zwitteration of hyaluronic acid for the nanoscale fabrication of low-fouling surfaces. *J. Mater. Chem. B* 4, 4084–4091. doi: 10.1039/C6TB01022A

Conflict of Interest Statement: The authors declare that the research was conducted in the absence of any commercial or financial relationships that could be construed as a potential conflict of interest.

ORIGINAL RESEARCH
published: 21 May 2019
doi: 10.3389/fchem.2019.00364

Boron Nitride Nanotube Addition Enhances the Crystallinity and Cytocompatibility of PVDF-TrFE

Anup Poudel[1†], Marc A. Fernandez[1†], Syed A. M. Tofail[2] and Manus J. P. Biggs[1*]

[1] CURAM, SFI Centre for Research in Medical Devices, National University of Ireland Galway, Galway, Ireland, [2] Department of Physics, and Bernal Institute, University of Limerick, Limerick, Ireland

Analysis of the cellular response to piezoelectric materials has been driven by the discovery that many tissue components exhibit piezoelectric behavior *ex vivo*. In particular, polyvinylidene fluoride and the trifluoroethylene co-polymer (PVDF-TrFE) have been identified as promising piezo and ferroelectric materials with applications in energy harvesting and biosensor devices. Critically, the modulation of the structural and crystalline properties of PVDF-TrFE through annealing processes and the addition of particulate or fibrous fillers has been shown to modulate significantly the materials electromechanical properties. In this study, a PVDF-TrFE/boron-nitride nanotube composite was evaluated by modulated differential scanning calorimetry to assess the effects of boron nitride nanotube addition and thermal annealing on the composite structure and crystal behavior. An increased beta crystal formation [f(β) = 0.71] was observed following PVDF-TrFE annealing at the first crystallization temperature of 120°C. In addition, the inclusion of boron nitride nanotubes significantly increased the crystal formation behavior [f(β) = 0.76] and the mechanical properties of the material. Finally, it was observed that BNNT incorporation enhance the adherence and proliferation of human tenocyte cells *in vitro*.

Keywords: Piezoelectric materials, tissue engineering, PVDF-TrFE/BNNT, MDSC, crystallinity

Edited by:
Carlo Augusto Bortolotti,
University of Modena and Reggio Emilia, Italy

Reviewed by:
Tamara Posati,
Italian National Research Council (CNR), Italy
Senentxu Lanceros-Mendez,
University of Minho, Portugal

***Correspondence:**
Manus J. P. Biggs
manus.biggs@nuigalway.ie

† These authors have contributed equally to this work

Specialty section:
This article was submitted to Organic Chemistry, a section of the journal Frontiers in Chemistry

Received: 14 January 2019
Accepted: 02 May 2019
Published: 21 May 2019

Citation:
Poudel A, Fernandez MA, Tofail SAM and Biggs MJP (2019) Boron Nitride Nanotube Addition Enhances the Crystallinity and Cytocompatibility of PVDF-TrFE. Front. Chem. 7:364. doi: 10.3389/fchem.2019.00364

BACKGROUND AND INTRODUCTION

Piezoelectric polymeric materials have shown great promises in biomedical engineering, finding applications as pressure/tactile sensors for catheters (Sharma et al., 2012), energy harvesting devices for orthopedic implants (Safaei et al., 2018) and ultrasonic devices for piezoelectric ablation/surgery (Labanca et al., 2008). Recently, piezoelectric polymers and their composites have garnered special interest as active scaffolds for tissue engineering applications due to their facile processibility, flexibility, biocompatibility, and electromechanical properties, and have shown to promote cell functionality, proliferation and growth *in vitro* (Hitscherich et al., 2016; Wu et al., 2018).

The ferroelectric, piezoelectric and pyroelectric properties of these polymers, depends on the polymorphic crystalline phases present within their semi-crystalline polymer matrix (Boccaccio et al., 2002; Gregorio, 2006; Lutkenhaus et al., 2010), which can be modulated through various physicomechanical processing techniques (Karode et al., 2018). In particular, Poly(vinylidene fluoride) [PVDF], a semi-crystalline fluorinated polymer has been studied extensively as a ferroelectric material, demonstrating five different crystal phases (α-phase, β-phase, α]-phase γ-phase, ε-phase, and δ-phase) (Cui et al., 2015). Among these, β-phase rich PVDF formulations have received much attention due to their pyroelectric and piezoelectric properties (Wu et al., 2019). Although β-phase crystalinity in melt or drop-casted PVDF is relatively low, multiple studies have reported that post-processing approaches can increase the formation of the β-phase content in PVDF (Gregorio, 2006; Martins et al., 2014; Cui et al., 2015). In particular, the addition of fillers, through annealing with varying pressures and temperatures and controlled cooling rates, mechanical stretching, and electric poling have been reported to modulate PVDF β-phase content.

In addition, the copolymer Poly(vinylidene fluoride)- trifluoro ethylene (PVDF-TrFE) possesses an increased β-phase content relative to PVDF, without the need for further processing requirements (Martins et al., 2014). It has been reported however, that annealing of PVDF-TrFE between the Curie and melt temperatures, further increases the β-phase crystallinity, due to enhanced molecular movement with increased temperature (Zeng et al., 2009; Lau et al., 2013). The addition of micro and nanoscale fillers has also been shown to alter the piezoelectric, thermal and mechanical behavior of PVDF with the formation of additional phases between the polymer and the filler interface (Karode et al., 2018; Mayeen et al., 2018). However, the dynamics of polymorphism mechanisms in PVDF-TrFE and its composites with the addition of different nano/micro fillers are still not well-understood, restricting the use of piezoelectric composites as smart electromechanical materials.

A key tenet of tissue engineering is biomimetic design of materials capable of providing support for cell growth, proliferation, and differentiation. With respect to tendon tissue engineering, tenocyte-seeded scaffolds have been explored widely *in vitro* and *in vivo*; however, under conventional culture, tenocytes show rapid senescence and phenotypic drift. PVDF-TrFE has recently been explored as a biomaterial for orthopedic and tendon specific applications and has been shown to modulate differential cell function *in vitro* (Ribeiro et al., 2015; Hitscherich et al., 2016; Sobreiro-Almeida et al., 2017). Critically, cells have been shown to be highly sensitive to the presence of different PVDF crystal types, crystallinity, and surface properties (roughness, chemistry, and surface free energy) which necessitates tailored surface functionalization approaches (Ribeiro et al., 2012; Martins et al., 2014) (i.e., to enhance cell adhesion), resulting in modulated piezoelectric output, collectively affecting polymer cytocompatibility (Betz et al., 2003; Klee et al., 2003). Furthermore, PVDF and PVDF-TrFE demonstrate excellent resistance to chemical modification, leading to poor functionalization potential (Klee et al., 2003).

In this study, the percentage of β-phase crystallinity in PVDF-TrFE and a PVDF-TrFE/bornon nitride nanotube (BNNT) nanocomposite is evaluated under different annealing temperatures using Fourier-transform infrared spectroscopy (FTIR) and differential scanning calorimetry (DSC). In addition, the molecular movement and crystal formation process of ferroelectric PVDF-TrFE and PVDF-TrFE/BNNT composites, was assessed via modulated differential scanning calorimetry (MDSC) to evaluate the relaxation phenomena of these materials. Finally, in order to assess PVDF-TrFE/BNNT composites, as tendon specific biomaterials, the mechanical (tensile analysis) and cytocompatibility (*in vitro* studies with primary human tenocytes) was assessed in poly acrylic acid functionalized materials.

MATERIALS AND METHODS

PVDF-TrFE Film Preparation

The PVDF-TrFE (70-30 mol %, MW = 300 kDa) copolymer was purchased from Solvay in powder form. Boron Nitride Nanotubes (BNNT) were obtained from BNNT Ltd. PVDF-TrFE was dissolved in a 1:1 ratio DMF/acetone mixture with a solute ratio of 5:1, and cast onto a glass plate to form films of 20–30 um thickness. BNNTs were subjected to ultrasonication for 4 h in a 1:1 ratio DMF/acetone mixture before the addition of PVDF-TrFE. Solution of PVDF-TrFE were subjected to varying drying temperatures as described below. After solvent evaporation, the films were further subjected to a subsequent 12 h of further annealing at the drying temperature.

Differential Scanning Calorimetry (DSC) and Fourier-transform Infrared Spectroscopy (FTIR)

DSC experiments were carried out on all samples using a TA instrument 2000. Samples (5–8 mg) encapsulated in Tzeropans were quenched at a rate of 2°C/min to −75°C and kept under isothermal conditions for 3 min followed by heating at 10°C/min to 160°C follow by cooling at 10°C/min.

β-phase analysis was conducted with Attenuated Total Reflectance- Fourier Transfer Infrared Spectroscopy (ATR-FTIR). Infrared spectra of all materials and nanocomposites were obtained with a VARIAN 600 ATR-FTIR at room temperature. All data were collected between 600 cm^{-1} and 4000 cm^{-1} with an average of 32 individual scans. Using the absorption band of α and β phases at 532 cm^{-1} and 846 cm^{-1}, the fraction of β-phase [F(β)] was calculated using the following equation

$$F(\beta) = \frac{X_\beta}{X_\alpha + X_\beta} = \frac{A_\beta}{1.26A_\alpha + A_\beta} \tag{1}$$

where X_α and X_β are the crystalline mass fractions of the α and β phases and A_α and A_β correspond to absorption bands at 532 cm^{-1} and 846 cm^{-1}, respectively. It was assumed that absorption bands follow the Beer-Lambert law with an absorption coefficient of $K_\alpha = 6.1 \times 104\ \mathrm{cm}^2/\mathrm{mol}$ and $K_\beta = 7.7 \times 104\ \mathrm{cm}^2/\mathrm{mol}$.

Modulated Differential Scanning Calorimetry (MDSC)

MDSC experiments were carried out using a TA instrument 2000. An oscillation time period of 60 s and an amplitude of ±0.47°C was used during the heating and cooling cycles. Samples were purged with liquid nitrogen at 50 ml/min of cooling. Eight milligram of each sample were encapsulated and sealed in Tzero pans. For all experiments, samples were isothermally maintained for 3 min at the beginning and end of the heating and cooling runs and subjected to a sample quenching process from room temperature to −75°C. Samples were kept under isothermal conditions for 3 min followed by heating at 3°C/min. A similar method was previously implemented for microphase and molecular movement studies using a different copolymer (Karode et al., 2017; Poudel et al., 2017).

Tensile Analysis

Tensile analysis of thin films was performed using a Zwick/Roell Z010 with a 1 kN load cell, a crosshead speed of 500 mm/min and a maximum extension of 500%. Thin films were prepared according to ASTM D 882. Results were presented as average values of $n = 5$ replicate experiments with standard deviation.

Electrical Poling and Quasi-Static Measurement of Piezoelectric Coefficient

Electrical poling was carried out using direct current (dc) voltage. Thin films were clamped between two steel electrodes and subjected to an electric field of 100 V/um which was applied at 80°C for 10 min. The piezoelectric d33 coefficient of the thin films was measured by sandwiching the films between the electrodes which applied a quasi-static oscillatory force of 250 mN at a frequency of 111 Hz using a commercial piezometer (PM300, Piezotest, UK).

Cytocompatibility Studies

Fibronectin Functionalization

Pristine PVDF-TrFE and PVDF-TrFE/BNNT substrates were oxygen plasma treated for 45 s at 30 W and with an oxygen flow rate of 30 ml/min to form surface hydroperoxides (Völcker et al., 2001). Subsequently, hydroperoxides decomposed due to thermal gradients to produced secondary radicals to initiate the polymerization of acrylic acid (AAc). After oxygen plasma polymerization, treated surfaces were immersed in a 20% v/v AAc aqueous solution previously purged with nitrogen at 90°C using a reflux system to avoid changes in concentration. Next, the pAAc functionalized surfaces were rinsed with distilled H20 for 18 h to remove unreacted monomers. Finally, caboxyl groups were activated with 0.1 M EDC and 0.1 M NHS (1:1) for 1 h. Immediately after films were immersed in a fibronectin solution (Sigma-aldrich, F1141-1MG) (10 ug/ml) for 2 h at room temperature.

Tenocyte Cell Culture

Human tendon derived cells were harvested from patellar tendon during tendon grafting operations after obtaining written informed consent. From these tissue specimens human primary tenocytes were isolated and cultured. All cells were maintained in Dulbecco's Modified Eagle's Medium (DMEM/F-12 with Glutamax, Gibco-BRL) supplemented with penicillin (100 U ml−1), streptomycine (10 μg ml^{-1}) (both Sigma-Aldrich) and 10% fetal calf serum (Gibco-BRL). Cells were detached by incubation with 0.05% trypsin for 5 min at 37°C. They were identified as tenocytes through their characteristic growth pattern and by detection of scleraxis (SCX) and tenomodulin (TNMD) expression. The studies were performed with cells at passage 2–3 and a total of 3 donors were used for all assays.

Live/Dead Assay

Viable cells were seeded at a density of 5000 per well in 96-well ($n = 5$) plates for quantitative analysis and in 4-well glass bottom chamber slide for fluorescent microscopy. Tenocytes were cultured for 1, 3, or 7 days. Untreated live and dead cells were used as controls for quantitative analysis. A Live/Dead Assay (Life Technologies) was used to visualize viable and necrotic cells. After 1, 5, and 10 days, samples were washed with PBS and stained with calcein and ethidium bromide from the kit as recommended by manufacturer. The cells were incubated with the stock solution for 25 min and protected from light. The well plates were immediately analyzed with a Varioskan Flash plate reader. Samples were subsequently imaged on an Olympus IX81 inverted fluorescent microscopy with 20× objective.

Cell Proliferation Assay

For cell proliferation analysis, tenocytes were seeded onto all experimental and control films in a 6-well plate at 4.5×10^4 cells/film ($n = 3$). Cell metabolic activity and proliferation were assessed by Alamar Blue assay (Sigma-Aldrich). The cells were incubated in medium supplemented with 10% (v/v) Alamar Blue dye for 4 h and the absorbance at 570 and 590 nm measured in a 96-well plate using a Varioskan Flash Plate reader. Non-seeded biomaterial in the same medium was used as a negative control.

Statistical Analysis

Data was analyzed using Minitab 8 and was presented as mean ± SD from three or more separate experiments, as indicated. A Student's *T*-test (for single comparison) or one-way ANOVA (for multigroup comparisons). Tukey *post hoc* analysis was used to identify statistical significance.

RESULTS AND DISCUSSIONS

PVDF-TrFE and PVDF-TrFE/BNNT thin films were formulated via a drop-casting approach in a co-solvent of Acetone/DMF. It has been previously observed that although DMF is a better solvent for PVDF, acetone and DMF mixtures modulate the porosity and the dielectric breakdown strength of PVDF films (Chen et al., 2017) through control of solvent evaporation (California et al., 2011). In addition, solvent-cast PVDF-TrFE films formed through the evaporation of DMF at room temperature are associated with large diameter pores (μm sized) (Nunes-Pereira et al., 2015; Bodkhe et al., 2017; Ribeiro et al., 2018) which decreased with the use of a co-solvent of DMF and acetone without major alteration to the materials piezoelectric behavior (Chen et al., 2017). Furthermore, the addition of acetone to DMF favors low evaporation temperature with promotion of beta phase formation (Cui et al., 2015).

Digital brightfield microscopy of solvent-cast 0.5 wt.% and 1 wt.% BNNT nanocomposite films indicated BNNT dispersion without aggregation. Conversely, solvent-cast 1.5% w/v BNNT nanocomposite films were observed to contain BNNT agglomerations as (**Figures 1A–D**). However, use of further dispersal techniques as described previously could be

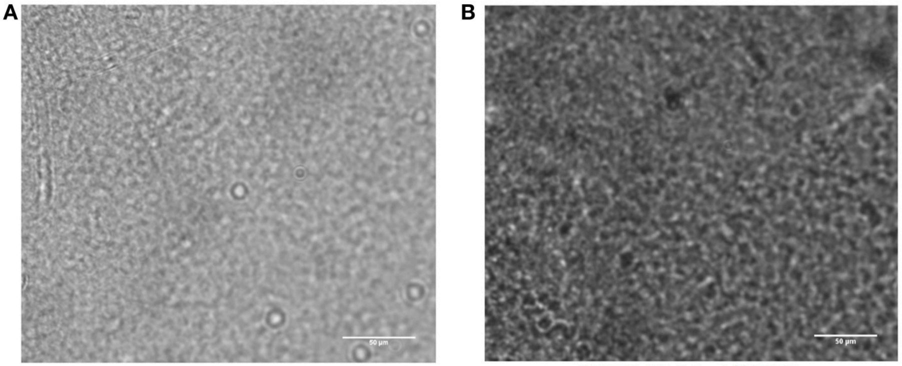

PVDF-TrFE

PVDF-TrFE+ 0.5 wt.% BNNT

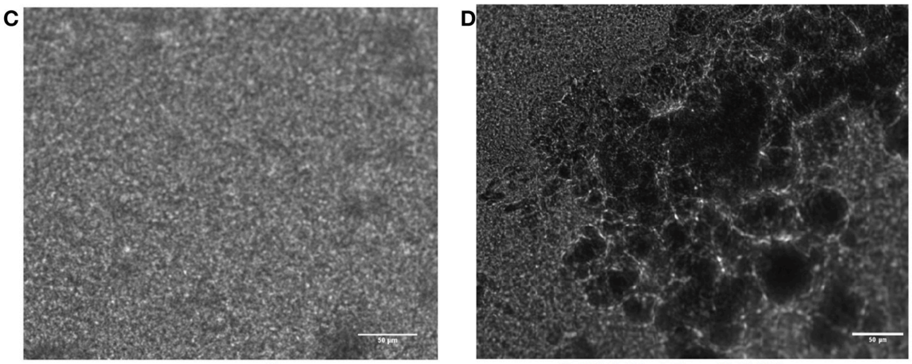

PVDF-TrFE+ 1 wt. % BNNT

PVDF-TrFE+ 1.5 wt. % BNNT

FIGURE 1 | Digital microscopy images of **(A)** PVDF-TrFE **(B)** PVDF-TrFE+1% BNNT, **(C)** PVDF-TrFE+1% BNNT and **(D)** PVDF-TrFE +1.5% BNNT.

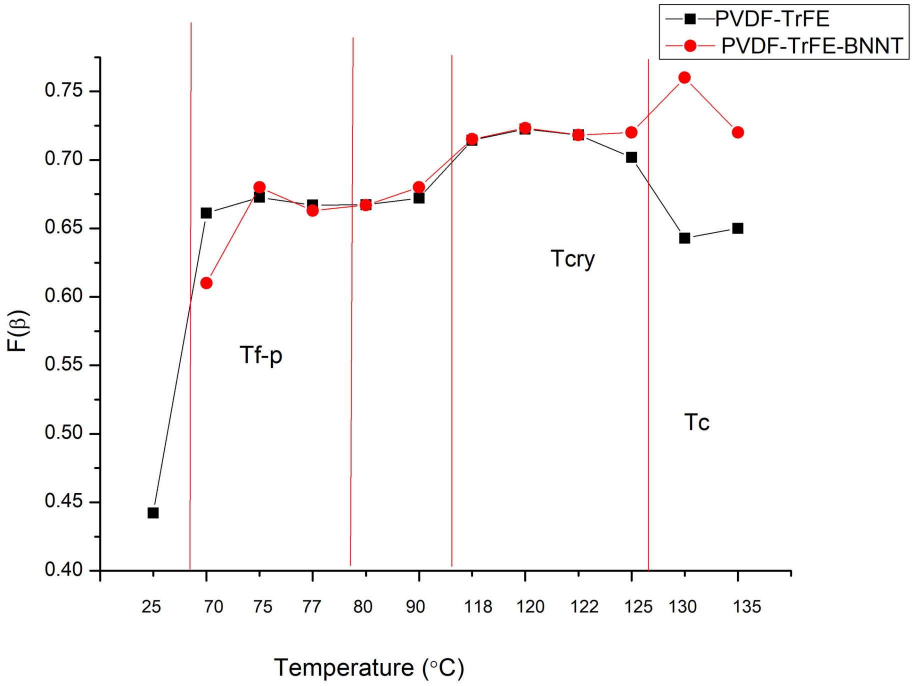

FIGURE 2 | FTIR analysis of the β-phase fraction in pristine PVDF-TRFE and PVDF-TRFE/BNNT nanocomposites annealed under different temperature conditions for 12 h.

used for better dispersion of BNNT at higher percentage in the polymer matrix and will be investigated in a follow-up study (Karode et al., 2018; Poudel et al., 2019). 1 wt.% BNNT nanocomposite films were subsequently selected for the focus of this study as the alteration of crystalline behavior of polymers upon the addition of a nanoscale filler is more pronounced when the fillers wt.% is sufficiently lower than the threshold concentration at which agglomeration occurs (Karode et al., 2018).

As the β-phase content of PVDF-TrFE and PVDF-TrFE composites has a direct impact on the piezoelectric properties of a polymer, the β-phase fraction was assessed using FTIR in samples subjected to a 12 h annealing process with temperatures ranging from 25 to 130°C. It was observed that

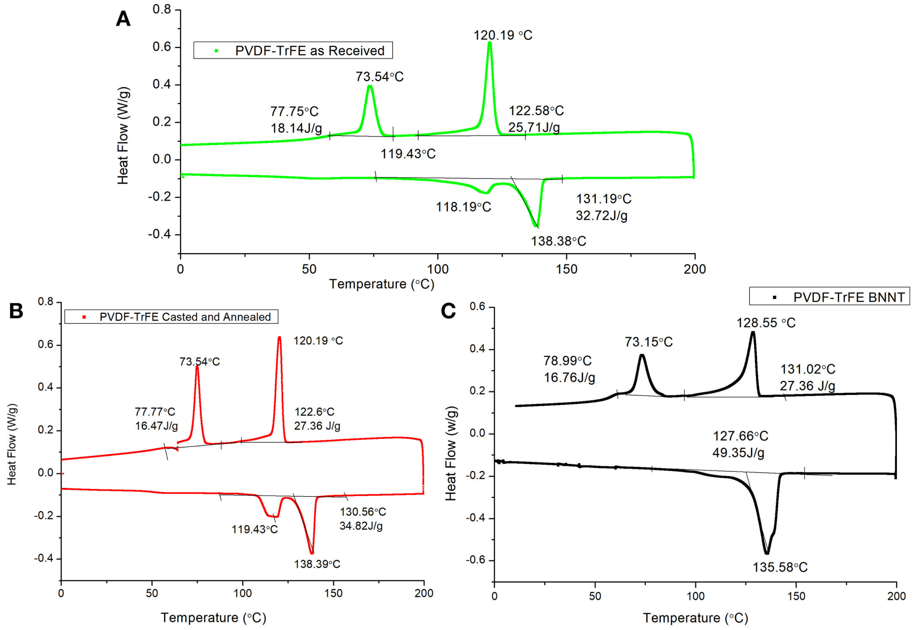

FIGURE 3 | Representative DSC curves of **(A)** PVDF-TrFE as-received, **(B)** Solvent-cast PVDF-TrFE annealed at 120°C and **(C)** Solvent-cast PVDF-TrFE BNNT 1 wt.% nanocomposite annealed at 120°C.

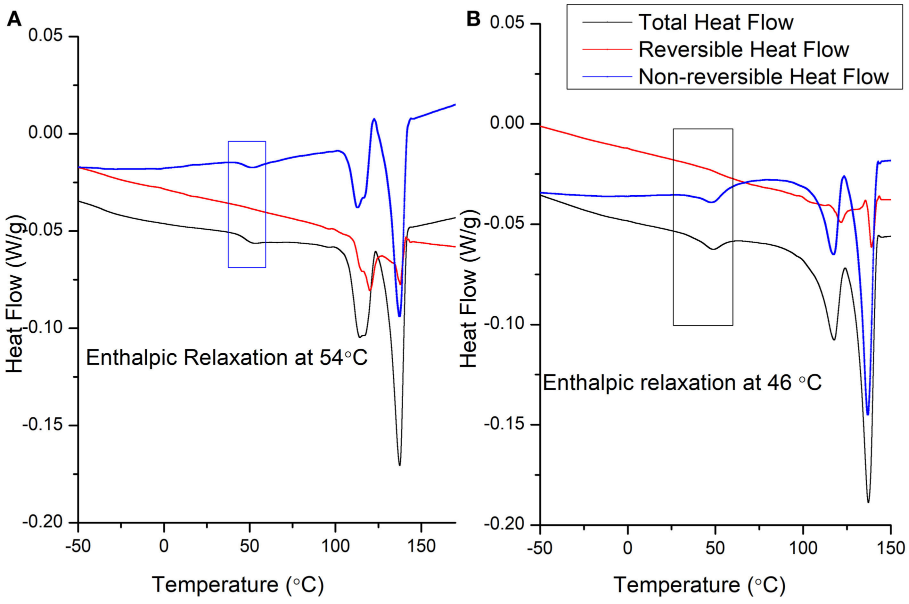

FIGURE 4 | Representative MDSC heating cycle curves of **(A)** as-received PVDF-TrFE and **(B)** solvent-cast PVDF-TrFE films annealed at 120°C.

the annealing temperature had a direct impact on the β-phase formation in PVDF-TrFE films, with the highest β-phase content in pristine PVDF-TrFE observed in samples annealed at 120°C, just above the T_c Curie temperature. Similarly, PVDF-TrFE/BNNT nanocomposites annealed at 120°C possessed a beta fraction [F(β)] equal to 0.72, similar to that of PVDF-TrFE annealed at 120°C (**Figure 2**). However, annealing of PVDF-TrFE/BNNT at 130°C resulted in a higher F(β) value, which was further investigated using DSC and MDSC techniques.

Conversely, annealing above 135°C was excluded as PVDF-TrFE started to melt above this temperature (**Figure 2**). Here,

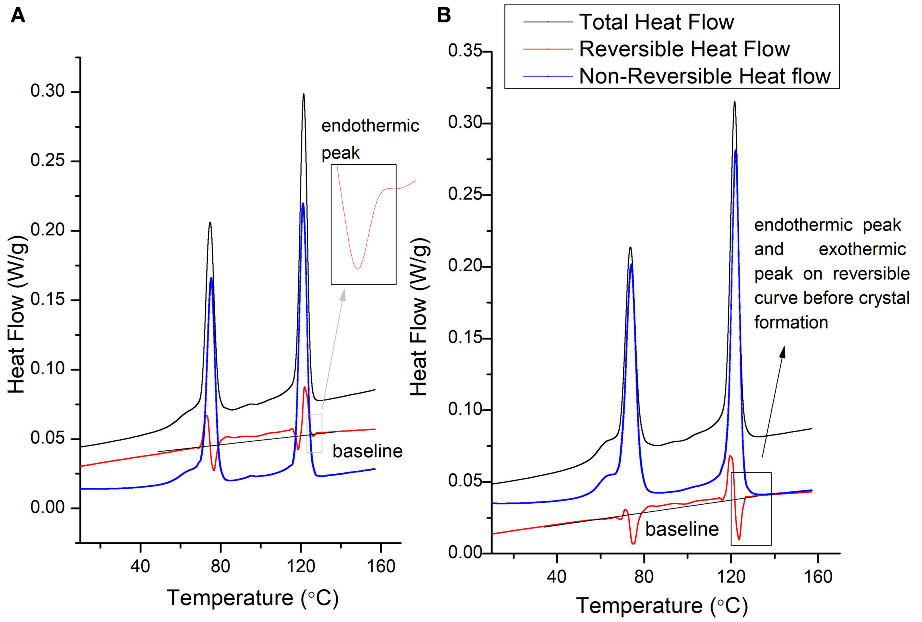

FIGURE 5 | Representative MDSC cooling cycle curves of **(A)** as-received PVDF-TrFE and **(B)** solvent-cast PVDF-TrFE films annealed at 120°C.

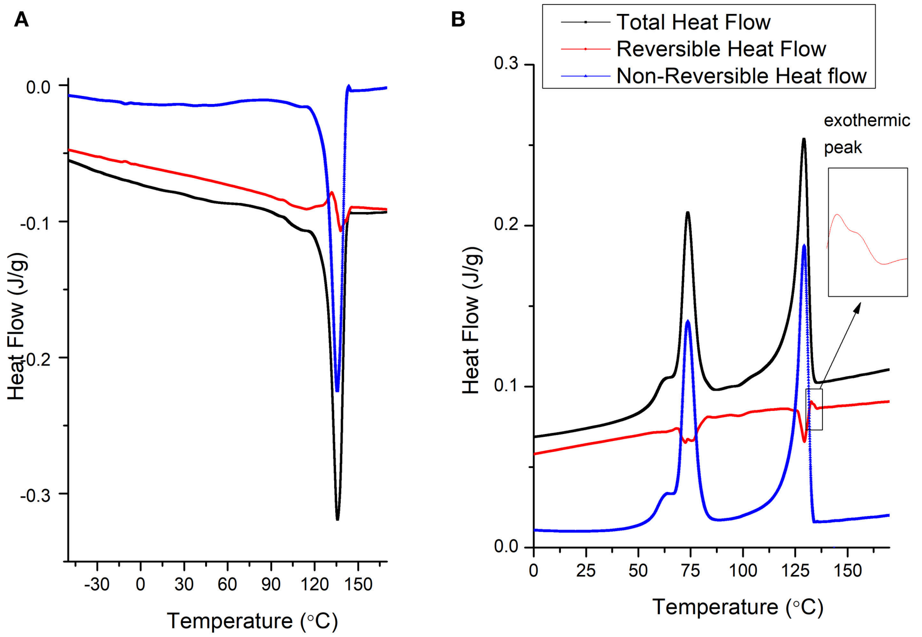

FIGURE 6 | Representative MDSC curves of solvent-cast PVDF-TrFE BNNT 1 wt.% nanocomposites annealed at 120°C **(A)** heating cycle and **(B)** cooling cycle.

the F(β) was observed to decrease as the annealing temperature approached the T_m and to decrease significantly when the samples were subjected to room-temperature drying and annealing conditions. It has been reported previously that β-phase crystallinity is substituted by a high α-phase content when PVDF is quenched from the melt or annealed at room temperature (Ramasundaram et al., 2008). Ramasundaram et al. also observed that the fraction of β-phase, F(β) in PVDF decrease as the annealing temperature increases above 120°C. This was not observed with PVDF-TrFE in this study, perhaps due to the rapid β-phase crystallization occurring in PVDF-TrFE (Lutkenhaus et al., 2010).

Figures 3A–C shows representative DSC curves (heating and cooling of 5°C/min) of PVDF -TrFE (as-received), solvent-cast PVDF-TrFE annealed at 120°C, and solvent-cast PVDF-TrFE/BNNT 1 wt.% annealed at 120°C. During the heating and cooling cycles two clear peaks were observed for PVDF-TrFE samples representing crystal formation during the heating and cooling processes (**Figure 3A**). It has been hypothesized previously that the first endothermic peak represents the phase transformation (termed the ferroelectric Curie temperature), and is characteristic of piezoelectric polymers (Martins et al., 2014), while the second endothermic peak represents the polymer melting temperature (T_m). After the copolymer was solvent cast and annealed at 120°C, the two melting peaks became narrow (unannealed PVDF-TrFE ranging from 118.1°C to 138.3°C and annealed PVDF-TrFE ranging from 119.4°C to 138.3°C), as a result of the increased content of all-trans chains in the copolymer (**Figure 3B**). The addition of BNNT resulted in an increase in the observed curie temperature of the polymer, yet no difference in the T_c and T_m temperature relative to pristine PVDF-TrFE. The T_c in PVDF-TrFE/BNNT 1wt.% nanocomposites occurred over a broad range which is thought to be due to the formation of a large number of crystals and overlapping thermal events (**Figure 3C**).

In addition, the observed enthalpy of the heat of melting and total heat flow (ΔH) was greater in PVDF-TrFE/BNNT 1wt.% nanocomposites, suggesting an enhanced crystallinity of the PVDF-TrFE matrix through the addition of BNNTs. During the cooling cycle, the first crystal formation occurred at ∼120°C, although crystal formation was initiated at ∼122°C. It has been hypothesized that the paraelectric to ferroelectric transition occurs at low temperatures in PVDF, which was identified here to occur at 73°C.

TABLE 1 | Mechanical properties of solvent-cast PVDF-TrFE films annealed at room temperature and 120°C and solvent-cast PVDF-TrFE BNNT 1 wt.% nanocomposite films annealed at 120°C.

Materials	Young's modulus (MPa)	Modulus of resilience (MPa)	Modulus of toughness (MPa)
PVDF-TrFE annealed at RT	466.2 ± 38.8	51.77 ± 4.2	2517.01 ± 294.2
PVDF-TrFE annealed at 120°C	801.2 ± 32.8	65.72 ± 6.6	3307.06 ± 252.3
PVDF-TrFE and BNNT 1 wt % annealed at 120°C	1009.1 ± 56.2	112.26 ± 12.06	988.23 ± 102.3

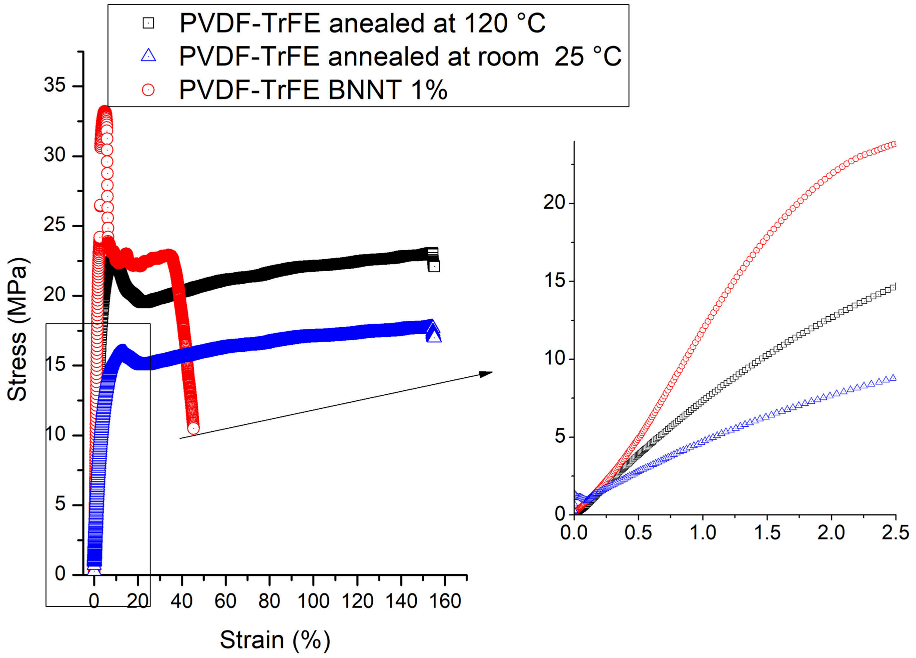

FIGURE 7 | Tensile stress-strain analysis of solvent-cast PVDF-TrFE films annealed at room temperature and 120°C and solvent-cast PVDF-TrFE BNNT 1 wt.% nanocomposite films annealed at 120°C.

The low heat of enthalpy noted in as-received PVDF-TrFE samples relative to solvent-cast PVDF-TrFE films annealed at 120°C and solvent-cast PVDF-TrFE/BNNT 1 wt.% nanocomposites annealed at 120°C suggested a low crystallinity was present in PVDF-TrFE (as-received). The percentage of heat of enthalpy, which is directly corelated to percentage of crystallinity, of PVDF-TrFE was increased by 6.5% when annealed at 120°C and by 50% with the addition of BNNT 1 wt.% compared to PVDF-TrFE as-received. A significant difference in total crystallinity however was also noted between PVDF-TrFE annealed and PVDF-TrFE/BNNT, which both possessed a high crystallinity.

In order to assess a correlation between polymer crystallization and molecular moment phenomena in pristine PVDF-TrFE (as-received), solvent-cast PVDF-TrFE films annealed at 120°C and solvent-cast PVDF-TrFE/BNNT 1 wt.% nanocomposites annealed at 120°C, modulated differential scanning calorimetry (MDSC) was performed to resolve overlapping kinetic events into reversing and non-reversing DSC curves. This technique has been recently used to characterize complex block polymers, but has not been fully utilized to characterize the molecular movement and crystallization behavior of PVDF-TrFE (Knopp et al., 2016; Karode et al., 2017).

Figures 4A,B indicate the MDSC curves of as-received PVDF-TrFE and solvent-cast PVDF-TrFE films annealed at 120°C. The total heat flow is divided into two main events (i) a reversing curve, which directly measures the specific heat capacity, which in turn is a measure of the change in the molecular movement within a polymer occurring in a time scale shorter than a modulation time period (Lutkenhaus et al., 2010; Karode et al., 2017). Similarly, (ii) the non-reversing curve, indicates kinetic phenomena which occur with a time duration greater than the modulation time period. The first transition, an enthalpic relaxation was observed in as-received PVDF-TrFE at ∼54°C yet was shifted to 47°C in solvent-cast PVDF-TrFE films annealed at 120°C. Previous studies suggest that this shift in the

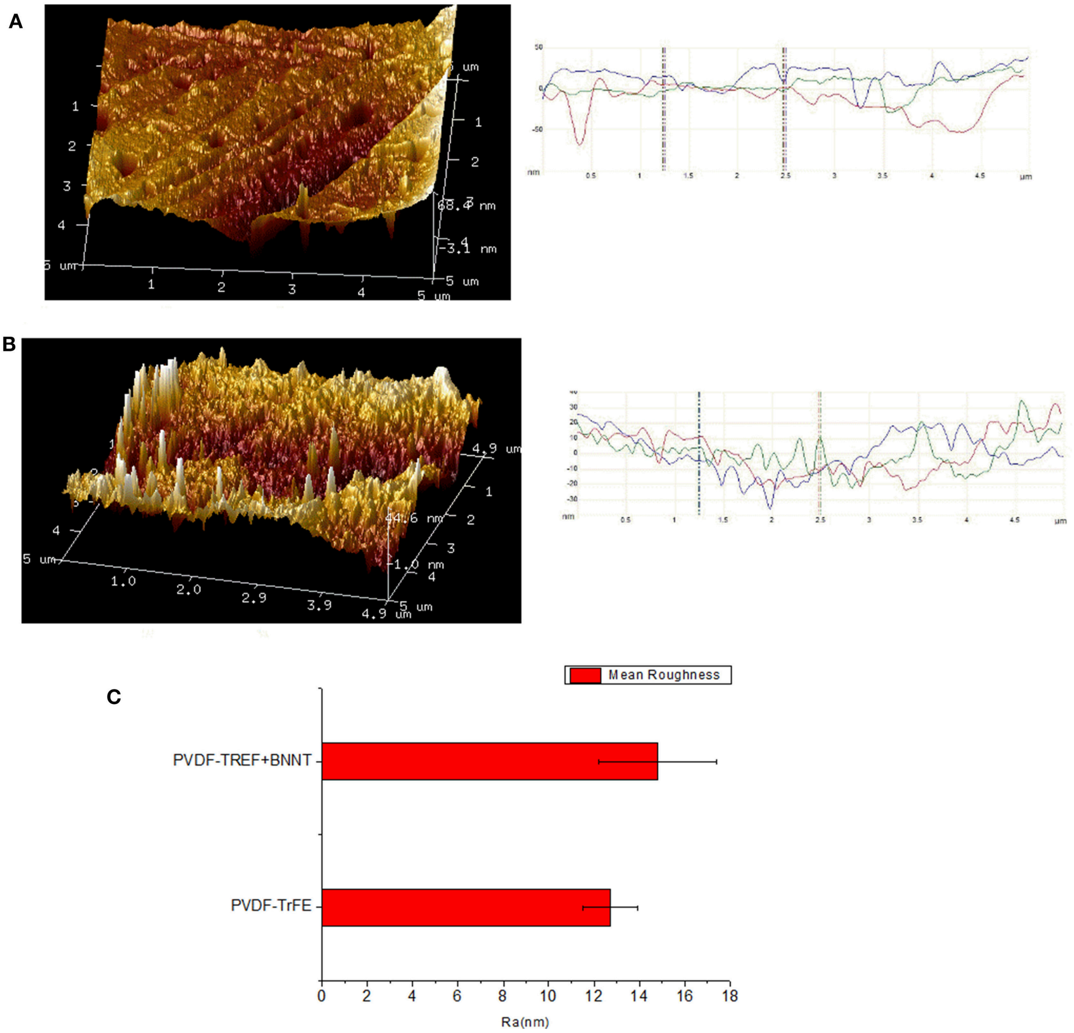

FIGURE 8 | (A) AFM surface analysis of PVDF-TrFE and **(B)** PVDF-TrFE +1 wt.% BNNT. **(C)** Mean roughness (Ra) of PVDF-TrFE and PVDF-TrFE +1 wt.% BNNT.

enthalpic relaxation temperature is due to the phase segregation within a copolymer which occur during the thermal annealing process. This type of thermal relaxation observed in copolymers is responsible for the initiation of the molecular movement which occur at the interface of two thermally incompatible phase domains, i.e., crystalline-amorphous domains or different crystalline-crystalline domains. The second endothermic peaks observed at ∼125°C and 138°C in as-received PVDF-TrFE and solvent-cast PVDF-TrFE films annealed at 120°C respectively represent kinetic phenomena, as demonstrated by the non-reversing curve. The initial endothermic peak, observed at ∼125°C was followed by an exothermic peak at ∼129°C (cold crystallization) in the total and non-reversible curve of both annealed and non-annealed PVDF-TrFE indicates fusion of the metastable phase of the copolymer into more stable crystal forms. Due to the kinetic phenomena observed prominently in the non-reversible heat flow curve relative to the reversible heat flow curve. The final endothermic peak at ∼138°C is assigned to the fusion of stable crystals and is clearly observed in the reversable as well as non-reversible heat flow curves in both as-received and annealed PVDF-TrFE formulations, suggesting the final melting point of all formed crystals.

The MDSC cooling cycle for as-received PVDF-TrFE (**Figure 5A**) and solvent-cast PVDF-TrFE films annealed at 120°C (**Figure 5B**) suggests that the crystallization phenomena represent a kinetic process, however, a change in the molecular movements (endothermic and exothermic phenomena in the reversible curve) as a function of specific heat capacity was observed during crystallization. The initiation of molecular movement in both solvent casted and as-received PVDF-TrFE (denoted by endothermic followed by exothermic phenomena) occurred just above the Curie temperature (the temperature at which a significant degree of crystals were formed in this copolymer), during the crystal formation process. The initial endothermic peak during the cooling cycle suggested a significant molecular movement before the initiation of crystal formation. This phenomenon was followed by a restriction of molecular movement due to the initiation of crystal formation and was denoted by an exothermic peak in the reversible cooling cycle curve. Previous studies suggest that during annealing of the polymer, a high degree of molecular movement occurs, favoring high β-phase crystallinity in annealed PVDF-TrFE (Lau et al., 2013). As observed in the reversible cooling cycle curve, the restricted molecular movement in as-received PVDF-TrFE

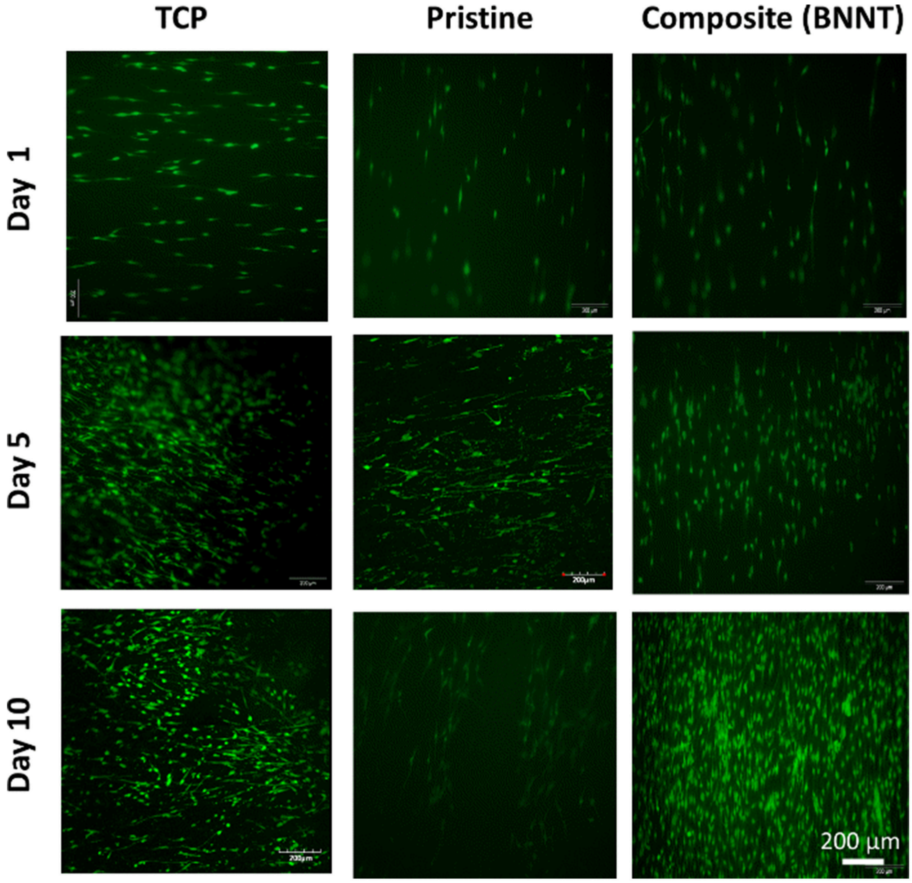

FIGURE 9 | Live/dead assay of human tenocytes cultured for 1, 5 and 10 days *in vitro* on unpoled pristine solvent-cast PVDF-TrFE films annealed at 120°C and (B) solvent-cast PVDF-TrFE 1 wt. % BNNT nanocomposite films annealed at 120°C.

occurred over the range of the experimental temperatures as the curve remained above the baseline, resulting in heterogeneous β-phase crystal formation. Conversely, solvent-cast PVDF-TrFE films annealed at 120°C were associated with a more homogenous crystal formation, as molecular movements were more restricted relative to the non-annealed samples.

Annealing of the copolymers at any temperature between the Curie and melt temperatures however, may not have provided sufficient molecular restriction for a high degree of β-phase crystallinity due to (a) the formation of temperature mediated phase-separated domains and (b) crystal formation from melt may not always occur in between the Curie and melt temperature observed at 118°C and 138°C respectively.

With the addition of 1 wt. % BNNT to the PVDF-TrFE matrix, no enthalpic relaxation was observed at low temperatures during the heating cycle, and the composite showed a single melting point as observed in the total heat flow curve (**Figure 6A**). This suggests a high interaction of BNNT with different PVDF-TrFE crystal domains, resulting in a slow relaxation of copolymer chains due to (a) high amorphous domain entanglement and (b) modulated inter-crystal crystallization. Confirmation of different crystal formation phenomena requires crystallization studies, which remains a major future study for this work. Moreover, due to the high interaction between polymer chains and the incorporated BNNTs, the modulation time used (60 s) was not long enough to observe the reversible process at a melting point in the reversible heat flow curve. However, the polymer chain movement occurred within 60 s for pristine PVDF-TrFE as observed in **Figure 4**.

During the crystallization temperature of the cooling cycle (**Figure 6B**), solvent-cast PVDF-TrFE BNNT 1 wt.% nanocomposites annealed at 120°C demonstrated a low molecular movement in the reversing curve compared to both annealed and non-annealed PVDF-TrFE samples. However, crystals were formed mainly due to kinetics process, as observed in the non-reversible curves and minor molecular movement was observed during the crystal formation process at the crystallization temperature. Interestingly, initiation of restriction (a small exothermic peak on the reversing curve) occurred at 132°C in solvent-cast PVDF-TrFE BNNT 1 wt.% nanocomposites annealed at 120°C, a temperature 12°C higher than observed with pristine PVDF-TrFE formulations, suggesting the nucleation of crystals at higher temperatures through BNNT addition. This early restriction of molecular movement is also suggested by an observed increase in the viscoelastic properties of PVDF-TrFE BNNT 1 wt.% nanocomposites, resulting in an increased Young's modulus and modulus of resilience relative to both pristine PVDF-TrFE formulations (**Figure 7**; **Table 1**).

In addition, the modulus of toughness and the percentage of elongation in pristine solvent-cast PVDF-TrFE annealed at room temperature decreased sharply with the addition of BNNT 1 wt. %, which was attributed to a high entanglement of BNNTs with the amorphous phase of PVDF-TrFE, leading to a low extension capability. Similarly, solvent-cast PVDF-TrFE annealed at 25°C was associated with a low Young's modulus and modulus of resilience. Failure did not occur at 150% strain in both pristine PVDF-TrFE samples, however, solvent-cast PVDF-TrFE BNNT 1 wt.% nanocomposites annealed at 120°C were observed to fail at 40% strain.

AFM analysis of PVDF-TrFE and PVDF-TrFE BNNT 1 wt. % films was performed to assess surface topography and to measure the surface roughness (**Figure 8**). The mean surface roughness of solvent-cast PVDF-TrFE films annealed at 120°C and solvent-cast PVDF-TrFE BNNT 1 wt.% nanocomposite films annealed at 120°C was found to be 12.7 ± 1.2 nm and 14.8 ± 2.6 nm

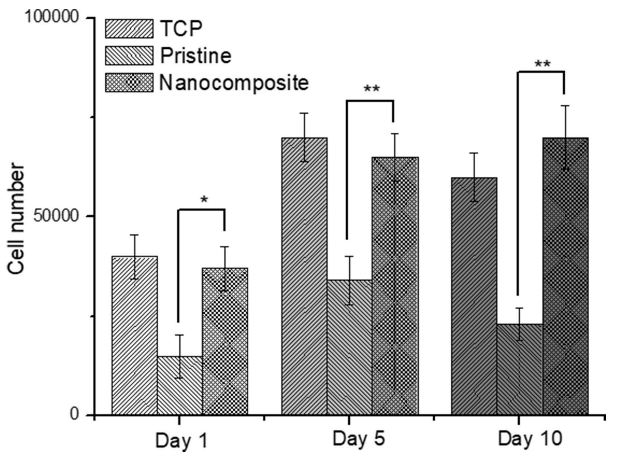

FIGURE 10 | Total cell number of human tenocytes cells cultured on pristine annealed PVDF-TrFE and annealed PVDF-TrFE 1 wt. % BNNT nanocomposite films for 1, 5, and 10 days *in vitro*. Results are mean ± STD, * indicates a P-value of <0.05, ** indicates a P-value < 0.01 with respect to pristine non-poled samples.

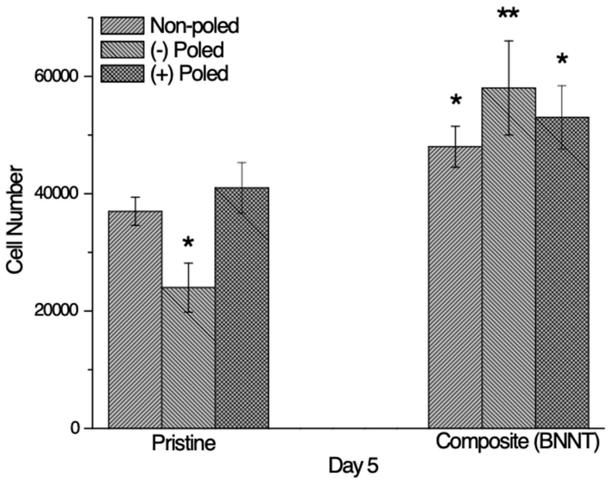

FIGURE 11 | Total cell number of human tenocytes cells cultured on unpolarized and polarized pristine annealed PVDF-TrFE and annealed PVDF-TrFE 1 wt. % BNNT nanocomposite films for 5 days *in vitro*. Results are mean ± STD, * indicates a P-value of < 0.05, ** indicates a P-value < 0.01with respect to pristine non-poled samples.

respectively. Although, the overall mean roughness between formulations was not statistically significant, the surface profile measured along the x, y plane by parallel line to x-axis at y equal to 1 (blue), 2 (red), and 3 (green) showed higher frequencies of roughness patterns in all BNNT composites compared to pristine PVDF-TrFE substrates. This analysis revealed that the addition of BNNT affected the surface morphology and frequency of surface roughness of PVDF-TrFE formulations, which could be directly corelated with the material crystallinity and crystal size as described by the MDSC process.

All unpolled sample types possessed a piezoelectric d33 coefficient of zero when assessed with quasi static direct piezoelectricity measurement. Both PVDF-TrFE and PVDF-TrFE-BNNT 1 wt. % BNNT nanocomposite annealed at 25°C, were associated with arcing during the poling operation, the occurrence of which was related to the presence of porosity in the polymer film. Conversely, solvent-cast PVDF-TrFE films annealed at 70°C demonstrated an improved ability to be poled to a maximum piezoelectric coefficient of 7 pC/N. These films however could not be poled with a field of 100 V/μm due to arcing. It is suggested that the evaporation rate of the co-polymer solvent was decreased at lower temperatures which caused defects in the film resulting in dielectric breakdown during poling. However, solvent-cast PVDF-TrFE films annealed at 120°C sustained a poling voltage of 100 V/μm, demonstrating improved dielectric breakdown strength due to lower porosity. These films showed a d33 coefficient of >11 pC/N. Similarly, solvent-cast PVDF-TrFE 1 wt. % BNNT nanocomposite films annealed at 120°C sustained higher poling voltages, relatively increased crystallinity and a piezoelectric d33 constant between 9 and 14 pC/N.

In-vitro Analysis of Material Cytocompatibility

In order to assess the ability of PVDF-TrFE materials to support tissue interfacing applications, annealed PVDF-TrFE and annealed PVDF-TrFE 1 wt. % BNNT nanocomposite films were progressed to cell viability studies for up to 10 days in culture, using tissue culture plastic (TCP) as a control substrate. It was observed that cell viability was maintained on all experimental and control substrates and significant cell death was not observed (**Figure 9**). However, cell proliferation assays confirmed that cells cultured on PVDF-TrFE/BNNT nanocomposites demonstrated enhanced proliferation for up to 10 days in culture relative to pristine annealed PVDF-TrFE films (**Figure 10**).

After 1 day in culture it was observed, that the incorporation of BNNT resulted in an increase in cell adhesion. In particular, a 2-fold increase in total cell number was observed on annealed PVDF-TrFE 1 wt. % BNNT nanocomposite films relative to cells cultured on pristine annealed PVDF-TrFE films. This trend was maintained at day 5 and was increased by day 10. This effect can be attributed to the observed nanotopography present on annealed PVDF-TrFE 1 wt. % BNNT nanocomposite films. Alternatively, it can be inferred that cell adhesion is enhanced by the electrically neutral surface of BNNTs that act as an anchoring site for cells (Giannini et al., 2018).

As previously demonstrated by Biggs et al. (2010, 2017), the cellular topographical sensing machinery is capable of detecting discrete differences in their extracellular environment down to the nanometer level (Fernandez-Yague et al., 2015). Similarly, Giannini et al. observed increased adhesion of fibroblasts cultured on surfaces characterized by protruding nanotubes. Furthermore, Zhang et al. (2015), demonstrated that cell Rho A–mediated cell proliferation increased with increasing surface roughness on surfaces produced by aggregation of nanotubes compared to flat surfaces. Finally, Genchi et al demonstrated that incorporation of BNNT in PVDF-TrFE can promote the differentiation of human osteoblasts *in vitro* (Genchi et al., 2018).

Although topographical factors contribute to the creation and maintenance of an optimal microenvironment for cell growth *in vitro*, a physical consideration of piezoelectric surfaces is the remnant polarization after poling which charges the materials surfaces. This electrical polarization can be either positive or negative and may affect cell adhesion or proliferation. In order to investigate the role of surface charge on tenocyte adhesion and proliferation, cells were cultured on polarized and unpolarized pristine annealed PVDF-TrFE and annealed PVDF-TrFE 1 wt. % BNNT nanocomposite films for 5 days.

Interestingly, it was observed that negatively charged annealed PVDF-TrFE films reduced tenocyte adhesion and proliferation relative to unpoled and positively charged pristine annealed PVDF-TrFE films (**Figure 11**). This can be explained as an electrostatic response. Since the membrane of tendon cells is also charged negatively it can be inferred that electrostatic repulsion can compete with integrin mediated cell attachment. In a similar study performed by Ribero et al. changes in cell proliferation were also observed as a consequence of the state of polarization of a PVDF surfaces (Ribeiro et al., 2018). Conversely, the anti-proliferative effect of negatively charged pristine annealed PVDF-TrFE films was not observed in negatively charged annealed PVDF-TrFE 1 wt. % BNNT nanocomposite films. In addition, it was clearly observed that cells attached and proliferate better on composite samples regardless of the polarization state. Again, it can be inferred that this effect is attributed to the modified substrate topography as a result of the BNNT incorporation and also to the electrically neutral surface presented by BNNTs that might act as an anchoring site for cells adhesion.

CONCLUSION

Here, for the first time, evidence has been presented on increased β-phase formation and total crystallinity in PVDF-TrFE by incorporating BNNT as a second phase using modulated differential scanning calorimetry (MDSC). It also concludes that the annealing temperature appears to be critical for maximizing the β-phase formation. Incorporation of BNNT resulted in increased mechanical properties, melting and crystallization temperatures, and crystallinity via restriction of molecular movement. A poly acrylic acid/fibronectin functionalization approach was employed to promote cell adhesion and PVDF-TRFE/BNNT nanocomposites were shown to induce increased cell attachment and sustained proliferation relative to pristine PVDF-TrFE. Furthermore, the inclusion of BNNTs were observed to negate the anti-adhesive effects of negatively charged PVDF-TrFE surfaces. This study shows that PVDF-TrFE/BNNT nanocomposite hold great potential for tissue engineering applications.

AUTHOR CONTRIBUTIONS

AP and MAF were involved in doing experimental works and writing a paper. SAMT and MJPB were involved in direct supervision of the work.

FUNDING

This work was funded through the SFI Center for Research in Medical Devices (CÚRAM) (Grant agreement no. 13/RC/2073) and through SFI/BBSRC joint funding (Grant agreement no. 16/BB SRC/3317).

ACKNOWLEDGMENTS

The authors wish to acknowledge Science Foundation Ireland (SFI) for financial assistance. The authors also acknowledge the assistance of James Britton (NUI Galway), Garry Warren from (University of Limerick), and Nireeksha S. Kardoe (Teleflex Medical, Athlone).

REFERENCES

Betz, N., Begue, J., Gonçalves, M., Gionnet, K., Déléris, G., and Le Moël, A. (2003). Functionalisation of PAA radiation grafted PVD. *Nucl. Instr. Methods Phys. Res.* 208, 434–441. doi: 10.1016/S0168-583X(03)00900-5

Biggs, M. J., Richards, R. G., and Dalby, M. J. (2010). Nanotopographical modification: a regulator of cellular function through focal adhesions. *Nanomedicine* 6, 619–633. doi: 10.1016/j.nano.2010.01.009

Biggs, M. J. P., Fernandez, M., Thomas, D., Cooper, R., Palma, M., Liao, J., et al. (2017). The functional response of mesenchymal stem cells to electron-beam patterned elastomeric surfaces presenting micrometer to nanoscale heterogeneous rigidity. *Adv. Materials* 29:1702119. doi: 10.1002/adma.201702119

Boccaccio, T., Bottino, A., Capannelli, G., and Piaggio, P. (2002). Characterization of PVDF membranes by vibrational spectroscopy. *J. Memb. Sci.* 210, 315–329. doi: 10.1016/S0376-7388(02)00407-6

Bodkhe, S., Turcot, G., Gosselin, F. P., and Therriault, D. (2017). One-step solvent evaporation-assisted 3D printing of piezoelectric PVDF nanocomposite structures. *ACS Appl. Mat. Interf.* 9, 20833–20842. doi: 10.1021/acsami.7b04095

California, A., Cardoso, V. F., Costa, C. M., Sencadas, V., Botelho, G., Gómez-Ribelles, J. L., et al. (2011). Tailoring porous structure of ferroelectric poly(vinylidene fluoride-trifluoroethylene) by controlling solvent/polymer ratio and solvent evaporation rate. *Eur. Polymer J.* 47, 2442–2450. doi: 10.1016/j.eurpolymj.2011.10.005

Chen, D., Chen, K., Brown, K., Hang, A., and Zhang, J. X. J. (2017). Liquid-phase tuning of porous PVDF-TrFE film on flexible substrate for energy harvesting. *Appl. Phys. Lett.* 110:153902. doi: 10.1063/1.4980130

Cui, Z., Tavajohi, N., Yongbing, H., Enrico, Z., Young, D., Leea, M., et al. (2015). Crystalline polymorphism in poly(vinylidenefluoride) membranes. *Prog. Polymer Sci.* 51, 94–126. doi: 10.1016/j.progpolymsci.2015.07.007

Fernandez-Yague, M. A., Larrañaga, A., Gladkovskaya, O., Stanley, A., Tadayyon, G., Guo, Y., et al. (2015). Effects of polydopamine functionalization on boron nitride nanotube dispersion and cytocompatibility. *Bioconjug. Chem.* 26, 2025–2037. doi: 10.1021/acs.bioconjchem.5b00257

Genchi, G. G., Sinibaldi, E., Ceseracciu, L., Labardi, M., Marino, A., Marras, S., et al. (2018). Ultrasound-activated piezoelectric P (VDF-TrFE)/boron nitride nanotube composite films promote differentiation of human SaOS-2 osteoblast-like cells. *Nanomedicine* 14, 2421–2432. doi: 10.1016/j.nano.2017.05.006

Giannini, M., Primerano, C., Berger, L., Giannaccini, M., Wang, Z., Landi, E., et al. (2018). Nano-topography: quicksand for cell cycle progression? *Nanomedicine* 14, 2656–2665. doi: 10.1016/j.nano.2018.07.002

Gregorio, Jr, R. (2006). Determination of the α, β, and γ crystalline phases of poly (vinylidene fluoride) films prepared at different conditions. *J. Appl. Polymer Sci.* 100, 3272–3279. doi: 10.1002/app.23137

Hitscherich, P., Wu, S., Gordan, R., Xie, L. H., Arinzeh, T., and Lee, E. J. (2016). The effect of PVDF-TrFE scaffolds on stem cell derived cardiovascular cells. *Biotechnol. Bioeng.* 113, 1577–1585. doi: 10.1002/bit.25918

Karode, N., Poudel, A., Fitzhenry, L., Matthews, S., Redington, W., Walsh, P., et al. (2018). Crystallization behavior of pebax–graphene composite matrix with and without supercritical carbon dioxide assisted polymer processing technique. *Crystal Growth Design* 18, 3938–3952. doi: 10.1021/acs.cgd.8b00277

Karode, N. S., Poudel, A., Fitzhenry, L., Matthews, S., Walsh, P. R., Coffey, A. B., et al. (2017). Evaluation of interfacial region of microphase-separated SEBS using modulated differential scanning calorimetry and dynamic mechanical thermal analysis. *Polymer Test.* 62, 268–277. doi: 10.1016/j.polymertesting.2017.07.006

Klee, D., Ademovic, Z., Bosserhoff, A., Hoecker, H., Maziolis, G., and Erli, H. J. (2003). Surface modification of poly (vinylidenefluoride) to improve the osteoblast adhesion. *Biomaterials* 24, 3663–3670. doi: 10.1016/S0142-9612(03)00235-7

Knopp, M. M., Löbmann, K., Elder, D. P., Rades, T., and Holm, R. (2016). Recent advances and potential applications of modulated differential scanning calorimetry (mDSC) in drug development. *Eur. J. Pharmaceut. Sci.* 87, 164–173. doi: 10.1016/j.ejps.2015.12.024

Labanca, M., Azzola, F., Vinci, R., and Rodella, L. F. (2008). Piezoelectric surgery: twenty years of use. *Br. J. Oral. Maxillof. Surg.* 46, 265–269. doi: 10.1016/j.bjoms.2007.12.007

Lau, K., Liu, Y., Chen, H., and Withers, R. L. (2013). Effect of annealing temperature on the morphology and piezoresponse characterisation of poly (vinylidene fluoride-trifluoroethylene) films via scanning probe microscopy. *Adv. Condens. Matter Phys.* 2013:435938 doi: 10.1155/2013/435938

Lutkenhaus, J. L., McEnnis, K., Serghei, A., and Russell, T. P. (2010). Confinement effects on crystallization and curie transitions of poly(vinylidene fluoride-co-trifluoroethylene). *Macromolecules* 43, 3844–3850. doi: 10.1021/ma100166a

Martins, P., Lopes, A. C., and Lanceros-Mendez, S. (2014). Electroactive phases of poly(vinylidene fluoride): determination, processing and applications. *Prog. Polymer Sci.* 39, 683–706. doi: 10.1016/j.progpolymsci.2013.07.006

Mayeen, A., Kala, M. S., Jayalakshmy, M. S., Thomas, S., Rouxel, D., Philip, J., et al. (2018). Dopamine functionalization of BaTiO 3: an effective strategy for the enhancement of electrical, magnetoelectric and thermal properties of BaTiO 3-PVDF-TrFE nanocomposites. *Dalton Trans.* 47, 2039–2051. doi: 10.1039/C7DT03389C

Nunes-Pereira, J., Ribeiro, S., Ribeiro, C., Gombek, C. J., Gama, F. M., Gomes, A. C., et al., (2015). Poly(vinylidene fluoride) and copolymers as porous membranes for tissue engineering applications. *Polymer Test.* 44, 234–241. doi: 10.1016/j.polymertesting.2015.05.001

Poudel, A., Karode, N., Fitzhenry, L., Kennedy, L., Matthews, S., Walsha, P., et al. (2017). Investigation of the thermal, mechanical, electrical and morphological properties of supercritical carbon dioxide assisted extrusion of microphase-separated poly(styrene-ethylene/butylene-styrene). *J. Supercrit. Fluids* 130, 1–9. doi: 10.1016/j.supflu.2017.07.013

Poudel, A., Karode, N. S., McGorry, P., Walsh, P., Lyons, J., Kennedy, J., et al. (2019). Processing of nanocomposites using supercritical fluid assisted extrusion for stress/strain sensing applications. *Composites Part B Eng.* 165, 397–405. doi: 10.1016/j.compositesb.2019.01.098

Ramasundaram, S., Yoon, S., Kim, K. J., and Lee, J. S. (2008). Direct preparation of nanoscale thin films of poly (vinylidene fluoride) containing β-crystalline phase by heat-controlled spin coating. *Macromol. Chem. Phys.* 209, 2516–2526. doi: 10.1002/macp.200800501

Ribeiro, C., Costa, C. M., Correia, D. M., Nunes-Pereira, J., Oliveira, J., Martins, P., et al. (2018). Electroactive poly(vinylidene fluoride)-based structures for advanced applications. *Nat. Protoc.* 13:681. doi: 10.1038/nprot.2017.157

Ribeiro, C., Panadero, J. A., Sencadas, V., Lanceros-Méndez, S., Tamaño, M. N., Moratal, D., et al. (2012). Fibronectin adsorption and cell response on electroactive poly (vinylidene fluoride) films. *Biomed. Materials* 7:035004. doi: 10.1088/1748-6041/7/3/035004

Ribeiro, C., Sencadas, V., Correia, D. M., and Lanceros-Méndez, S. (2015). Piezoelectric polymers as biomaterials for tissue engineering applications. *Colloids Surf. B Biointerfaces* 136, 46–55. doi: 10.1016/j.colsurfb.2015.08.043

Ribeiro, S., Gomes, A. C., Etxebarria, I., Lanceros-Méndez, S., and Ribeiro, C. (2018). Electroactive biomaterial surface engineering effects on muscle cells differentiation. *Mat. Sci. Eng.* 92, 868–874. doi: 10.1016/j.msec.2018.07.044

Safaei, M., Meneghini, R. M., and Anton, S. R. (2018). Energy harvesting and sensing with embedded piezoelectric ceramics in knee implants. *IEEE/ASME Trans. Mechatr.* 23, 864–874. doi: 10.1109/TMECH.2018.2794182

Sharma, T., Je, S.-S., Gill, B. S., and Zhang, X. (2012). Patterning piezoelectric thin film PVDF–TrFE based pressure sensor for catheter application. *Sensors Actuat. A Phys.* 177, 87–92. doi: 10.1016/j.sna.2011.08.019

Sobreiro-Almeida, R., Tamaño-Machiavello, M. N., Carvalho, E. O., Cordón, L., Doria, S., Senent, L., et al. (2017). Human mesenchymal stem cells growth and osteogenic differentiation on piezoelectric poly(vinylidene fluoride) microsphere substrates. *Int. J. Mol. Sci.* 18:2391. doi: 10.3390/ijms18112391

Völcker, N., Klee, D., Höcker, H., and Langefeld, S. (2001). Functionalization of silicone rubber for the covalent immobilization of fibronectin. *J. Mat. Sci.* 12, 111–119. doi: 10.1023/A:1008938525489

Wu, L., Jing, M., Liu, Y., Ning, H., Liu, X., et al. (2019). Power generation by PVDF-TrFE/graphene nanocomposite films. *Composites Part B Eng.* 164, 703–709. doi: 10.1016/j.compositesb.2019.01.055

Wu, S., Chen, M. S., Maurel, P., Lee, Y. S., Bunge, M. B., and Arinzeh, T. L. (2018). Aligned fibrous PVDF-TrFE scaffolds with Schwann cells support neurite extension and myelination *in vitro*. *J. Neur. Eng.* 15:056010. doi: 10.1088/1741-2552/aac77f

Zeng, Z.-G., Zhu, G.-D., Zhang, L., and Yan, X.-J. (2009). Effect of crystallinity on polarization fatigue of ferroelectric P (VDF-TrFE) copolymer films. *Chin. J. Polymer Sci.* 27, 479–485. doi: 10.1142/S025676790900414X

Zhang, H., Yang, S., Masako, N., Lee, D. J., Cooper, L. F., Ko, C. C. (2015). Proliferation of preosteoblasts on TiO 2 nanotubes is FAK/RhoA related. *RSC Adv.* 5, 38117–38124. doi: 10.1039/C4RA16803H

Conflict of Interest Statement: The authors declare that the research was conducted in the absence of any commercial or financial relationships that could be construed as a potential conflict of interest.

frontiers in Chemistry

ORIGINAL RESEARCH
published: 21 May 2019
doi: 10.3389/fchem.2019.00363

3D Hybrid Scaffolds Based on PEDOT:PSS/MWCNT Composites

Akhila K. Jayaram[1], Charalampos Pitsalidis[1], Ellasia Tan[2], Chrysanthi-Maria Moysidou[1], Michael F. L. De Volder[3], Ji-Seon Kim[2] and Roisin M. Owens[1]**

[1] Department of Chemical Engineering and Biotechnology, University of Cambridge, Cambridge, United Kingdom, [2] Department of Physics and Centre for Plastic Electronics, Imperial College London, London, United Kingdom, [3] Department of Engineering, University of Cambridge, Cambridge, United Kingdom

Conducting polymer scaffolds combine the soft-porous structures of scaffolds with the electrical properties of conducting polymers. In most cases, such functional systems are developed by combining an insulating scaffold matrix with electrically conducting materials in a 3D hybrid network. However, issues arising from the poor electronic properties of such hybrid systems, hinder their application in many areas. This work reports on the design of a 3D electroactive scaffold, which is free of an insulating matrix. These 3D polymer constructs comprise of a water soluble conducting polymer (PEDOT:PSS) and multi-walled carbon nanotubes (MWCNTs). The insertion of the MWCNTs in the 3D polymer matrix directly contributes to the electron transport efficiency, resulting in a 7-fold decrease in resistivity values. The distribution of CNTs, as characterized by SEM and Raman spectroscopy, further define the micro- and nano-structural topography while providing active sites for protein attachment, thereby rendering the system suitable for biological/sensing applications. The resulting scaffolds, combine high porosity, mechanical stability and excellent conducting properties, thus can be suitable for a variety of applications ranging from tissue engineering and biomedical devices to (bio-) energy storage.

Keywords: carbon nanotubes, conducting scaffolds, porous, PEDOT:PSS, electrode

Edited by:
Carlo Augusto Bortolotti,
University of Modena and Reggio Emilia, Italy

Reviewed by:
Tamara Posati,
Italian National Research Council (CNR), Italy
Stefano Carli,
Istituto Italiano di Tecnologia, Italy

****Correspondence:***
Charalampos Pitsalidis
cp645@cam.ac.uk
Roisin M. Owens
rmo37@cam.ac.uk

Specialty section:
This article was submitted to Organic Chemistry, a section of the journal Frontiers in Chemistry

Received: *29 January 2019*
Accepted: *02 May 2019*
Published: *21 May 2019*

Citation:
Jayaram AK, Pitsalidis C, Tan E, Moysidou C-M, De Volder MFL, Kim J-S and Owens RM (2019) 3D Hybrid Scaffolds Based on PEDOT:PSS/MWCNT Composites. Front. Chem. 7:363. doi: 10.3389/fchem.2019.00363

INTRODUCTION

Conducting polymer (CP) scaffolds belong to a novel class of scaffold materials that combine the softness of the polymer scaffolds and the electrical properties of conducting polymers (Lee, 2013; Wan et al., 2015; Zhou et al., 2018). Their unique set of features, including electrical conductivity, compatibility with tissue and a 3D porous structure that can take any desired form and shape, is reminiscent of their organic nature (Arash et al., 2014; Balint et al., 2014; Wang et al., 2014; Guex et al., 2017). While traditional inorganic materials such as silicon offer room for processing or further modification/functionalization, they are limited by inefficient biological coupling due to the formation of oxide layers upon interfacing with electrolytes (Rivnay et al., 2016). Therefore, CP scaffolds can offer viable alternatives to existing biomaterials for a range of applications, wherein electrical conductivity can be necessary for medical applications such as simulating/recording tissues (Kim et al., 2018), as well as for 3D tissue engineering (Guo and Ma, 2018).

Advances in materials science and tissue engineering as well as manufacturing techniques have enabled the advent of smart, multifunctional scaffolds with tailored architectures able to promote cell alignment and adhesion, release biomolecules on demand, and promote cell growth and differentiation in response to electrical stimulation (Ghasemi-Mobarakeh et al., 2011). Such conducting scaffolds or hybrid structures are typically formed by incorporating an electrically conducting material in insulating hydrophilic networks. Until now, the incorporation of CPs in a prefabricated insulating scaffold has dominated the field of electrically conducting scaffolds (Hardy et al., 2013; Zubair et al., 2017). However, the synthesis of single-component CP scaffolds offers the possibility of improved electrical properties while decreasing the complexity of the system (Wan et al., 2015). Single component CP scaffolds can be formed by either self-assembly of the conjugated polymeric chains or by modifying the CP with water-soluble and chemically crosslinkable moieties. One recent example of a single-component CP scaffold is based on poly(3,4-ethylene dioxythiophene (PEDOT) doped with poly(styrene sulfonate) (PSS) where the latter acts as counter ion for hole doping the CP while allowing it to be water dispersible. Such 3D structures made from PEDOT:PSS have been realized using freeze drying, with high versatility in forms and shapes as well as in the structural and functional properties (Wan et al., 2015; Guex et al., 2017; Iandolo et al., 2018). Recent studies further reported on how the mechanical, electrical and structural properties of the resulting PEDOT:PSS scaffolds could be modified by mixing the CP aqueous dispersion with other materials to meet different application requirements (Inal et al., 2017; Del Agua et al., 2018). Additionally, in our latest work we showed that single walled carbon nanotubes (SWCNTs) addition resulted in a substantial increase in the PEDOT:PSS scaffold conductivity and device performance (Pitsalidis et al., 2018a).

CNTs are 1D materials that demonstrate ballistic transport of electrons under certain conditions (Saito et al., 1998). Resistivity as low as 10^6 Ω^{-1} cm^{-1} was reported in single walled carbon nanotubes (SWCNTs) (Purewal et al., 2007), while multi-walled carbon nanotubes (MWCNTs) have shown resistivity of 5×10^6 Ω^{-1} cm^{-1} (Schönenberger et al., 1999); the difference being attributed to the change in respective diameters (Lekawa-Raus et al., 2014). The increased length of carbon nanotubes can promote conduction, provided it is within the length scale of the ballistic regime (Sundqvist et al., 2008) and that the CNTs form a good percolated network. One of the most exciting directions of CNT-based materials and structures is the use of CNT/polymer composites due to their enhanced mechanical (high strength and durability upon formation of a percolated network) and electrical properties (Ajayan et al., 2000; Behabtu et al., 2013; Lin et al., 2013; Arash et al., 2014). Indeed, combining CNTs with a conducting polymer greatly improves the charge transport efficiency while renders the resulting structure or film sensitive to chemical and/or environmental changes (Gou et al., 2015). Interestingly, the incorporation of water-soluble conjugated polymers/CNTs mixtures are of great interest for electrochemical devices and biosensors as they can enhance signal transduction and the range of detection (Gao et al., 2003; Xu et al., 2006).

The present study builds on our previous work (Pitsalidis et al., 2018a), aiming to systematically investigate the effect of MWCNTs addition on the PEDOT:PSS scaffold properties. As such we describe the fabrication and characterization of 3D conducting polymer scaffolds based on oxidized high-aspect ratio MWCNTs and PEDOT:PSS mixtures. The resulting 3D electrodes exhibit nanostructured porous morphology, substantially lower impedance compared to pristine scaffolds and excellent cytocompatibility. Furthermore, we demonstrate the biofunctionalization capability of our system using a bioactive peptide [poly-L-lysine (PLL)]. We believe that such 3D hybrid electrodes will open new directions for bio-interfacing and tissue engineering applications.

MATERIALS AND METHODS

Preparation of the PEDOT:PSS/MWCNT Scaffolds

The hybrid materials were prepared by mixing PEDOT: PSS and MWCNT solutions in various ratios. MWCNTs from Microphase (LLCNT, 300 μm in length) or Nanocyl (NC7000, 1.5 μm in length) were oxidized using nitric acid (HNO_3) in a microwave reactor (Anton Paar Multiwave Pro). PEDOT: PSS solution (Clevios PH-1000, Heraeus) of 1.25 wt% was mixed with 0.5 wt% 4-dodecylbenzenesulfonic acid (DBSA, Sigma Aldrich) and 3 wt% 3-glycidoxypropyltrimethoxysilane (GOPS, Sigma Aldrich). GOPS acted as a crosslinker while DBSA was shown to improve conductivity in previous studies (Inal et al., 2017). Subsequently, the above solution was mixed with MWCNTs through sonication for 10 min in the following MWCNT:(PEDOT:PSS) ratios: 1:1 and 2:3. The resultant solution was pipetted into a 96-well plate (Eppendorf) with a volume of approximately 250 μL per well. In order to enable electrical measurements, small strips of gold-plated polyimide (Kapton®, DuPont) were inserted in some of the wells prior to pipetting of solution. The well plate was placed in a freeze dryer (VirTis Advantage Plus) and frozen from 5 to −50°C at a rate of −0.45°C/min. The drying phase involved an initial temperature ramp to −45°C and a subsequent ramp to 20°C. The scaffolds were brought to room temperature after the heat-treatment stage. Prior to characterization, the samples were heated at 70°C on a hotplate for at least 3 h in order to promote the crosslinking of the PEDOT:PSS based scaffolds. A summary of the process and the resulting scaffold structures are shown in **Figure 1**.

Characterization of MWCNTs With Raman Spectroscopy

All samples were measured as prepared using Raman spectroscopy acquired from Renishaw inVia Raman Microscope in a backscattering configuration. All measurements were performed with samples placed inside a Linkam THMS600 stage under continuous nitrogen purging. The calibration of the filter and grating were performed using a Si reference peak at 520 cm^{-1}. A HeNe laser was used to produce the excitation source at 633 nm and 10% of 12 mW laser intensity under 50x magnification. The Raster 2D mapping was measured at each 10 μm step within filled square area of 40 and 60 μm across both axis.

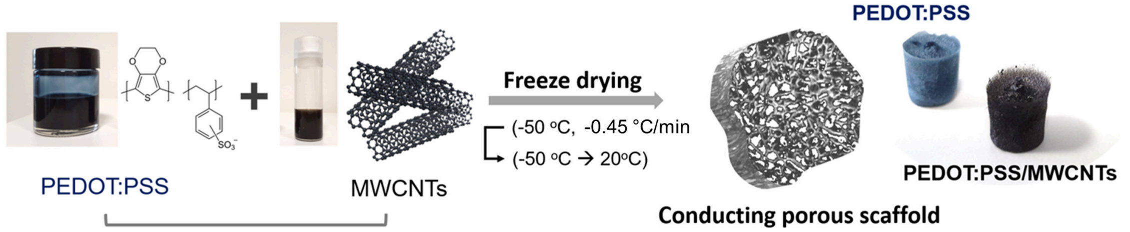

FIGURE 1 | Schematic diagram and images showing the components and the process used for the fabrication of the 3D conducting scaffolds. The photos show free-standing conducting scaffolds based on PEDOT:PSS and PEDOT:PSS/MWCNTs.

Optical Characterization of PEDOT:PSS/MWCNT Scaffolds

The microstructure and surface morphology of the scaffolds were analyzed using Scanning Electron Microscopy (SEM, Helios Nanolab DualBeam, FEI). The samples were removed from the well plate and mounted on an aluminum stub with carbon conductive tape. The beam voltage used was 5 kV and the beam current was maintained at 50 pA.

Swelling Studies of PEDOT:PSS/MWCNT Scaffolds

The measurement of liquid uptake, or swelling, was performed on the scaffolds by immersing them in Phosphate Buffered Saline (PBS, Sigma Aldrich, pH = 7.4) solution for 2, 4, 6, and 24 h, respectively. The scaffolds were weighed prior to immersion to measure the dry weight (W_d). Post immersion, they were dried thoroughly with tissue paper and weighed again to obtain the wet weight (W_w). The following equation was used to calculate the swelling (L) of the scaffolds (Shahini et al., 2014; Kucinska-Lipka et al., 2017):

$$L = \frac{Ww - Wd}{Wd} \times 100 \tag{1}$$

Two slices and four measurements per scaffold type were used for calculations to account for variability. The mean of these four measurements was taken as the swelling index of the scaffold.

Pore Size Distribution of PEDOT:PSS/MWCNT Scaffolds

The pore size distribution of the scaffolds was measured using image analysis of SEM micrographs (Park et al., 2002). Fifty pores per sample were manually selected at random and their diameters were measured using *ImageJ*. Further graphical analysis was performed using Origin. Box plots were plotted to enable visualization of differences among samples.

Biofunctionalization of PEDOT:PSS/MWCNT Scaffolds

Based on previous work of our group (Pappa et al., 2017), we functionalized the scaffolds with poly-L-lysine (PLL). Briefly, samples were fully immersed in a 1 mg/mL fluorescein isothiocyanate (FITC)-labeled PLL (MW: 15–30 kDa, Sigma-Aldrich) solution in Phosphate Buffered Saline (PBS, Sigma Aldrich) and kept at room temperature, in dark overnight. The next day, the scaffolds were immersed in a 1M NaCl solution and sonicated for 1 min to remove the excess of PLL-FITC. Both unwashed and washed samples were mounted on glass bottom microscopy dishes (MatTek Corporation) and FITC fluorescence was detected upon excitation at 488 nm with a confocal microscope (Axio Observer Z1, Carl Zeiss MicroImaging GmbH).

Electrical Characterization of PEDOT:PSS/MWCNT Scaffolds

The impedance of the electrodes was evaluated using a two-electrode system configuration. The conducting scaffold was designated as the working electrode through the attachment of a gold-plated Kapton® strip while a reticulated (vitreous) glassy carbon was used as the counter electrode, with PBS acting as the electrolyte. AC voltages of frequencies ranging from 0.1 Hz to 10^5 Hz were applied and the response was measured using an impedance analyzer (Metrohm Autolab).

3D Cell Culture Experiments

Telomerase Immortalized Fibroblasts (TIFs), labeled with Red Fluorescent Protein (RFP—TIF LifeAct) were cultured in Advanced DMEM (Gibco, Life technologies) supplemented with 20% Fetal Bovine Serum (FBS, Sigma Aldrich), 1% Glutamine (Gibco, Life technologies), 2% HEPES (Gibco, Life technologies), 0.5% penicillin-streptomycin (10,000 U/ml, Gibco, Life technologies) and 0.1% Gentamycin (Sigma Aldrich). The day before seeding, scaffolds were fully hydrated and kept at 4°C overnight and the next day, they were sterilized with 70% ethanol and then immersed in complete growth medium for 2 h, to allow for protein adhesion. After washing the scaffolds with fresh medium, 100 μL of 2×10^6 cells in suspension were seeded on top of each sample and cells were incubated for 1.5 h. Then fresh medium was added to maintain the cell culture. Two days later, cells in the scaffolds were fixed with 4% paraformaldehyde (PFA) for 15 min and washed extensively with PBS. Then the samples were observed under a confocal microscope (Axio Observer Z1, Carl Zeiss MicroImaging GmbH) to check cell adhesion and proliferation in the porous network of the scaffolds.

RESULTS AND DISCUSSION

Morphology and Structure

Visual observations of pristine PEDOT:PSS scaffolds and those with MWCNTs (**Figure 1**) show a clear color difference, preliminarily indicating the presence of MWCNTs in the resulting structure. The color of the former is bluish, while the latter dispersion is distinctly black, consistent with previous reports showing that CNTs act as black absorbers (Yang et al., 2008). The good dispersibility of oxidized MWCNTs in water facilitates their incorporation within the polymeric matrix. The resulting free-standing scaffolds showed extensive pore interconnectivity and excellent structural integrity both in dry state as well as in wet medium (i.e., PBS). The macroscopic fragility and elasticity of the scaffolds were investigated (2:3 volume ratio) in a qualitative manner by performing compression tests and estimating the response of the material to a unidirectional compressive load (**Figure S1**). The scaffolds were found to recover their initial shape (in ∼10 s) after exposing them to a compression of about 60%, indicative of their good elastic properties and mechanical durability. **Figures 2A**,**B** show that the macroscopic porosity of the scaffolds does not change appreciably upon increasing the fraction of MWCNTs in the mixture, within the concentration range tested in this paper. However, the hybrid scaffolds exhibited decreased uniformity when compared to pristine PEDOT:PSS scaffolds, as can be seen in **Figure S2**. Additionally, the relatively smooth topography observed at the pores of the pristine PEDOT:PSS scaffolds is replaced by a nanostructured topography which is associated with the presence of MWCNTs, as observed in **Figures 2C**,**D**. Increasing their fraction (2:3) resulted in a more extensive network of MWCNTs covering the pore surface. The presence of such domains could be linked to phase separation phenomena between PEDOT:PSS and MWCNTs during the freeze drying process.

The elemental composition around these domains was further investigated using Raman spectroscopy. The integrated peak area ratios between the D-band signal from the MWCNT and the symmetric vibrational mode of the PEDOT:PSS $C_\alpha = C_\beta$ (1,420 cm-$^{-1}$) were used to construct Raman maps showing MWCNT chemical homogeneity. The domains appear clustered for the hybrid material with lower concentration of MWCNTs, as shown in **Figure 2E**. In contrast, an even coverage was observed in the material with higher concentration of MWCNTs, as seen in **Figure 2F**. The presence of nanoscale roughness due to the MWCNT domains is of particular significance to biological applications as cells prefer moderately rough surfaces (Gentile et al., 2010; Zhou et al., 2018). Moreover, such domains can participate in the localization of functionalization moieties. It should be noted that the PEDOT:PSS Raman peaks are strongly influenced by changes in the electrical properties of PEDOT:PSS such as doping level (Garreau et al., 1999). In particular, the principal peak related to the $C_\alpha = C_\beta$ symmetric vibrational mode will change with respect to the full width half maximum, peak position and relative intensity ratios to other PEDOT:PSS peaks. Such changes are associated with the structural transformation induced by altering the doping level of PEDOT:PSS. These Raman spectral features are not seen in the PEDOT:PSS/MWCNT hybrid scaffolds (**Figure S3**), which indicates that the intrinsic doping level of PEDOT:PSS maintained constant between different composition ratios. Thus, suggesting that the enhanced electrical properties are

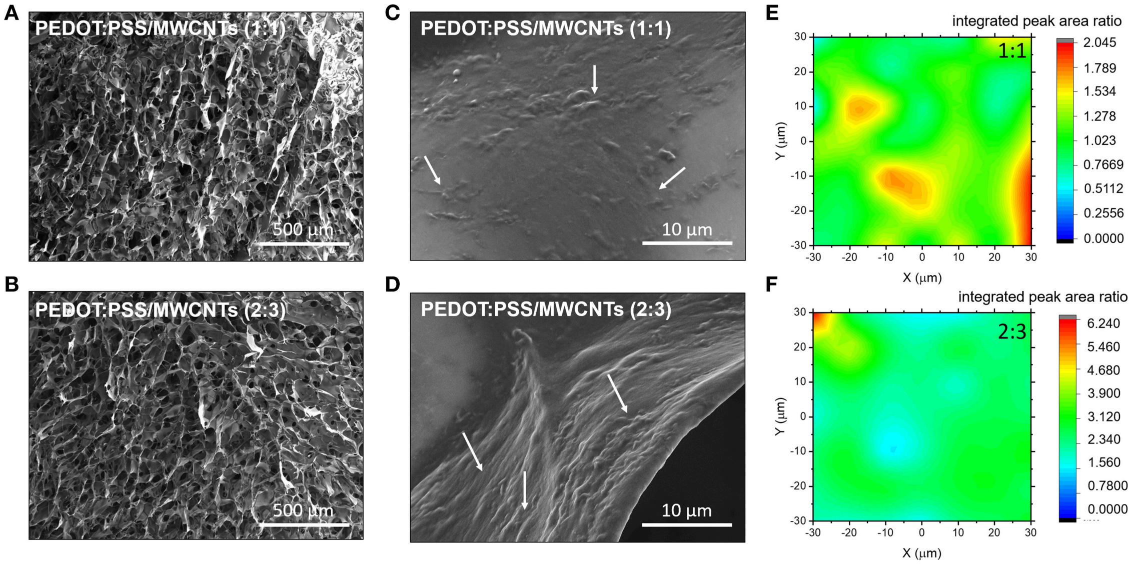

FIGURE 2 | SEM Images of the with PEDOT:PSS/MWCNT scaffold in **(A)** 1:1 ratio and **(B)** 2:3 ratio. White arrows at the corresponding magnified images **(C,D)** highlight the presence of CNT domains. Normalized 2D Raman maps showing integrated peak area ratio of the D-band signal arising from MWCNT to PEDOT:PSS for the different ratio; **(E)** 1:1, **(F)** 2:3.

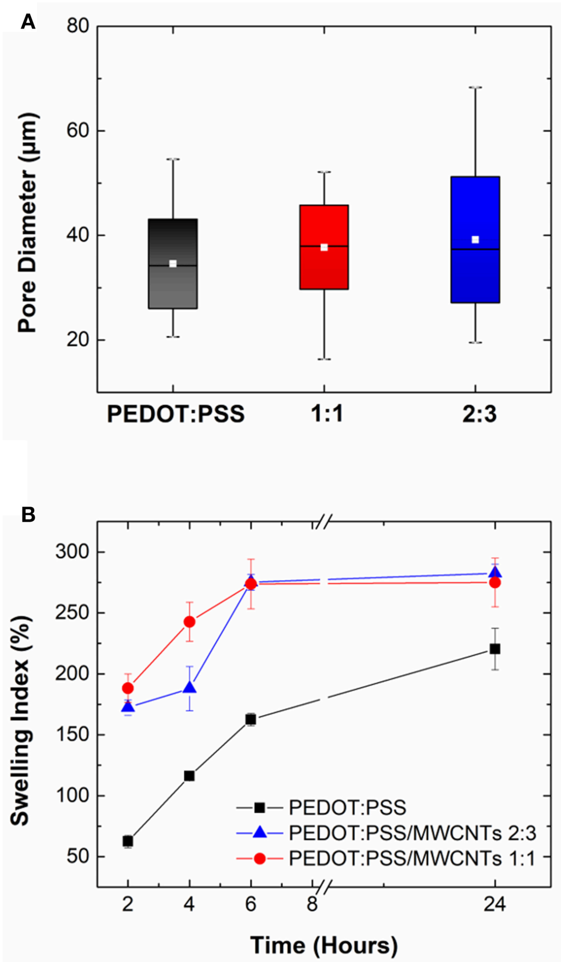

FIGURE 3 | (A) Box plot highlighting variation in pore size distribution of PEDOT:PSS/MWCNT scaffold in 1:1 ratio (red), 2:3 ratio (blue) compared to pristine PEDOT:PSS scaffold (black). Colored boxes denote the range where 25–75% of the values in the dataset lie, white line refers to the mean pore diameter and whiskers indicate the maximum and minimum values, respectively. **(B)** Swelling index (%) of PEDOT:PSS/MWCNT scaffold in 1:1 ratio (red) and 2:3 ratio (blue) in comparison with pristine PEDOT:PSS scaffold (black) at $t = 2$, 4, 6, and 24 h. Error bars indicate variability between measurements.

not due to the MWCNTs acting as dopants but alternatively contributing to the conductive pathways with an even coverage in the 3D scaffold.

Pore Size Distributions

Measurements obtained through image analysis showed that pores in pristine PEDOT:PSS scaffolds had diameters ranging from 20 to 54 μm while PEDOT:PSS/MWCNT scaffolds displayed ranges of 16–52 μm (1:1 ratio) and 19–68 μm (2:3 ratio), respectively. The box plots in **Figure 3A** indicate that the pristine scaffold has a comparable mean pore diameter (34 μm) to those of the two composites (37 μm, 39 μm). The interquartile range which refers to the range where 25–75% of diameters lie (denoted by the shaded boxes) also follows a similar trend. Hence, the pore diameters obtained are of a sufficient diameter to promote cell growth (Karageorgiou and Kaplan, 2005; Li et al., 2013) which is further corroborated by cytocompatibility studies detailed in 3.6.

Swelling Capacity

The swelling capacity of PEDOT:PSS/MWCNT scaffolds is seen to be higher than that of pristine PEDOT:PSS scaffolds at all time points, as shown in **Figure 3B**. However, there is no significant difference between the two PEDOT:PSS/MWCNT scaffolds. Following incubation for 2 h, the former were seen to have a liquid uptake 3 times (172–188%) that of the latter (62%). The trend of higher liquid uptake continued at longer timescales ($t = 24$ h), although the difference among the samples was now lowered (275–282.5% for CNT scaffolds vs. 220% for pristine scaffolds). The differences can be attributed to the lower relative content of PSS in the PEDOT:PSS/MWCNT scaffolds, as well as to the increase in surface area arising from the microstructure imparted by the CNTs. The swelling

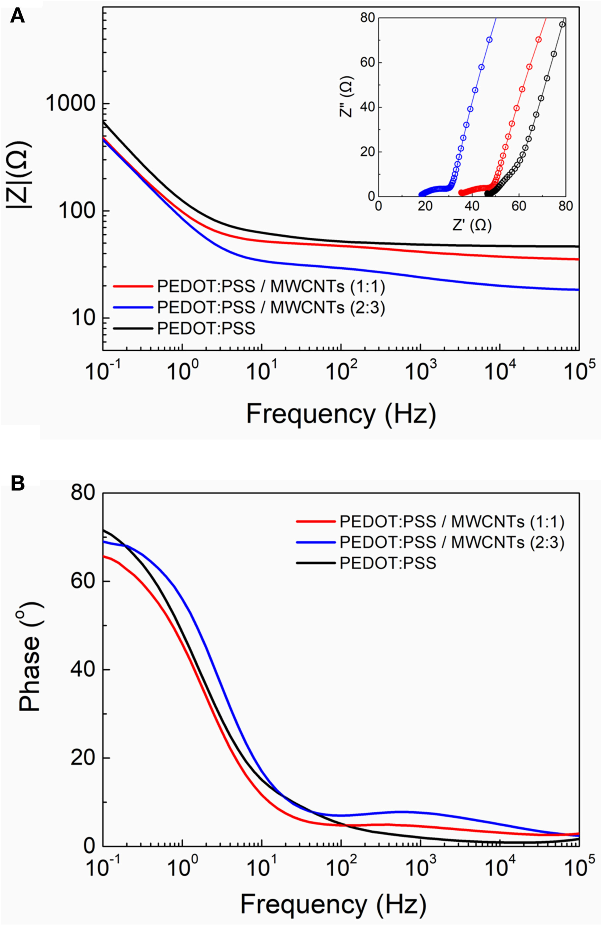

FIGURE 4 | Comparative electrochemical impedance spectroscopy measurements of the PEDOT:PSS and PEDOT:PSS/MWCNT electrodes showing the **(A)** Bode plot (Inset shows the Nyquist plots) and **(B)** the corresponding phase angle diagram.

capacity is of significant importance for the use of these scaffolds in tissue engineering applications as the ability to retain water promotes cell proliferation and perfusion of nutrients (Zhu and Marchant, 2011; Slaughter et al., 2013).

Electrical Properties

The macroscopic conductivity of the MWCNTs-based scaffolds in their dry form was assessed by measuring the resistance between two contact points of the scaffolds (**Figure S4**). The incorporation of MWCNTs was found to have a pronounced effect on the conductivity of the scaffolds, as expected. The measured electrical resistance was approximately 7 times lower compared to the pristine PEDOT:PSS samples, while only slight variations were observed between the two different MWCNTs ratios.

Furthermore, the scaffolds were electrically characterized by means of electrochemical impedance spectroscopy (EIS). For this set of experiments scaffold-based electrodes were fabricated and measured inside an electrochemical cell. As shown in **Figure 4A**, the MWCNTs based scaffold electrodes exhibited lower impedance values over the whole frequency spectra when compared to the neat PEDOT:PSS electrodes. At high frequencies the electrodes showed a flat curve characteristic, typically observed for good conducting materials. The apparent differences in the impedance magnitude can be attributed to alterations in the electrical conductivity arising by the inclusion of more electroactive sites in the case of MWCNTs based scaffolds. This effect is more pronounced for the high ratio MWCNTs electrodes. The same trend can be observed at a mid-frequency range (100–1,000 Hz). These observations indicate that the use of MWCNTs have a direct contribution in the enhancement of conductivity in these systems and may offer better sensitivity and operation window for electrical monitoring of biological systems. Moreover, the characteristic "line" observed in the Nyquist plots at the very low frequencies (see inset graphs) is related to ionic diffusion in the bulk of the porous scaffolds. Deviations from "ideal" Warburg diffusion (45° slope) can be attributed to variations in the pore distribution and/or pore geometry within the bulk of the scaffolds (Cooper et al., 2017). Additionally, the MWCNTs based scaffolds exhibited only slight variations compared to pristine, which can be described by a marginal decrease in the phase magnitude (from ∼70° to ∼65°) at low frequencies and a presence of a broad peak at the mid/high frequency range (100–1,000 Hz) (**Figure 4B**).

We also investigated the use of shorter length MWCNTs (Nanocyl NC7000, 1.5 µm in length) as the size of the CNTs has been shown to play an important role on the overall morphology and electronic properties of CNT-based composites (Russ et al., 2013; Zhou et al., 2015). We thus observed a similar micro-morphology to that of the long MWCNTs-based scaffolds with a nanostructured topography featured by dense ridges at the walls of the pores (**Figures S5A,B**). Further, we compared the electrochemical properties between the short and the long MWCNTs-based scaffolds by means of EIS (**Figure S5C**). Interestingly, only a slight increase in the impedance magnitude at the mid/high frequency regime can be observed for the short MWCNTs scaffolds. This can be attributed to the formation of a more extensive conducting network within the long MWCNT-based scaffolds. Nevertheless, short MWCNTs based scaffolds showed overall excellent characteristics, thus represent a cost efficient and very promising alternative to the long MWCNTs based scaffolds.

Functionalization Capability

The FITC conjugated bioactive molecule PLL was seen to adsorb on all samples post-incubation, irrespective of whether MWCNTs were present or not. In the case of MWCNT scaffolds this can be explained by the formation of electrostatic interactions between the highly positively charged PLL and the negatively charged oxidized MWCNTs (Ling et al., 2014). However, when the samples were subjected to high ionic strength buffer solution (1M NaCl) in order

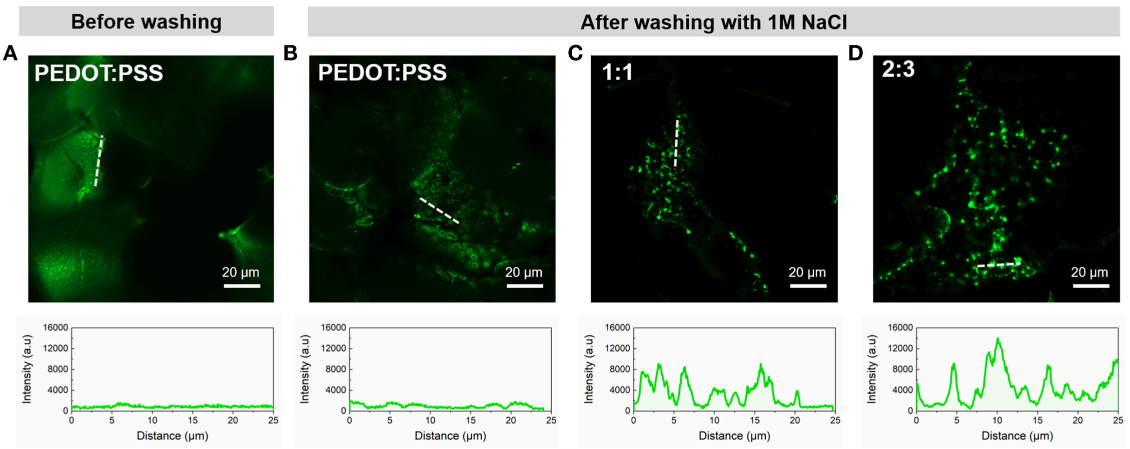

FIGURE 5 | Representative confocal microscopy images of the scaffolds functionalized with PLL-FITC pre- and post-washing and corresponding intensity profiles of regions indicated by white dotted lines; **(A)** PEDOT:PSS scaffold before washing and **(B)** PEDOT:PSS, **(C)** PEDOT:PSS/MWCNT (1:1), and **(D)** PEDOT:PSS/MWCNT (2:3) after-washing with 1M NaCl.

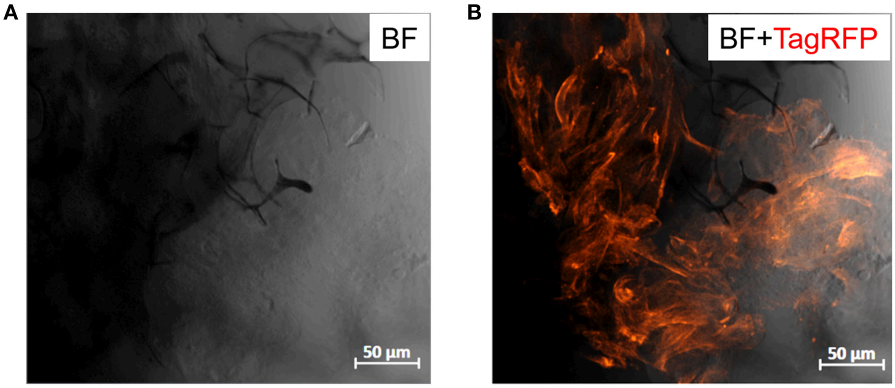

FIGURE 6 | Confocal images of PEDOT:PSS/MWCNTs (2:3) after 2 days in culture with TIF LifeAct cells. **(A)** Bright-field channel illustrating the scaffold porous network (dark gray-black) covered with cells (light gray), **(B)** Bright-field and far-red channels merged highlighting the actin filaments of TIF cytoskeleton (dark orange), as well as the cell growth and penetration into the pores of the scaffold.

to remove the excess of PLL-FITC, substantial differences were apparent. The pristine PEDOT:PSS CP scaffold (**Figures 5A**,**B**) showed lower fluorescent intensity due to the absence of localized binding, as expected from the non-specific adsorption of PLL on the smooth microstructure. In contrast, **Figures 5C**,**D** show significantly higher fluorescent intensities across the PEDOT:PSS/MWCNT hybrid scaffolds in addition to localized "hotspots." These hotspots can be attributed to the presence of CNT domains in the scaffolds, as evidenced by SEM images and Raman mapping described in section Morphology and Structure. As CNTs have already been demonstrated to improve neurite outgrowth and projection in neural tissue engineering (Hu et al., 2004; Lovat et al., 2005), we assume that the presence of such "hotspots" could possibly provide favorable sites for cell attachment and adhesion, as well as for guiding cell growth (Hirata et al., 2012; Imaninezhad et al., 2018).

Cytocompatibility

The compatibility of PEDOT:PSS with cell cultures is well-established (Ramuz et al., 2015; Ohayon et al., 2017). Several organic electronic schemes, developed by us and others, utilize this material with biological models (e.g., barrier forming cells) for biosensing and monitoring applications (Pappa et al., 2018; Pitsalidis et al., 2018b). Our group has shown that PEDOT:PSS scaffolds are apt structures for generating 3D cell cultures, thanks to their soft, tissue-like nature (Inal et al., 2017). More recently, we developed a 3D bioelectronic device integrated into an electrochemical transistor configuration, that supports the 3D cell culture growth while simultaneously allows for real-time monitoring of the different cell growth stages in a quantitative manner (Pitsalidis et al., 2018a). Herein, we investigated whether the incorporation of the MWCNTs in the PEDOT:PSS scaffolds can affect their cytocompatibility. TIF LifeAct cells (TIFs tagged with RFP labeling the actin filaments in the cytoskeleton), were chosen as a model cell line due to their auto-fluorescence, facilitating faster and more efficient optical monitoring obviating the need for immunofluorescence staining assays, as well as due to their ability to produce extracellular matrix, coating the surface of the scaffolds. The 3D cell culture was maintained in a multi-well plate, where the samples were suspended in complete growth medium. The optical observation (confocal microscopy) of the growth and spreading of the cells over the scaffold was assessed after 2 days. As shown in **Figure 6,** TIFs appeared to spread over the scaffold, although not in full confluency, presumably because of the short duration of the cell culture. However, the characteristic fibrous shape and individual cell domains of TIFs were formed, in consistence with previous observations (Inal et al., 2017). Although preliminary, these results are promising for engineering PEDOT:PSS/MWCNTs hybrid scaffolds that can serve as hosts of 3D cell culture systems.

CONCLUSIONS

CP scaffolds have come to the fore as multifunctional smart biomaterials acting simultaneously as templates for 3D tissue growth as well as recording or stimulating electrodes for the growing tissue. Such dual capabilities have great implications in tissue engineering both *in vitro* and *in vivo*. Likewise, 3D electrodes that are structurally and mechanically compliant with tissue can also have significant implications in next generation medical prosthesis and bioelectronic therapies. In previous studies we have highlighted the potential of PEDOT:PSS as an excellent candidate material for the formation of 3D porous biomimetic structures/electrodes promoting tissue growth in 3D and allowing for quantitative assessment of tissue formation to be elucidated through deconvolution of the electrical measurements. In this work, we have performed a systematic study on the effect of MWCNTs addition on the electronic and morphological properties of PEDOT:PSS scaffolds. Alongside the enhancement in the electrical conductivity, the MWCNT-modified scaffolds exhibited good cytocompatibility and biofunctionalization (i.e., PLL) capability, important for biosensing and cell attachment (i.e., to promote adhesion of specific cell types). Overall, such high-performance systems can be useful for applications where electronic performance is particularly important, such as in applications for tissue stimulation and electronic implants.

AUTHOR CONTRIBUTIONS

CP and AJ contributed equally to this work. CP and AJ developed the scaffolds and perform electrical characterization. AJ performed the morphological characterization and the functionalization of the scaffolds. Cell experiments and confocal measurements were carried out by C-MM. ET characterized the films using Raman spectroscopy. CP conceived the idea. RO, CP, MD, and J-SK supervised the research work and reviewed the results. CP and AJ wrote the paper.

FUNDING

This work was supported by the EPSRC Cambridge NanoDTC, EP/L015978/1.

ACKNOWLEDGMENTS

The authors would like to acknowledge Dr. Sarah Jessl and Kate Sanders for their assistance in CNT preparation. They would also like to thank Dr. Anna-Maria Pappa for helpful discussions around functionalization of the hybrid systems.

SUPPLEMENTARY MATERIAL

The Supplementary Material for this article can be found online at: https://www.frontiersin.org/articles/10.3389/fchem.2019.00363/full#supplementary-material

REFERENCES

Ajayan, P. M., Schadler, L. S., Giannaris, C., and Rubio, A. (2000). Single-walled carbon nanotube-polymer composites: strength and weakness. *Adv. Mater.* 12, 750–753. doi: 10.1002/(SICI)1521-4095(200005)12:10<750::AID-ADMA750>3.0.CO;2-6

Arash, B., Wang, Q., and Varadan, V. K. (2014). Mechanical properties of carbon nanotube/polymer composites. *Sci. Rep.* 4:6479. doi: 10.1038/srep06479

Balint, R., Cassidy, N. J., and Cartmell, S. H. (2014). Conductive polymers: towards a smart biomaterial for tissue engineering. *Acta Biomater.* 10, 2341–2353. doi: 10.1016/J.ACTBIO.2014.02.015

Behabtu, N., Young, C. C., Tsentalovich, D. E., Kleinerman, O., Wang, X., Ma, A. W. K., et al. (2013). Strong, light, multifunctional fibers of carbon nanotubes with ultrahigh conductivity. *Science* 339, 182–186. doi: 10.1126/science.1228061

Cooper, S. J., Bertei, A., Finegan, D. P., and Brandon, N. P. (2017). Simulated impedance of diffusion in porous media. *Electrochim. Acta*. 251, 681–689. doi: 10.1016/j.electacta.2017.07.152

Del Agua, I., Marina, S., Pitsalidis, C., Mantione, D., Ferro, M., Iandolo, D., et al. (2018). Conducting polymer scaffolds based on poly(3,4-ethylenedioxythiophene) and Xanthan gum for live-cell monitoring. *ACS Omega* 3, 7424–7431. doi: 10.1021/acsomega.8b00458

Gao, M., Dai, L., and Wallace, G. G. (2003). Biosensors based on aligned carbon nanotubes coated with inherently conducting polymers. *Electroanalysis* 15, 1089–1094. doi: 10.1002/elan.200390131

Garreau, S., Louarn, G., Buisson, J. P., Froyer, G., and Lefrant, S. (1999). *In situ* spectroelectrochemical Raman studies of poly(3,4-ethylenedioxythiophene) (PEDT). *Macromolecules* 32, 6807–6812. doi: 10.1021/ma9905674

Gentile, F., Tirinato, L., Battista, E., Causa, F., Liberale, C., di Fabrizio, E. M., et al. (2010). Cells preferentially grow on rough substrates. *Biomaterials* 31, 7205–7212. doi: 10.1016/j.biomaterials.2010.06.016

Ghasemi-Mobarakeh, L., Prabhakaran, M. P., Morshed, M., Nasr-Esfahani, M. H., Baharvand, H., Kiani, S., et al. (2011). Application of conductive polymers, scaffolds and electrical stimulation for nerve tissue engineering. *J. Tissue Eng. Regen. Med.* 5, e17–e35. doi: 10.1002/term.383

Gou, P., Kraut, N. D., Feigel, I. M., Bai, H., Morgan, G. J., Chen, Y., et al. (2015). Carbon nanotube chemiresistor for wireless pH sensing. *Sci. Rep.* 4:4468. doi: 10.1038/srep04468

Guex, A. G., Puetzer, J. L., Armgarth, A., Littmann, E., Stavrinidou, E., Giannelis, E. P., et al. (2017). Highly porous scaffolds of PEDOT:PSS for bone tissue engineering. *Acta Biomater.* 62, 91–101. doi: 10.1016/j.actbio.2017.08.045

Guo, B., and Ma, P. X. (2018). Conducting polymers for tissue engineering. *Biomacromolecules* 19, 1764–1782. doi: 10.1021/acs.biomac.8b00276

Hardy, J. G., Lee, J. Y., and Schmidt, C. E. (2013). Biomimetic conducting polymer-based tissue scaffolds. *Curr. Opin. Biotechnol.* 24, 847–854. doi: 10.1016/j.copbio.2013.03.011

Hirata, E., Akasaka, T., Uo, M., Takita, H., Watari, F., and Yokoyama, A. (2012). Carbon nanotube-coating accelerated cell adhesion and proliferation on poly (L-lactide). *Appl. Surf. Sci.* 262, 24–27. doi: 10.1016/j.apsusc.2012.01.012

Hu, H., Ni, Y., Montana, V., Haddon, R. C., and Parpura, V. (2004). Chemically functionalized carbon nanotubes as substrates for neuronal growth. *Nano Lett.* 4, 507–511. doi: 10.1021/nl035193d

Iandolo, D., Pennacchio, F. A., Mollo, V., Rossi, D., Dannhauser, D., Cui, B., et al. (2018). Electron microscopy for 3D scaffolds-cell biointerface characterization. *Adv. Biosyst.* 3:1800103. doi: 10.1002/adbi.201800103

Imaninezhad, M., Schober, J., Griggs, D., Ruminski, P., Kuljanishvili, I., and Zustiak, S. P. (2018). Cell attachment and spreading on carbon nanotubes is facilitated by integrin binding. *Front. Bioeng. Biotechnol.* 6:129. doi: 10.3389/fbioe.2018.00129

Inal, S., Hama, A., Ferro, M., Pitsalidis, C., Oziat, J., Iandolo, D., et al. (2017). Conducting polymer scaffolds for hosting and monitoring 3D cell culture. *Adv. Biosyst.* 1:1700052. doi: 10.1002/adbi.201700052

Karageorgiou, V., and Kaplan, D. (2005). Porosity of 3D biomaterial scaffolds and osteogenesis. *Biomaterials* 26, 5474–5491. doi: 10.1016/j.biomaterials.2005.02.002

Kim, S.-M., Kim, N., Kim, Y., Baik, M.-S., Yoo, M., Kim, D., et al. (2018). High-performance, polymer-based direct cellular interfaces for electrical stimulation and recording. *NPG Asia Mater.* 10, 255–265. doi: 10.1038/s41427-018-0014-9

Kucinska-Lipka, J., Marzec, M., Gubanska, I., and Janik, H. (2017). Porosity and swelling properties of novel polyurethane – ascorbic acid scaffolds prepared by different procedures for potential use in bone tissue engineering. *J. Elastomers Plast.* 49, 440–456. doi: 10.1177/0095244316672093

Lee, J. Y. (2013). Electrically conducting polymer-based nanofibrous scaffolds for tissue engineering applications. *Polym. Rev.* 53, 443–459. doi: 10.1080/15583724.2013.806544

Lekawa-Raus, A., Patmore, J., Kurzepa, L., Bulmer, J., and Koziol, K. (2014). Electrical properties of carbon nanotube based fibers and their future use in electrical wiring. *Adv. Funct. Mater.* 24, 3661–3682. doi: 10.1002/adfm.201303716

Li, X., Wang, L., Fan, Y., Feng, Q., Cui, F. Z., and Watari, F. (2013). Nanostructured scaffolds for bone tissue engineering. *J. Biomed. Mater. Res. Part A* 101, 2424–2435. doi: 10.1002/jbm.a.34539

Lin, H., Li, L., Ren, J., Cai, Z., Qiu, L., Yang, Z., et al. (2013). Conducting polymer composite film incorporated with aligned carbon nanotubes for transparent, flexible and efficient supercapacitor. *Sci. Rep.* 3:1353. doi: 10.1038/srep01353

Ling, X., Wei, Y., Zou, L., and Xu, S. (2014). Functionalization and dispersion of multiwalled carbon nanotubes modified with poly-l-lysine. *Colloids Surfaces A Physicochem. Eng. Asp.* 443, 19–26. doi: 10.1016/j.colsurfa.2013.10.053

Lovat, V., Pantarotto, D., Lagostena, L., Cacciari, B., Grandolfo, M., Righi, M., et al. (2005). Carbon nanotube substrates boost neuronal electrical signaling. *Nano Lett.* 5, 1107–1110. doi: 10.1021/nl050637m

Ohayon, D., Pitsalidis, C., Pappa, A. M., Hama, A., Zhang, Y., Gallais, L., et al. (2017). Laser patterning of self-assembled monolayers on PEDOT:PSS films for controlled cell adhesion. *Adv. Mater. Interfaces* 4, 1–8. doi: 10.1002/admi.201700191

Pappa, A. M., Inal, S., Roy, K., Zhang, Y., Pitsalidis, C., Hama, A., et al. (2017). Polyelectrolyte layer-by-layer assembly on organic electrochemical transistors. *ACS Appl. Mater. Interfaces* 9, 10427–10434. doi: 10.1021/acsami.6b15522

Pappa, A. M., Parlak, O., Scheiblin, G., Mailley, P., Salleo, A., and Owens, R. M. (2018). Organic electronics for point-of-care metabolite monitoring. *Trends Biotechnol.* 36, 45–59. doi: 10.1016/j.tibtech.2017.10.022

Park, S. N., Park, J. C., Kim, H. O., Song, M. J., and Suh, H. (2002). Characterization of porous collagen/hyaluronic acid scaffold modified by 1-ethyl-3-(3-dimethylaminopropyl)carbodiimide cross-linking. *Biomaterials* 23, 1205–1212. doi: 10.1016/S0142-9612(01)00235-6

Pitsalidis, C., Ferro, M. P., Iandolo, D., Tzounis, L., Inal, S., and Owens, R. M. (2018a). Transistor in a tube: a route to three-dimensional bioelectronics. *Sci. Adv.* 4:eaat4253. doi: 10.1126/sciadv.aat4253

Pitsalidis, C., Pappa, A. M., Porel, M., Artim, C. M., Faria, G. C., Duong, D. D., et al. (2018b). Biomimetic electronic devices for measuring bacterial membrane disruption. *Adv. Mater.* 30, 1–8. doi: 10.1002/adma.201803130

Purewal, M. S., Hong, B. H., Ravi, A., Chandra, B., Hone, J., and Kim, P. (2007). Scaling of resistance and electron mean free path of single-walled carbon nanotubes. *Phys. Rev. Lett.* 98, 2–5. doi: 10.1103/PhysRevLett.98.186808

Ramuz, M., Hama, A., Rivnay, J., Leleux, P., and Owens, R. M. (2015). Monitoring of cell layer coverage and differentiation with the organic electrochemical transistor. *J. Mater. Chem. B* 3, 5971–5977. doi: 10.1039/C5TB00922G

Rivnay, J., Inal, S., Collins, B. A., Sessolo, M., Stavrinidou, E., Strakosas, X., et al. (2016). Structural control of mixed ionic and electronic transport in conducting polymers. *Nat. Commun.* 7, 1–9. doi: 10.1038/ncomms11287

Russ, M., Rahatekar, S. S., Koziol, K., Farmer, B., and Peng, H. X. (2013). Length-dependent electrical and thermal properties of carbon nanotube-loaded epoxy nanocomposites. *Compos. Sci. Technol.* 81, 42–47. doi: 10.1016/j.compscitech.2013.03.011

Saito, R., Dresselhaus, G., and Dresselahaus, M. (1998). *Physical Properties of Carbon Nanotubes*. London: Imperial College Press.

Schönenberger, C., Bachtold, A., Strunk, C., Salvetat, J. P., and Forró, L. (1999). Interference and interaction in multi-wall carbon nanotubes. *Appl. Phys. A Mater. Sci. Process.* 69, 283–295. doi: 10.1007/s003390051003

Shahini, A., Yazdimamaghani, M., Walker, K. J., Eastman, M. A., Hatami-Marbini, H., Smith, B. J., et al. (2014). 3D conductive nanocomposite scaffold for bone tissue engineering. *Int. J. Nanomed.* 9, 167–181. doi: 10.2147/IJN.S54668

Slaughter, B. V., Khurshid, S. S., Fisher, O. Z., Khademhosseini, A., and Peppas, N. A. (2013). Hydrogels in regenerative medicine. *Adv. Mater.* 21, 279–302. doi: 10.1016/B978-0-323-22805-3.00012-8

Sundqvist, P. A., Garcia-Vidal, F. J., and Flores, F. (2008). Electronic transport in carbon nanotubes: diffusive and localized regimes. *Phys. Rev. B Condens. Matter Mater. Phys.* 78, 1–5. doi: 10.1103/PhysRevB.78.205427

Wan, A. M.-D., Inal, S., Williams, T., Wang, K., Leleux, P., Estevez, L., et al. (2015). 3D conducting polymer platforms for electrical control of protein conformation and cellular functions. *J. Mater. Chem. B* 3, 5040–5048. doi: 10.1039/C5TB00390C

Wang, K., Wu, H., Meng, Y., and Wei, Z. (2014). Conducting polymer nanowire arrays for high performance supercapacitors. *Small* 10, 14–31. doi: 10.1002/smll.201301991

Xu, Y., Ye, X., Yang, L., He, P., and Fang, Y. (2006). Impedance DNA biosensor using electropolymerized polypyrrole/multiwalled carbon nanotubes modified electrode. *Electroanalysis* 18, 1471–1478. doi: 10.1002/elan.200603544

Yang, Z. P., Ci, L., Bur, J. A., Lin, S. Y., and Ajayan, P. M. (2008). Experimental observation of an extremely dark material made by a low-density nanotube array. *Nano Lett.* 8, 446–451. doi: 10.1021/nl072369t

Zhou, H., Han, G., Xiao, Y., Chang, Y., and Zhai, H. J. (2015). A comparative study on long and short carbon nanotubes-incorporated polypyrrole/poly(sodium 4-styrenesulfonate) nanocomposites as high-performance supercapacitor electrodes. *Synth. Met.* 209, 405–411. doi: 10.1016/j.synthmet.2015.08.014

Zhou, Z., Liu, X., Wu, W., Park, S., Miller, A. L., Terzic, A., et al. (2018). Effective nerve cell modulation by electrical stimulation of carbon nanotube embedded conductive polymeric scaffolds. *Biomater. Sci.* 6, 2375–2385. doi: 10.1039/c8bm00553b

Zhu, J., and Marchant, R. E. (2011). Design properties of hydrogel tissue-engineering scaffolds. *Expert Rev. Med. Devices* 8, 607–626. doi: 10.1586/erd.11.27

Zubair, N. A., Rahman, N. A., Lim, H. N., and Sulaiman, Y. (2017). Production of conductive PEDOT-coated PVA-GO composite nanofibers. *Nanoscale Res. Lett.* 12:113. doi: 10.1186/s11671-017-1888-0

Conflict of Interest Statement: The authors declare that the research was conducted in the absence of any commercial or financial relationships that could be construed as a potential conflict of interest.

frontiers
in Chemistry

ORIGINAL RESEARCH
published: 11 June 2019
doi: 10.3389/fchem.2019.00409

Size-Dependent Photophysical Behavior of Low Bandgap Semiconducting Polymer Particles

Tersilla Virgili [1]*, Chiara Botta [2], Marta M. Mróz [1], Laurie Parrenin [3], Cyril Brochon [3], Eric Cloutet [3], Eleni Pavlopoulou [3], Georges Hadziioannou [3] and Mark Geoghegan [4]

[1] IFN-CNR Dipartimento di Fisica, Politecnico di Milano, Milan, Italy, [2] Laboratory Istituto per lo Studio delle Macromolecole, CNR-ISMAC, Milan, Italy, [3] Laboratoire de Chimie des Polymères Organiques (LCPO) UMR 5629, CNRS-Université de Bordeaux-Bordeaux INP, Pessac, France, [4] Department of Physics and Astronomy, University of Sheffield, Sheffield, United Kingdom

The photophysics of water and propan-1-ol suspensions of poly [N-9”-heptadecanyl-2,7-carbazole-*alt*−5,5-(4,7-di-2-thienyl-2′,1′,3′- benzothiadiazole)] (PCDTBT) nanoparticles and mesoparticles has been studied by ultrafast spectroscopy. High molar mass polymer (HMM $>$ 20 kg/mol) forms nanoparticles with around 50 nm diameter *via* mini-emulsion post-polymerization, while low molar mass (LMM $<$ 5 kg/mol) polymer prepared by dispersion polymerization results in particles with a diameter of almost one order of magnitude larger (450 ± 50 nm). In this study, the presence of excited-states and charge separated species was identified through UV pump and visible/near-infrared probe femtosecond transient absorption spectroscopy. A different behavior for the HMM nanoparticles has been identified compared to the LMM mesoparticles. The nanoparticles exhibit typical features of an energetically disordered conjugated polymer with a broad density of states, allowing for delayed spectral relaxation of excited states, while the mesoparticles show a J-aggregate-like behavior where interchain interactions are less efficient. Stimulated emission in the red-near infrared region has been found in the mesoparticles which indicates that they present a more energetically ordered system.

Keywords: transient absorption spectroscopy, PCDTBT, nanoparticles, semiconducting polymers, optoelectronics

OPEN ACCESS

Edited by:
Carlo Augusto Bortolotti,
University of Modena and Reggio Emilia, Italy

Reviewed by:
Juan Cabanillas-Gonzalez,
Madrid Institute for Advanced Studies, Spain
Mindy Levine,
University of Rhode Island, United States

***Correspondence:**
Tersilla Virgili
tersilla.virgili@polimi.it

Specialty section:
This article was submitted to Organic Chemistry, a section of the journal Frontiers in Chemistry

Received: *30 January 2019*
Accepted: *20 May 2019*
Published: *11 June 2019*

Citation:
Virgili T, Botta C, Mróz MM, Parrenin L, Brochon C, Cloutet E, Pavlopoulou E, Hadziioannou G and Geoghegan M (2019) Size-Dependent Photophysical Behavior of Low Bandgap Semiconducting Polymer Particles. Front. Chem. 7:409. doi: 10.3389/fchem.2019.00409

INTRODUCTION

Semiconducting polymer particles and nanoparticles with optical properties are of considerable importance for applications in a diverse range of technologies including light-emitting diodes (Wong, 2017), solar cells (Zhou et al., 2014; Jana et al., 2017), biosensing (Wu and Chiu, 2013; Chan and Wu, 2015; Xu et al., 2015), and cancer phototherapy (Li et al., 2018; Meng et al., 2018). Advantages of polymer particles include generally good optically stability, relatively routine preparation through emulsion polymerization or precipitation routes (Pecher and Mecking, 2010), and ready functionalization for different applications (Feng et al., 2013).

Some work has addressed the size dependence of the optical properties of semiconducting polymer nanoparticles but there is no conclusive narrative linking size to optical properties. In some experiments considering nanoparticles of different diameters, there was only limited evidence of size-dependent optical behavior (Lin et al., 2017; Peters et al., 2018). In experiments concerning polythiophenes (Kurokawa et al., 2004; Lee et al., 2010) and a polyfluorene copolymer (Pras et al., 2010) it was observed that smaller particles induce a blue shift in the emission spectra. By way of contrast however, decreasing nanoparticle size has led to a red shift in emission spectra of a poly(*p*-phenylene vinylene) (PPV) derivative (Sun et al., 2014), an observation that is not supported by experiments in which a different PPV derivative were allowed to aggregate in solution (Grey et al., 2006). Aggregated particles are therefore expected to behave differently to individual particles and one can therefore suppose that chain conformation and packing within the particles play an important role in their optoelectronic behavior. Indeed, this conclusion was reached by considering size-dependent brightness, which increased with increasing particle size less than would be expected by considering the number of fluorophores present in the volume (Sun et al., 2014). Certainly, experiments reporting the crystalline behavior of poly(3-hexylthiophene) nanoparticles showed that chain ordering controlled the optical behavior of these polymers (Labastide et al., 2011; Nagarjuna et al., 2012).

Poly[*N*-9"-heptadecanyl-2,7-carbazole-*alt*-5,5-(4′,7′-di-2-thienyl-2′,1′,3′-benzothiadiazole)] (PCDTBT) is a promising low bandgap polymer for bulk heterojunction solar cells (Blouin et al., 2007, 2008). It is an alternating copolymer comprising benzothiadiazole, thiophene, and carbazole units and is remarkable for its exceptional thermal stability (Blouin et al., 2008). Nanoparticles of PCDTBT blended with ([6,6]-phenyl-C_{71}-butyric acid methyl ester) ($PC_{71}BM$) have been demonstrated in bulk-heterojunction photovoltaic devices (D'Olieslaeger et al., 2017; Prunet et al., 2018). Different methods are available to create such particles, including the preparation of a miniemulsion comprising $PC_{71}BM$, PCDTBT, and a surfactant in an appropriate solvent (D'Olieslaeger et al., 2017; Parrenin et al., 2017) or by first dissolving the components (PCDTBT and $PC_{61}BM$ or $PC_{71}BM$) in a good solvent (tetrahydrofuran, THF) which is then dispersed in an excess of a non-solvent, water (Wang et al., 2016; Prunet et al., 2018). After the THF has been allowed to evaporate, a nanoparticle dispersion remains. It is however possible to prepare PCDTBT as particles of different sizes using different concentrations of the polymer in THF solution added to water (Parrenin et al., 2017). Particles of different optical sizes have been produced using a Suzuki cross-coupling dispersion polymerization, which were stabilized by a polymeric surfactant (Parrenin et al., 2015). PCDTBT nanoparticles can also be produced by the same routes as for the blends in the absence of the fullerene acceptor (Wang et al., 2016; Parrenin et al., 2017; Prunet et al., 2018).

Ultrafast transient absorption spectroscopy has previously been used to study the optical properties of PCDTBT in solution, in film form, and in fullerene blends. In thin films and in solution, relaxation from the π-π^* interband transition is seen to be similar and rapid (Banerji et al., 2010), with an initial relaxation process occurring on time scales less than the ~100 fs resolution of the experiment. Although a singlet exciton is formed within 1 ps, this is rather slow compared to the charge separation timescales occurring in blends with fullerenes (Tong et al., 2010). However, further transient absorption experiments were able to show that charge-transfer intermediate states do not play a significant role in the generation of photocurrent in the blends and that free charge carriers are generated directly and rapidly. Why Coulombically-bound excitons are bypassed in these systems is unresolved, but recent work has shown (using a modified transient absorption set-up) that there is some ordering at heterojunction interfaces, which may be responsible for the ability to create free charges after photoexcitation (Jakowetz et al., 2017).

Here, ultrafast spectroscopy was used to study the photophysics of water and propan-1-ol suspensions of different (PCDTBT) particle size in two forms: high molar mass (HMM) nanoparticles and larger mesoparticles of low molar mass (LMM). We have found that the HMM nanoparticles exhibit typical features of an energetically disordered conjugated polymer with a broad density of states, allowing for delayed spectral relaxation of excited states, while the LMM mesoparticles show a J-aggregate-like behavior where interchain interactions are less efficient. Moreover, stimulated emission in the red-near infrared region has been found in the LMM particles, which results from a more energetically ordered system.

MATERIALS AND METHODS

Samples

Two routes to create PCDTBT particles (see **Figure 1A** for chemical structure) were used. High molar mass (HMM) nanoparticles were created as previously described (Parrenin et al., 2017). PCDTBT was first synthesized (Wakim et al., 2009) before being dissolved in chloroform. This was then added to an aqueous solution of sodium dodecyl sulfate (SDS) and sonicated to form a miniemulsion. Heating at 70°C allowed the chloroform to evaporate, leaving a nanoparticle dispersion in water. The PCDTBT was determined to have number-average molar mass, $M_\mathrm{n} = 20.2$ kDa, and a dispersity of 2.2. The mean particle diameter was determined by transmission electron microscopy to be 50 nm (**Figure 2S**). Low molar mass (LMM) PCDTBT mesoparticles were created as previously described (Parrenin et al., 2015). PCDTBT was synthesized by Suzuki cross-coupling polymerization in a propanol solution with poly(vinyl pyrrolidone) (PVP) added as a surfactant. The quantity of PVP allowed the particle size to be adjusted in the range of 0.33–1.3 μm (**Figure 1S**), with an almost completely uniform distribution. The PCDTBT number-average molar mass was determined to be 4.5 kDa, with dispersity 2.1. Chloroform solutions (40 mg/mL) were prepared by dissolving the two different particles and then thin solid-state films of the two HMM and LMM polymers are prepared by spin coating.

Steady State Absorption and Photoluminescence Spectra

Absorption and emission spectra were acquired using a Shimadzu UV-3600 spectrophotometer and a Horiba Scientific Fluoromax-4 spectrofluorometer, respectively. The excitation wavelength for the emission spectra was 390 nm.

Ultrafast Spectroscopy

Time-resolved measurements were performed using a homebuilt femtosecond pump–probe setup (Virgili et al., 2013). A

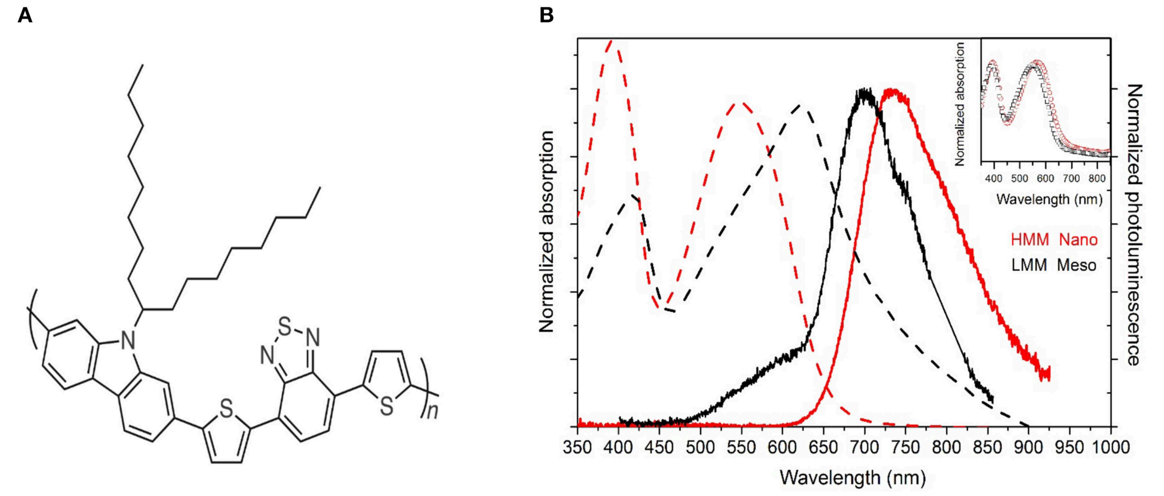

FIGURE 1 | (A) Chemical structure of PCDTBT. **(B)** Normalized absorption (broken line) and photoluminescence spectra (solid line) for the HMM nanoparticle (red) and LMM mesoparticle (black) suspensions. The absorption spectra of spin coated films from the HMM (red open circles) and LMM (black open squares) pristine polymers are also shown in the inset. The pristine polymers are in film form after spin-coating from chloroform solution.

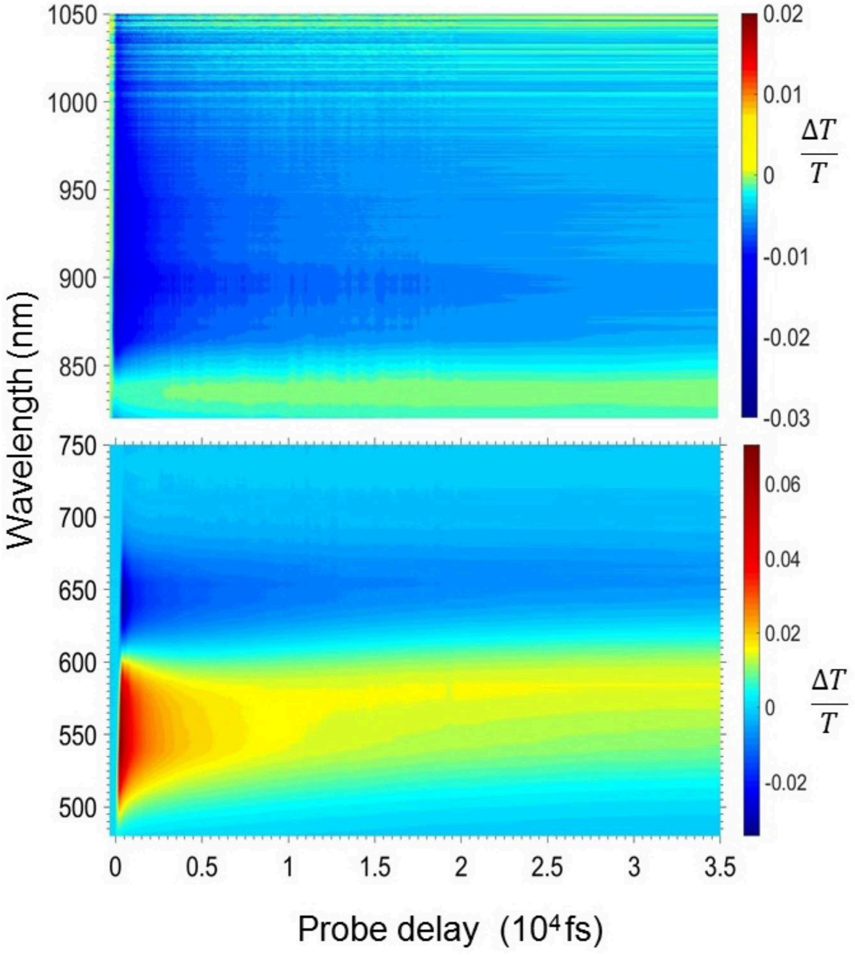

FIGURE 2 | 2-Dimensional $\Delta T/T$ map in the visible (bottom panel) and the near infrared (top panel) region for the HMM nanoparticle suspension.

Ti:sapphire regenerative amplifier (Libra, Coherent) was used as a laser source, delivering 100 fs pulses at a central wavelength of 800 nm with 4 mJ pulse energy at a repetition rate of 1 kHz. For the excitation pulses, the second harmonic of the fundamental wavelength has been used ($\lambda = 400$ nm). In order to minimize bimolecular effects, the excitation density was kept to ~1.2 mJ cm^{-2}. White light generated with a 2 mm-thick sapphire plate was used as a probe in the visible-near infrared range from 450 to 1,100 nm (the region between 750 and 820 nm cannot be detected due to the strong presence of the fundamental laser excitation). For a spectrally-resolved detection of the probe light, spectrographs and CCD arrays were used. The chirp in the white light pulse (the zero delay between the pump and the probe beams is different for different probe wavelengths) was taken into account during the analysis and evaluation of the two-dimensional (wavelength and time) $\Delta T(\lambda,\tau)/T$ maps before extraction of the spectral and temporal data using homemade software. Overall, a temporal resolution of at least 150 fs was achieved for all excitation wavelengths.

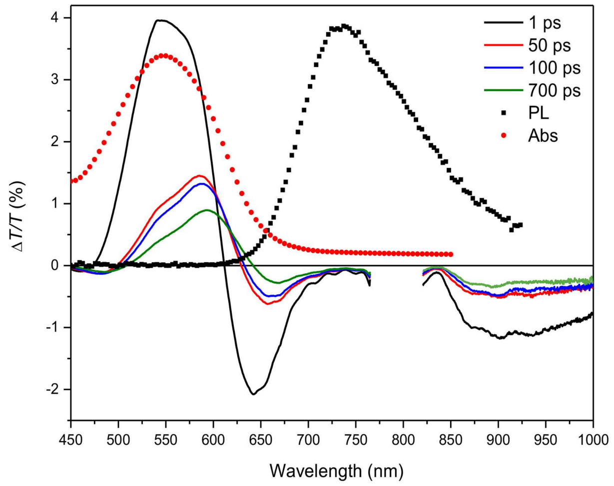

FIGURE 3 | $\Delta T/T$ spectra at different probe delays (see legend in the figure) compared to the absorption (Abs, red solid circles) and photoluminescence (PL) emission (black solid squares) spectra for the HMM nanoparticle suspension.

RESULTS AND DISCUSSION

Steady-State Spectra

PCDTBT is characterized by a relatively large donor-acceptor repeat unit. The absorption spectrum consists of several broad bands, which are ascribed to the lowest π-π^* interband transition, as is commonly observed in donor-acceptor copolymers of similar chemical structure (Westerling et al., 2007). The emission instead occurs with a large Stokes shift caused by the dissipation of energy in excess of equilibrium in photoexcited carriers during their relaxation, vibrational relaxation, localization of the excitation, exciton formation, exciton migration, and structural relaxation (Westerling et al., 2007; Banerji et al., 2010; Lin et al., 2017). The final state is a localized ground-state exciton.

Figure 1B shows the absorption and emission spectra of the two different particle suspensions. The absorption spectrum of the HMM nanoparticles (red broken line) is similar to that of previously reported PCDTBT films, exhibiting two broad (around 480 meV) transitions with peaks at 390 (more intense) and at 550 nm (less intense). In agreement with earlier work (Banerji et al., 2010; Etzold et al., 2011) the two bands were identified as the π-π^*-transition of the first and second excited singlet states (S_1 and S_2). Excitation into the higher-energy band at 400 nm leads to a broad and unstructured emission between 620 and 920 nm (red solid line), peaking at 735 nm in the steady-state spectrum with a Stokes shift of around 185 nm corresponding to 570 meV.

The absorption spectrum of the LMM suspension (black broken line) is quite different from those previously reported for PCDTBT (Banerji et al., 2010; Etzold et al., 2011). In contrast to what would be expected from considering the lower molar mass of the polymer (Shao and Vanden Bout, 2017), both transition peaks are red-shifted by around 150 meV, and also their relative intensity is changed, with the transition at 620 nm being more intense than that at 410 nm. The long wavelength absorption tail is likely to be due to the Rayleigh scattering of light from the particles (McQuarrie, 2000). The photoluminescence (PL) emission (black solid line in **Figure 1B**) surprisingly shows a Stokes shift of only 230 meV; in fact, the main peak of the emission is at 700 nm. The emission shows also a weak shoulder at around 580 nm, probably due to residual PVP surfactant (see **Figure 3S**) and/or dimers (Scarongella et al., 2013). The absence of energy transfer to the PCDTBT polymer despite the strong overlap between the absorption and emission of the two compounds reveals that those materials are in the suspension and not inside the nanoparticles so that their presence can be neglected in the following photophysical study. Moreover, µRaman measurements were performed on the particles and the presence of PVP was not detected (**Figure 4S**). The red-shift of the LMM PCDTBT mesoparticle absorption spectrum together with the strong reduction of the Stokes shift with respect to the HMM PCDTBT nanoparticle suspension indicate a different packing of the polymer chains.

To determine whether this behavior is due to the different molar mass of the polymers, HMM, and LMM particles were dissolved in chloroform and then spin coated to prepare uniform thin films. The absorption spectra of the two films are reported in the inset of **Figure 1B**. The spectra are very similar indicating that differences in particle optical properties can be attributed only to the different particle sizes rather than to their different molar mass or synthetic routes. Transient transmission measurements were also performed on those spin coated films (**Figure 5S**), which did not show significant differences in the photophysics of the two polymers. Any contribution due to molar mass is discussed below in the Discussion subsection.

The differences in the steady-state absorption-emission spectra of polymeric assemblies are commonly analyzed within an HJ-aggregate model (Spano, 2010; Baghgar et al., 2014; Ziffer et al., 2018). According to this model the different coupling types are spectroscopically identified by the intensity ratio between 0–0

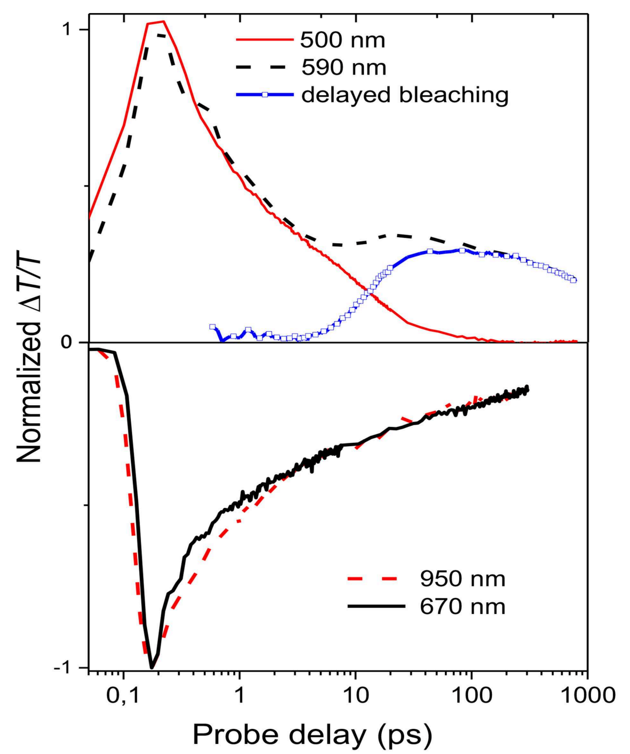

FIGURE 4 | Normalized decay traces at different wavelengths (see legend in the figure) The blue line representing the delayed bleaching is calculated by subtracting the normalized decay at 500 nm from the one at 590 nm.

and 0–1 vibrational transitions where the integer numbers refer to the vibrational quanta in the respective initial and final states. This ratio is larger (smaller) than unity for intrachain (interchain) coupling, i.e., J-like (H-like) behavior.

Here for the HMM suspension absorption spectrum, the π-π^*-transition of the first singlet state S_1 is a broad band where it is not easy to identify the 0–0 and the 0–1 vibrational transitions. However, it is clear that for the LMM suspension the main absorption peak is red-shifted with respect to the HMM suspension while the PL peak is blue-shifted as expected for J-aggregate-like behavior, which is generally associated with stronger intrachain than interchain coupling. From the optical properties it appears therefore that the mesoparticles obtained with the LMM polymer possess larger intrachain electronic coupling between monomer repeat units, probably due to a higher backbone planarity.

Ultrafast Spectroscopy

Nanoparticles

Figures 2–4 show the photophysics of the HMM nanoparticle suspension. **Figure 2** presents the 2D map of the transient transmission $\Delta T(\lambda,\tau)/T$ in the visible (470–750 nm) and the near infrared spectrum (820–1,050 nm) in the first 35 ps after excitation. The measured signal is

$$\frac{\Delta T\left(\lambda,\tau\right)}{T}=\frac{T_{\text{pump}}-T_{\text{no pump}}}{T_{\text{no pump}}},$$

where T_{pump} and $T_{\text{no pump}}$ are the probe transmission intensities after and before the pump excitation. A yellow-red signal represents a positive $\Delta T/T$ signal corresponding to a bleaching of the ground state or stimulated emission (SE) from excited states, while blue signal indicates the presence of a photoinduced absorption (PIA) band. The 2D map shows a positive band between 500 and 620 nm and two photoinduced absorption bands at around 650 and 900 nm.

The $\Delta T/T$ spectra, shown in **Figure 3**, display the temporal evolution of the three bands at four probe delays after the pump pulse. A comparison with the absorption and photoluminescence spectra allows discrimination between the signal due to ground-state bleaching and the excited-state stimulated emission. The positive signal with peak at 550 nm due to the overlap with the absorption spectrum (red filled circles) is assigned to the bleaching while the negative signals are attributed to polaron states as already reported (Banerji et al., 2010; Etzold et al., 2011).

Figure 4 shows the decay time traces at 500 and 590 nm corresponding, respectively, to the higher and lower energy exciton in the bleaching band and at 670 and 950 nm representing the peaks of the two absorption bands. It is noteworthy that the higher energy exciton (solid red line) presents one decay with a time constant of around 7 ps, while the one at 590 nm (broken black line) has two contributions: one fast decay similar to the one at 500 nm and a second contribution which grows at later time. To extrapolate only the second decay, the normalized decay at 500 nm was subtracted from that at 590 nm. The result, shown as the blue line in **Figure 4**, indicates that the lower energy exciton presents a component which is not instantaneous but due to energy transfer from higher energetic sites with a diffusion time of around 40 ps. The time traces at 670 and 950 nm are similar, which indicates that the two photoinduced absorption bands are related to the same population of charged states and that they are created instantaneously within the experimental time resolution (150 fs).

It has been previously shown that the long tail in the PCDTBT absorption spectrum indicates the presence of localized states near the band edge (Banerji et al., 2010). Those states can be seen as spectroscopic units of polymeric segments with different conjugation lengths; after photoexcitation the presence of those states can produce an energy transfer from higher to lower energetic states. Once formed the singlet excitons can hop to and between localized states and change their spatial position and the exciton hopping typically leads to a progressive red shift of the fluorescence spectrum, which slows in time as the number of nearby states with lower energy decreases (Banerji et al., 2010). In the nanoparticle suspension, the excitation energy transfer is from the higher energy units (polymer segments with a shorter conjugation length) to lower energy units (longer conjugation length) as represented by the decay traces at 500 and 590 nm (**Figure 4**).

Mesoparticles

Figures 5–7 show the photophysics of the LMM mesoparticle suspension. **Figure 5** presents the 2D map of the $\Delta T/T$ signal in the visible (470–750 nm) and the near infrared spectral region (820–1,050 nm) in the first 35 ps after excitation. Again, the

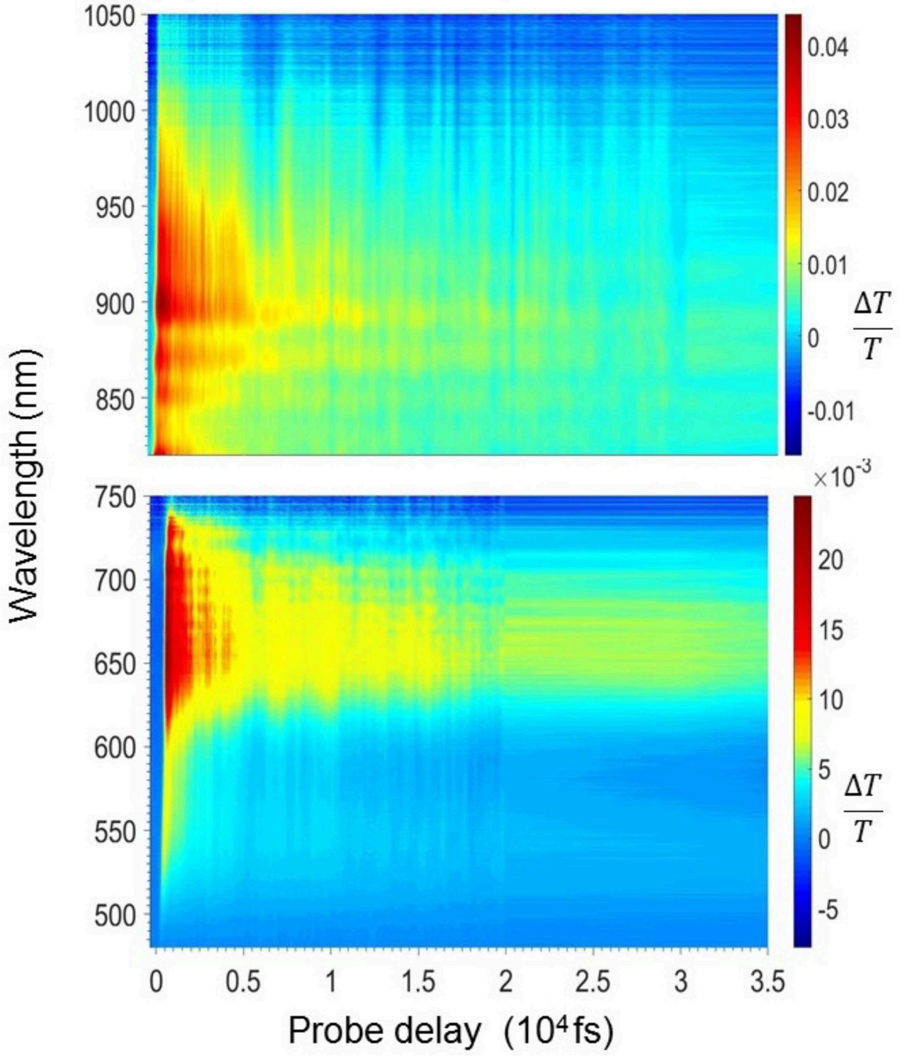

FIGURE 5 | 2-Dimensional $\Delta T/T$ map in the near infrared (bottom panel) and the visible (top panel) region for the LMM mesoparticle suspension.

yellow-red signal represents bleaching or stimulated emission, while the blue data are negative $\Delta T/T$ due to photoinduced absorption bands. The map is substantially, in the first 35 ps, a positive band ranging from 500 to 1,000 nm.

Figure 6 shows the transient transmission spectra at different probe delays. The spectra at 1 ps probe delay is positive in the entire spectral region, and by comparing the spectrum with the absorption and the photoluminescence data, it can be concluded that the signal is an overlap between the bleaching of the ground state and stimulated emission. Increasing the probe delay (green line in **Figure 6**) results in a new photoinduced absorption band that appears at ∼600 and at 950 nm, and is attributed to charged states as previously reported (Banerji et al., 2010; Etzold et al., 2011; Provencher et al., 2014). Surprisingly the positive band extends until the near infrared region where a contribution from stimulated emission is evident. This can be concluded because the absorption signal is much less significant in this region. The overlap of the SE with the PIA band due to the photogenerated charges in this spectral region makes the PL efficiency very low and consequently undetectable in the PL measurements. As an aside, it is important to note from the transient transmission data that there is no indication of a signal coming from residual PVP surfactant present in the solution, as occurred in the photoluminescence spectrum, which indicates that its presence is negligible.

To confirm the origin of the positive transient signal, the dynamics at 520, 600, 670, and 950 nm are compared in **Figure 7**. The decays are similar in first 10 ps indicating that the decay of the singlet exciton states is the origin of the photoinduced signal. After 10 ps, $\Delta T/T$ at 600 and 950 nm becomes negative; the positive signal at these wavelengths overlaps with a negative photoinduced absorption band that is attributed to charged-state formation as previously reported (Provencher et al., 2014).

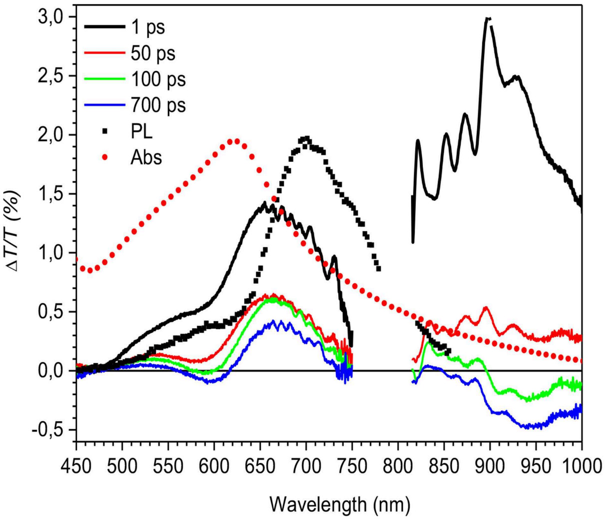

FIGURE 6 | Δ*T*/*T* spectra at different probe delays (see legend in the figure) compared to the absorption (Abs, red solid circles) and photoluminescence (PL) emission (black solid squares) spectra for the LMM mesoparticle suspension.

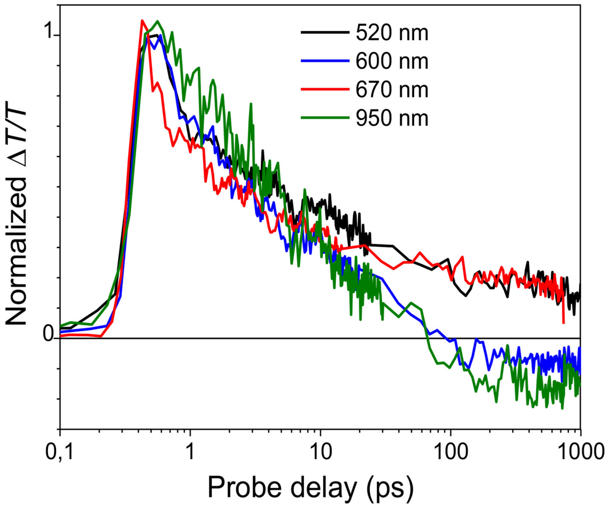

FIGURE 7 | Normalized decay traces at different wavelengths (see legend in the figure) for the LMM mesoparticle suspension.

Discussion

The transient transmission spectra for the different particle suspensions, as for the steady state absorption and emission spectra, are completely different. While the small polymer particles present a photophysics similar to a disordered polymer film, the large particles behave in a completely different way. There are three important differences: Firstly, in the LMM mesoparticle suspension there is *no indication* of the typical PCDTBT exciton energy transfer from the higher energetic states to the lowest state while in the nanoparticle suspension this effect is evident (see blue line in **Figure 4**). Secondly, the signal from the charged states (blue line in **Figure 7**) is weak and is not instantaneous in the LMM suspension while the charges are instantaneously generated in the HMM suspension (see black solid line in **Figure 4**). Finally, stimulated emission occurs in the near infrared region only for the LMM suspension. All of these properties indicate a less efficient interchain interaction strengthening the idea that the LMM particle suspension has a more J-aggregate-like behavior that is not observed in the HMM-nanoparticle suspension.

It has been demonstrated in a range of different polymer systems that the strength of interchain vs. intrachain interactions, resulting in modulation between predominately H- vs. J-aggregate-like behavior, can be tuned systematically by parameters such as solvent casting and annealing (Khan et al., 2004; Eder et al., 2017), pressure (Niles et al., 2012), regioregularity (Clark et al., 2007), and molar mass (Paquin et al., 2013). From the perspective of classical polymer science, it is established that polymers of low molar mass form unconnected, extended-chain crystals. Due to the non-entangled nature of these relatively short-chain macromolecules, this leads to a polycrystalline, one-phase morphology. In contrast, with materials of molar mass larger than the entanglement molar mass, typically two-phase morphologies are obtained, which comprise crystalline moieties embedded in largely amorphous regions, whereby individual macromolecules bridge multiple domains of order (Wunderlich, 1976; Paquin et al., 2013). For poly(3-hexylthiophene) it was found that the macromolecules in aggregated regions of high molar mass polymer adopt a more planar conformation compared to low molar mass materials. This results in the observed increase in intrachain exciton coherence. In contrast, shorter chains seem to lead to more disordered architectures (Paquin et al., 2013). In contrast to those previous results, here the low molar mass particle suspension presents a J-aggregate-like behavior (i.e., more intrachain interaction) but not the high molar mass suspension.

These results indicate that the means of particle preparation affects not only the particle size but also the packing of the polymer chains inside the particles, which dramatically changes their spectroscopic properties. Given that the optical properties of the thin films have been shown to be similar (**Figure 1B** and **Figure 5S**), it is unlikely that the molar mass plays a significant role. It is known that polymer molar mass does affect crystallization (Cheng et al., 1992), and were this to be a factor in the preparation process, then low molar mass polymers may be less well-stacked or less planar than their larger counterparts due, for example, to free chain ends, which would increase the likelihood of localized excitons and greater energetic order. It is nevertheless difficult to envisage how particle size alone can control whether or not excitons are localized, and so the possibility that the method of preparing the PCDTBT particles plays a role cannot be discounted.

CONCLUSION

The photophysics of poly[N-9′-heptadecanyl-2,7-carbazole-*alt*−5,5-(4,7-di-2-thienyl-2′,1′,3′- benzothiadiazole] (PCDTBT) nanoparticle and mesoparticle suspensions has been investigated.

The nanoparticles present a similar behavior of the pristine polymer, with a large Stokes shift and the presence of many localized states near the band edge. The efficient energy transfer from the higher energetic state to the lowest one happens in a time constant of around 7 ps. In these nanoparticles no stimulated emission is detected due to the presence of a photoinduced absorption band related to charged states which overlap the stimulated emission spectral region. The mesoparticles have a completely different behavior. The peak of the absorption spectrum is red-shifted and narrower than that of the nanoparticle suspension, and the Stokes shift is reduced as well as the efficiency of charges formation indicating a more evident J-aggregate-like behavior (fewer interchain interactions) compared to the nanoparticle suspension. Moreover, stimulated emission is detected in the near infrared region for the mesoparticle suspension. It is concluded that the method of particle preparation is crucial not only to determine the particle size but also to change the packing state of the polymer backbones that strongly affects the photophysical properties of the PCDTBT polymer.

AUTHOR CONTRIBUTIONS

The project was devised by TV and MG and supervised by TV, MG, and EP. Data contained in the paper were obtained and analysed by TV, MM, and ChB in Milan. Micro-Raman spectroscopy and preparatory and comparative absorption and photoluminescence data were obtained and analysed in Bordeaux by LP, EP, CyB, and EC. All authors contributed to the scientific discussion of the results. The manuscript was written by TV and MG, although all authors contributed and approved the final version.

ACKNOWLEDGMENTS

MG is grateful to the Politecnico di Milano and CNR-ISMAC for hosting him in Milan. TV and MM acknowledge the project TIMES from Regione Lombardia. In Bordeaux, LP, CyB, EC, EP, and GH acknowledge the financial support from the ADEME Project ISOCEL number 1182C0212 and from Region Nouvelle Aquitaine. This work was performed within the framework of the LCPO/Arkema/ANR Industrial Chair HOMERIC ANR-13-CHIN-0002-01 with grant number AC-2013-365. Micro-Raman spectroscopy experiments were performed at the Institute of Molecular Science of the University of Bordeaux with the help of Dr T. Tassaing.

SUPPLEMENTARY MATERIAL

The Supplementary Material for this article can be found online at: https://www.frontiersin.org/articles/10.3389/fchem.2019.00409/full#supplementary-material

REFERENCES

Baghgar, M., Labastide, J. A., Bokel, F., Hayward, R. C., and Barnes, M. D. (2014). Effect of polymer chain folding on the transition from H- to J-aggregate behavior in P3HT nanofibers. *J. Phys. Chem. C* 118, 2229–2235. doi: 10.1021/jp411668g

Banerji, N., Cowan, S., Leclerc, M., Vauthey, E., and Heeger, A. J. (2010). Exciton formation, relaxation, and decay in PCDTBT. *J. Am. Chem. Soc.* 132, 17459–17470. doi: 10.1021/ja105290e

Blouin, N., Michaud, A., Gendron, D., Wakim, S., Blair, E., Neagu-Plesu, R., et al. (2008). Toward a rational design of poly(2,7-carbazole) derivatives for solar cells. *J. Am. Chem. Soc.* 130, 732–742. doi: 10.1021/ja0771989

Blouin, N., Michaud, A., and Leclerc, M. (2007). A low-bandgap poly(2,7-carbazole) derivative for use in high-performance solar cells. *Adv. Mater.* 19, 2295–2300. doi: 10.1002/adma.200602496

Chan, Y.-H., and Wu, P.-J. (2015). Semiconducting polymer nanoparticles as fluorescent probes for biological imaging and sensing. *Part. Part. Syst. Charact.* 32, 11–28. doi: 10.1002/ppsc.201400123

Cheng, S. Z. D., Chen, J., Barley, J. S., Zhang, A., Habenschuss, A., and Zschack, P. R. (1992). Isothermal thickening and thinning processes in low molecular-weight poly(ethylene oxide) fractions crystallized from the melt. 3. Molecular weight dependence. *Macromolecules* 25, 1453–1460. doi: 10.1021/ma00031a015

Clark, J., Silva, C., Friend, R. H., and Spano, F. C. (2007). Role of intermolecular coupling in the photophysics of disordered organic semiconductors: aggregate emission in regioregular polythiophene. *Phys. Rev. Lett.* 98:206406. doi: 10.1103/PhysRevLett.98.206406

D'Olieslaeger, L., Pfannmöller, M., Fron, E., Cardinaletti, I., Van Der Auweraer, M., Van Tendeloo, G., et al. (2017). Tuning of PCDTBT:PC71BM blend nanoparticles for eco-friendly processing of polymer solar cells. *Sol. Energy Mater. Sol. Cells* 159, 179–188. doi: 10.1016/j.solmat.2016.09.008

Eder, T., Stangl, T., Gmelch, M., Remmerssen, K., Laux, D., Höger, S., et al. (2017). Switching between H- and J-type electronic coupling in single conjugated polymer aggregates. *Nat. Commun.* 8:1641. doi: 10.1038/s41467-017-01773-0

Etzold, F., Howard, I. A., Mauer, R., Meister, M., Kim, T. D., Lee, K.-S., et al. (2011). Ultrafast exciton dissociation followed by nongeminate charge recombination in PCDTBT:PCBM photovoltaic blends. *J. Am. Chem. Soc.* 133, 9469–9479. doi: 10.1021/ja201837e

Feng, L., Zhu, C., Yuan, H., Liu, L., Lv, F., and Wang, S. (2013). Conjugated polymer nanoparticles: preparation, properties, functionalization and biological applications. *Chem. Soc. Rev.* 42, 6620–6633. doi: 10.1039/c3cs60036j

Grey, J. K., Kim, D. Y., Norris, B. C., Miller, W. L., and Barbara, P. F. (2006). Size-dependent spectroscopic properties of conjugated polymer nanoparticles. *J. Phys. Chem. B* 110, 25568–25572. doi: 10.1021/jp065990a

Jakowetz, A. C., Böhm, M. L., Sadhanala, A., Huettner, S., Rao, A., and Friend, R. H. (2017). Visualizing excitations at buried heterojunctions in organic semiconductor blends. *Nat. Mater.* 16, 551–557. doi: 10.1038/nmat4865

Jana, B., Ghosh, A., and Patra, A. (2017). Photon harvesting in conjugated polymer-based functional nanoparticles. *J. Phys. Chem. Lett.* 8, 4608–4620. doi: 10.1021/acs.jpclett.7b01936

Khan, A. L. T., Sreearunothai, P., Herz, L. M., Banach, M. J., and Köhler, A. (2004). Morphology-dependent energy transfer within polyfluorene thin films. *Phys. Rev. B* 69:085201. doi: 10.1103/PhysRevB.69.085201

Kurokawa, N., Yoshikawa, H., Hirota, N., Hyodo, K., and Masuhara, H. (2004). Size-dependent spectroscopic properties and thermochromic behavior in poly(substituted thiophene) nanoparticles. *ChemPhysChem* 5, 1609–1615. doi: 10.1002/cphc.200400117

Labastide, J. A., Baghgar, M., Dujovne, I., Venkatraman, B. H., Ramsdell, D. C., Venkataraman, D., et al. (2011). Time- and polarization-resolved photoluminescence of individual semicrystalline polythiophene (P3HT) nanoparticles. *J. Phys. Chem. Lett.* 2, 2089–2093. doi: 10.1021/jz200958x

Lee, S. J., Lee, J. M., Cho, H.-Z., Koh, W. G., Cheong, I. W., and Kim, J. H. (2010). Poly(thiophene) nanoparticles prepared by Fe^{3+} -catalyzed oxidative polymerization: a size-dependent effect on photoluminescence property. *Macromolecules* 43, 2484–2489. doi: 10.1021/ma9023747

Li, J., Rao, J., and Pu, K. (2018). Recent progress on semiconducting polymer nanoparticles for molecular imaging and cancer phototherapy. *Biomaterials* 155, 217–235. doi: 10.1016/j.biomaterials.2017.11.025

Lin, Y., Dong, C., Cao, F., Xiong, L., Gu, H., and Xu, H. (2017). Size-dependent optical properties of conjugated polymer nanoparticles. *RSC Adv.* 7, 55957–55965. doi: 10.1039/C7RA12164D

McQuarrie, D. A. (2000). *Statistical Mechanics.* Sausalito, CA: University Science Books.

Meng, Z., Hou, W., Zhou, H., Zhou, L., Chen, H., and Wu, C. (2018). Therapeutic considerations and conjugated polymer-based photosensitizers for photodynamic therapy. *Macromol. Rapid Commun.* 39:1700614. doi: 10.1002/marc.201700614

Nagarjuna, G., Baghgar, M., Labastide, J. A., Algaier, D. D., Barnes, M. D., and Venkataraman, D. (2012). Tuning aggregation of poly(3-hexylthiophene) within nanoparticles. *ACS Nano* 6, 10750–10758. doi: 10.1021/nn305207b

Niles, E. T., Roehling, J. D., Yamagata, H., Wise, A. J., Spano, F. C., Moulé, A. J., et al. (2012). J-aggregate behavior in poly-3-hexylthiophene nanofibers. *J. Phys. Chem. Lett.* 3, 259–263. doi: 10.1021/jz201509h

Paquin, F., Yamagata, H., Hestand, N. J., Sakowicz, M., Bérubé, N., Côté, M., et al. (2013). Two-dimensional spatial coherence of excitons in semicrystalline polymeric semiconductors: effect of molecular weight. *Phys. Rev. B* 88:155202. doi: 10.1103/PhysRevB.88.155202

Parrenin, L., Brochon, C., Hadziioannou, G., and Cloutet, E. (2015). Low bandgap semiconducting copolymer nanoparticles by Suzuki cross-coupling polymerization in alcoholic dispersed media. *Macromol. Rapid Commun.* 36, 1816–1821. doi: 10.1002/marc.201500324

Parrenin, L., Laurans, G., Pavlopoulou, E., Fleury, G., Pecastaings, G., Brochon, C., et al. (2017). Photoactive donor-acceptor composite nanoparticles dispersed in water. *Langmuir* 33, 1507–1515. doi: 10.1021/acs.langmuir.6b04496

Pecher, J., and Mecking, S. (2010). Nanoparticles of conjugated polymers. *Chem. Rev.* 110, 6260–6279. doi: 10.1021/cr100132y

Peters, M., Seneca, S., Hellings, N., Junkers, T., and Ethirajan, A. (2018). Size-dependent properties of functional PPV-based conjugated polymer nanoparticles for bioimaging. *Colloids Surf. B* 169, 494–501. doi: 10.1016/j.colsurfb.2018.05.055

Pras, O., Chaussy, D., Stephan, O., Rharbi, Y., Piette, P., and Beneventi, D. (2010). Photoluminescence of 2,7-poly(9,9-dialkylfluorene-*co*-fluorenone) nanoparticles: effect of particle size and inert polymer addition. *Langmuir* 26, 14437–14442. doi: 10.1021/la1011742

Provencher, F., Bérubé, N., Parker, A. W., Greetham, G. M., Towrie, M., Hellmann, C., et al. (2014). Direct observation of ultrafast long-range charge separation at polymer-fullerene heterojunctions. *Nat. Commun.* 5:4288. doi: 10.1038/ncomms5288

Prunet, G., Parrenin, L., Pavlopoulou, E., Pecastaings, G., Brochon, C., Hadziioannou, G., et al. (2018). Aqueous PCDTBT:PC71BM photovoltaic inks made by nanoprecipitation. *Macromol. Rapid Commun.* 39:1700504. doi: 10.1002/marc.201700504

Scarongella, M., Laktionov, A., Rothlisberger, U., and Banerji, N. (2013). Charge transfer relaxation in donor–acceptor type conjugated materials. *J. Mater. Chem. C* 1, 2308–2319. doi: 10.1039/c3tc00829k

Shao, B., and Vanden Bout, D. A. (2017). Probing the molecular weight dependent intramolecular interactions in single molecules of PCDTBT. *J. Mater. Chem. C* 5, 9786–9791. doi: 10.1039/C7TC02255G

Spano, F. C. (2010). The spectral signatures of Frenkel polarons in H- and J-aggregates. *Acc. Chem. Res.* 43, 429–439. doi: 10.1021/ar900233v

Sun, K., Chen, H., Wang, L., Yin, S., Wang, H., Xu, G., et al. (2014). Size-dependent property and cell labeling of semiconducting polymer dots. *ACS Appl. Mater. Interfaces* 6, 10802–10812. doi: 10.1021/am502733n

Tong, M., Coates, N. E., Moses, D., Heeger, A. J., Beaupre, S., and Leclerc, M. (2010). Charge carrier photogeneration and decay dynamics in the poly(2,7-carbazole) copolymer PCDTBT and in bulk heterojunction composites with PC70BM. *Phys. Rev. B* 81:125210. doi: 10.1103/PhysRevB.81.125210

Virgili, T., Forni, A., Cariati, E., Pasini, D., and Botta, C. (2013). Direct evidence of torsional motion in an aggregation-induced emissive chromophore. *J. Phys. Chem. C* 117, 27161–27166. doi: 10.1021/jp4104504

Wakim, S., Beaupré, S., Blouin, N., Aich, B.-R., Rodman, S., Gaudiana, R., et al. (2009). Highly efficient organic solar cells based on a poly(2,7-carbazole) derivative. *J. Mater. Chem.* 19, 5351–5358. doi: 10.1039/b901302d

Wang, S., Singh, A., Walsh, N., and Redmond, G. (2016). Surfactant-free, low band gap conjugated polymer nanoparticles and polymer:fullerene nanohybrids with potential for organic photovoltaics. *Nanotechnology* 27:245601. doi: 10.1088/0957-4484/27/24/245601

Westerling, M., Aarnio, H., Österbacka, R., Stubb, H., King, S. M., Monkman, A. P., et al. (2007). Photoexcitation dynamics in an alternating polyfluorene copolymer. *Phys. Rev. B* 75:224306. doi: 10.1103/PhysRevB.75.224306

Wong, M. Y. (2017). Recent advances in polymer organic light-emitting diodes (PLED) using non-conjugated polymers as the emitting layer and contrasting them with conjugated counterparts. *J. Electron. Mater.* 46, 6246–6281. doi: 10.1007/s11664-017-5702-7

Wu, C., and Chiu, D. T. (2013). Highly fluorescent semiconducting polymer dots for biology and medicine. *Angew. Chem. Int. Ed.* 52, 3086–3109. doi: 10.1002/anie.201205133

Wunderlich, B. (1976). *Macromolecular Physics.* New York, NY: Academic Press.

Xu, X., Liu, R., and Li, L. (2015). Nanoparticles made of π-conjugated compounds targeted for chemical and biological applications. *Chem. Commun.* 51, 16733–16749. doi: 10.1039/C5CC06439B

Zhou, X., Belcher, W., and Dastoor, P. C. (2014). Solar paint: from synthesis to printing. *Polymers* 6, 2832–2844. doi: 10.3390/polym6112832

Ziffer, M. E., Jo, S. B., Liu, Y., Zhong, H., Mohammed, J. C., Harrison, J. S., et al. (2018). Tuning H- and J-aggregate behavior in π-conjugated polymers via noncovalent interactions. *J. Phys. Chem. C* 122, 18860–18869. doi: 10.1021/acs.jpcc.8b05505

Conflict of Interest Statement: The authors declare that the research was conducted in the absence of any commercial or financial relationships that could be construed as a potential conflict of interest.

frontiers in Chemistry

ORIGINAL RESEARCH
published: 10 July 2019
doi: 10.3389/fchem.2019.00484

Formation of Monolithic Ion-Selective Transport Media Based on “Click” Cross-Linked Hyperbranched Polyglycerol

Tobias Abrahamsson [1†], ***David J. Poxson*** [1†], ***Erik O. Gabrielsson*** [1†], ***Mats Sandberg*** [2†], ***Daniel T. Simon*** [1*] ***and Magnus Berggren*** [1†]

[1] Laboratory of Organic Electronics, Department of Science and Technology, Linköping University, Norrköping, Sweden,
[2] RISE Acreo AB, Norrköping, Sweden

Edited by:
John George Hardy,
Lancaster University, United Kingdom

Reviewed by:
Basem Moosa,
KAUST Catalysis Center (KCC),
Saudi Arabia
Radek Cibulka,
University of Chemistry and
Technology in Prague, Czechia

****Correspondence:***
Daniel T. Simon
daniel.simon@liu.se
orcid.org/0000-0002-2799-3490

† Tobias Abrahamsson
orcid.org/0000-0002-3615-1850
David J. Poxson
orcid.org/0000-0002-4246-8723
Erik O. Gabrielsson
orcid.org/0000-0002-0302-226X
Mats Sandberg
orcid.org/0000-0002-0631-3804
Magnus Berggren
orcid.org/0000-0001-5154-0291

Specialty section:
This article was submitted to
Organic Chemistry,
a section of the journal
Frontiers in Chemistry

Received: *21 March 2019*
Accepted: *24 June 2019*
Published: *10 July 2019*

Citation:
Abrahamsson T, Poxson DJ, Gabrielsson EO, Sandberg M, Simon DT and Berggren M (2019) Formation of Monolithic Ion-Selective Transport Media Based on “Click” Cross-Linked Hyperbranched Polyglycerol. Front. Chem. 7:484. doi: 10.3389/fchem.2019.00484

In the emerging field of organic bioelectronics, conducting polymers and ion-selective membranes are combined to form resistors, diodes, transistors, and circuits that transport and process both electronic and ionic signals. Such bioelectronics concepts have been explored in delivery devices that translate electronic addressing signals into the transport and dispensing of small charged biomolecules at high specificity and spatiotemporal resolution. Manufacturing such “iontronic” devices generally involves classical thin film processing of polyelectrolyte layers and insulators followed by application of electrolytes. This approach makes miniaturization and integration difficult, simply because the ion selective polyelectrolytes swell after completing the manufacturing. To advance such bioelectronics/iontronics and to enable applications where relatively larger molecules can be delivered, it is important to develop a versatile material system in which the charge/size selectivity can be easily tailormade at the same time enabling easy manufacturing of complex and miniaturized structures. Here, we report a one-pot synthesis approach with minimal amount of organic solvent to achieve cationic hyperbranched polyglycerol films for iontronics applications. The hyperbranched structure allows for tunable pre multi-functionalization, which combines available unsaturated groups used in crosslinking along with ionic groups for electrolytic properties, to achieve a one-step process when applied in devices for monolithic membrane gel formation with selective electrophoretic transport of molecules.

Keywords: hyperbranched polyglycerol, polyelectrolyte, multi-functionalization, thiol-ene, cross-linking, ion-selective, electrophoretic transport

INTRODUCTION

Organic bioelectronics (Wei, 1998; Berggren and Richter-Dahlfors, 2007; Someya et al., 2016) comprises the research and engineering field in which the coupling of biomolecules and electronic charges, in organic electro-active materials, is utilized to achieve sensing or actuation of processes and reactions in various biological systems. During the last decade, major interest in this field has included the development and engineering of devices that convert electronic addressing signals into the delivery of small-sized charged biomolecules. In one embodiment, planar drug delivery electrodes, based on conjugated polymers pre-loaded with a biomolecule, have been explored

(Kontturi et al., 1998; Abidian et al., 2006; Wadhwa et al., 2006). Upon electronically addressing these electrodes, their oxidation state changes, triggering release of the pre-loaded biomolecule. This effect is driven by the changes in electrostatic and morphological properties of the electrode bulk upon switching. In another embodiment, the mixed ion-electron conduction of two separated conjugated polymer electrodes are combined with the selective ion transport of a membrane to form a class of electrophoretic drug delivery devices, called organic electronic ion pumps (OEIPs) (Isaksson et al., 2007; Simon et al., 2009; Arbring Sjöström et al., 2018). By addressing the two polarizable electrodes of the OEIP an electric field is established along the ion selective channel, enabling the selective delivery of small ($\lesssim$200 g/mol) charged biomolecules, transported from a reservoir to a target system. Such OEIP devices have successfully been explored to deliver neurotransmitters and ions in various applications, especially targeting actuation and suppression of neuronal processes and signaling *in vitro* (Tybrandt et al., 2009; Williamson et al., 2015; Jonsson et al., 2016) and *in vivo* (Simon et al., 2009; Jonsson et al., 2015; Proctor et al., 2018).

The monolithic ion-selective channel of an OEIP should exhibit a high and selective conductivity for the desired charged (bio)molecule, along with manufacturability of miniaturized structures to enable application *in vitro* or *in vivo*. Furthermore, to match the scale of target biological systems and provide the highest degree of proximity and spatiotemporal precision, OEIPs are generally fabricated with ion-selective channels on the micrometer scale (width, approaching the scale of a single cell) and thickness of hundreds of nanometers (based on their thin-film nature). To date, most OEIPs and related iontronic devices (Arbring Sjöström et al., 2018) have utilized linear polyelectrolyte systems, such as polystyrenesulfonate or quaternized poly(vinylbenzyl chloride), processed into features using classical thin film processing techniques. As produced, these features are dry and when immersed into electrolytes and media, the ion-selective conductor swells due to considerable uptake of water and electrolyte solutes, leading to frequent mechanical failure of the devices and low production yield. Recently, our group has demonstrated capillary-based OEIPs, where the monolithic ion transport channel is formed inside a free-standing glass capillary (Poxson et al., 2019; Seitanidou et al., 2019). These devices take advantage of the glass capillary (generally $\leq$60 μm outer diameter) as both the encapsulation and substrate for the ion channel. As such, the encapsulation is in place during fabrication, enabling the channel to remain hydrated (if stored properly) continuously from fabrication to end-use.

Formation and operation of ion-selective monolithic ion transport media in microfluidic or capillary-based channels places a range of demands on the design of the molecules and reactions forming the given transport medium. Most importantly, the medium should comprise a continuous porous structure through the monolithic body where the pore size should permit mobility of the targeted charged molecules. The pores should, however, not be so large as to permit macroscopic flow. Further, the number density of fixed charges should be sufficient for ion-selective transport, and the distribution of charges should be as homogeneous as possible. Moreover, the monolithic ion transport medium should be obtained by polymerization of molecules via reactions that can be triggered by external stimuli such as heat or actinic irradiation under atmospheric conditions to form bonds that are stable at the extreme pH-values that may occur in ion transport devices (Seitanidou et al., 2017). For straightforward filling of the microfluidic channel, the composition forming the ion transport medium (monomers and polymerization initiators) should exist as a single-phase fluid to enable filling using a minimum of solvent. Mechanically, the formed monolithic ion transport medium should exhibit a cohesive strength sufficient to tolerate solvent exchange and exhibit a good adhesion to the channel walls. We have selected thiol-ene click coupling to form the cross-links between monomers upon irradiation, since the thiol-ene coupling reaction tolerates the presence of air oxygen and proceeds to produce cross-links that are stable at the pH-values reached during OEIP operation (Hoyle and Bowman, 2010). As a structural building block, we have selected polyfunctional hyperbranched and dendrimeric molecules. These polyfunctional dendrimers can be substituted with groups for cross-linking as well as ionic groups with controlled degrees of substitution. It is of course important that the structural unit, the dendrimer, is formed by bonds that are stable to conditions of an OEIP under operation. Therefore, we have opted for polyether dendrimers having hydroxyl terminal groups since the ether groups are relatively stable to extreme pH values.

The use of thiol-ene chemistry calls for the presence of carbon-carbon double bonds as well as thiol groups. We have selected to functionalize the dendrimers with allyl groups for coupling with a second molecule, a thiol-terminated polyether. In addition to allyl-groups, the dendrimers are functionalized with groups carrying either positive or negative charges. To form the covalently cross-linked ion-transport medium with thiol-ene coupling, radical initiators must also be present, in addition to the allyl-functional dendrimers and thiol-functionalized cross-linkers, and these components must exist as a single-phase mixture with blending at the molecular level in the composition. For this reason, there is a need to add a minimal amount of solvent to form the single-phase composition. The amount of solvent should be minimal and constitute a minority component in the composition to avoid formation of large voids in the formed ion-transport channel, which would lead to breakdown of Donnan exclusion (charge selectivity) (Kontturi et al., 2008).

Here we report a new type of material synthesized and characterized based on a hyperbranched polyglycerol foundational structure, which has been multi-functionalized with different degrees of allyl and triphenylphosphonium groups. The click chemistry polymerization between the cationic polyelectrolyte mixed with tri-functional polythiol cross-linker has been achieved via thermal and photo-initiation. The sol-gel process of the macromolecules has formed insoluble free-standing membranes, capable of selective electrophoretic transportation of large aromatic molecules in OEIP structures. Due to solubility properties of the hyperbranched polyelectrolyte, these types of gel membranes can be prepared with a minimal amount of organic solvent with pre-hydrated states for OEIPs, iontronics, and other such organic (bio)electronic devices.

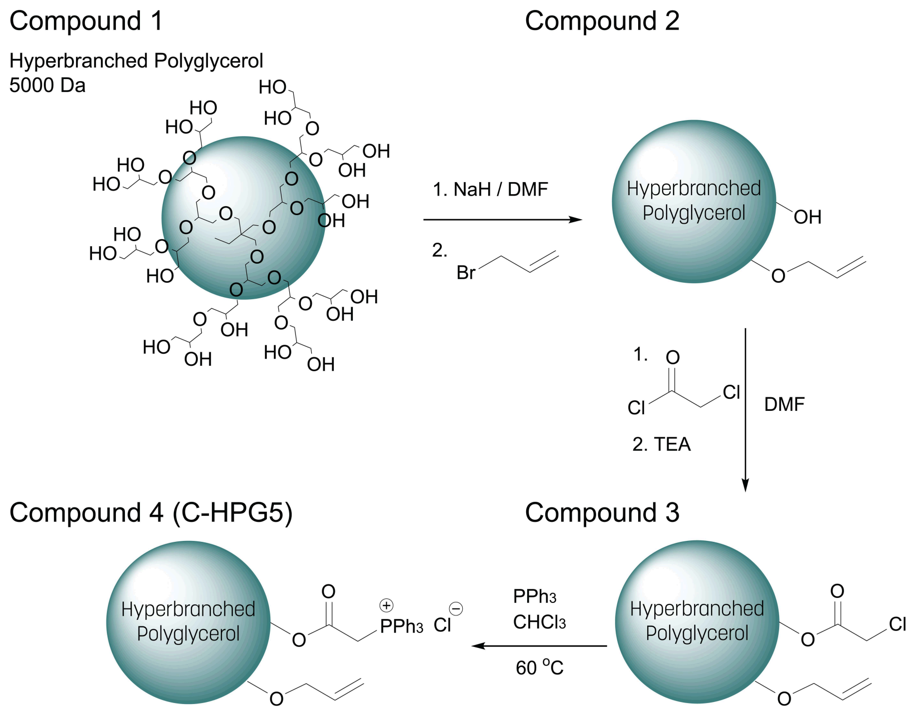

SCHEME 1 | Synthetic multi-functionalization of hydroxyl end-groups of (1) Hyperbranched Polyglycerol 5000 Da (simplified structural representation) with (2) allyl and (3) chloroacetate. (4) Chloride substituted with triphenylphosphine into charged phosphonium (C-HPG5).

RESULTS

Synthesis and Structural Characterization

The multi-functionalization synthesis of the hyperbranched polyglycerol (5,000 Da) was carried out step wise, utilizing the multiple terminal hydroxyl groups of the polymer (**Scheme 1**). In the initial step, allylation was performed on the polymer resulting in a degree of substitution of ∼ 10% (**Figure S1a**) and distinct alkene carbon signals were detected in C-NMR (**Figure S1b**). This characterization was calculated via ^{1}H-NMR spectroscopy where the integral ratio of the specific functionalities' protons was compared to the integral ratio of the core polymer's structure protons (Equation 1), assuming the correlation with the number of terminal groups equal to the number of repeating units of the polymer (Gode et al., 2006; Burakowska and Haag, 2009).

$$DS\,(\%) = \left(\frac{I_{H-func.}}{H_{func.}} / \frac{I_{H-core}}{H_{core}} \right) \times 100 \qquad (1)$$

The remaining hydroxyl groups were then converted into esters by introducing chloroacetyl functionality, though signal overlapping occurred between the newly introduced protons located at the α-chloroacetate and the previously incorporated methylene protons neighboring to the alkene groups, thus somewhat obstructing the values of integration. Regardless, a well-defined characteristic peak was observed (**Figure S2a**) with an integral magnitude in accordance with a high degree of functionalization of ∼90% chloroacetate (**Figure S2a** equation). Likewise, the functionalization shifts of the outer layer protons located at secondary and tertiary carbons which previously had hydroxyl (primary, secondary) functionality, became ester (primary, secondary) functionalities resulting in downfield shifts. This made the further estimation of the different functionalities much more difficult. The hyperbranched polyglycerol's solubility changed drastically with the incorporation of the hydrophobic α-chloroacetylate groups to the polymer, rendering it insoluble in hydrophilic solvents, emphasizing the crucial role of the surface functionalities of the hyperbranched polymers role in interacting with its surrounding environment (Türk et al., 2007; Thota et al., 2016).

The relationship between surface functionalization and solubility was also observed in the final synthetic step of the polymer where ionic functionality was introduced to the macromolecular structure—rendering it again soluble in polar solvents—by nucleophilic substitution of the α-chloride with triphenylphosphine, quaternizing the phosphor into positively charged phosphonium (Matveeva et al., 2003). This final synthetic step resulted in cationically-functionalized hyperbranched polyglycerol with molecular weights of 5 kDa (C-HPG5, **Scheme 1**, Compound 4). The values obtained from the NMR peak integration of the introduced triphenyl functionality (**Figure 1**) lead to yields of the quaternization reactions between 60 and 70% (**Figure S3**), though solvent peak signals in the polymer region along with functionality shift overlap complicate this estimation.

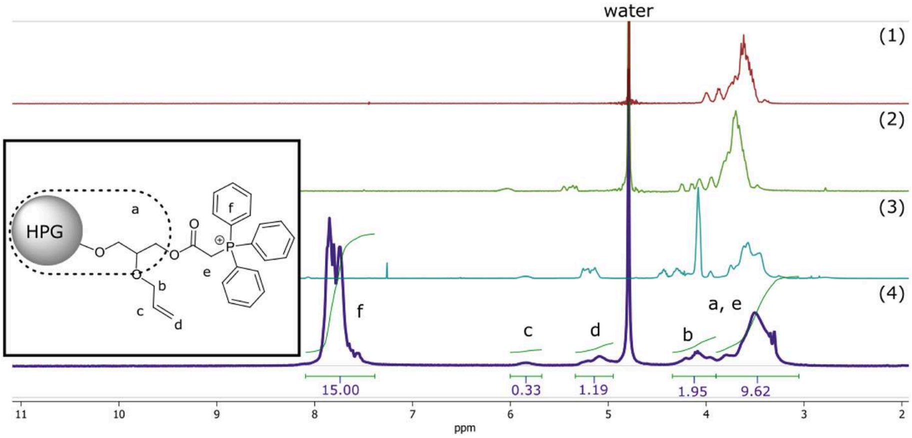

FIGURE 1 | ^{1}H-NMR of compound 1–4. Simplified representation of C-HPG5 chemical structure with assigned and integrated peaks (4). Assigned protons of allyl (b and d) integral signals regions overlap with outer core protons of HPG (a) depending on functionality.

Peak splitting was observed in the NMR spectra for the peak associated with the six-membered phenyl rings of the phosphonium, which can be related to the presence of different structural conformation over phosphor (Aganova et al., 2014) seen in ^{31}P- and ^{13}C-NMR. ^{31}P-NMR studies of C-HPG5 also showed solvent-dependent peak splitting (**Figure S3c**). There was a partial split of the phosphonium signal seen in methanol-d_6, but not exhibited in D_2O.

The amphiphilic nature displayed of the triphenylphosphonium hyperbranched polyelectrolyte (C-HPG5) made it easily solubilized in very small amounts of methanol solution with up to 3 g/mL (80 wt %) of C-HPG5 polymer. This demonstrates high solubility capabilities of the hyperbranched polyelectrolyte with significant amounts of charged surface functionalities (Kłos and Sommer, 2010). In combination with the hydrophobic triphenyl groups, this renders the C-HPG5 polymer soluble/processable from both protic and aprotic solvent mixtures. This important feature was utilized in the subsequent cross-linking, where components such as initiators and cross-linking agents exhibit much more lipophilic solubilities. The versatile solubility also makes the C-HPG5 polyelectrolyte able to interface the system of hydrophilic cationic charges and hydrophobic interfaces in low amounts of solution.

Thermal Cross-Linking

To obtain the cross-linked hyperbranched polyglycerol electrolyte, the triphenylphosphonium and allyl functionalized HPG (C-HPG5, Compound 4) was first mixed with Thiocure ETTMP 1300 (ethoxylated-trimethylpropan tri(3-mercaptopropionate)) with AIBN (2,2′-azobis(2-methylpropionitrile)), and TATATO (1,3,5-triallyl-1,3,5-triazine-2,4,6(1H,3H,5H)-trione) in water/methanol mixtures or DMSO, applying high concentration kinetics before thermal-initiated crosslinking (**Figure 2**).

The thiol-ene click chemistry reaction (Hoyle and Bowman, 2010; Trey et al., 2010) allowed the formation of large amounts of the cross-linked insoluble free-standing gel from versatile, inexpensive starting materials. Our initial experiments showed that synthetic mixtures under high concentration kinetic control successfully cross-linked with both anionic or cationic functional groups (e.g., sulfonate or phosphonium) by applying photo-initiated surface chemistry for the formation of anionic or cationic exchange membrane (AEM or CEM) gel materials. Unfortunately, we found that the thermally-initiated cross-linking reaction did not proceed in solution for the cationic C-HPG5 without addition of TATATO (Kasprzak et al., 2009), independent of the inclusion or exclusion of the thiol cross-linker Thiocure 1300 (**Table 1**, TM1-3). With several different reaction conditions applied, the concentration was observed to play a crucial role for the success of the thermally-initiated sol-gel: lower concentration of C-HPG5 polyelectrolyte combined with the same equivalents of reactants (as TM1) did not lead to successful gel formation (**Table 1**, TM4-5). To ensure that the final gels consisted primarily of the C-HPG5 polyelectrolyte material, the concentrations of the other components were reduced to levels corresponding to theoretically calculated 1:1:1 ratios of allyl-thiol-allyl for the three components, in accordance with the ∼10–20% allyl functionalized C-HPG5. This formulation did successfully cross-link, emphasizing the high concentration kinetics requirement (**Table 1**, TM6, **Figure 2b**). The exact concentration limit of the polyelectrolyte for the reaction wasn't defined in methanol, though attempts with similar reaction conditions in DMSO proved able to form a continuous gel at $1.13\,\text{g mL}^{-1}$, nearly half the concentration as T1-3 or T6-7 (**Table 1**, TD1-2, **Figure 2c**). The lower degree of porosity was attributed to the higher boiling point of the solvent, which was also observed in TM1 with the crosslinking conducted in either methanol or 1-propanol (**Figure S4**).

Experiments with catalytic amounts of AIBN (0.2 wt%) were also conducted (**Table 1**, TM7). This formulation resulted in an insoluble gel, though without high amounts of visible porosity compared to the TM1 (6.5 wt%, **Figure 3**) formulation. Gelling with high amounts of AIBN initiator exhibited pronounced pores, formed from the boiling of solvent during the solidification. However, reducing AIBN concentration

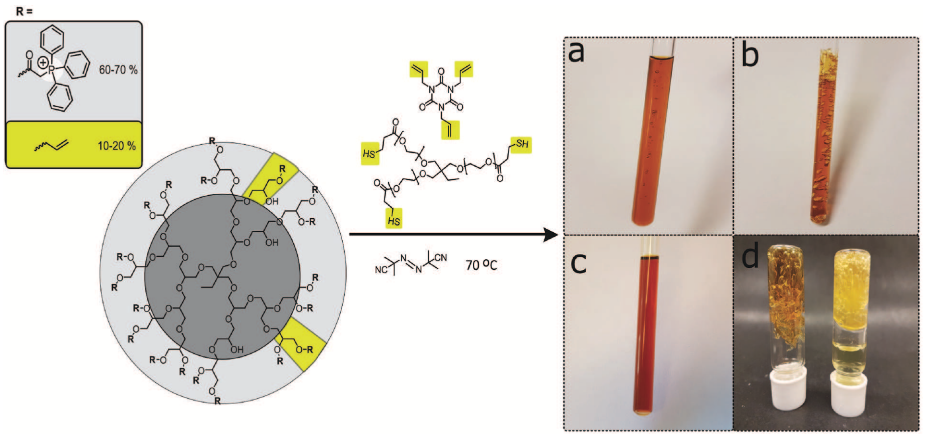

FIGURE 2 | High concentration liquid mixtures of C-HPG5 polymer, Thiocure® ETTMP 1300, TATATO, and AIBN for thermal-initiated cross-linking and formation of gel membranes. Highlighted cross-linking units in yellow. **(a)** Initial heating stage with small bubbles formed due to boiling methanol. **(b)** Finalized cross-linking in methanol resulted in a porous insoluble gel network, while **(c)** in DMSO a more consistent gel was formed due to the higher boiling point solvent. **(d)** The cross-linked gels were able to withstand solvent swelling in methanol (left) and solvent exchange to H_2O (right).

TABLE 1 | Thermal cross-linking formulations.

Thermal cross-link	C-HPG5 (g mL^{-1})	Thiocure 1300 (g mL^{-1})	TATATO (g mL^{-1})	AIBN (g mL^{-1})	Gel formation
TM1$_{\text{MeOH}}$	2	2	0.11	0.34	Yes
w/10%H20	2	2	0.11	0.34	Yes
w/propanol	2	2	0.11	0.34	Yes
TM2$_{\text{MeOH}}$	2	-	0.11	0.34	No
TM3$_{\text{MeOH}}$	2	2	-	0.34	No
TM4$_{\text{MeOH}}$	0.2	0.2	0.01	0.03	No
TM5$_{\text{MeOH}}$	0.5	0.13	0.03	0.07	No
TM6$_{\text{MeOD}-d4}$	2	0.56	0.10	0.10	Yes
TM7$_{\text{MeOH,cata.}}$	2	2	0.11	0.01	Yes
TD1$_{\text{DMSO}}$	1.13	1.13	0.06	0.19	Yes
TD2$_{\text{DMSO}-d6\text{,NMR}}$	1.13	0.29	0.06	0.06	Yes

to catalytic amounts enabled incorporating methanol more continuously into the gel. N_2-gas evolution from AIBN initiator breakdown may also play a role in pore formation.

NMR Monitoring of Thermal Cross-Linking

Components were combined in DMSO-d_6 according to formulation TD2 (**Table 1**) and transferred into an NMR-tube. Following 5 min of sonification and deaerating with N_2-gas, the tube was sealed and placed inside a Varian Oxford 300 MHz NMR spectrometer. When the tube had reached a temperature of 70°C, the first spectrum was collected, and we proceeded to monitor the crosslinking reaction. The process was carried out by locking all the parameters according to the initial spectrum (to prevent re-shimming) and spectra were then collected every minute (**Figure 4**). After the heating had proceeded for 11 min with no significant change in intensity between spectra, the gelification process began. The sol-gel reaction proceeded with a rapid velocity and with the spectrum collected at minute 12, a change in the integral intensity was already observed (intensity ∼27,000 → 20,000). Within the time frame of 2 min, the entire solution had solidified, characterized by a substantial loss of signal intensity (**Figure 4**, 12–14 min) and broadening of the spectrum's overall signatures. Due to a rapid build-up of high pressure inside the tube during the gelification process, the monitoring was terminated after 14 min. A somewhat increased integral intensity (∼8,000 → 9,000) between the last two time points (13–14 min) could be seen, which is related to the overall broadening of signal intensity across the entire spectrum.

Photo-Initiated Cross-Linking

A series of free-standing transparent membranes were synthesized by drop-casting solutions (**Table 2**) on glass, Teflon, or gold substrates followed by UV exposure for 10 min at 365 nm (10 mJ/cm^2). These membranes were then peeled off from the substrate surfaces, displaying soft, flexible properties while remaining intact after soaking in solvents such as deionized water and methanol along with solvent exchange (**Figure S5**). It was also observed that when the membranes had been equilibrated in

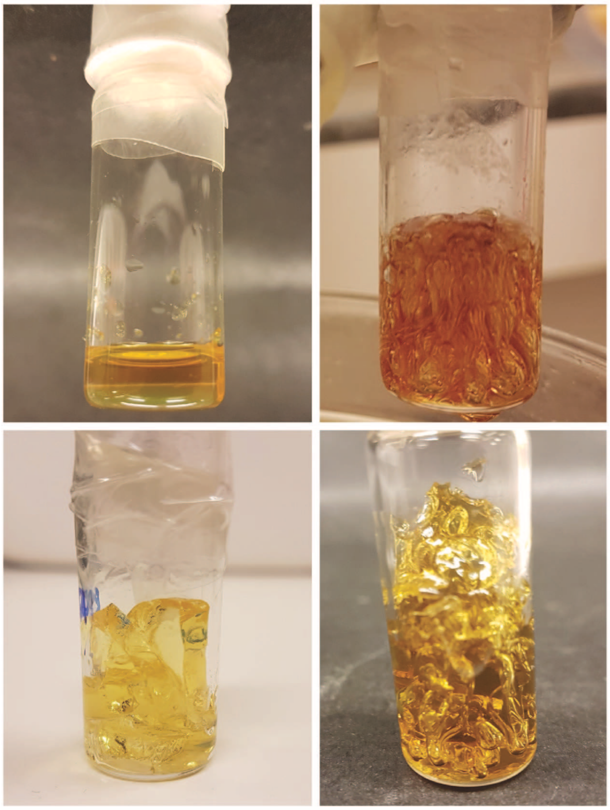

FIGURE 3 | Top row: Catalytic amount of AIBN (0.2 wt%) resulted in a more continuous gel (left) while high amounts (6.5 wt%) led to more porosity (right). Bottom row: Respective gels swelled in methanol. The catalytic gel (left) was cut into pieces to illustrate that an insoluble gel formation had occurred.

deionized water, the mechanical strength was somewhat reduced, resulting in more brittle—but still flexible—gels.

In the series of drop-casting formulations (**Table 2**), the Thiocure 1300 component was reduced so as to reach the theoretically calculated 1:1:1 ratio with the unsaturated allyl functionality (~10 mol %) of the C-HPG5 in relation to the allyl of TATATO and the thiol. We thus aimed to achieve a membrane consisting primarily of C-HPG5 polymer (UVC4). We also reduced the composition concentration (0.5 g/mL C-HPG5) to investigate if the photo-initiated surface crosslinking could proceed at lower concentrations in comparison with thermally-initiated cross-linking (UVC2-4). These formulations did proceed to gelification, and in the two latter cases we were able to use a 50/50 blend of water/methanol as solvent (**Figures S5**, **S6**). The addition of water was intended to both reduce the factor of organic solvent and to ensure less solvent evaporation (higher boiling point) during the UV-curing process. Not only was membrane formation still possible with the 50/50 water/methanol solvent, but the resulting membranes were in a pre-hydrated state due to incorporation of water. With minimum amounts of other reagent components such as catalytic amounts of photo-initiator (UVC3) and a predominant C-HPG5 composition mixture (UVC4), we demonstrate the ability to formulate and crosslink into membranes at both low and high concentrations. This is due to the solubility of the cationic hyperbranched polyelectrolyte, whereas the limiting factor otherwise lies with the miscibility of the initiator and cross-linker.

Utilization in Organic Electronic Ion Pumps

To characterize the C-HPG5 membrane's anion transport capabilities, we fabricated OEIPs using a micro-molding in capillaries (MIMIC) technique (Kim et al., 1996) (**Figure 5A**). OEIPs were manufactured by pouring and curing PDMS into ~2 mm thick films on a glass master substrate with a (photolithographically) pre-patterned SU-8 pattern on top of it, defining the ion channel geometry (**Figure 5A**-1). The width and height of the SU-8 pattern were measured to be 85 and 43 µm, respectively, using an optical profilometer (**Figure S7**). The PDMS was cut into small blocks, consisting of two separated electrolyte reservoirs connected by a capillary channel with an average length of 7.1 mm. After surface activation by treatment with O_2 plasma, the PDMS was bonded to glass substrates (**Figure 5A**-3). The channels were filled with C-HPG5 cross-linking solution (formulation UVC4) by capillary force according to the MIMIC technique (**Figure S8a**). Following UV cross-linking as described above, the C-HPG5-based AEM was formed (**Figure 5A**-4) where the homogeneity and continuity was studied using scanning electron microscopy (**Figure S8b**). The bonded PDMS mold was left on the device to act as an encapsulation layer.

Devices were tested and characterized with source and target electrolyte solutions of 100 mM NaCl(aq) with PEDOT:PSS on polyethylene terephthalate (PET) strips used as replaceable electrodes. Cl^- ion transport through the C-HPG5 membrane was achieved by applying a constant current of 100 nA between the PEDOT:PSS electrodes (**Figure S9**) (voltage was recorded continuously). Assuming perfect permselectivity and using the OEIP's channel geometry and voltage measurements (from 4 OEIP devices tested), the conductivity (ρ) for Cl^- ions was calculated using the formula:

$$\rho = \frac{l \times I}{w \times h \times V} \tag{2}$$

where l, w, and h are the length, width, and height of the channel, and I and V the measured current and voltage. An average conductivity value of $0.24 \pm 0.02\,\mathrm{S\ m^{-1}}$ for in the C-HPG5 polyelectrolyte channel was calculated (**Table 3**).

As a demonstration of the C-HPG5 polyelectrolyte's capability to electrophoretically transport larger and more rigid molecular structures, the dye molecule methyl blue^{2-} (10mM(aq), **Figure 5B**), was used as a source electrolyte. The transport of methyl blue^{2-} was readily observed visually as the blue dye gradually filled the channel (**Figure 5C**).

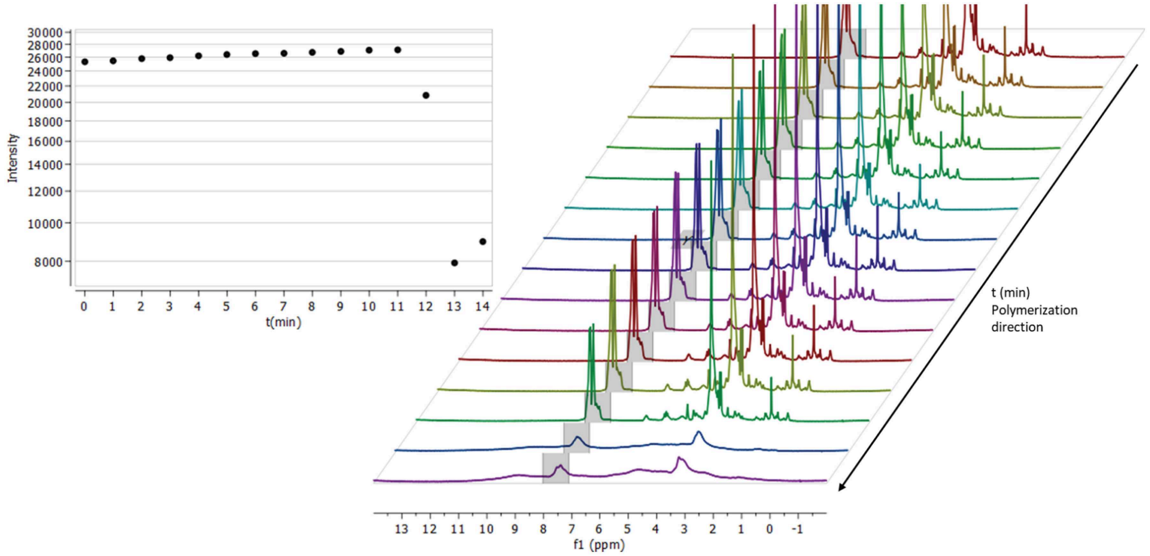

FIGURE 4 | Thermal initiated crosslinking with C-HPG5 at 70°C in DMSO, monitored by collecting 1H-NMR (300 MHz) spectra every minute (right). Integral of the triphenyl functionalities intensity (gray region in spectra) plotted against time (left). When the reaction is initiated it occurs at an extremely fast rate, distinguished by the rapid loss of the signal intensity.

TABLE 2 | Photo-initiated cross-linking formulations.

Photo cross-link	C-HPG5 (g mL^{-1})	Thiocure 1300 (g mL^{-1})	TATATO (g mL^{-1})	Irgacure 2959 (g mL^{-1})	Gel formation
UVC1$_{MeOH}$	1	1	0.06	0.28	Yes
UVC2$_{MeOH}$	0.5	0.5	0.03	0.12	Yes
UVC3$_{MeOH/H20}$	0.5	0.26	0.03	0.007	Yes
UVC4$_{MeOH/H20}$	0.5	0.13	0.03	0.03	Yes

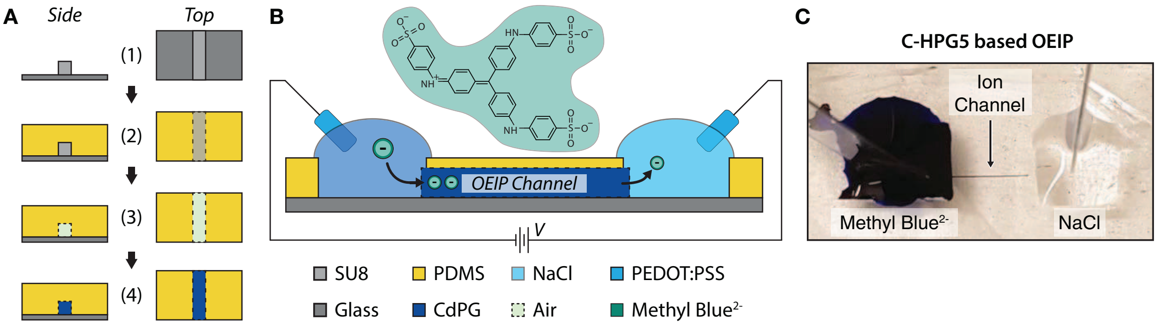

FIGURE 5 | C-HPG5-based OEIP device. **(A)** Schematic of OEIP MIMIC fabrication: (1) SU-8 is patterned on glass substrate; (2) PDMS cured over SU-8 pattern; (3) PDMS with molded void is transferred to a UV-ozone-treated glass substrate; (4) C-HPG5 is filled into PDMS void via capillary force and UV cross-linked. **(B)** Schematic profile of fabricated C-HPG5 based OEIP and chemical structure of methyl blue. **(C)** Photograph of C-HPG5-based OEIP during operation. Methyl blue in the source reservoir is electrophoretically transported through the C-HPG5 AEM channel toward the target electrolyte, NaCl(aq), due to applied voltage between the PEDOT:PSS electrodes. At the time point of the photograph, the front of methyl blue had nearly reached the target electrolyte.

DISCUSSION

The polymer core of hyperbranched polyglycerol (5,000 Da) used in this study was chosen as it has been well-studied since its original synthesis (Sunder et al., 1999), with low polydispersity (Sunder et al., 2000), high degree of branching ("dendrimer-like") structure (Abbina et al., 2017), biocompatibility (Frey and Haag, 2002; Calderón et al., 2010; Wilms et al., 2010), and thoroughly elucidated structural properties (Baille et al., 2004; Kainthan et al., 2006; Schubert et al., 2016). This versatile material, coupled with the stability of the unreactive ether bonds, allowed the final polyelectrolyte membrane to operate at elevated pH and

TABLE 3 | C-HPG5-based OEIP characterization (100 mM NaCl(aq) as source and target electrolytes).

Dev.	Length (mm)	Width (μm)	Height (μm)	Cross section area (μm^2)	Current (nA)	Voltage (V)	Conductivity (S m^{-1})
1	7.0	85	43	3,655	100	0.73	0.26
2	6.5	85	43	3,655	100	0.75	0.24
3	7.5	85	43	3,655	100	0.85	0.24
4	7.3	85	43	3,655	100	0.89	0.22
Avg.	7.1 ± 0.4						± 0.02

voltages without structural breakdown. Previous studies have reported hyperbranched polyglycerols with cationic side-group functionalization (Schwab and Mecking, 2005) as well as alkene functionalities for thiol-ene click chemistry reactions (Fu et al., 2008; Killops et al., 2008; Nilsson et al., 2008; Trey et al., 2010). In this study, we demonstrate the possibility of precisely tailoring the properties of the hyperbranched polyglycerols with multi-functionalization by controlled introduction of both charged cationic and allyl groups. This multi-functionalization enabled thiol-ene crosslinking with tri-thiolated polyethylene glycol (Thiocure ETTMP 1300), forming a uniform charged membrane network primarily consisting of branched polyethylene glycol structures. The resulting membranes were then incorporated as the ion channel in OEIPs and demonstrated to be able to sustain selective electrophoretic "ion pumping" in this device configuration.

With the initial step of allylation (**Scheme 1**), the degree of substitution (DS) was calculated from the ^{1}H-NMR spectra (**Figure S1a**) to ∼10 % following addition of 0.2 eq. (to eq. –OH of HPG5) of NaH base followed by addition of 0.2 eq. allylbromide to the HPG5 in DMF solvent. Though the resulting allyl functionalization corresponded to half the amount of added reagents, this was ultimately attributed to the freshness of the NaH reagent used in the synthesis. Initial trial reactions (not included) resulted in a DS ∼15–20%. Likewise, a higher degree of allyl functionalization (40–60%) could be achieved in DMF by utilizing more equivalents of NaH and allylbromide reagents. Regardless, the resulting degree of 10% allyl groups was deemed sufficient, and repeated synthesis resulted in overall DS 10–20% with the calculated ^{1}H-NMR estimation.

In the proceeding reaction, excess chloroacetyl chloride was used to ensure full conversion of the remaining hydroxyl groups of the (allyl-)HPG5, which could be clearly observed in the ^{1}H- and ^{13}C-NMR (**Figures S2a,b**). By ^{1}H-NMR integral calculation via α-protons of the chloroacetyl signal compared to HPG5 core protons (**Figure S2a**), a DS could be estimated to >100% (clearly an overestimation). The overestimation arises due to signal overlapping from the allyl functionality (HPG-O-C$\underline{H}_2$-CH=CH$_2$) with new chemical shifts arising from protons corresponding to HPG5 located close to the introduced ester functionalities (HPG-C$\underline{H}$-COO-CH$_2$Cl and HPG-C$\underline{H}_2$-COO-CH$_2$Cl). By calculating the integral of the chloroacetyl α-proton signal integral toward the HPG5 including the allyl functionality signals (estimating 10% DS for 5H), a more realistic DS value of ∼90% was obtained.

In the final synthetic step of substituting triphenylphosphine and quaternizating the phosphor into charged phosphonium, the DS was calculated as above, with the triphenyl integral signals toward combining the other shifts, resulting in an estimation of ∼60% (**Figure S3a**). These large functionalization groups increased the molecular weight of the HPG5 considerably, from 5 to ∼20 kDa (approximated theoretical molecular weight calculation), and thus dominate the overall signal. An interesting observation in the ^{13}C-NMR was the strong signals from the phenyl carbons (**Figure S3b**), which dominated the intensity and seemed to suppress the rest of the structure's spectra, making it hard to achieve and render a clear resolution for the total structure. With ^{31}P-NMR, a distinct shift from the triphenylphosphine reagent signal of −5.6 ppm into a broad quaternized phosphonium signal ∼19–20 ppm was observed. Interestingly, an extra peak at 32 ppm was detecting in methanol-d_4 solution, which was not seen in deuterium oxide solution of the C-HPG5 (**Figure S3c**). This was attributed to the possibility of solvent-dependent structural conformation of the triphenylphosphonium functionality (Aganova et al., 2014).

In studying the thermal cross-linking of the C-HPG5, various requirements for the success of the reaction were derived. First, it was found that adding a small amount of TATATO was crucial for cross-linking with Thiocure ETTMP 1300. Second, we observed a dependency on high concentration formulation (**Table 1**), which led to a very swift observable gel formation. A possible explanation could be connected with the survival of radical species for initiation of the reaction with AIBN. The substantial macromolecular sizes of both C-HPG5 polymer and Thiocure 1300 cross-linker alone could have rendered the arrangement of the system too slow for cross-linking radical reactions to take place. The smaller TATATO may diffuse more readily and associate with the macromolecules' functionalities to perform chain-transfer in the polymerization mechanism—quickly enough for the radical species' survival. It was also observed that the equivalents of radical initiator AIBN were not associated with the success of the thermally initiated gel membrane formation, with 6.5 wt% and 0.2 wt% (**Figure 3**; **Table 1**, TM1 and TM7). But the AIBN equivalents did affect the pore size formation in the membrane by the evaporation of the low boiling point solvent. This may have been due to the crosslinking density formed and thiol-ene conversion efficiency of AIBN (Uygun et al., 2010) coupled with the solvent incorporation, and possibly related to N$_2$-gas evolution from the radical species breakdown.

In situ monitoring of thermal cross-linking in DMSO-d_6 (**Figure 4**) indicated that the reaction initiated after ∼12 min, and proceeded in an ultra-fast (within ∼1 min) polymerization with substantial signal intensity loss, ppm shift, and broadening of the entire spectrum. Since the sample was heated at 70°C for thermal initiation of AIBN, DMSO evaporation was not an issue and was thus ruled out as a cause of signal intensity loss. The initiation delay may be related to the presence of oxygen-forming less-reactive radicals (Cook et al., 2008) and/or the requirement for the macromolecular mixture components to arrange in a kinetically favorable orientation, with functionalities associated with each other. The resulting smooth homogenous gels (**Figure 2c**; **Table 1**, $\text{TD2}_{\text{DMSO}-d6}$) were attributed to the high boiling point DMSO solvent, high concentration polymer mixture, and low amounts of AIBN initiator.

Free-standing membranes of C-HPG5 (**Figure S5**) were achieved in a straightforward manner using photo-initiation (Irgacure 2959, curing at 365 nm). The absence of elevated temperature enabled the use of a water/methanol solvent mixture, resulting in pre-hydrated membranes without large solvent evaporation pores. Adjusting various formulation and fabrication parameters with C-HPG5, such as solvent, polymer concentration, and thermal/photo-initiation, allows for a range of customizable hyperbranched polyelectrolyte membranes with specific nanocomposite properties and electrophoretic transport capabilities (Demina et al., 2010). Both the photo- and thermal-initiated gels comprising 70–75% C-HPG5 (excluding solvent content) were able to withstand drying, swelling, and solvent exchange such as methanol and water (**Figure S6**). These materials displayed soft, flexible characteristics, especially in the dry state, while being more brittle in the fully hydrated state.

One of the general interests in hyperbranched/dendritic polymers is their ability to contain solvents and molecules (Oudshoorn et al., 2006; Wang et al., 2010; Zhang et al., 2013; Pedron et al., 2017). The C-HPG5 polymer, with its large amount of triphenylphosphonium charged functionality, displayed amphiphilic solvating capabilities in a very small amount of solution (80% w/w in methanol), providing the possibility of processing the polymer with low amounts of organic solvents. A possible explanation could be related to structural arrangement, where the compact, spherical shape of hyperbranched macromolecules (Kainthan et al., 2006) makes them amenable to close-packing. By utilizing these covalently-arranged three-dimensional polymer structures coupled with charged surface functionalities, well-defined/tuned cavities in the close-packing between the different macromolecules could provide selective ion transport channels. This leads to our more specific interest in hyperbranched/dendritic polymers: their use as ion transport materials for OEIPs and other iontronic devices (Arbring Sjöström et al., 2018). The C-HPG5 polymer was thus demonstrated as the ion transport channel in an OEIP system, with a specific formulation chosen to achieve molding via the MIMIC technique (**Table 2**, UVC4, **Figure S8**). Stable electrophoretic transport of Cl^- was observed in the C-HPG5 channels, resulting in an average ionic conductivity of 0.24 ± 0.02 S/m. By employing methyl blue at the source, ionic exchange and transportation of the large anionic (799.81 g/mol) dye molecule were accomplished through the cationic hyperbranched polyelectrolyte membrane.

In conclusion, demands for new ionically charged organic materials capable of versatile manufacturing processing, selective ion transport including large/aromatic compounds, and biocompatibility sets increasing requirement on the polyelectrolytes used in organic (bio)electronics. We have synthesized a new type of multi-functionalized hyperbranched polyglycerol with cationic charges and functionalities for click chemistry cross-linking (thermal- and photo-initiated), to form monolithic membranes. The membrane network formation reaction was investigated, which by initiation proceeded in an ultra-rapid fashion to form insoluble gels capable of solvent exchange and large anionic electrophoretic transportation. The amphiphilic nature of the polyelectrolyte allows for simple implementation to create pre-formed hydrated/loaded membranes applied directly into devices.

MATERIALS AND METHODS

Hyperbranched polyglycerol used with molecular weight corresponding to 5,000 Da and degree of branching 53.6%, based on GPC and inverse gated ^{13}C-NMR, respectively, was purchased from NanoPartica GmbH. Thiocure® ETTMP 1300 was obtained from Bruno Bock Chemische. All other chemicals were purchased from Merck-Sigma Aldrich with highest purity and used as received. Dialysis tubing Spectra/Por© Regenerated Cellulose with molecular weight cut-off (MWCO) were bought from Spectrum Laboratories. Synthesis reactions were carried out in nitrogen atmosphere, with glassware dried in a 110°C oven. Reaction solvents DMF and chloroform were pre-dried (>16 h) with 4 Å molecular sieves and deaerated with nitrogen (30–60 min) prior to use. For the functionalization of hyperbranched polyglycerol 5,000 Da, reagent equivalents were calculated and used corresponding to relative hydroxyl functionality (67.5). ^{1}H-, ^{13}C- and ^{31}P-NMR analysis were recorded at 300, 75, and 121 MHz, respectively, on a Varian Oxford 300 MHz spectrometer using internal solvent peaks as reference (Gottlieb et al., 1997). NMR FID files were processed with MestReNova v12.04-22023 (Mestrelab Research S.L.).

Allyl-Hyperbranched Polyglycerol (Compound 2)

Hyperbranched polyglycerol (HPG, 5,000 Da, Compound 1) (2 g, 27.00 mmol –hydroxyl functionality) was dissolved in dry DMF (54 mL) followed by addition of sodium hydride (60% oil dispersion, 216 mg, 5.40 mmol, 0.2 equivalents) and was left to stir for 2 h under nitrogen atmosphere at room temperature. Allyl bromide (468 μL, 5.40 mmol, 0.2 equivalents) was added and the reaction was left overnight (16 h) until it was quenched with ice chips. The solvent was reduced via rotary evaporation and the residuals were re-dissolved in H_2O (60 mL), filtered with a 0.45 μm PVDF membrane, washed twice with ethyl acetate (2 × 60 mL). Dialysis in H_2O was then performed with a regenerated cellulose (3,500 Da MWCO) membrane. Water was removed by rotary evaporation and the product was placed *in vacuo* to yield a transparent white/yellow viscous gel (Compound 2).

^{1}H NMR (300 MHz, Deuterium Oxide) δ: 6.17–5.94 (m, 1H, -OCH$_2$C$\underline{\text{H}}$=CH$_2$), 5.53–5.29 (m, 2H, -OCH$_2$CH=C$\underline{\text{H}}_2$), 4.32–4.12 (m, 2H, -OC$\underline{\text{H}}_2$CH=CH$_2$), 4.12–3.38 (m, 5H, $\underline{\text{dPG}}$), 1.55–1.36 (m, 2H, TMP$_{\text{core}}$ -C$\underline{\text{H}}_2$CH$_3$), 1.03–0.88 (m, 3H, TMP$_{\text{core}}$ -CH$_2$C$\underline{\text{H}}_3$).

^{1}H NMR (300 MHz, DMSO-d_6) δ: 6.03–5.75 (m, 1H, -OCH$_2$C$\underline{\text{H}}$=CH$_2$), 5.35–5.02 (m, 2H, -OCH$_2$CH=C$\underline{\text{H}}_2$), 4.94–4.40 ($\underline{\text{H}}$O-HPG), 4.14–3.86 (m, 2H, -OC$\underline{\text{H}}_2$CH=CH$_2$), 3.86–2.87 (m, 5H, $\underline{\text{dPG}}$), 1.37–1.16 (m, 2H, TMP$_{\text{core}}$ -C$\underline{\text{H}}_2$CH$_3$), 0.88–0.69 (m, 3H, TMP$_{\text{core}}$ -CH$_2$C$\underline{\text{H}}_3$).

^{13}C NMR (75 MHz, DMSO-d_6) δ: 135.88, 135.51, 116.61, 116.25, 80.00, 78.11, 72.99, 71.56, 71.03, 70.58, 69.65, 69.01, 68.73, 63.13, 61.09.

Chloroacetate-Allyl-Hyperbranched Polyglycerol (Compound 3)

Allyl-HPG5 (Compound 2) (1,108 mg, 13.50 mmol) was dissolved in dry DMF (27 mL) and cooled with an ice bath. A solution of chloroacetyl chloride (2.68 mL, 33.75 mmol, 2.5 eq.) in dry DMF (18 mL) was prepared and added drop-wise to the polymer solution under stirring and nitrogen atmosphere, followed by slow drop-wise addition of triethylamine (1.88 mL, 13.50 mmol, 1 eq.). The reaction was left to stir for 16 h at room temperature, quenched with ice chips, and filtered through a 0.45 µm PVDF membrane. Solvent volume was reduced via evaporation and the residuals were dissolved in chloroform (50 mL). The organic phase was washed with H_2O (50 mL), brine (50 mL), and H_2O (2 × 50 mL), and dried with $MgSO_4$. The salts were filtered off, the chloroform was removed via rotary evaporation, and the product was placed *in vacuo* to yield a brown viscous oil (Compound 3).

^{1}H NMR (300 MHz, Chloroform-d) δ: 5.96–5.76 (m, 1H, -OCH$_2$C$\underline{\text{H}}$=CH$_2$), 5.31–5.02 (m, 2H, -OCH$_2$CH=C$\underline{\text{H}}_2$), 4.52-4.22 (m, 3H, HPG-C$\underline{\text{H}}$COO-CH$_2$Cl, HPG-C$\underline{\text{H}}_2$COO-C$\underline{\text{H}}_2$Cl), 4.14–4.03 (m, 2H, -COOC$\underline{\text{H}}_2$Cl), 4.21–3.91 (m, 2H, -OC$\underline{\text{H}}_2$CH=CH$_2$), 3.87–3.19 (m, 5H, $\underline{\text{hPG}}$), 1.50–1.26 (m, 2H, TMP$_{\text{core}}$ -C$\underline{\text{H}}_2$CH$_3$), 0.92–0.74 (m, 3H, TMP$_{\text{core}}$ -CH$_2$C$\underline{\text{H}}_3$);

^{13}C NMR (75 MHz, Chloroform-d) δ 167.37, 167.09, 166.94, 166.85, 135.29, 134.66, 117.45, 116.94, 78.89, 77.58, 77.16, 76.74, 73.11, 72.27, 71.73, 71.33, 70.60, 69.91, 69.26, 69.13, 68.28, 66.79, 65.26, 64.04, 63.83, 41.05, 40.84, 40.68.

Triphenylphosphoniumacetate-Allyl-Hyperbranched Polyglycerol Chloride (Compound 4, C-HPG5)

Chloroacetate-allyl-HPG5 (Compound 3) (1.32 mg, 9.00 mmol) was dissolved in chloroform (18 mL) together with triphenylphosphine (4.73 g, 18.02 mmol, 2 eq.) in a microtube that was sealed with a cap and purged with N_2-gas. The reaction mixture was left to stir for 16 h at 60°C after which the solvent was removed by evaporation. Remaining crude product was dissolved in a minimum amount of methanol and trituration were performed by pouring cold diethyl ether to precipitate the product. The diethyl ether was decanted and the procedure was repeated four times after which remaining solvents were removed with rotary evaporation. The remaining product was dissolved in water and dialysis in the medium with a regenerated cellulose membrane (3,500 Da MWCO) was performed. Azeotropic evaporation with toluene (2 × 20 mL) were performed and the remains were placed *in vacuo* to yield a solid yellow crystalline product (Compound 4, C-HPG5).

^{1}H NMR (300 MHz, Methanol-d_4) δ: 8.22–7.45 (m, 15H, -P$^+\underline{\text{Ph}_3}$), 6.00–5.71 (m, 1H, -OCH$_2$C$\underline{\text{H}}$=CH$_2$), 5.33–4.90 (m, 2H, -OCH$_2$CH=C$\underline{\text{H}}_2$; m, 1H, HPG-C$\underline{\text{H}}$COO-), 4.35–3.86 (m, 2H,-OC$\underline{\text{H}}_2$CH=CH$_2$; m, 2H, HPG-C$\underline{\text{H}}_2$COO-), 3.84–2.91 (m, 2H, -COOC$\underline{\text{H}}_2$P$^+$Ph$_{3;}$ m, 5H, $\underline{\text{HPG}}$).

^{13}C NMR (75 MHz, Methanol-d_4) δ: 165.98, 136.57, 135.15, 135.01, 133.73, 133.11, 132.98, 131.58, 131.41, 130.04, 129.88, 120.00, 118.81, 117.44, 117.19, 79.87, 74.04, 73.27, 72.19, 71.17, 68.97, 42.17, 30.86.

^{31}P NMR (121 MHz, Methanol-d_4) δ 32.16, 20.64–19.56 (m).

^{31}P NMR (121 MHz, Deuterium Oxide) δ: 19.94–19.06 (m).

Thermal Cross-Linking Gel

C-HPG5 (400 mg, 1.135 mmol, Compound 4) was dissolved in methanol in a vial (200 µL) and mixed together with Thiocure 1300 ETTMP (400 mg, 0.303 mmol), Triallyl-1,3,5-triazine-2,4,6(1H,3H,5H)-trione (21 mg, 0.084 mmol), and 2,2'-Azobis(2-methylpropionitrile) (2 mg, 0.012 mmol) by vortexing. The vial was deaerated, sealed and heated to 75 °C overnight into an insoluble continuous gel.

Thermal Cross-Linking Gel for NMR

C-HPG-5 (341 mg, Compound 4) was added into a vial and dissolved in DMSO-d_6 (300 µL) by vortexing for 5 min. This was followed by addition of Thiocure 1300 ETTMP (89 mg), triallyl-1,3,5-triazine-2,4,6(1H,3H,5H)-trione (18 mg, 0.072 mmol), and 2,2′-Azobis(2-methylpropionitrile) (17 mg, 0.104 mmol) which was vortexed an additional 5 min into a homogenous viscous solution. The mixture was transferred into an NMR-tube, deaerated with N_2-gas, sealed with a cap, and heated for 15 min at 70°C inside a Varian Oxford 300 MHz spectrometer, where the reaction was monitored by acquisition of a ^{1}H-NMR spectra collected every minute.

Organic Electronic Ion Pump Fabrication

PDMS Master Mold Fabrication

SU-8 3050 (MicroChem Corp.) was spin-coated (5 s spread at 500 rpm, 30 s spin at 3,000 rpm) on a 4 silicon wafer and soft baked on a leveled hot plate (1 min hold at 65°C, increasing with 10°C/min to 95°C, and hold for 15 min). After cooling, the wafer was exposed through a plastic mask with 300 mJ/cm^2 (measured at 365 nm) using a Karl Suss MA/BM 6 mask aligner equipped with an I-line filter. The exposed parts were cross-linked by ramped hard bake (as soft bake, but final hold at 95 °C for 5 min) and developed using two baths of mr-Dev 600 (Micro resist technology GmbH), each for 5 min, followed by a 10 s rinse in isopropanol and drying using N_2. The final SU-8 pattern was additionally hard baked at 110°C for 5 min.

PDMS Master Mold Characterization

The width and depth of the SU-8 pattern was measured with an optical profilometer (Sensofar PLu Neox) using a 50x confocal objective.

PDMS Mold

PDMS (DowSil Sylgard 184) was prepared at a 10:1 base/curing agent ratio, and mixed and degassed. The blend was poured on the PDMS master mold to a thickness of ∼2 mm and cured on a hot plate (1 h at 120°C). The PDMS mold was carefully peeled off the master, and cut into pieces, with each piece containing a capillary channel connecting two electrolyte reservoirs.

Channel Filling

Glass wafers were cleaned using Hellmanex® III, rinsed, and baked prior to use. Glass wafers and PDMS pieces were O_2-plasma treated (100 W at 800 mTorr for 5 min) and subsequently immediately bonded together. C-HPG5 (50 mg, Compound 4), Thiocure 1300 ETTMP (13 mg, 0.01 mmol), 1,3,5-triallyl-1,3,5-triazine-2,4,6(1H,3H,5H)-trione (2.6 mg, 0.010 mmol), and 2-hydroxy-4′-(2-hydroxyethoxy)-2-methylpropiophenone (3.4 mg, 0.015 mmol) were dissolved in methanol (50 µL) and water (50 µL). The solution was vortexed for 2 min and the channels were filled by capillary action by placing 1 µL of membrane solution at one end. The polyelectrolyte was cross-linked for 10 min in a Karl Suss MA/BM 6 mask aligner (flood exposure, 10 mJ/cm^2 measured at 365 nm) under nitrogen atmosphere. The channels were then soaked in 0.1 mM KCl solution by placing droplets at the inlet and outlet for 3 h.

Scanning Electron Microscopy Imaging

Channels were prepared as above but on a silicon wafer with 50 nm gold deposited by thermal evaporation. Further, to enable removal of the mold after filling and AEM crosslinking, neither the substrate or PDMS mold were activated by plasma. Finally, a 5 nm layer of gold was evaporated on top of the AEM. Images were acquired using a Zeiss Sigma 500 Gemini scanning electron microscope at 2 kV acceleration voltage and with the in-lens secondary electron detector.

Channel Characterization

The conductivity of C-HPG5-based OEIPs were determined by placing PEDOT:PSS (coated on polyethylene terephthalate) electrodes in 0.1 M NaCl(aq) electrolytes on both side of the channel, applying a current of 100 nA, and measuring the required driving voltage using a Keithley Source Meter 2612 (Tektronix, Inc.). To assess the transport of larger molecules, the source solution was exchanged to the dye molecule methyl blue^{2-} (10 mM aqueous).

DATA AVAILABILITY

The datasets generated for this study are available on request to the corresponding author.

AUTHOR CONTRIBUTIONS

TA performed all synthesis and chemical characterization. DP and EG fabricated and characterized OEIP devices. MS advised and planned synthesis and chemical characterization. DS, MB, and MS conceived of the project. TA wrote the manuscript, with assistance from EG, MS, and DS.

FUNDING

Major funding for this project was provided by the Swedish Foundation for Strategic Research. Additional funding was provided by the Swedish Government Strategic Research Area in Materials Science on Advanced Functional Materials at Linköping University, the Önnesjö Foundation, and the Knut and Alice Wallenberg Foundation.

ACKNOWLEDGMENTS

The authors wish to thank Dr. Roger Gabrielsson for his assistance in development and synthesis throughout this project, Prof. Peter Konradsson for guidance and fruitful discussions, and Marie Jakesova for assistance with scanning electron microscopy imaging.

SUPPLEMENTARY MATERIAL

The Supplementary Material for this article can be found online at: https://www.frontiersin.org/articles/10.3389/fchem.2019.00484/full#supplementary-material

REFERENCES

Abbina, S., Vappala, S., Kumar, P., Siren, E. M. J., La, C. C., Abbasi, U., et al. (2017). Materials chemistry B hyperbranched polyglycerols: recent advances in synthesis, biocompatibility and biomedical applications. *J. Mater. Chem. B* 5, 9241–9420. doi: 10.1039/C7TB02515G

Abidian, M. R., Kim, D. H., and Martin, D. C. (2006). Conducting-polymer nanotubes for controlled drug release. *Adv. Mater.* 18, 405–409. doi: 10.1002/adma.200501726

Aganova, O., Galiullina, L., Aganov, A., Shtyrlin, Y., Pugachev, M., Shtyrlin, N., et al. (2014). The study of the conformation and dynamics of the new quaternary phosphonium salts by NMR spectroscopy. *Appl. Magn. Reson.* 45, 653–665. doi: 10.1007/s00723-014-0544-4

Arbring Sjöström, T., Berggren, M., Gabrielsson, E. O., Janson, P., Poxson, D. J., Seitanidou, M., et al. (2018). A decade of iontronic delivery devices. *Adv. Mater. Technol.* 3:1700360. doi: 10.1002/admt.201700360

Baille, W. E., Zhu, X. X., and Fomine, S. (2004). Study of self-diffusion of hyperbranched polyglycidols in poly(vinyl alcohol) solutions and gels by pulsed-field gradient NMR spectroscopy. *Macromolecules* 37, 8569–8576. doi: 10.1021/ma049588a

Berggren, M., and Richter-Dahlfors, A. (2007). Organic bioelectronics. *Adv. Mater.* 19, 3201–3213. doi: 10.1002/adma.200700419

Burakowska, E., and Haag, R. (2009). Dendritic polyglycerol core-double-shell architectures: synthesis and transport properties. *Macromolecules* 42, 5545–5550. doi: 10.1021/ma9005044

Calderón, M., Quadir, M. A., Sharma, S. K., and Haag, R. (2010). Dendritic polyglycerols for biomedical applications. *Adv. Mater.* 22, 190–218. doi: 10.1002/adma.200902144

Cook, W. D., Chen, F., Pattison, D. W., Hopson, P., and Beaujon, M. (2008). Thermal polymerization of thiol–ene network-forming systems Wayne. *Polym. Int.* 57, 171–180. doi: 10.1002/pi.2314

Demina, O. A., Demin, A. V., Gnusin, N. P., and Zabolotskii, V. I. (2010). Effect of an aprotic solvent on the properties and structure of ion-exchange membranes. *Polym. Sci. Ser. A* 52, 1270–1282. doi: 10.1134/S0965545X10120059

Frey, H., and Haag, R. (2002). Dendritic polyglycerol : a new versatile biocompatible material. *Rev. Mol. Biotechnol.* 90, 257–267. doi: 10.1016/S1389-0352(01)00063-0

Fu, Q., Liu, J., and Shi, W. (2008). Preparation and photopolymerization behavior of multifunctional thiol–ene systems based on hyperbranched aliphatic polyesters. *Prog. Org. Coatings* 63, 100–109. doi: 10.1016/j.porgcoat.2008.04.014

Gode, P., Hult, A., Jannasch, P., Johansson, M., Karlsson, L., Lindbergh, G., et al. (2006). A novel sulfonated dendritic polymer as the acidic component in proton conducting membranes. *Solid State Ionics* 177, 787–794. doi: 10.1016/j.ssi.2005.12.031

Gottlieb, H. E., Kotlyar, V., and Nudelman, A. (1997). NMR chemical shifts of common laboratory solvents as trace impurities. *J. Org. Chem.* 62, 7512–7515. doi: 10.1021/jo971176v

Hoyle, C. E., and Bowman, C. N. (2010). Thiol-ene click chemistry. *Angew. Chem. Int. Ed.* 49, 1540–1573. doi: 10.1002/anie.200903924

Isaksson, J., Kjäll, P., Nilsson, D., Robinson, N., Berggren, M., and Richter-Dahlfors, A. (2007). Electronic control of Ca^{2+} signalling in neuronal cells using an organic electronic ion pump. *Nat. Mater.* 6, 673–679. doi: 10.1038/nmat1963

Jonsson, A., Inal, S., Uguz, I., Williamson, A. J., Kergoat, L., Rivnay, J., et al. (2016). Bioelectronic neural pixel: Chemical stimulation and electrical sensing at the same site. *Proc. Natl. Acad. Sci. U.S.A.* 113, 9440–9445. doi: 10.1073/pnas.1604231113

Jonsson, A., Song, Z., Nilsson, D., Meyerson, B. A., Simon, D. T., Linderoth, B., et al. (2015). Therapy using implanted organic bioelectronics. *Sci. Adv.* 1:e1500039. doi: 10.1126/sciadv.1500039

Kainthan, R. K., Muliawan, E. B., Hatzikiriakos, S. G., and Brooks, D. E. (2006). Synthesis, characterization, and viscoelastic properties of high molecular weight hyperbranched polyglycerols. *Macromolecules* 39, 7708–7717. doi: 10.1021/ma0613483

Kasprzak, S. E., Martin, B., Raj, T., and Gall, K. (2009). Synthesis and thermomechanical behavior of (qua)ternary thiol-ene(/acrylate) copolymers. *Polymer* 50, 5549–5558. doi: 10.1016/j.polymer.2009.09.044

Killops, K. L., Campos, L. M., and Hawker, C. J. (2008). Robust, efficient, and orthogonal synthesis of dendrimers via thiol-ene "click" chemistry. *J. Am. Chem. Soc.* 130, 5062–5064. doi: 10.1021/ja8006325

Kim, E., Xia, Y., and Whitesides, G. M. (1996). Micromolding in capillaries: applications in materials science. *J. Am. Chem. Soc.* 118, 5722–5731. doi: 10.1021/ja960151v

Kłos, J. S., and Sommer, J.-U. (2010). Simulations of terminally charged dendrimers with flexible spacer chains and explicit counterions. *Macromolecules* 43, 4418–4427. doi: 10.1021/ma1003997

Kontturi, K., Murtomäki, L., and Manzanares, J. A. J. A. (2008). "Chapter 4: Ionic transport processes," in *Electrochemistry and Membrane Science* (Oxford: Oxford University Press), 126–231. doi: 10.1093/acprof:oso/9780199533817.001.0001

Kontturi, K., Pentti, P., and Sundholm, G. (1998). Polypyrrole as a model membrane for drug delivery. *J. Electroanal. Chem.* 453, 231–238. doi: 10.1016/S0022-0728(98)00246-0

Matveeva, E. D., Podrugina, T. A., Grishin, Y. K., Tkachev, V. V., Zhdankin, V. V., Aldoshin, S. M., et al. (2003). Synthesis and structure of mixed phosphonium-iodonium ylide. *Russ. J. Org. Chem.* 39, 536–541. doi: 10.1023/A:1026011902365

Nilsson, C., Simpson, N., Malkoch, M., Johansson, M., and Malmström, E. (2008). Synthesis and thiol-ene photopolymerization of allyl-ether functionalized dendrimers. *J. Polym. Sci. A Polym. Chem.* 46, 1339–1348. doi: 10.1002/pola.22474

Oudshoorn, M. H. M., Rissmann, R., Bouwstra, J. A., and Hennink, W. E. (2006). Synthesis and characterization of hyperbranched polyglycerol hydrogels. *Biomaterials* 27, 5471–5479. doi: 10.1016/j.biomaterials.2006.06.030

Pedron, S., Pritchard, A. M., Vincil, G. A., Andrade, B., Zimmerman, S. C., and Harley, B. A. C. (2017). Patterning three-dimensional hydrogel microenvironments using hyperbranched polyglycerols for independent control of mesh size and stiffness. *Biomacromolecules* 18, 1393–1400. doi: 10.1021/acs.biomac.7b00118

Poxson, D. J., Gabrielsson, E. O., Bonisoli, A., Linderhed, U., Abrahamsson, T., Matthiesen, I., et al. (2019). Capillary fiber-based electrophoretic delivery device. *ACS Appl. Mater. Interfaces* 11, 14200–14207. doi: 10.1021/acsami.8b22680

Proctor, C. M., Slézia, A., Kaszas, A., Ghestem, A., del Agua, I., Pappa, A.-M., et al. (2018). Electrophoretic drug delivery for seizure control. *Sci. Adv.* 4:eaau1291. doi: 10.1126/sciadv.aau1291

Schubert, C., Osterwinter, C., Tonhauser, C., Schömer, M., Wilms, D., Frey, H., et al. (2016). Can hyperbranched polymers entangle? Effect of hydrogen bonding on entanglement transition and thermorheological properties of hyperbranched polyglycerol melts. *Macromolecules* 49, 8722–8737. doi: 10.1021/acs.macromol.6b00674

Schwab, E., and Mecking, S. (2005). Synthesis and properties of highly branched polycations with an aliphatic polyether scaffold. *J. Polym. Sci. A Polym. Chem.* 43, 4609–4617. doi: 10.1002/pola.20983

Seitanidou, M., Franco-Gonzalez, J. F., Sjöström, T. A., Zozoulenko, I., Berggren, M., and Simon, D. T. (2017). pH dependence of γ-aminobutyric acid iontronic transport. *J. Phys. Chem. B* 121, 7284–7289. doi: 10.1021/acs.jpcb.7b05218

Seitanidou, M., Tybrandt, K., Berggren, M., and Simon, D. T. (2019). Overcoming transport limitations in miniaturized electrophoretic delivery devices. *Lab. Chip* 19, 1427–1435. doi: 10.1039/C9LC00038K

Simon, D. T., Kurup, S., Larsson, K. C., Hori, R., Tybrandt, K., Goiny, M., et al. (2009). Organic electronics for precise delivery of neurotransmitters to modulate mammalian sensory function. *Nat. Mater.* 8, 742–746. doi: 10.1038/nmat2494

Someya, T., Bao, Z., and Malliaras, G. G. (2016). The rise of plastic bioelectronics. *Nature* 540, 379–385. doi: 10.1038/nature21004

Sunder, A., Frey, H., and Mülhaupt, R. (2000). Hyperbranched polyglycerols by ring-opening multibranching polymerization. *Macromol. Symp.* 153, 187–196. doi: 10.1002/1521-3900(200003)153:1<187::AID-MASY187>3.0.CO;2-I

Sunder, A., Hanselmann, R., Frey, H., and Mülhaupt, R. (1999). Controlled synthesis of hyperbranched polyglycerols by ring-opening multibranching polymerization. *Macromolecules* 32, 4240–4246. doi: 10.1021/ma990090w

Thota, B. N. S., Urner, L. H., and Haag, R. (2016). Supramolecular architectures of dendritic amphiphiles in water. *Chem. Rev.* 116, 2079–2102. doi: 10.1021/acs.chemrev.5b00417

Trey, S. M., Nilsson, C., Malmström, E., and Johansson, M. (2010). Thiol-ene networks and reactive surfaces via photoinduced polymerization of allyl ether functional hyperbranched polymers. *Prog. Org. Coatings* 67, 348–355. doi: 10.1016/j.porgcoat.2009.10.023

Türk, H., Shukla, A., Rodrigues, P. C. A., Rehage, H., and Haag, R. (2007). Water-soluble dendritic core-shell-type architectures based on polyglycerol for solubilization of hydrophobic drugs. *Chem. A Eur. J.* 13, 4187–4196. doi: 10.1002/chem.200601337

Tybrandt, K., Larsson, K. C., Kurup, S., Simon, D. T., Kjäll, P., Isaksson, J., et al. (2009). Translating electronic currents to precise acetylcholine-induced neuronal signaling using an organic electrophoretic delivery device. *Adv. Mater.* 21, 4442–4446. doi: 10.1002/adma.200900187

Uygun, M., Tasdelen, M. A., and Yagci, Y. (2010). Influence of type of initiation on thiol-ene "click" chemistry. *Macromol. Chem. Phys.* 211, 103–110. doi: 10.1002/macp.200900442

Wadhwa, R., Lagenaur, C. F., and Cui, X. T. (2006). Electrochemically controlled release of dexamethasone from conducting polymer polypyrrole coated electrode. *J. Control. Release* 110, 531–541. doi: 10.1016/j.jconrel.2005.10.027

Wang, Q., Mynar, J. L., Yoshida, M., Lee, E., Lee, M., Okuro, K., et al. (2010). High-water-content mouldable hydrogels by mixing clay and a dendritic molecular binder. *Nature* 463, 339–343. doi: 10.1038/nature08693

Wei, Y. (1998). Molecular electronics–the future of bioelectronics. *Supramol. Sci.* 5, 723–731. doi: 10.1016/S0968-5677(98)00112-6

Williamson, A. J., Rivnay, J., Kergoat, L., Jonsson, A., Inal, S., Uguz, I., et al. (2015). Controlling epileptiform activity with organic electronic ion pumps. *Adv. Mater.* 27, 3138–3144. doi: 10.1002/adma.201500482

Wilms, D., Stiriba, S.-E., and Frey, H. (2010). Hyperbranched polyglycerols: from the controlled synthesis of biocompatible polyether polyols to multipurpose applications. *Acc. Chem. Res.* 43, 129–141. doi: 10.1021/ar900158p

Zhang, H., Patel, A., Gaharwar, A. K., Mihaila, S. M., Iviglia, G., Mukundan, S., et al. (2013). Hyperbranched polyester hydrogels with controlled drug release and cell adhesion properties. *Biomacromolecules* 14, 1299–1310. doi: 10.1021/bm301825q

Conflict of Interest Statement: MS is employed by the independent state-owned research institute RISE Acreo AB. DP, DS, MB, and TA are shareholders in the small, researcher-controlled intellectual property company OBOE IPR AB (oboeipr.com), which owns the patents related to this research.

The remaining author (EG) declares that the research was conducted in the absence of any commercial or financial relationships that could be construed as a potential conflict of interest.

frontiers in Chemistry

ORIGINAL RESEARCH
published: 10 October 2019
doi: 10.3389/fchem.2019.00667

A Study on the Stability of Water-Gated Organic Field-Effect-Transistors Based on a Commercial p-Type Polymer

Rosaria Anna Picca [1,2], Kyriaki Manoli [1,2], Eleonora Macchia [1,3], Angelo Tricase [1], Cinzia Di Franco [4], Gaetano Scamarcio [2,4,5], Nicola Cioffi [1,2] and Luisa Torsi [1,2,3]**

[1] Dipartimento di Chimica, Università degli Studi di Bari "Aldo Moro", Bari, Italy, [2] Consorzio per lo Sviluppo dei Sistemi a Grande Interfase, Unità di Bari, Bari, Italy, [3] The Faculty of Science and Engineering, Center for Functional Materials, Åbo Akademi University, Turku, Finland, [4] CNR - Istituto di Fotonica e Nanotecnologie, Unità di Bari, Bari, Italy, [5] Dipartimento Interateneo di Fisica "M. Merlin", Università degli Studi di Bari "Aldo Moro", Bari, Italy

Edited by:
Wolfgang Knoll,
Austrian Institute of Technology (AIT), Austria

Reviewed by:
Maria Daniela Angione,
Trinity College Dublin, Ireland
Sven Ingebrandt,
RWTH Aachen University, Germany

***Correspondence:**
Rosaria Anna Picca
rosaria.picca@uniba.it
Luisa Torsi
luisa.torsi@uniba.it

Specialty section:
This article was submitted to Organic Chemistry, a section of the journal Frontiers in Chemistry

Received: *21 January 2019*
Accepted: *18 September 2019*
Published: *10 October 2019*

Citation:
Picca RA, Manoli K, Macchia E, Tricase A, Di Franco C, Scamarcio G, Cioffi N and Torsi L (2019) A Study on the Stability of Water-Gated Organic Field-Effect-Transistors Based on a Commercial p-Type Polymer. Front. Chem. 7:667. doi: 10.3389/fchem.2019.00667

Robust electrolyte-gated organic field-effect-transistors (OFETs) are particularly needed for the development of biosensing devices. However, when a FET biosensor operates in aqueous environments or even in real biological fluids, some critical issues may arise due to the possible lack of environmental long-term and/or operational stability. An important source of instability is associated with the degradation of the organic electronic channel materials such as for instance, poly-3-hexylthiophene (P3HT), a benchmark commercially available p-type organic semiconductor. In this work, the investigation of critical parameters, such as the control over spurious electrochemical phenomena as well as the operating conditions that can affect water-gated OFETs lifetime, is reported, together with a proposed modeling of the P3HT stability curve over 1 week in water. The investigation of possible morphological/chemical modifications occurring at the polymer surface after operating in water for 2 weeks was carried out. Moreover, it is proven how the addition of a gel layer can extend the P3HT based water-gated OFET shelf life up to 2 months.

Keywords: poly-3-hexylthiophene, electrolyte-gated OFET, degradation, pulsed mode, biosensors

INTRODUCTION

The use of organic field-effect-transistors (OFETs) as sensors (Torsi et al., 2013; Li et al., 2018; Surya et al., 2019) has received a tremendous boost in the last decades thanks to the advent of low-cost fabrication strategies as well as of flexible and/or stretchable substrates (Kim et al., 2013; Manoli et al., 2015). However, their exploitation and commercialization as real-life sensors have been limited by the organic polymer degradation occurring when the device is operated in aqueous environments (Knopfmacher et al., 2014; Wang et al., 2016; Zhang et al., 2016). Extensive literature on the operational and environmental stability of organic semiconductors have been reported for devices working with solid-state dielectrics (Salleo et al., 2005; Sirringhaus, 2009; Bobbert et al., 2012; Nikolka et al., 2016; Lee et al., 2017; Jia et al., 2018) addressing the role of external agents (e.g., water, oxygen, light) in reducing the device performance. Evidences of device degradation encompass the increased hysteresis on transfer curves and leakage (I_G) for successive measurements, threshold voltage (V_T) shift, on current (I_{on}) decrease with time

(Sirringhaus, 2009). Such behavior has been mainly ascribed to the uncompensated charged trapped in deep localized states in the semiconductor also caused by spurious electrochemical processes (Sirringhaus, 2005; Beatrup et al., 2014; Porrazzo et al., 2014). For example, the presence of polaronic states can cause an increased susceptibility to the electrochemical degradation (Wade et al., 2015). In fact, the presence of hole polarons under device operation is found to make polaron degradation pathways accessible (Beatrup et al., 2014). Moreover, a charge transfer complex may be formed with oxygen (favored under light) leading to instability (Bellani et al., 2014).

Some alternatives to overcome such drawbacks have been proposed, such as the inclusion of ZnO nanophases in the bioreceptor layer of OFET biosensors (Picca et al., 2018) or polymer encapsulation (Yu et al., 2016; Lee et al., 2017). More recently, electrolyte-gated devices (EGOFETs) have emerged as interesting devices that can operate in the sub-volt regime (Panzer and Frisbie, 2008; Kergoat et al., 2010; Cramer et al., 2013) thus paving the way to their application in label-free ultra-sensitive biosensors (Mulla et al., 2015; Macchia et al., 2018a,b, 2019a,b).

In EGOFETs, two electrical-charge-double-layers (EDL) are built: one at the gate/electrolyte and the other at the electrolyte/organic semiconductor interfaces. When water serves as electrolyte, the EDL capacitance is remarkably high, being in the order of few $\mu F^* cm^{-2}$ (Cramer et al., 2013). In such an architecture, the direct contact between the organic semiconductor (OS) layer and the aqueous environment rises concerns about the already investigated degradation induced in such polymers by electrochemical processes that occur in water (de Leeuw et al., 1997; Sharma et al., 2010; Bobbert et al., 2012), that are particularly detrimental leading to unstable EGOFETs on prolonged use (Cramer et al., 2013; Bellani et al., 2014; Porrazzo et al., 2014). Until now, only few studies about EGOFET devices have addressed this issue reporting on stability over time (Zhang et al., 2016) or under harsh environments (Porrazzo et al., 2014; Algarni et al., 2016). In this work, poly-3-hexylthiophene (P3HT) was chosen as benchmark p-type OS used to fabricate water-gated OFETs, employing a bulk gold foil as gate electrode. At first, the reduction of hysteretic behavior was demonstrated by setting up a suitable measuring protocol. Moreover, environmental (incubation in HPLC water) and operational stability (cycling mode) studies were carried out demonstrating the main role of the electrolyte over the measuring conditions in device degradation. A suitable cell was also designed to overcome the problem of water evaporation during measurements. Interestingly, P3HT degradation was modeled in terms of I_D decrease with a two-phase exponential decay function indicating that a first process occurs within few hours, whereas a second one has a time constant in the order of 35 h. It was demonstrated that a similar trend is mainly associated to V_T negative shift with time. A strategy to extend EGOFET use over the months was also investigated. Additional morphological and spectroscopic characterizations performed on as-prepared and used devices provided information about the response of P3HT film to water contact on a long time scale (2 weeks).

MATERIALS AND METHODS

Fabrication of EGOFET Devices

Highly n-doped silicon substrates, covered by 300-nm thermally grown SiO_2, were purchased from Si-Mat®. Source (S) and drain (D) interdigitated electrodes were photo-lithographically patterned on the Si/SiO_2 wafer. To this end, a Ti (99.995%) film (5 nm thick) was deposited as adhesion layer prior of the Au (99.99%) film (50 nm thick) deposition by electron-beam evaporation. The S&D interdigitated electrodes have a channel length (L) of 5 µm and a channel width (W) of 10,560 µm. Poly(3-hexylthiophene-2,5-diyl) (regioregular, electronic grade, 99.995% trace metal basis, average M_n ∼17,500, Sigma-Aldrich), P3HT, was used as p-type OS throughout the study. The polymer was first dissolved in chlorobenzene (2.6 mg/mL), and then the solution was sonicated for 20 min prior to filtration through a PTFE 0.2 µm syringe filter. Before depositing the OS film, substrates bearing the interdigitated electrodes were cleaned under ultrasounds in an acetone bath (10′) followed by a similar step in 2-propanol and finally dried under nitrogen. P3HT film was spin coated at 2,000 rpm for 20 s and annealed at 90°C for 10 min. A channel area of $6.4 \cdot 10^{-3}$ cm^2 was estimated (Macchia et al., 2018a). The gate electrode (G) consisted of an Au bulk sheet (total area ∼1.5 cm^2) mounted in L-configuration, whose water immersed area was about 0.6 cm^2. When specified, a channel consisting of P3HT/ZnO nanoparticles hybrid layer was prepared by spin coating starting from a filtered P3HT solution mixed with ZnO nanoparticles (Picca et al., 2015) (1.5 mg/mL final concentration).

A suitable well for performing long-term studies under water was designed and fabricated to prevent possible water evaporation. It consists of a polystyrene (PS) cell glued with polydimethylsiloxane on the substrate. A PTFE tube connects the cell to a proper water reservoir in order to keep the water level constant in the well. The well is filled with 1.2 mL of water (HPLC-grade, Honeywell Riedel-de Haën) acting as gating medium. The scheme and the picture of the measuring set up are presented in **Figure 1**.

EGOFET Electrical Characterization

All the devices were characterized by means of a Keithley 4200-SCS semiconductor characterization system in air at room temperature (20–22°C) in a dark box. The drain current (I_D) was acquired scanning the gate voltage (V_G) between 0.1 and −0.5 V, keeping the drain voltage (V_D) at −0.4 V. The voltage step was set at 0.01 V. The source is grounded as typical in common source configuration measurements. Forward and backward scans were performed to evidence the occurrence of hysteretic behavior. A suitable measuring protocol was also set up as described in the results section. The potential window was defined according to the need to prevent any electrochemical process to occur and affect the EGOFET. To this aim, gate current (I_G) was also registered in order to monitor any spurious electrochemical process. Electrical figures-of-merit (μ_{FET} and V_T) were extracted from the I_D-V_G transfer characteristics in the saturation regime according to a well-known procedure (Torsi and Dodabalapur, 2005) and are averaged on 10 different devices ($n = 10$) operated

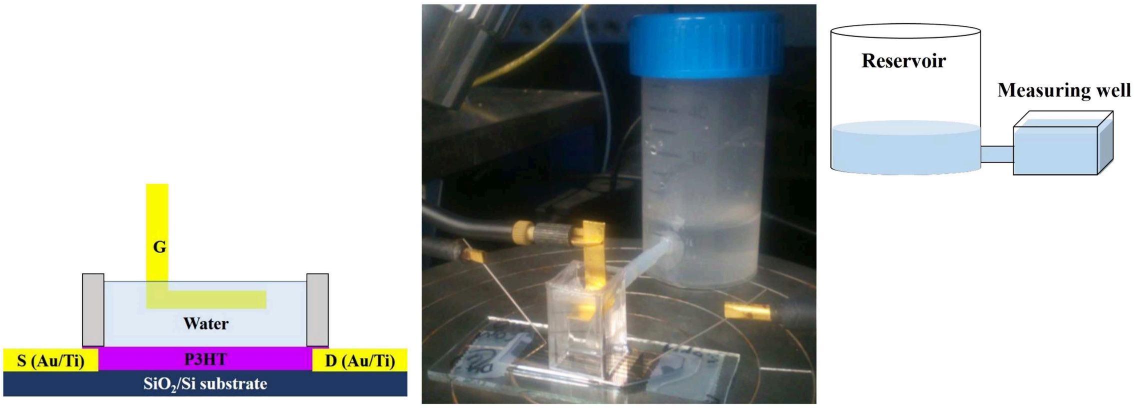

FIGURE 1 | Scheme and picture of the set up used for studying EGOFET devices. A top-gate bottom-contacts configuration is adopted.

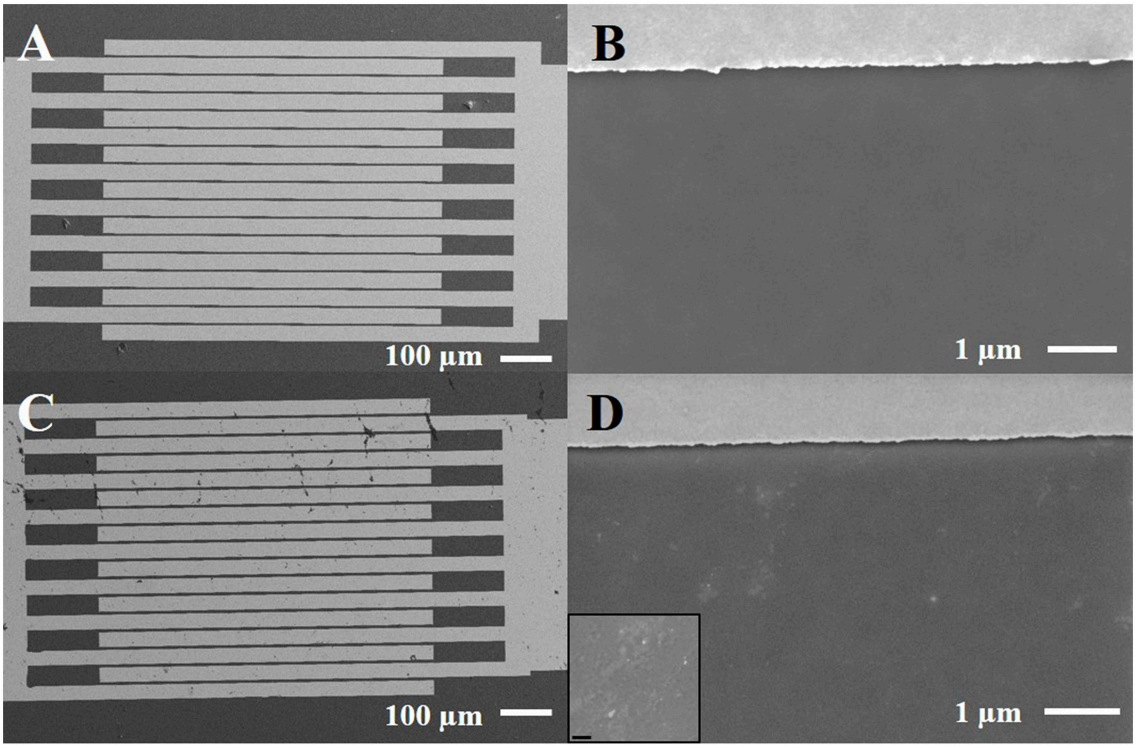

FIGURE 2 | Scanning electron micrographs of P3HT film deposited onto interdigitated electrodes, before **(A,B)** and after 2 weeks under water **(C,D)**. The inset refers to a zoom at higher magnification (scale bar corresponds to 200 nm) of the exposed sample.

in independent measurements. Error bars refer to one standard deviation calculated considering $n = 10$.

Morphological Analysis

Scanning electron microscopy (SEM) was applied to investigate the in-plane homogeneity of OS films deposited by spin coating. Analysis was performed by means of a Carl Zeiss Σigma field emission SEM on films prepared, both on interdigitated electrodes and on SiO_2/Si substrates. The probing electron beam was set at an acceleration voltage of 3–5 kV acquiring images at different magnifications in top-view. SE2 type detector was used to acquire the overall image of the device (**Figures 2A,C**), whereas the detailed view of the samples was recorded with the in-lens detector (**Figures 2B,D**).

Atomic Force Microscopy (AFM) characterization was performed on P3HT-based EGOFETs, just after their preparation and after contact with water for 2 weeks. AFM images were collected with a NT-MDT mod. Ntegra microscope in semi-contact mode using a tip apex size of 10 nm at a frequency $f = 180$ kHz. For each sample, areas of $3 \times 2\,\mu$m were investigated.

The Image Analysis Software was used to evaluate the surface roughness as route mean squared (RMS) on at least three representative areas of the sample.

X-ray Photoelectron Spectroscopy Surface Analysis

P3HT-based FETs were analyzed by means of X-ray photoelectron spectroscopy (XPS) using a PHI Versaprobe II Spectrometer. A monochromatized Al Kα radiation (1486.6 eV) was used. Survey spectra were acquired with a pass energy of 117.4 eV; whereas high-resolution (HR) spectra were acquired with a pass energy of 58.7 eV. C1s, O1s, Si2p, S2p, Au4f regions were investigated. Both as-prepared and used samples were characterized. MultiPak$^{\mathrm{TM}}$ (v. 9.7.0.1, PHI-ULVAC) software was used to process the data. Binding energy (BE) scale was corrected taking as reference C1s component at 284.8 eV. Three representative areas of the sample were collected to evaluate the chemical surface composition.

RESULTS AND DISCUSSION

SEM Characterization of P3HT Films

P3HT organic semiconductor has been typically successfully used by our group as active channel in FET biosensors with different architectures (Angione et al., 2012; Magliulo et al., 2013; Macchia et al., 2016). As a general procedure, P3HT films were prepared by spin-coating starting from a chloroform solution. However, SEM investigation on similar samples showed that P3HT layers were not uniform due to the presence of some voids and agglomerates (Sportelli et al., 2017). Chlorobenzene was then selected because of its higher boiling point as alternative solvent to improve layer uniformity and crystallinity, in agreement with what previously reported in the literature (Kergoat et al., 2011). SEM images of typical P3HT films, freshly deposited on a plain SiO_2/Si substrate and on gold electrodes, are presented in **Figures 2A,B**. It is evident that a rather uniform OS layer is formed confirming the advantages of processing P3HT from chlorobenzene. The very same samples were put in contact with water for 2 weeks and used as EGOFET devices (*vide infra*) and then characterized by SEM to evaluate a possible modification of layer uniformity. Additional features appear in the images (**Figures 2C,D**), though it seems that they are mainly related to the effect of water evaporation and presence of dust/salt particles (see the inset of the Figure). In fact, cracks and/or delamination of the polymer are not evident.

AFM Characterization of the OS Layer

Figure 3 shows two typical AFM images of an area of a P3HT FET, before (a) and after (b) 2-week exposure to water. RMS was calculated as an estimate of the roughness in both cases. A general increase in the roughness going from 0.5 ± 0.1 nm for pristine samples to 1.6 ± 0.2 nm after use was found. The low roughness observed on freshly prepared films is indicative of the goodness of the solvent using for processing the polymer in agreement with SEM results. After 2-week contact with water, the RMS increment can be attributed to a sort of polymer swelling. Nonetheless, dramatic changes in the surface morphology are not visible which account for the preservation of the FET modulation, at least in the investigated time scale.

XPS Characterization of P3HT Active Layers

The surface chemical composition of fresh and used P3HT-based devices was determined by XPS analysis (**Table 1**). The chemical composition does not seem particularly affected by contact with water, apart the higher oxygen content. Such finding is confirmed by spectral comparison of C1s, O1s, S2p regions (**Figure 4**) acquired before and after long exposure to water. Slight increment in carbon oxygenated components is observed (BE > 286 eV) suggesting a certain chemical degradation of the polymer. Nonetheless, the lineshape of S2p signal is preserved suggesting no oxidation on Sulfur. Interestingly, increment in the oxygen content is correlated to the presence of hydroxyl groups in addition to the O1s component ascribed to SiO_2 (BE = 532.5 ± 0.2 eV) (National Institute of Standards and Technology, 2012). XPS results suggest then that a partial modification of the polymer occurs within the investigated period, accounting for

TABLE 1 | Typical surface chemical composition of fresh ($t = 0$) and aged ($t = 15$ days in water) P3HT samples.

Sample ID	C%	S%	O%	Si%	Au%
P3HT ($t = 0$ day)	79.6	5.7	9.1	5.3	0.3
P3HT ($t = 15$ days)	80.5	5.4	10.9	3.0	0.2

Error on atomic percentages (At%) is ±0.2% for Au and ±0.5% for all the other elements.

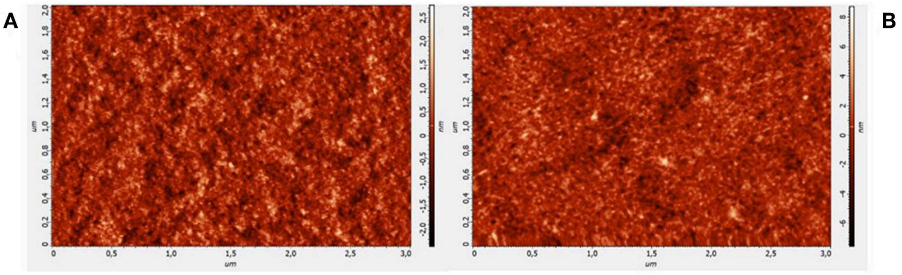

FIGURE 3 | AFM images of P3HT film deposited onto interdigitated electrodes, before **(A)** and after 2 weeks under water **(B)**.

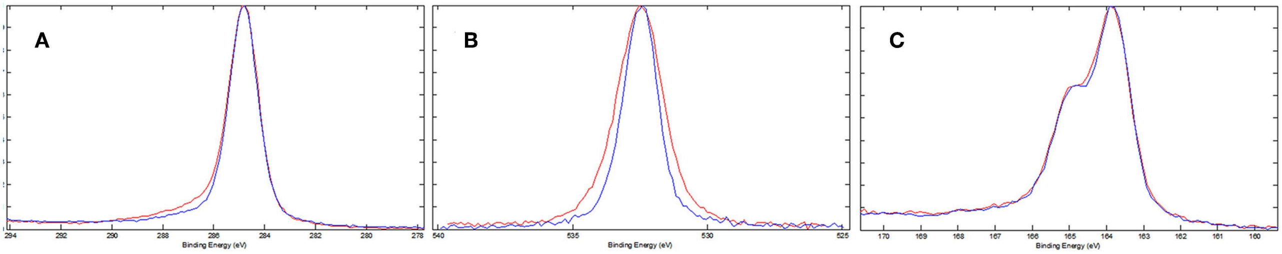

FIGURE 4 | C1s **(A)**, O1s **(B)**, S2p **(C)** XP regions registered for P3HT-based FETs, before (blue curves) and after contact with water for 2 weeks (red curves).

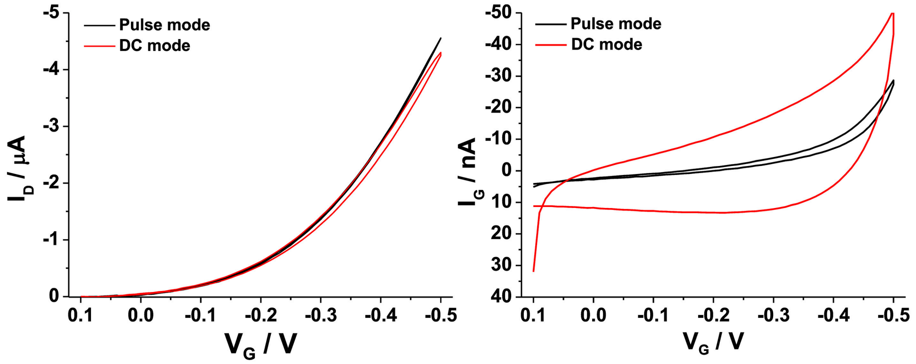

FIGURE 5 | I_D-V_G **(left)** and I_G-V_G **(right)** curves registered on a P3HT water-gated FET in pulse (black curves) or continuous (red curves) mode.

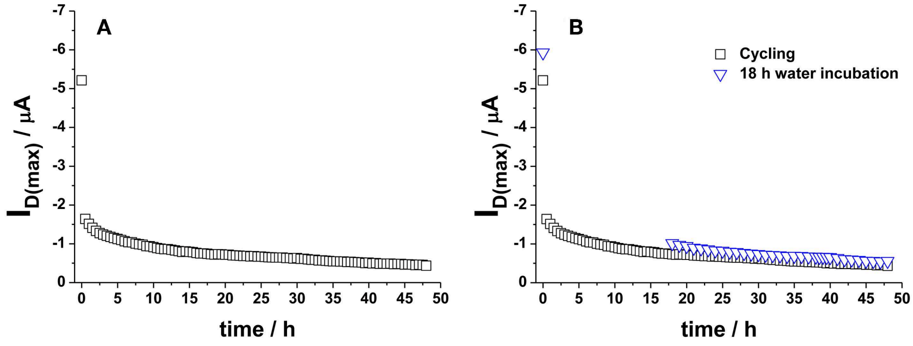

FIGURE 6 | (A) $I_{D(max)}$ (measured at $V_G = -0.5$ V) variation over 48 h when cycling mode is applied to water-gated P3HT FET. Data refer to transfer curves acquired every 30 min. **(B)** Comparison between $I_{D(max)}$ values reported in **(A)** and $I_{D(max)}$ registered on a water-gated P3HT FET incubated in water for 18 h (without operating it) (blue hollow triangles).

the increased roughness and the reduced electrical performance upon long exposure to water.

The Measuring Protocol

As anticipated, hysteresis, i.e., the difference between I_D values measured in the forward and backward gate voltage sweep, is one of the main issues that can arise when OFET devices are operated. In these cases, this behavior has been often attributed to the presence of moisture in the OS layer or at the OS/dielectric interface, especially when SiO_2 is used as gate dielectric (Bobbert et al., 2012). On the other hand, water-gated OFETs show minor hysteresis phenomena. This is mainly attributed to the absence of proton trapping in a dielectric and the occurrence of their neutralization by water autoprotolysis (Cramer et al., 2013). Hysteresis can be influenced by the sweeping potential window and by the scan rate of the applied potential (Panzer et al., 2005). For example, it was shown that scanning the V_G from the *off* to the *on* state (and *vice versa*) by applying pulses of alternating polarities was a suitable method to get hysteresis-free transfer curves in P3HT based FETs (Manoli et al., 2014). In this work, a similar protocol was adopted as reported in the **Supplementary Material**. It was observed that, regarding

V_G sweep protocol, keeping the *on* time equal to 10 ms (+1 s cumulative measure time) as compared to the *off* time (1 s) and selecting −0.05 V as base voltage, gave the best results. This means that a slow scan rate of about 40 mV/s is applied to V_G. Moreover, the V_D set at a maximum value of −0.4 V, was also pulsed keeping the *on* time (1 s) longer than the *off* time (0.1 s) at 0 V. A comparison between the performances of water-gated P3HT FETs operated in the DC-mode (red curves) or in the pulse-mode (black curves) is presented in **Figure 5**. The drain and the leakage currents (I_G) are reported as a function of V_G for the two cases. Apparently, the pulse mode contributes to measure a slightly increase I_D, and more relevantly to measure an almost hysteresis-free and reduced gate leakage current level. Taking the current values at $V_G = -0.5$ V, the ratio I_D/I_G in the pulse-mode was about twice the one measured in the DC-mode.

Operational Stability

The definition of a proper measurements protocol was beneficial to improve EGOFET performance level; however, it was not sufficient in limiting the degradation phenomena and hence the device long-term stability and reliability. In this respect, it is worth to dwell into the operational stability as well. A general scheme reported in literature involves the use of the so-called bias-stress mode consisting in the application of a continuous gate bias over time (Sirringhaus, 2009), though other approaches based on the cycling measurements of transfer curves have also been applied (Hwang et al., 2011). In this work, the interest was focused on the aspects connected with the application of EGOFETs as biosensing platforms; therefore, the operational stability of P3HT based devices was studied in water. To this aim, the typical sensing protocol followed in our laboratory in single-molecule detection (Macchia et al., 2018a) was simulated and the transfer curves of the fabricated devices were measured every half an hour using water and Au sheet as gating medium and gate electrode, respectively. A 30 min interval was chosen to mimic the time generally passing between two successive exposures to analyte solutions in a conventional sensing experiment. In fact, it is fundamental to get highly stable devices before using them in sensing platforms (Macchia et al., 2019b). P3HT based devices were then tested just after their fabrication. An example of the variation of the maximum current, $I_{D(max)}$ (measured at $V_G = -0.5$ V), over 48 h is shown in **Figure 6A**. It can be seen that a dramatic decrease in current occurs in the first cycles, whereas the current level almost reaches a steady state after 24 h. This trend was not surprising considering that the devices are not operated in an inert atmosphere. An alternative approach was explored to discriminate both the role of the measuring environment and of the operational protocol. Some devices were kept in contact with water just after their preparation (pristine sample) without operating them for the first 18 h. In this case, $I_{D(max)}$ variation over time (blue hollow triangles) is presented in **Figure 6B**. Interestingly, the two experiments led to very similar results, thus suggesting that the pronounced initial I_D decrease is essentially correlated to the adjustment of the polymer film in water environment. Quantitatively, a current decay of about 35% was generally observed for both the 18 h-cycled or the 18 h-water-incubated samples as reported in **Figure 7**. This fundamental aspect has never been clearly addressed in previous works about operational stability of OFET devices in water. It is worth noting that a similar decay was also reported for devices based on OS blended with polystyrene after 11 h of operation in water. In this case, a current decrease rate of about 3%/h was reported (Zhang et al., 2016). In this work, we observed that devices comprising a commercial P3HT seem more stable even in the first day after their preparation. After this period, the current drift is typically reduced and is around 1%/h allowing the P3HT based device to be very well suited to be used in ultra-sensitive biosensing experiments (Macchia et al., 2019b).

The timescale of this characterization was further extended taking into account the variation of the electrical figures-of-merit, μ_{FET}, V_T, and $I_{D(max)}$, over a time lease of 2 weeks. In this case, the devices were kept in water and measured in cycling mode for 5 h per day. The current values at $t = 0$ day and at $t = 15$ days are given in **Table 2**. The EGOFET devices comprising a P3HT channel material modified with an n-type nanostructured oxide were also tested under the same conditions. Such investigation was undertaken because in our previous studies ZnO nanoparticles were implemented in OFETs giving good performance in terms of electrical properties (Picca et al., 2015) and stability (Picca et al., 2018).

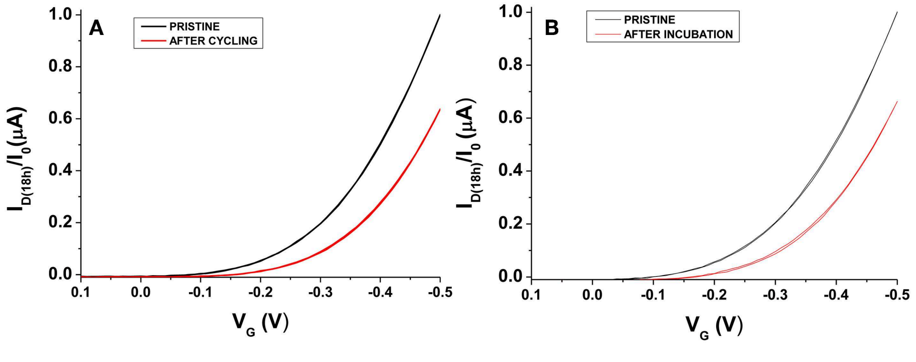

FIGURE 7 | I_D-V_G curves taken before (black) and after (red) 18 h for water-gated P3HT FETs operated in cycle mode **(A)** or just put in contact in water **(B)**. I_D has been normalized on the initial I_D value (I_0).

TABLE 2 | Device figures of merit estimated on fresh and aged samples (used for 2 weeks).

Sample ID	μ_{FET} (cm^{2}V^{-1}s^{-1})	V_T (V)	$\lvert I_{D(max)} \rvert$ (μA)
P3HT (*t* = 0 day)	$(5 \pm 2)*10^{-2}$	−0.03 ± 0.05	2.8 ± 1.2
P3HT (*t* = 15 days)	$(4 \pm 2)*10^{-2}$	−0.16 ± 0.05	1.1 ± 0.8
P3HT/ZnO (*t* = 0 day)	$(7 \pm 3)*10^{-2}$	−0.04 ± 0.03	5 ± 2
P3HT/ZnO (*t* = 15 days)	$(7 \pm 3)*10^{-2}$	−0.13 ± 0.03	3 ± 2

A comparison with P3HT devices bearing ZnO nanoparticles (P3HT/ZnO) is shown. Errors refer to one standard deviation for n = 10.

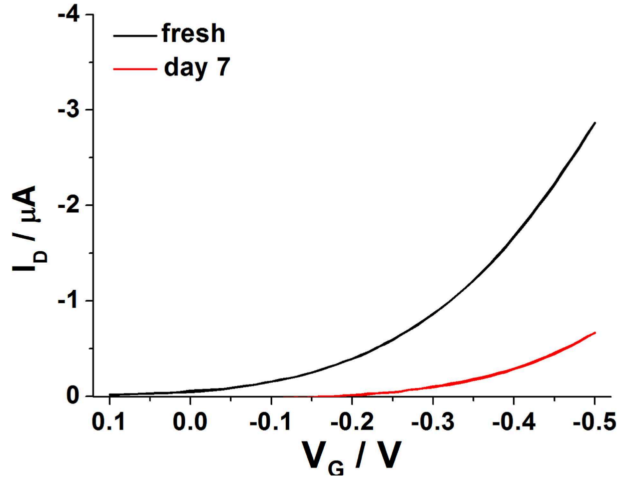

FIGURE 8 | Typical transfer curves registered on a water-gated P3HT FET, just after fabrication (black line) and after 7 days (red line).

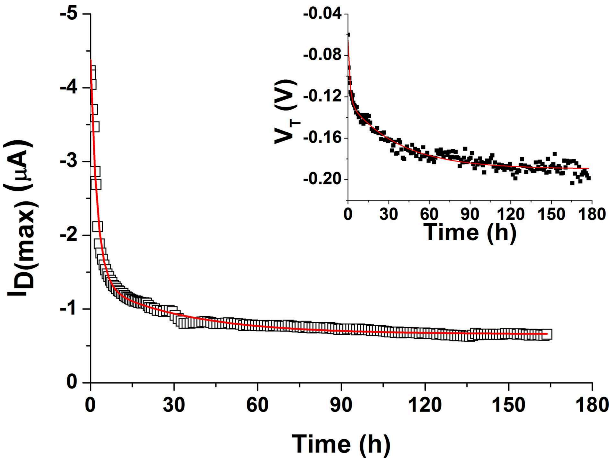

FIGURE 9 | Modeling of P3HT degradation over 7 days, expressed as $I_{D(max)}$ vs. time. In the inset, the shift in the threshold voltage is also fitted with the same function.

At a first inspection, it can be observed that the device degradation translates into a negative shift of the threshold voltage, V_T. Interestingly, mobility seems almost unaffected by the prolonged device operation in water. Similar findings were reported in other systems, as well. Moreover, the electrical performance and the stability of the devices were not significantly improved by the addiction of the ZnO nanostructures. This is not so surprising since in the previous work ZnO was deposited as separate layer underneath the P3HT film in a functional bio-interlayer OFET biosensor, thus behaving as capturing layer for water molecules at the interface between P3HT and the solid dielectric (Picca et al., 2018). On the other hand, recent data on water-gated devices based on P3HT films modified with WS_2 nanotubes showed an increased operational stability, quite likely due to the nanoscale morphology of the active blend layer (Macchia et al., 2018c).

As expected, the degradation cannot be avoided but it is in the order of the one reported for EGOFETs based on other materials. In fact, the current level was reduced of about 30% of its original value after 7 days (**Figure 8**), in agreement with data available in literature (Zhang et al., 2016). Furthermore, the study was focused on the modeling of device degradation under the experimental conditions explored in this work. In the past, works related to devices operating with a solid-state dielectric under bias stress proved that the V_T shift correlates with current decay, whereas mobility is almost unchanged (Salleo et al., 2005). Bias stress instability translates into a voltage threshold shift, and hence into I_D decay, which can be generally modeled with a single exponential decay function (Zhang et al., 2009). In the paper by Salleo et al. (2005) it was also observed that on a very short timescale (<100 s) almost all the charged traps could be recovered after bias removal indicating that these defect states have a short lifetime and are probably located in the more ordered regions of the organic semiconductor. In the same work, a long-lived component of trapped charges was also invoked. These traps are characterized by slow kinetics as they can last for days, thus being responsible for the observed lower V_T shift. It is believed that they are present in deep states, quite likely distributed in the disordered portions of P3HT.

In the field of EGOFETs, little is known about device degradation under operation and empirical approaches are typically employed to describe their behavior, typically carrying out the studies on a limited period (hours). Based on the experimental conditions employed in this work, the degradation of the prepared devices was followed in terms of $I_{D(max)}$ decay and V_T variation over 7 days (**Figure 9**). A double exponential decay function, expressed as $y = A1*\exp(-x/t1) + A2*\exp(-x/t2) + y0$, was used to fit both parameters. It is worth mentioning that such expression was already used in other works to describe recovery in pulse duty cycle studies (Miyadera et al., 2008; Manoli et al., 2014). However, both previous papers referred to OFET systems. The two extracted time constants (t1, t2) are similar for both drain current and threshold voltage changes, in agreement with previous observations. In particular, t1 is 1.8 ± 0.5 h and t2 is 35 ± 3 h. This means that two distinct processes impact on P3HT degradation processes occurring at different times. The first decay is responsible for the "rapid" current loss in the initial time-frame right after the incubation in water. Such trend could be in principle recovered within few days after stress removal (Sirringhaus, 2009). The second process may result from the presence of uncompensated immobile charges in the OS

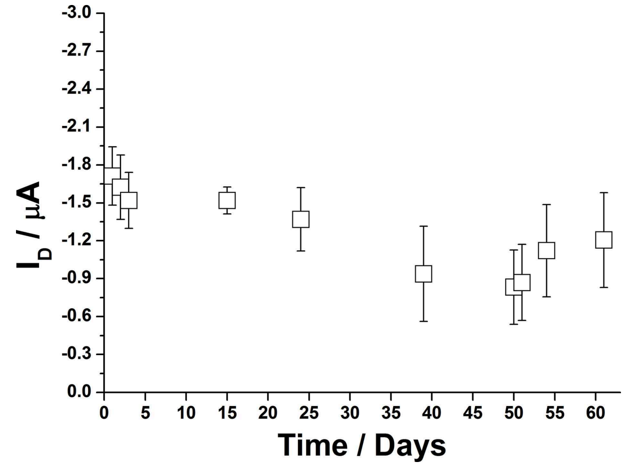

FIGURE 10 | Long-term stability of P3HT based EGOFETs, stored with a protecting layer of agarose gel. Error bars refer to one standard deviation calculated on three devices.

film. Obviously, due to continuous contact with the electrolyte, other effects such as the partial penetration of water in the P3HT film as well as formation of a passivating oxide layer on gold should be also taken into account. In particular, AFM and XPS results indicate that slight modifications in terms of morphology and composition of the polymer occur when devices are operated in water over a long period thus supporting the existence of degradation pathways responsible for the irreversible components of the decay model. It was generally reported that water molecules can penetrate the OS layer being then enclosed in the polymer nanovoids and causing trap formation (Nikolka et al., 2016; Zuo et al., 2019). This means that the latter component of degradation cannot be easily recovered and further studies will be necessary to clarify this behavior.

Shelf Life Extension

An important aspect for the development of EGOFET biosensors is related to their storage as well as to the possibility to use them several times. When continuously operated in water, it was observed that the very maximum time frame in which P3HT based OFETs can be used is about 20 days as upper limit. A protocol for improving their durability was then applied. As a proof-of-concept, agarose gel was employed as protecting layer for the P3HT channel when the device was not in use. In the proposed set up, $1\%_w$ agarose (300 μL) solution was poured on the P3HT film and let jellify directly in the measuring well. Then, the devices could be stocked in the dark at ambient conditions. The important point is that the device was constantly kept in contact with the water trapped in the gel-matrix. When needed, the agarose film could be easily removed and substituted with water for further device electrical characterization. After use, the gel layer could be deposited again. Shelf life was evaluated in terms of I_D measured on different days by acquiring a transfer curve, as reported in **Figure 10**. It can be seen that currents fluctuate in the order of the microampere, thus suggesting that agarose can be suitable for this application. More extensive studies will be performed to consider alternative protecting agents and/or strategies to further extend EGOFET durability.

CONCLUSIONS

The investigation of the degradation processes occurring on P3HT film serving as semiconducting channel material in water-gated field-effect-transistors was carried out adopting the measurement protocols successfully set in single-molecule biosensing experiments. A benchmark polymer without any additional treatment was used in the development of water-gated FETs to study its reliability on prolonged use. It was observed that no hysteresis and limited leakage currents were achieved not only by operating the OS in a voltage range where typical parasitic electrochemical processes are absent (i.e., water electrolysis, polymer oxidation), but also by the suitable set up of the measuring protocol. Furthermore, it was shown that water incubation more than operation in cycling mode is responsible for the initial abrupt current loss occurring in the first 20 h. Such behavior accounts for the unavoidable presence of water in between the polymer chains. The role of degradation in water for long period was also highlighted by SEM, AFM, and XPS analyses demonstrating that roughness increases and additional hydroxyl moieties are present. A model of P3HT EGOFET degradation operating the device over 1 week continuously was proposed suggesting that the current loss is due to the V_T shift by a bi-exponential decay. On the other hand, P3HT based devices could keep their electrical performance over a prolonged period if stored under ambient conditions with a protecting layer of agarose gel. Though we are aware that particular conditions and materials were applied in this study, this work can be a guide to investigate aspects of EGOFET device stability which could be critical for their use in transistor biosensors.

DATA AVAILABILITY STATEMENT

All datasets generated for this study are included in the manuscript/**Supplementary Files**.

AUTHOR CONTRIBUTIONS

RP, KM, EM, and AT carried out the EGOFET fabrication, including measuring cell design, and the electrical characterization. RP wrote the first draft of the manuscript and performed XPS characterization. KM set up the measuring protocol. CD and GS were responsible for interdigitated electrode fabrication, SEM, and AFM analyses. NC contributed to the investigation of spurious electrochemical processes. LT supervised the overall study, coordinated the team, and revised the manuscript as approved by all the authors.

ACKNOWLEDGMENTS

RP acknowledges the financial support of Fondo di Sviluppo e Coesione 2007-2013–APQ Ricerca Regione Puglia Programma regionale a sostegno della specializzazione intelligente e della sostenibilità sociale ed ambientale–Future In Research project #B164PG8 (BEND: Biosensori elettronici intelligenti per la diagnosi precoce di malattie neurodegenerative). Additional grants are acknowledged for partial financial support: SiMBiT: Single molecule bio-electronic smart system array for clinical testing funded by the European Commission under H2020 program, grant #824946, MIUR PON - e-DESIGN: Combination of Design, Electronics and Multifunctional Materials for New Aesthetic Components (ARS01_01158).

SUPPLEMENTARY MATERIAL

The Supplementary Material for this article can be found online at: https://www.frontiersin.org/articles/10.3389/fchem.2019.00667/full#supplementary-material

REFERENCES

Algarni, S. A., Althagafi, T. M., Naim, A. A., and Grell, M. (2016). A water-gated organic thin film transistor as a sensor for water-borne amines. *Talanta* 153, 107–110. doi: 10.1016/j.talanta.2016.01.068

Angione, M. D., Cotrone, S., Magliulo, M., Mallardi, A., Altamura, D., Giannini, C., et al. (2012). Interfacial electronic effects in functional biolayers integrated into organic field-effect transistors. *Proc. Natl. Acad. Sci.U.S.A.* 109, 6429–6434. doi: 10.1073/pnas.1200549109

Beatrup, D., Wade, J., Biniek, L., Bronstein, H., Hurhangee, M., Kim, J.-S., et al. (2014). Polaron stability in semiconducting polymer neat films. *Chem. Commun.* 50, 14425–14428. doi: 10.1039/C4CC06193D

Bellani, S., Fazzi, D., Bruno, P., Giussani, E., Canesi, E. V., Lanzani, G., et al. (2014). Reversible P3HT/oxygen charge transfer complex identification in thin films exposed to direct contact with water. *J. Phys. Chem. C* 118, 6291–6299. doi: 10.1021/jp4119309

Bobbert, P. A., Sharma, A., Mathijssen, S. G., Kemerink, M., and de Leeuw, D. M. (2012). Operational stability of organic field-effect transistors. *Adv. Mater.* 24, 1146–1158. doi: 10.1002/adma.201104580

Cramer, T., Campana, A., Leonardi, F., Casalini, S., Kyndiah, A., Murgia, M., et al. (2013). Water-gated organic field effect transistors – opportunities for biochemical sensing and extracellular signal transduction. *J. Mater. Chem. B* 1, 3728–3741. doi: 10.1039/c3tb20340a

de Leeuw, D. M., Simenon, M. M. J., Brown, A. R., and Einerhand, R. E. F. (1997). Stability of n-type doped conducting polymers and consequences for polymeric microelectronic devices. *Int. Conf. Sci. Technol. Synth. Met.* 87, 53–59. doi: 10.1016/S0379-6779(97)80097-5

Hwang, D. K., Fuentes-Hernandez, C., Kim, J., Potscavage, W. J., Kim, S.-J., and Kippelen, B. (2011). Top-gate organic field-effect transistors with high environmental and operational stability. *Adv. Mater.* 23, 1293–1298. doi: 10.1002/adma.201004278

Jia, X., Fuentes-Hernandez, C., Wang, C.-Y., Park, Y., and Kippelen, B. (2018). Stable organic thin-film transistors. *Sci. Adv.* 4:eaao1705. doi: 10.1126/sciadv.aao1705

Kergoat, L., Battaglini, N., Miozzo, L., Piro, B., Pham, M.-C., Yassar, A., et al. (2011). Use of poly(3-hexylthiophene)/poly(methyl methacrylate) (P3HT/PMMA) blends to improve the performance of water-gated organic field-effect transistors. *Org. Electron.* 12, 1253–1257. doi: 10.1016/j.orgel.2011.04.006

Kergoat, L., Herlogsson, L., Braga, D., Piro, B., Pham, M.-C., Crispin, X., et al. (2010). A water-gate organic field-effect transistor. *Adv. Mater.* 22, 2565–2569. doi: 10.1002/adma.200904163

Kim, S. H., Hong, K., Xie, W., Lee, K. H., Zhang, S., Lodge, T. P., et al. (2013). electrolyte-gated transistors for organic and printed electronics. *Adv. Mater.* 25, 1822–1846. doi: 10.1002/adma.201202790

Knopfmacher, O., Hammock, M. L., Appleton, A. L., Schwartz, G., Mei, J., Lei, T., et al. (2014). Highly stable organic polymer field-effect transistor sensor for selective detection in the marine environment. *Nat. Commun.* 5:2954. doi: 10.1038/ncomms3954

Lee, E. K., Lee, M. Y., Park, C. H., Lee, H. R., and Oh, J. H. (2017). Toward environmentally robust organic electronics: approaches and applications. *Adv. Mater.* 29:1703638. doi: 10.1002/adma.201703638

Li, H., Shi, W., Song, J., Jang, H.-J., Dailey, J., Yu, J., et al. (2018). Chemical and biomolecule sensing with organic field-effect transistors. *Chem. Rev*. 119, 3–35. doi: 10.1021/acs.chemrev.8b00016

Macchia, E., Alberga, D., Manoli, K., Mangiatordi, G. F., Magliulo, M., Palazzo, G., et al. (2016). Organic bioelectronics probing conformational changes in surface confined proteins. *Sci. Rep.* 6:28085. doi: 10.1038/srep28085

Macchia, E., Manoli, K., Holzer, B., Di Franco, C., Ghittorelli, M., Torricelli, F., et al. (2018a). Single-molecule detection with a millimetre-sized transistor. *Nat. Commun.* 9:3223. doi: 10.1038/s41467-018-05235-z

Macchia, E., Manoli, K., Holzer, B., Di Franco, C., Picca, R. A., Cioffi, N., et al. (2019a). Selective single-molecule analytical detection of C-reactive protein in saliva with an organic transistor. *Anal. Bioanal. Chem.* 411, 4899–4908. doi: 10.1007/s00216-019-01778-2

Macchia, E., Romele, P., Manoli, K., Ghittorelli, M., Magliulo, M., Kovács-Vajna, Z. M., et al. (2018b). Ultra-sensitive protein detection with organic electrochemical transistors printed on plastic substrates. *Flex. Print. Electron.* 3:034002. doi: 10.1088/2058-8585/aad0cb

Macchia, E., Tiwari, A., Manoli, K., Holzer, B., Ditaranto, N., Picca, R. A., et al. (2019b). Label-free and selective single-molecule bioelectronic sensing with a millimeter-wide self-assembled monolayer of anti-immunoglobulins. *Chem. Mater*. 31, 6476–6483. doi: 10.1021/acs.chemmater.8b04414

Macchia, E., Zak, A., Picca, R. A., Manoli, K., Di Franco, C., Cioffi, N., et al. (2018c). improved performance p-type polymer (P3HT) / n-type nanotubes (WS2) electrolyte gated thin-film transistor. *MRS Adv.* 3, 1525–1533. doi: 10.1557/adv.2018.311

Magliulo, M., Mallardi, A., Mulla, M. Y., Cotrone, S., Pistillo, B. R., Favia, P., et al. (2013). Electrolyte-gated organic field-effect transistor sensors based on supported biotinylated phospholipid bilayer. *Adv. Mater.* 25, 2090–2094. doi: 10.1002/adma.201203587

Manoli, K., Magliulo, M., Mulla, M. Y., Singh, M., Sabbatini, L., Palazzo, G., et al. (2015). printable bioelectronics to investigate functional biological interfaces. *Angew. Chem. Int. Ed.* 54, 12562–12576. doi: 10.1002/anie.201502615

Manoli, K., Patrikoussakis, M. M., Magliulo, M., Dumitru, L. M., Mulla, M. Y., Sabbatini, L., et al. (2014). Pulsed voltage driven organic field-effect transistors for high stability transient current measurements. *Org. Electron.* 15, 2372–2380. doi: 10.1016/j.orgel.2014.06.034

Miyadera, T., Minari, T., Wang, S. D., and Tsukagoshi, K. (2008). Dynamic bias stress current instability caused by charge trapping and detrapping in pentacene thin film transistors. *Appl. Phys. Lett.* 93:213302. doi: 10.1063/1.3037213

Mulla, M. Y., Tuccori, E., Magliulo, M., Lattanzi, G., Palazzo, G., Persaud, K., et al. (2015). Capacitance-modulated transistor detects odorant binding protein chiral interactions. *Nat. Commun.* 6:6010. doi: 10.1038/ncomms7010

National Institute of Standards and Technology (2012). *XPS Database. NIST X-Ray Photoelectron Spectrosc. Database Version 41*. Available online at: http://srdata.nist.gov/xps

Nikolka, M., Nasrallah, I., Rose, B., Ravva, M. K., Broch, K., Sadhanala, A., et al. (2016). High operational and environmental stability of high-mobility conjugated polymer field-effect transistors through the use of molecular additives. *Nat. Mater.* 16, 356–362. doi: 10.1038/nmat4785

Panzer, M. J., and Frisbie, C. D. (2008). Exploiting ionic coupling in electronic devices: electrolyte-gated organic field-effect transistors. *Adv. Mater.* 20, 3177–3180. doi: 10.1002/adma.200800617

Panzer, M. J., Newman, C. R., and Frisbie, C. D. (2005). Low-voltage operation of a pentacene field-effect transistor with a polymer electrolyte gate dielectric. *Appl. Phys. Lett.* 86:103503. doi: 10.1063/1.1880434

Picca, R. A., Manoli, K., Luciano, A., Sportelli, M. C., Palazzo, G., Torsi, L., et al. (2018). Enhanced stability of organic field-effect transistor biosensors bearing electrosynthesized ZnO nanoparticles. *Sens. Actuators B Chem.* 274, 210–217. doi: 10.1016/j.snb.2018.07.128

Picca, R. A., Sportelli, M. C., Hötger, D., Manoli, K., Kranz, C., Mizaikoff, B., et al. (2015). Electrosynthesis and characterization of ZnO nanoparticles as inorganic component in organic thin-film transistor active layers. *Electrochim. Acta* 178, 45–54. doi: 10.1016/j.electacta.2015.07.122

Porrazzo, R., Bellani, S., Luzio, A., Lanzarini, E., Caironi, M., and Antognazza, M. R. (2014). Improving mobility and electrochemical stability of a water-gated polymer field-effect transistor. *Org. Electron.* 15, 2126–2134. doi: 10.1016/j.orgel.2014.06.002

Salleo, A., Endicott, F., and Street, R. A. (2005). Reversible and irreversible trapping at room temperature in poly(thiophene) thin-film transistors. *Appl. Phys. Lett.* 86:263505. doi: 10.1063/1.1968437

Sharma, A., Mathijssen, S. G. J., Cramer, T., Kemerink, M., de Leeuw, D. M., and Bobbert, P. A. (2010). Anomalous current transients in organic field-effect transistors. *Appl. Phys. Lett.* 96:103306. doi: 10.1063/1.3339879

Sirringhaus, H. (2005). Device physics of solution-processed organic field-effect transistors. *Adv. Mater.* 17, 2411–2425. doi: 10.1002/adma.200501152

Sirringhaus, H. (2009). Reliability of organic field-effect transistors. *Adv. Mater.* 21, 3859–3873. doi: 10.1002/adma.200901136

Sportelli, M. C., Picca, R. A., Manoli, K., Re, M., Pesce, E., Tapfer, L., et al. (2017). Surface analytical characterization of Streptavidin/poly(3–hexylthiophene) bilayers for bio-electronic applications. *Appl. Surf. Sci.* 420, 313–322. doi: 10.1016/j.apsusc.2017.05.086

Surya, S. G., Raval, H. N., Ahmad, R., Sonar, P., Salama, K. N., and Rao, V. R. (2019). Organic field effect transistors (OFETs) in environmental sensing and health monitoring: A review. *TrAC Trends Anal. Chem.* 111, 27–36. doi: 10.1016/j.trac.2018.11.027

Torsi, L., and Dodabalapur, A. (2005). Organic thin-film transistors as plastic analytical sensors. *Anal. Chem.* 77, 380A—387A. doi: 10.1021/ac053475n

Torsi, L., Magliulo, M., Manoli, K., and Palazzo, G. (2013). Organic field-effect transistor sensors: a tutorial review. *Chem. Soc. Rev.* 42, 8612–8628. doi: 10.1039/c3cs60127g

Wade, J., Wood, S., Beatrup, D., Hurhangee, M., Bronstein, H., McCulloch, I., et al. (2015). Operational electrochemical stability of thiophene-thiazole copolymers probed by resonant Raman spectroscopy. *J. Chem. Phys.* 142:244904. doi: 10.1063/1.4923197

Wang, D., Noël, V., and Piro, B. (2016). Electrolytic gated organic field-effect transistors for application in biosensors—a review. *Electronics* 5:9. doi: 10.3390/electronics5010009

Yu, D., Yang, Y.-Q., Chen, Z., Tao, Y., and Liu, Y.-F. (2016). Recent progress on thin-film encapsulation technologies for organic electronic devices. *Opt. Commun.* 362, 43–49. doi: 10.1016/j.optcom.2015.08.021

Zhang, Q., Leonardi, F., Casalini, S., Temiño, I., and Mas-Torrent, M. (2016). High performing solution-coated electrolyte-gated organic field-effect transistors for aqueous media operation. *Sci. Rep.* 6:39623. doi: 10.1038/srep39623

Zhang, X.-H., Tiwari, S. P., and Kippelen, B. (2009). Pentacene organic field-effect transistors with polymeric dielectric interfaces: performance and stability. *Org. Electron.* 10, 1133–1140. doi: 10.1016/j.orgel.2009.06.001

Zuo, G., Linares, M., Upreti, T., and Kemerink, M. (2019). General rule for the energy of water-induced traps in organic semiconductors. *Nat. Mater.* 18, 588–593. doi: 10.1038/s41563-019-0347-y

Conflict of Interest: The authors declare that the research was conducted in the absence of any commercial or financial relationships that could be construed as a potential conflict of interest.

Advantages of publishing in Frontiers

OPEN ACCESS
Articles are free to read
for greatest visibility
and readership

FAST PUBLICATION
Around 90 days
from submission
to decision

HIGH QUALITY PEER-REVIEW
Rigorous, collaborative,
and constructive
peer-review

TRANSPARENT PEER-REVIEW
Editors and reviewers
acknowledged by name
on published articles

Frontiers
Avenue du Tribunal-Fédéral 34
1005 Lausanne | Switzerland

Visit us: www.frontiersin.org
Contact us: info@frontiersin.org | +41 21 510 17 00

REPRODUCIBILITY OF RESEARCH
Support open data
and methods to enhance
research reproducibility

DIGITAL PUBLISHING
Articles designed
for optimal readership
across devices

FOLLOW US
@frontiersin

IMPACT METRICS
Advanced article metrics
track visibility across
digital media

EXTENSIVE PROMOTION
Marketing
and promotion
of impactful research

LOOP RESEARCH NETWORK
Our network
increases your
article's readership